Single Particle Structure of Exotic Strontium Isotopes

Using Single Neutron Transfer Reactions as a Tool to Study the Evolution of Nuclear Structure

by

Steffen James Cruz

M.Sci., The University of Birmingham, England, 2012

A THESIS SUBMITTED IN PARTIAL FULFILLMENT OF
THE REQUIREMENTS FOR THE DEGREE OF

DOCTOR OF PHILOSOPHY

in

The Faculty of Graduate and Postdoctoral Studies

(Physics)

THE UNIVERSITY OF BRITISH COLUMBIA

(Vancouver)

June 2017

Abstract

The sudden onset of ground state deformation and the emergence of shape-coexisting states in the vicinity of N$\sim$60 and Z$\sim$40 has been a subject of substantial interest for many years. It has been shown that the emergence of deformed low-energy configurations can be explained in the shell model by the evolution of single particle structure and the interaction between protons and neutrons in certain valence orbitals. However, the numerous theoretical models that have been developed for this transitional region are limited by the experimental data that is available. In particular, a description of the underlying single particle configurations of low energy states is essential for a detailed description of this region.

In this work, the single particle structure of states in ^{95}Sr and ^{96}Sr has been investigated through the one-neutron transfer reactions ^{94,95}Sr(d,p) in inverse kinematics at TRIUMF. In each of these experiments, a 5.5 MeV/u Sr beam was impinged on a 5.0 mg/cm^2 CD$_2$ target, and emitted particles and γ-rays were detected using the SHARC and TIGRESS detector arrays, respectively. Using an angular distribution analysis, firm spin assignments have been made for the first time of the low-lying 352 keV, 556 keV and 681 keV excited states in ^{95}Sr from ^{94}Sr(d,p), and a constraint has been made on the spin of the higher-lying 1666 keV excited state in ^{95}Sr. Similarly, angular distributions have been extracted for 12 states in ^{96}Sr from ^{95}Sr(d,p), and new experimental constraints have been assigned to the spins and parities of 8 states in ^{96}Sr. Additionally, two new states in ^{96}Sr have been identified in this work. A measurement of the mixing strength between the 1229 keV and 1465 keV shape-coexisting states in ^{96}Sr was also made, which was found to be $a^2 = 0.48(17)$.

Lay Summary

Neutron-rich isotopes of strontium exhibit an abrupt change of structure in their lowest energy states at the neutron number N=60. This sudden transition occurs as a result of the delicate interplay between several different nuclear structure phenomena. Such dramatic structural changes in nuclei are rarely observed and so they present a unique and exciting opportunity to learn about the nuclear force and to refine our theoretical tools. These exotic strontium isotopes have been a subject of substantial interest for a number of years, however a precise description of this region has been restricted by the very limited experimental data available.

In this work, a systematic study has been carried out to elucidate the structure of 17 states in ^{95}Sr (N=57) and ^{96}Sr (N=58) which are very important isotopes. These measurements can now be used to advance our understanding of this structural transition and also to benchmark current theoretical models.

Preface

This dissertation is original intellectual work by the author, S. Cruz. At the time of submission, the content of this thesis is unpublished.

All of the experimental work presented henceforth was carried out at TRIUMF, Canada's national laboratory for particle and nuclear physics and accelerator-based science in Vancouver, British Columbia. The proposal for this work (Exp. No. S1389) was written by the spokespeople Dr. K. Wimmer and Dr. R. Krücken, with some contributed calculations from this author. The experiments were carried out as part of a larger collaboration, with approximately 30 members. The primary contributions of the S1389 collaboration members were to oversee the data acquisition by volunteering for beam shifts and to assist with setting up the experimental apparatus.

All of the calibrations, analysis, results and calculations are the work of this author.

Table of Contents

List of Tables

List of Figures

Acknowledgements

First of all, thank you to Dr. Reiner Krücken for granting me this opportunity to carry out cutting-edge research at a world-class institution such as TRIUMF, and for your guidance and support throughout these years.

I would also like offer my most sincere gratitude to Dr. Peter Bender and Dr. Kathrin Wimmer for their tireless discussions and endless encouragement, particularly when I needed it most. Without you both I would probably still be calibrating SHARC (which will be discussed in section 4).

I would also like to extend my thanks to the S1389 collaboration members for their participation in the experiments, and especially to Dr. Greg Hackman for his contributions to this project.

To my supportive family and friends, thank you for your love and patience, and for always reminding me that home is just a phone call away.

Finally, I would like to thank my new friends in Canada. You have made these years unforgettable.

Dedication

To Carole,

whose footsteps will always be beside my own.

You continue to be my inspiration in life.

Chapter 1

Introduction

It was noted by Meyer and Jensen in 1949 [May49][HJS49] that experimentally observed systematic trends in binding energies and excited states energies across the nuclear landscape could be well-described by the existence of shell structure in nuclei. It was known at the time that the atomic shell model successfully predicts many of the chemical properties of atoms. The atomic shell model is based on the assumption that electrons are confined to well-defined orbitals, and that the motion of the electrons in these orbital is essentially independent. Similarly, in the nuclear shell model it is assumed that the protons and neutrons move in independent single particle orbitals, within a mean field that is generated by the interaction with all the other nucleons.

In the nuclear shell model, low-energy states are described by a residual interaction which acts between nucleons in the mean field [Hey90]. One aspect of the residual interaction is the strong pairing interaction which acts between like-nucleons within the same orbital. The pairing interaction allows like-nucleon pairs to gain additional binding energy by anti-aligning their intrinsic spins to $S = 0$. The importance of the pairing interaction is evidenced by the observation that all even-N, even-Z nuclei have total angular momentum (J) and parity (π) of $J^\pi = 0^+$ in their ground states. In addition to coupling nucleon pairs to $J = 0$, the pairing interaction is responsible for the scattering of nucleon pairs across valence orbitals, which in turn tends to cause partial occupancy of orbitals above the Fermi energy [Cas00]. The occupancy of these higher orbitals in turn depends on their energy relative to the Fermi energy.

One of the major predictions of the shell model is the existence of magic numbers [Kra88]. In so-called magic nuclei, there are substantial energy gaps between the filled orbitals and higher unfilled orbitals. Magic nuclei are especially bound because these large energy gaps strongly suppress the scattering of valence nucleons into the higher orbitals [Hey90], which is similar to

the role of filled electron shells in noble gases.

1.1 Deformation in Nuclei

An atomic nucleus can deform its shape in order to minimize its energy. This is observed across the nuclear landscape, both in ground states and excited states. Figure 1.1a shows the degree of predicted ground state quadrupole deformation across the nuclear chart. The dark blue regions of figure 1.1a indicate nuclei which are expected to have approximately spherical ground states, and these regions correspond to nuclei with magic numbers of protons and neutrons.

Another striking feature of figure 1.1a is that most nuclei are expected to have non-spherical shapes in their lowest energy states, which can be seen by the rather abrupt colour change in figure 1.1a as we depart from nuclei with magic numbers of protons and neutrons. It seems that even a small number of valence protons and neutrons outside of a closed core can drive the whole nucleus into a deformed shape. Clearly, the underlying shell structure of nuclei plays an important role in the propensity for nuclei to deform.

(a)   (b)
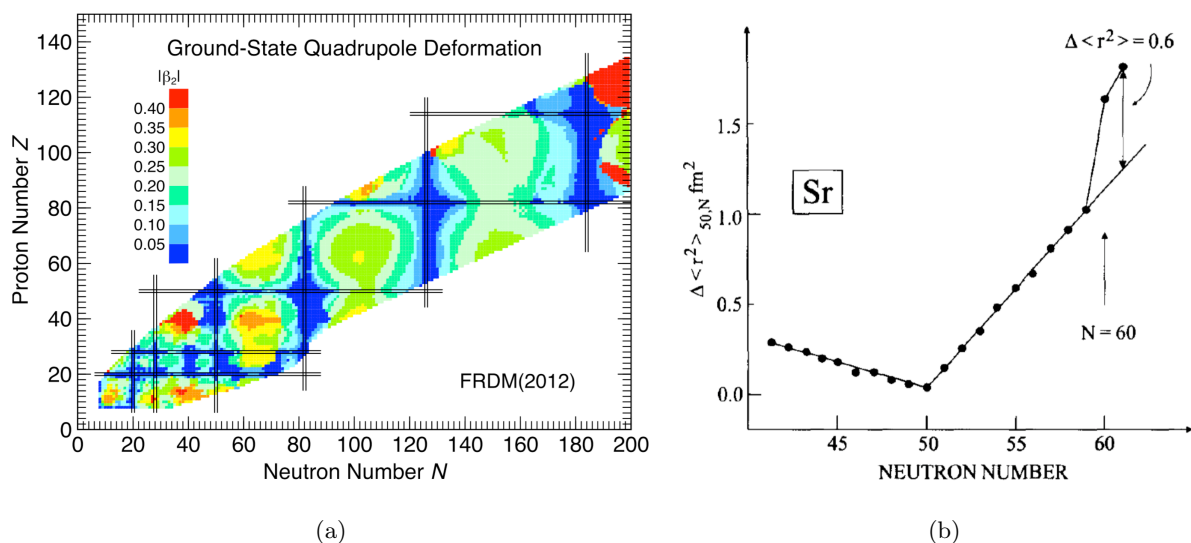
Figure 1.1: (a) Finite range drop model (FRDM) calculation of the ground state deformation across the nuclear chart (taken from [MSI$^+$16]). The solid lines correspond to nuclei with magic numbers of protons and neutrons, which are predicted to have spherical shapes. (b) Isotope shift across the Sr isotopic chain indicates that there is a sudden transition from spherical to deformed ground states at $N = 60$ (taken from [WZD$^+$99]).

There are two primary components of nuclear shell structure which must be understood in order to describe deformation. Firstly, the microscopic mechanism which drives nuclei to deformation is attributed to the long-range attractive proton-neutron $(p - n)$ residual interaction [Cas00]. The strongest component of the long-range $p - n$ residual interaction is the quadrupole term, which is why quadrupole deformation is particularly common in nuclei [Cas00]. This residual $p - n$ interaction allows the nucleus to gain additional binding energy by arranging protons and neutrons in certain ways across the valence orbitals, which in turn causes a departure from sphericity. Secondly, the size of the energy gaps between single particle orbitals above the Fermi energy plays a central role. If the energy spacing is small, the valence nucleons can scatter into valence orbitals which are above the Fermi energy and drive the nucleus into a low-energy deformed configuration. On the other hand, if the energy spacing is large, the valence nucleons are unable to scatter into higher orbitals and this favours spherical shapes. The size of these energy gaps is in turn dependent on the number of valence nucleons, due to the monopole component of the residual interaction (see section 1.4 for further details). In summary, the competition between deformed and spherical shapes in nuclei is governed by the evolution of single particle structure and the interplay between the short-range pairing and the long-range $p-n$ interactions.

Figure 1.1b shows experimental measurements of the isotope shift across the strontium (Sr) isotopic chain. The isotope shift, $\Delta\langle r^2 \rangle$, is a measure of the change in the nuclear radius between adjacent isotopes, and can be used to study to the evolution of the ground state shape across an isotopic chain. It can be seen in figure 1.1b that the radius of the ground state evolves gradually as a function of increasing neutron number, and reaches its minimum at $N = 50$. $N = 50$ is a magic number, and so this minimum can be explained in terms of a large energy gap which suppresses the scattering of valence nucleons above the Fermi surface and gives rise to a spherical ground state. The isotope shift continues to rise steadily as the number of neutrons increases beyond $N = 50$ due to increased occupation of higher-lying orbitals, up until $N = 60$, at which point a sudden increase in the ground state radius is observed. This indicates that a shape transition has taken place, and that the lowest energy configuration in Sr becomes a strongly deformed structure.

In some regions of the nuclear chart, there are spherical and deformed shapes which offer almost degenerate energy minimizations. This is remarkable, considering that the underlying single particle configurations are significantly different for spherical and deformed nuclei. In these cases, the shapes are said to be coexisting and in some cases can mix very strongly [WZD$^+$99][HW11]. In strongly mixed shape-coexisting states, the nucleus is therefore in a quantum superposition of two different many-body wavefunctions. Shape coexistence appears to be a unique feature of finite many-body quantum systems, and is intimately related to the physics of phase transitions [Cas00].

1.2   Onset of Deformation at $Z \sim 40$, $N \sim 60$

As was shown in figure 1.1b, it has been observed that Sr undergoes a ground state shape transition at $N = 60$. This shape transition is in fact observed in several nuclei in the $A \sim 100$ region, at $Z \sim 40$ and $N \sim 60$ [EMS88]. Another experimental indicator of deformation in nuclei can be found in the excited state spectrum. Deformed nuclei often have a very low energy first excited state compared to spherical nuclei, which is caused by the additional collective degrees of freedom. Figure 1.2a shows the energy of the first excited state, $E(2_1^+)$, for several even-even nuclei in the vicinity of $Z \sim 40$ and $N \sim 60$. It can be seen that there is a sudden drop in the $E(2_1^+)$ energy in Sr ($Z = 38$), Zr ($Z = 40$) and to a lesser degree, Mo ($Z = 42$) at $N = 60$. It can also be seen in figure 1.2a that the transition to deformation is much more gradual in the Ru ($Z = 44$) isotopic chain, which indicates that the proton degrees of freedom are important in this transitional region.

Given that the ground states of the $N = 60$ isotones ^{98}Sr and ^{100}Zr have strongly deformed shapes, it is clear that an inversion between sphericity and deformation in the low-lying states is taking place in this mass region. Beyond mean field calculations have been carried out [RGSR$^+$10], which predict the potential energy as a function of deformation. Figure 1.2b shows the theoretical potential energy curves for several isotopes of Sr, Zr and Mo. It can be seen that close to stability ($N = 52$ isotopes), the potential energy curves have a single minimum which corresponds to a spherical shape. As neutrons are added to these isotopes, multiple
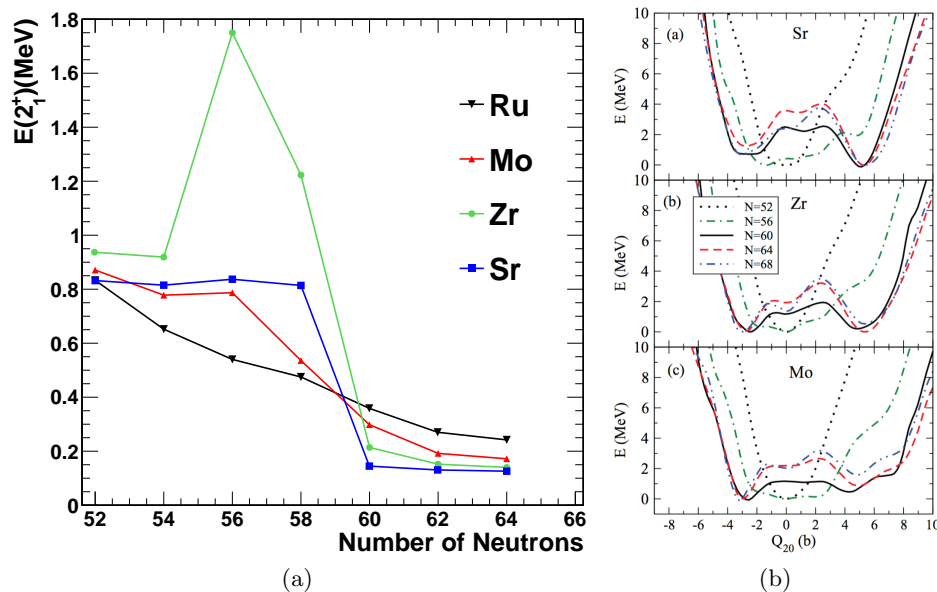
Figure 1.2: (a) Experimentally measured energy of the first excited (2_1^+) state in even-even nuclei in the vicinity of $Z \sim 40$ and $N \sim 60$ (data taken from [Lab]). (b) Beyond mean field calculations of potential energy as a function of quadrupole moment (Q_{20}) in Sr, Zr and Mo isotopic chains (taken from [RGSR$^+$10]).

minima begin to form in the potential energy curves up until $N = 60$, where the ground state (global minimum) becomes a deformed nuclear shape. In addition to this, it can be seen that the multiple minima in figure 1.2b are almost degenerate in energy and have different shapes, which is to say that they are predicted to be shape-coexisting.

It was demonstrated by Federman and Pittel [FP79] that the sudden onset of deformation in this region can be described in the shell model by the residual interaction between proton and neutron spin-orbit partner orbitals. Their proposed mechanism is illustrated in figure 1.3. As the number of neutrons increases beyond $N = 50$, the $\nu 1d\frac{5}{2}$ orbital is gradually filled (and is approximately full at $N = 56$) and the residual interaction between the valence neutrons gradually lowers the energy of the higher-lying $\nu 2s\frac{1}{2}$, $\nu 1d\frac{3}{2}$ and $\nu 0g\frac{7}{2}$ orbitals. As the number of neutrons approaches $N = 60$, there is increased occupancy of the neutron $\nu 0g\frac{7}{2}$ orbital in the low-lying states due to pair scattering across the Fermi surface. The residual $p - n$ interaction strongly affects orbitals with a large spatial overlap, and so the nucleus is able to lower its energy by re-arranging the valence protons so that they occupy the $\pi 0g\frac{9}{2}$ orbital in tandem with
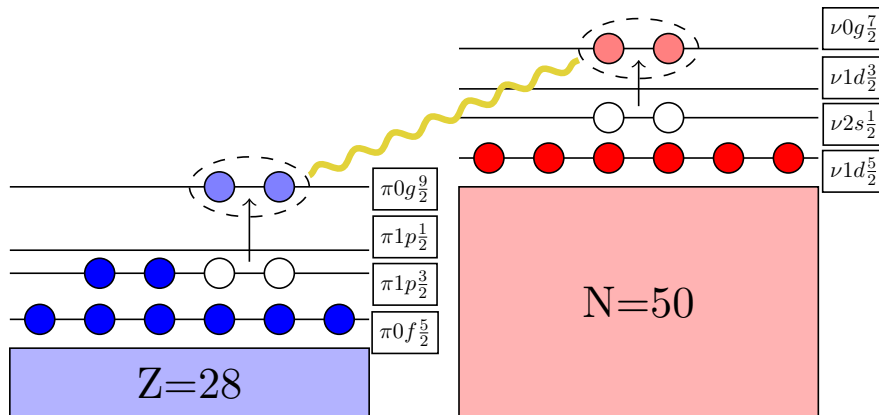
Figure 1.3: Federman and Pittel mechanism for the onset of deformation in ^{96}Sr [FP79].

the neutrons in the $\nu 0g\frac{7}{2}$ orbital. This particular configuration of valence protons and neutrons generates deformation, and so a competition between low energy spherical and deformed shapes arises.

It was also shown by Federman and Pittel that there is quenching of the proton $1p\frac{3}{2}$ and $1p\frac{1}{2}$ orbitals in the Sr and Zr isotopes [FPE84], which is to say they their spin-orbit splitting is reduced. This is evidenced by the constant $E(2_1^+)$ values for Sr isotopes for $N < 60$ in figure 1.2a, which is in contrast to the $E(2_1^+)$ values of the Zr isotones. At $N = 56$, the $E(2_1^+)$ values for Zr isotopes rises abruptly, which indicates that there are fully occupied orbitals with substantial energy gaps to unfilled orbitals above the Fermi energy. In other words, the increase in the $E(2_1^+)$ value at $N = 56$ is evidence for a significant shell closure as the $\nu 1d\frac{5}{2}$ orbital is filled. Contrastingly, the constant $E(2_1^+)$ values in Sr indicate that a low energy $J^\pi = 2^+$ configuration persists, which can be explained by a low energy $[\pi 1p\frac{3}{2}]^2_{J=2}[\pi 1p\frac{1}{2}]^2_{J=0}$ configuration. This quenching of the $\pi 1p$ orbitals results in a very similar energy gap between the Fermi energy and the $\pi 0g\frac{9}{2}$ orbital in Sr compared to Zr, and so it also serves to explain why both Sr and Zr undergo such similar shape transitions at $N = 60$ [Lab].

By generalizing the mechanism of Federman and Pittel to other nuclei in this mass region, it is also possible to discuss why the sudden transition to deformation is only seen in Sr and Zr. The energy gap between the valence $\pi 1p\frac{1}{2}$ and $\pi 0g\frac{9}{2}$ orbitals effectively regulates the onset of deformation for $Z \leq 40$ nuclei. For nuclei with $Z > 40$ such as Mo, there is already substantial occupation of the $\pi 0g\frac{9}{2}$ orbital and so the ground state shape transition is more gradual.

The sudden onset of ground state deformation in Sr and Zr at $N = 60$ is the result of a gradual lowering of the deformed configuration across several isotopes, which ultimately becomes the lowest energy state. In ^{96}Sr and ^{98}Zr, evidence for a deformed low-lying excited 0^+ state has been found and this is expected to have a similar structure as the deformed ground states in the $N = 60$ isotones [WZD$^+$99][HW11][LPK$^+$94]. The proposed evolution of the spherical and deformed structures is shown in figure 1.4, which compares their relative energy at $N = 58$ and $N = 60$. For an axially symmetric quadrupole-deformed nucleus, the shape of the surface, $R(\theta, \phi)$, is described by [Kra88]

$$R(\theta, \phi) = R_{\text{av}} \left[1 + \beta Y_{20}(\theta, \phi) \right] \qquad (1.1)$$

where R_{av} is the average nuclear radius, $Y_{20}(\theta, \phi)$ is the spherical harmonic for an orbital with orbital angular momentum $\ell = 2$ and z-projection of $\ell = 0$. The quadrupole deformation parameter β, which is used throughout this work is defined as

$$\beta = \frac{4}{3} \sqrt{\frac{\pi}{5}} \frac{\Delta R}{R_{\text{av}}} \qquad (1.2)$$

where ΔR is the difference in radius between the semimajor and seminor axes of the ellipse. Nuclei with a deformation parameter of $\beta > 0$ ($\beta < 0$) have a shape which is extended (contracted) along the z axis compared to the average radius and are described as prolate (oblate) spheroids. While the deformation of the ground state of the $N = 60$ isotones in figure 1.4 are known to be $\beta \sim 0.4$ [EMS88], less experimental evidence is available regarding the nature of the deformed states in the $N < 60$ isotones. In particular, the precise degree of deformation of the low-lying deformed 0^+ state in ^{96}Sr has not been measured. The deformation value of $\beta \sim 0.3$ that is given in figure 1.4 is therefore assumed, based on level energies (which is further discussed in section 1.3). The proposed evolution of spherical and deformed structures shown in figure 1.4 is supported by a recent experiment at ISOLDE by Clément et al., which demonstrated that the spherical structure in ^{98}Sr is indeed similar to the ground state spherical structure of ^{96}Sr [CZP$^+$16a][CZP$^+$16b].
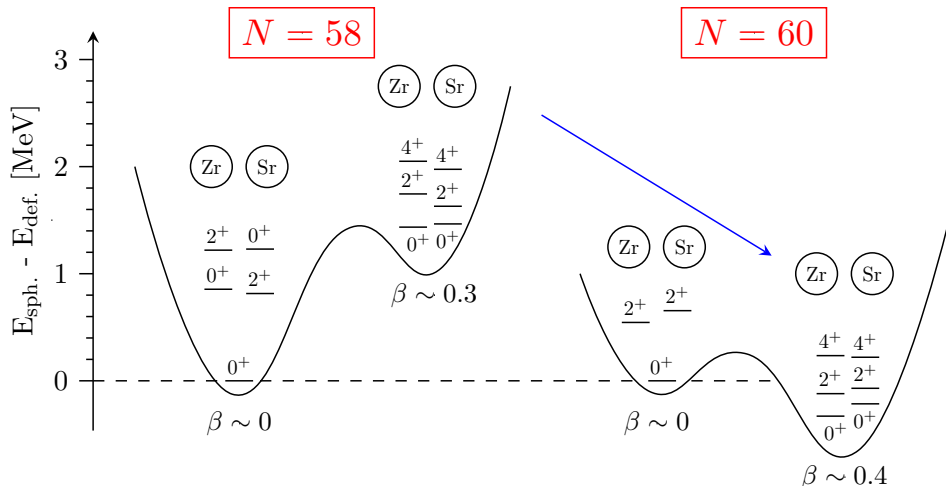
Figure 1.4: Proposed lowering of a deformed structure ($\beta > 0$) across Sr and Zr isotopes, which results in a ground state shape transition at $N = 60$. Adapted from [LPK$^+$94]. Energy levels that are associated with the spherical and deformed configurations are also drawn, and the data is taken from [Lab].

Shape coexistence in low-lying states has been identified in the neutron-rich $N = 58$ and $N = 60$ nuclei ^{96,98}Sr and ^{98,100}Zr, and this region remains a subject of substantial interest, both experimentally and theoretically [MXY$^+$12][RGSR$^+$10][SNL$^+$09][HEHJ$^+$00]. Unfortunately, little is currently known about the low energy states in this region. In ^{95}Sr, only the ground state spin and parity is firmly established. Similarly, many of the low-lying ^{96}Sr states do not have firm spin and parity assignments. It is therefore the intent of this work to firmly establish the spins and parities and to measure the single particle structure of the low-lying states, so that the onset of deformation and shape coexistence in this region can be better understood.

1.3 Shape Coexistence in ^{96}Sr

An experimental signature of shape-coexisting states that mix is an enhanced monopole transition strength, which is measured using conversion electron spectroscopy [WZD$^+$99]. The monopole transition strength $\rho^2(E0)$ between mixed states is

$$\rho^2(E0) = \left(\frac{3Z}{4\pi}\right)^2 a^2(1-a^2)\left[\Delta\left(\beta^2\right)\right]^2 \tag{1.3}$$

where a is the mixing amplitude and $\Delta(\beta)^2$ is the difference in deformations of the two configurations. In the case of mixing between a strongly deformed state and a nearly spherical state, $\Delta(\beta)^2 \simeq \beta^2$. A large $\rho^2(E0)$ value is therefore a valuable indicator of shape-coexisting states as it depends on both the mixing strength and the difference in deformation.

Several nuclei in the vicinity of $N \sim 60$ and $Z \sim 40$ have been found to have very large monopole transitions strengths with $\rho^2(E0) \sim 0.08 - 0.12$, compared to typical values of $\rho^2(E0) \leq 0.05$ in this mass region [WZD$^+$99]. One of the largest monopole transition strengths that have been measured in nuclei is between two low energy excited 0^+ states in ^{96}Sr, which has a $\rho^2(E0)$ value of 0.185(50) [Jun80]. Figure 1.5a shows the low energy states in ^{96}Sr, with the large $\rho^2(E0)$ value between the 1465 keV state and the 1229 keV state drawn as a thick black arrow. The sequence of levels built on top of the 1465 keV state in figure 1.5a shows a proposed rotational band, which is a spectroscopic signature of deformed nuclear structures [Cas00]. Rotational bands are sequences of levels which are interpreted to be the energy spectrum associated with rotating a deformed structure, with $E \propto J(J+1)$. The proposed rotational band shown in figure 1.5a would indicate a strongly deformed structure with $\beta \sim 0.3$, and this value was used in figure 1.4. Large quadrupole ($E2$) transition rates are also commonly observed between states within strongly deformed rotational bands. It should be noted, however, that a common structure underlying these states has not been experimentally verified, and the rotational band built on the 1465 keV state was proposed based on the spins, parities and energy spacing between the states. One can also argue that the relative branching ratio of decays from higher-lying states to the excited 0^+ states is an indicator of the mixing strength between them. If they are populated with roughly equal intensity through the decay of higher-lying states, then this suggests that they have similar transition matrix elements. At the time of this work, no γ-ray transitions to the 1465 keV ^{96}Sr state from higher states have been observed, which indicates that feeding from higher states is weak compared to the 1229 keV state. This is discussed more quantitatively in section 6.3.

It was also shown in the recent work of Clément et. al. that the 1229 keV 0_2^+ state appears to be dominated by a spherical configuration, while an observation of the 1465 keV 0_3^+ state was not reported [CZP$^+$16a][CZP$^+$16b]. Taken together, these experimental findings favour a

small mixing strength in equation 1.3.
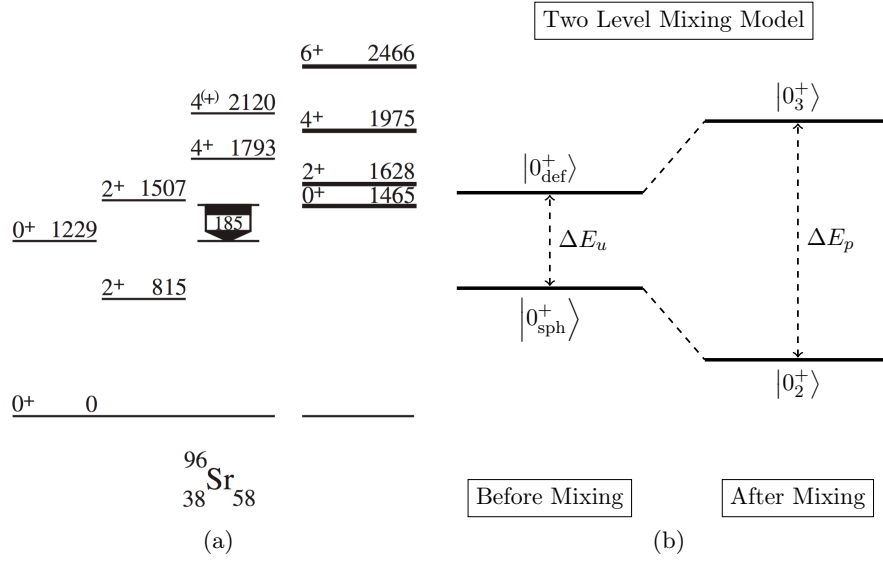
Figure 1.5: (a) Low energy states of ^{96}Sr, indicating the strong monopole transition strength (given in units of $\rho^2(E0)$x10^3) between excited 0^+ states (adapted from [HW11]). (b) Two level mixing model for coexisting states, where the unmixed states are assumed to be pure spherical and deformed configurations, respectively.

Two Level Mixing

A straightforward but very useful way to analyze the shape-coexisting 0^+ states in ^{96}Sr is through a two level mixing model, which is demonstrated in figure 1.5b. In this model, the two states initially exist as two distinct configurations with an energy separation of ΔE_u; one of which is nearly spherical and one of which is strongly deformed. A residual interaction V is then introduced which acts on the states.

$$\begin{pmatrix} E_1 & V \\ V & E_2 \end{pmatrix} \Psi = E\Psi \tag{1.4}$$

10

The interaction V causes the states to be pushed apart in energy and mixes the spherical and deformed configurations by an amount a such that

$$\left|0_2^+\right\rangle = a\left|0_{\text{sph}}^+\right\rangle + \sqrt{1-a^2}\left|0_{\text{def}}^+\right\rangle \tag{1.5}$$

$$\left|0_3^+\right\rangle = \sqrt{1-a^2}\left|0_{\text{sph}}^+\right\rangle - a\left|0_{\text{def}}^+\right\rangle \tag{1.6}$$

The energy separation between the two states after mixing, ΔE_p, is given by

$$\Delta E_p = \sqrt{(\Delta E_u)^2 + 4V^2} \tag{1.7}$$

From experiment, we know that $\Delta E_p = 235$keV, however the strength of the interaction and the initial energy separation ΔE_u is not known.

By measuring the mixing strength between the excited 0^+ states in ^{96}Sr, it will therefore be possible to determine the β value of the deformed structure for the first time by using equation 1.3, and this value can be compared to the ground state deformation of ^{98}Sr. In addition, information about the mixing between the excited 0^+ states in ^{96}Sr will also elucidate the level of degeneracy between the pure spherical and deformed configurations, which will help to refine theoretical models of this region.

1.4 Shell Model Calculations

In the shell model, the many-body Schrödinger equation is solved based on the assumption that low energy states in nuclei can be described without explicitly including all of the nucleons in the nucleus [Cas00]. For this reason, the nucleus is divided into two parts; an inert core and a valence space, as shown in figure 1.6. The core is defined as a set of fully occupied single particle orbitals, from which nucleons cannot be excited. Whenever possible, this is usually taken to be a full major oscillator shell. All nucleons outside of the core are then treated as valence nucleons which can couple to form different configurations and occupy different orbitals. The valence space (or model space) is usually limited to several valence orbitals outside of the

closed core. The shell model Hamiltonian is

$$\hat{H} = \sum_i \epsilon_i \hat{n}_i + \sum_{i,j,k,l} V_{ij,kl} \hat{a}_i^\dagger \hat{a}_j^\dagger \hat{a}_l \hat{a}_k \tag{1.8}$$

where $\hat{n}_i$, $\hat{a}_i^\dagger$ and $\hat{a}_i$ are the number operator, creation operator and annihilation operator for valence orbital i. The one-body term of the Hamiltonian describes the binding of each valence nucleon within a mean field potential. The solutions of the one-body part of the Hamiltonian give rise to the independent particle model, where the eigenvalues ϵ_i are are simply the bound states within the potential. The ϵ_i are normally referred to as the single particle energies (SPEs) of the Hamiltonian. The SPEs are adjusted phenomenologically so that the low energy spectra of nuclei in the vicinity of magic numbers (such as $N = 50$, see figure 1.3), where the independent model is an adequate description of low energy states, are well reproduced.

The two-body term in the Hamiltonian describes the nucleon-nucleon residual interaction within the valence space, and the $V_{ij,kl}$ are called the two-body matrix elements (TBMEs). The TBMEs make it possible for nucleons in the valence orbits i, j, k and l to interact with each other. This provides additional correlation energy and leads to the mixing of different configurations, which causes a departure from the simplistic independent particle model. The TBMEs contribute to the diagonal terms of the Hamiltonian matrix and also the off-diagonal terms. The diagonal terms contribute to the one-body SPEs, which gives rise to effective single particle energies (ESPEs).

The ESPEs describe the evolution of the underlying shell structure within the valence space as more nucleons are added and interact with each other. The ESPEs determine the energy gaps between the valence orbitals which in turn changes the energy of different single particle configurations, and can lead to a competition between different structures across an isotopic chain. The off-diagonal TBMEs act in a way that is closely resembles the two level mixing model that was presented in section 1.3, although they couple many nucleon pairs across multiple different orbitals. The TBMEs can be derived using first principles models such as Chiral Effective Field Theory (χEFT) for light nuclei and nuclei closed to magic numbers, but are generally determined phenomenologically using nucleon-nucleon scattering data.
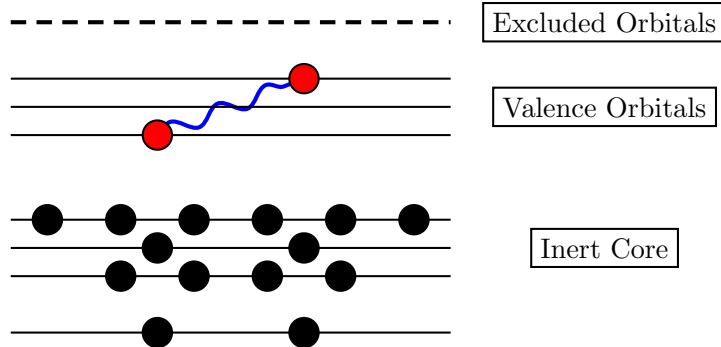
Figure 1.6: Shell model description of a nucleus. The residual interaction between valence nucleons (blue wavy line) causes different configurations to mix.

The Hamiltonian matrix therefore contains all allowed configurations of the valence nucleons across the valence orbitals, and must be solved using efficient matrix diagonalization algorithms. The matrix quickly becomes very large as the valence space increases, which is why a limited number of valence nucleons and orbitals are included.

The shell model code NushellX [BR14] was used to calculate the wavefunctions and energy levels of for ^{94,95,96}Sr. Two model spaces and interactions are available for the Z$\sim$40, N$\sim$60 region; jj45 [EHJH$^+$93] and glek [MWG$^+$90]. The jj45 interaction was developed for studies of heavier Sn isotopes, and it was found that the SPEs required substantial modification before the calculated levels of $Z \sim 40$, $N = 51$ nuclei were in reasonable agreement with the available experimental data. $N = 51$ nuclei were used to benchmark the interaction because these nuclei contain a single neutron outside of a closed shell. The low-energy states of $N = 51$ nuclei tend to be dominated by single neutron excitations, and so these states provide a reasonable measure of the valence orbital spacing. The glek interaction was developed for Y and Zr studies, and so only a small adjustment to the SPEs was necessary to give reasonable agreement with Sr experimental data.

The proton degrees of freedom are expected to play an important role in describing the low-lying states of neutron-rich Sr isotopes. As was discussed in section 1.2, the proposed quenching of the $1p$ orbitals indicates that proton excitations into the $1p\frac{1}{2}$ orbital are required to describe the low-lying states. The same is true for the $0g\frac{9}{2}$ orbital, which was also found to be important

for describing the structure of neutron-rich Zr isotopes. In this work, systematic shell model calculations were carried out using a series of model spaces for both of the available interactions so that the effect of adding proton degrees of freedom could be examined. It was not possible to carry out full model space calculations as the computational requirements exceeded available resources. The full model spaces associated with the jj45 and glek interactions, along with the truncated model spaces which were used in this work are summarized in table 1.1. It should also be noted that the shell model calculations assume a spherically symmetric nuclear potential, and so are only appropriate for states which are nearly spherical.

Interaction	Full Model Space	This Work : ⓐ	This Work : ⓑ	This Work : ⓒ
jj45 $[\pi]$	$0f\frac{5}{2}1p0g\frac{9}{2}$	$[1p\frac{3}{2}]^4$	up to $[1p\frac{3}{2}]^2[1p\frac{1}{2}]^2$	up to $[1p\frac{3}{2}]^0[1p\frac{1}{2}]^2[0g\frac{9}{2}]^2$
jj45 $[\nu]$	$1d2s0g\frac{7}{2}0h\frac{11}{2}$	$1d2s0g\frac{7}{2}$	same as ⓐ	same as ⓐ
glek $[\pi]$	$0f1p0g\frac{9}{2}$	$[1p\frac{3}{2}]^4$	up to $[1p\frac{3}{2}]^2[1p\frac{1}{2}]^2$	up to $[1p\frac{3}{2}]^0[1p\frac{1}{2}]^2[0g\frac{9}{2}]^2$
glek $[\nu]$	$1d2s0g$	$1d2s0g\frac{7}{2}$	same as ⓐ	same as ⓐ

Table 1.1: Summary of NushellX model spaces and interactions that were used (more details in the text).

As can be seen in table 1.1, the jj45 and glek interactions were developed for larger model spaces than were used in this work. In particular, the jj45 and glek interactions include the proton $0f$ orbitals in the model space. The proton $0f$ orbitals were required to be fully occupied in this work. It is expected that proton excitations from the $0f$ orbitals will not contribute significantly to the underlying configurations of the low energy states as they are significantly below the unoccupied valence orbitals. It should be noted that all orbitals which are included in the full model space and have nonzero occupations will contribute to the ESPEs of the orbitals, including those which are required to be fully occupied and inert.

A series of calculations were carried out for the low-lying states of ^{94,95,96}Sr, using three different model spaces which are denoted as ⓐ,ⓑ and ⓒ in table 1.1. Model space ⓐ required that the four valence protons outside of the full $0f$ orbitals were inert and only occupied the $1p\frac{3}{2}$ orbital, as denoted by $[1p\frac{3}{2}]^4$. Model space ⓑ included an extended proton valence space, where

the protons could scatter in an unconstrained way from the $1p\frac{3}{2}$ into the $1p\frac{1}{2}$ orbital, allowing up to $2p - 2h$ proton configurations as denoted by $[1p\frac{3}{2}]^2[1p\frac{1}{2}]^2$. Model space ⓒ included a further increased proton valence space, allowing all four $1p\frac{3}{2}$ protons to scatter into the $1p\frac{1}{2}$ and $0g\frac{9}{2}$ orbitals. A maximum of two protons were allowed to occupy the $0g\frac{9}{2}$ orbital so that the calculation size remained manageable. This enabled up to $4p - 4h$ proton configurations as denoted by $[1p\frac{3}{2}]^0[1p\frac{1}{2}]^2[0g\frac{9}{2}]^2$.

Similarly, the neutron valence spaces were truncated to make the calculations tractable. The neutron $0h\frac{11}{2}$ orbital was excluded from the jj45 model space as it has a large SPE compared to the other valence neutron orbitals, and also has negative parity. In this work, we are only interested in the low lying positive parity states which are populated through one neutron transfer. The $0h\frac{11}{2}$ would only contribute to the structure of these states through configurations such as $[0h\frac{11}{2}]^2$, which would be a very high energy configuration. For these reasons, the $0h\frac{11}{2}$ orbital is not expected to play a significant role in the low-lying states. Large scale shell model calculations that were carried out for the Zr isotopes by Sieja et al. [SNL$^+$09] predict very low occupancy of the $0h\frac{11}{2}$ orbital across all of the calculated states, which further indicates that this state can be neglected. All of the calculations that were carried out in this work using the glek interaction were required to have a fully occupied neutron $0g\frac{9}{2}$ orbital. This is reasonable as there is a large energy difference between the $0g\frac{9}{2}$ and the $1d\frac{5}{2}$ orbitals due to the $Z = 50$ shell closure, and so neutron excitations across the $Z = 50$ shell gap would be energetically expensive. In addition to a large energy gap, the $1d\frac{5}{2}$ orbital is expected to be almost fully occupied for nuclei with $N > 56$, which would inhibit the scattering of neutrons across the $Z = 50$ shell gap.

Figures 1.7 and 1.8 compare the shell model calculations that were carried out for ^{95}Sr using model spaces ⓐ, ⓐ and ⓐ to experimental data.

It can be seen in figure 1.7 that the jj45 interaction incorrectly predicts a $\frac{7}{2}^+$ ^{95}Sr ground state when any additional proton degrees of freedom are included. Given that the SPEs were optimized for $N = 51$ nuclei, such a discrepancy suggests that the TBMEs of the jj45 interaction may not be well suited to describing Sr isotopes. On the other hand, the calculated levels in

681    $(\frac{3}{2}^+, \frac{5}{2}^+)$
556    $(\frac{7}{2}^+)$

$\frac{3}{2}^+$
$\frac{5}{2}^+$

352    $(\frac{3}{2}^+)$

$\frac{3}{2}^+$
$\frac{1}{2}^+$

$\frac{7}{2}^+$ $\frac{1}{2}^+$

ⓐ   ⓑ   ⓒ   Experiment
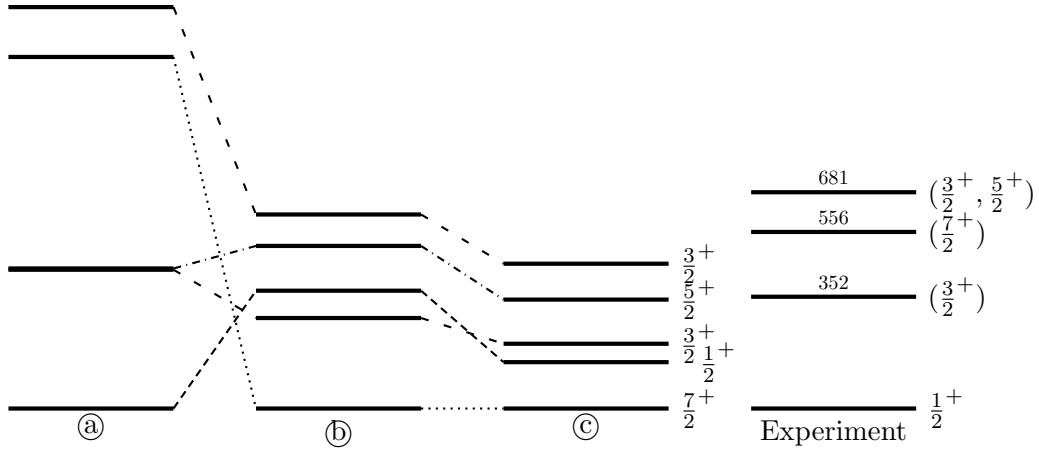
Figure 1.7: Selected low-lying ^{95}Sr states compared to shell model calculations using the jj45 model space and interaction with various proton valence spaces (more details in the text).

figure 1.8 show that the $\frac{1}{2}^+$ ground state of ^{95}Sr is correctly predicted for each of the proton valence spaces. Including the proton $1p\frac{1}{2}$ orbital in the model space led to an improvement in the calculated energy levels, with particularly good agreement between the excited $\frac{3}{2}^+$ and $\frac{7}{2}^+$ state energies and the experimental levels. The addition of the $0g\frac{9}{2}$ orbital in the proton valence space caused further lowering of the $\frac{7}{2}^+$ state energy. This indicates that there is a strongly attractive residual interaction between these orbitals. Calculations in model space ⓒ were computationally intensive and very time consuming, and optimizing the SPEs generally requires many iterations. For this reason, the SPE of the proton $0g\frac{9}{2}$ orbital was not modified from the original glek interaction. As a result, the over-binding effect that can be seen in figure 1.8 for the $\frac{7}{2}^+$ state in model space ⓒ may also be due to the SPE for the $0g\frac{9}{2}$ orbital.

Given that the TBMEs of the glek interaction were developed in this same mass region, they are better suited to studying Sr than the jj45 interaction. For this reason, only the glek interaction is compared to experimental data for the remainder of this thesis.

A consequence of the residual interaction $V_{ij,kl}$ is that the calculated shell model wavefunction of a given state consists of many different configurations with the same spin and parity. In general, these terms do not contribute equally and so in most cases the wavefunction is made up predominantly from one or a few important configurations. The wavefunction of the ^{95}Sr ground state, as calculated using the glek interaction in model space ⓐ, is shown in table 1.2.
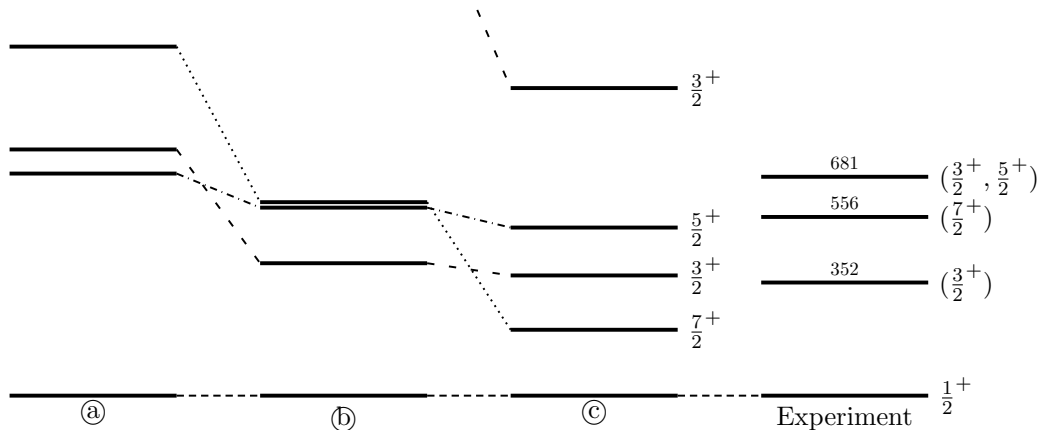
Figure 1.8: Selected low-lying ^{95}Sr states compared to shell model calculations using the glek model space and interaction with various proton valence spaces (more details in the text).

Configuration	$\nu1d\frac{5}{2}$	$\nu2s\frac{1}{2}$	$\nu1d\frac{3}{2}$	$\nu0g\frac{7}{2}$	a^2 [%]
(i)	6	1	0	0	82.63
(ii)	4	1	2	0	6.29
(iii)	5	1	1	0	5.13
(iv)	4	2	1	0	1.50
(v)	4	1	0	2	1.14
Occupation	5.70	1.01	0.25	0.04	96.69

Table 1.2: Wavefunction composition and orbital occupation numbers for the ^{95}Sr ground state. Each of the underlying configurations (i)-(v) are coupled to $J^\pi = \frac{1}{2}^+$. The occupation numbers are the weighted sum of the underlying configurations.

For orbitals which are not fully occupied, the nucleons may also couple to $J \neq 0$. An example of this would be the coupling of a $J = 2$ neutron pair in the $\nu1d\frac{5}{2}$ orbital to a $J = 2$ neutron pair in the $\nu1d\frac{3}{2}$ orbital to form a configuration with total $J = 0$, which is possible in configuration (ii). A similar configuration also exists for the $\nu1d\frac{5}{2}$ and $\nu0g\frac{7}{2}$ orbitals. The number of unpaired nucleons is called the seniority (ν). These configurations will usually play a small role in the overall wavefunctions due to the energy expense of breaking multiple nucleon pairs.

For model spaces ⓑ and ⓒ, there are many more components in the wavefunctions, such as the coupling between proton and neutron excitations. This makes it less straightforward to represent the underlying configurations of the many-body nuclear wavefunction. In model spaces which include proton and neutron degrees of freedom, it is common to discuss the total orbital occupation numbers instead. The occupation numbers are the expectation value for number of nucleons in each of the valence orbitals, and can have a value of up to $2j + 1$ for fully occupied

orbitals. Table 1.2 shows that in model space @, the $\frac{1}{2}^{+}$ ^{95}Sr ground state wavefunction is mostly made up of configuration (i), in which the neutron $1d\frac{5}{2}$ orbital is full and there is an unpaired neutron in the $2s\frac{1}{2}$ orbital. This is also reflected in the occupation numbers presented at the bottom of table 1.2, which predict that the $1d\frac{5}{2}$ orbital is effectively fully occupied and that there is a single neutron in the $2s\frac{1}{2}$ orbital.

The shell model wavefunctions can also be used to calculate the overlap between different states. In this way, the predicted cross section for ^{94,95}Sr(d,p) can be compared to the experimental data. A quantity of particular importance for this work are *spectroscopic factors*, which are described at the end of the next section. In section 6, spectroscopic factors that were calculated using the shell model are compared to the experimental results.

1.5 Transfer Reactions

Transfer reactions are a well established tool for studying the single particle structure of nuclei [Fes92]. In these reactions, a small number of valence nucleons are transferred from one nucleus to another and populate unfilled valence orbitals. By measuring the outgoing flux of particles from these reactions, detailed information of the populated orbitals can be obtained. This makes them a very useful tool for measuring the single particle configurations of nuclear states.

Transfer reactions are direct reactions, which means that they are peripheral collisions between nuclei that occur very quickly and are well-described as a single-step process. A single-step process has no intermediate state, and so the final state is related to the initial state in a straightforward way, which will be discussed later in this section. Consequently, other than the exchange of a small number of valence nucleons at the surface there is minimal rearrangement of the constituent nucleons within each of the nuclei. In contrast to this, nuclei can also undergo compound reactions where many nucleons participate in the process, forming a long-lived, highly excited state. In compound reactions, information of the initial state is lost and so they cannot be used to study single particle structure. Compound reactions tend to have larger cross sections than transfer reactions and can take place under the same experimental
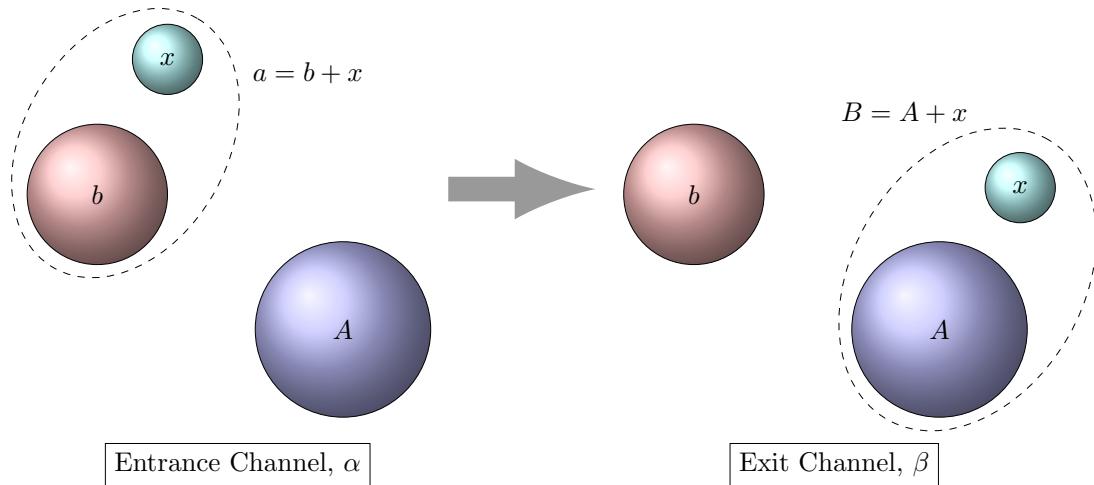
Figure 1.9: Schematic diagram of a transfer reaction.

conditions, which is often substantial source of background.

Transfer reactions are denoted by

$$a + A \rightarrow b + B \tag{1.9}$$

where $B = A + x$ is the target nucleus plus the transferred nucleons, $a = b + x$ is the beam nucleus plus the transferred nucleons and x represents the transferred nucleons. It is also common to write equation 1.9 as $A(a,b)B$. A and b are referred to as the core nuclei as they remain unchanged throughout the reaction, while B and a are referred to as composite nuclei as they contain the inert core nuclei plus the exchanged nucleons. The left side of equation 1.9 is called the entrance channel and is labelled by α, while the right side of equation 1.9 is called the exit channel and is labelled by β.

Figure 1.9 gives a schematic representation of a transfer reaction. As can be seen, the nucleons (x) are transferred from the initial composite system a and bind to the target core nucleus A to form a final composite system B. Both the initial and final states of this reaction involve two bodies, which means that the kinematics of the final state can be fully described by measuring either b or B.

The most commonly used transfer reactions involve the addition or subtraction of a single

nucleon from a nucleus of interest, which is called one-nucleon transfer. These reactions are especially useful as they avoid the complications that arise from the exchange of many-nucleon configurations. The cross sections for one-nucleon transfer reactions are also considerably larger than for many-nucleon transfer, which is an important consideration when studying exotic nuclei.

In this work, a series of Sr(d,p) reactions were carried out. In a (d,p) reaction, the neutron is stripped from the deuterium and populates an unfilled valence orbital in the target nucleus. The remaining proton is then measured, and from this measurement the details of the transferred neutron can be inferred. Deuterium is an ideal tool for one-nucleon transfer reactions as it is a well understood nucleus, it is loosely bound and is also readily available to laboratories.

1.5.1 DWBA Theory

Nuclear reactions are described mathematically using scattering theory. In this framework, the reaction is modelled as the scattering of a travelling wave upon an interaction potential. The wave subsequently scatters off the potential, and this induces a transition from the entrance channel α to the exit channel β. The scattered wave then propagates radially away from the target and interferes with the unreacted component of the incident wave, producing an interference pattern. The resulting interference pattern describes the expected intensity distribution of particles as a function of scattering angle in the exit channel, which is proportional to the angular distribution (or differential cross section) of the reaction. This process is illustrated in figure 1.10.

When the beam and target nuclei collide, there are numerous different reactions that can occur. The most important, and dominant, of these is elastic Coulomb scattering. The long-ranged Coulomb interaction distorts the waves far away from the interaction region. These asymptotic solutions are called Coulomb waves and are denoted by χ. As the cross sections for transfer reactions are smaller than elastic scattering, the transfer process can be approximated as a perturbation on the elastic scattering channel. This approximation is the basis of the Distorted Wave Born Approximation (DWBA) [Sat83].
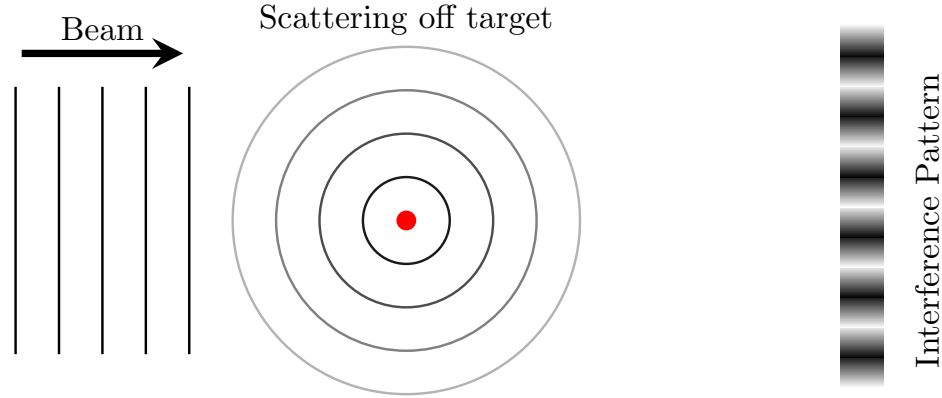
Figure 1.10: Schematic diagram of a nuclear reaction in scattering theory.

The elastic scattering channel is modelled mathematically through the use of a complex potential, where the real component of the potential describes elastic scattering and the imaginary component of the potential describes inelastic processes which remove flux from the reaction. This is called the optical model (or optical potential) [Hod71], as it is analogous to the scattering of light through a semi-opaque medium. The general form of the optical potential is

$$U(r) = U_c(r, R_c) - V_0 f(r, R_0, A_0) - iW_D \frac{d}{dr} f(r, R_D, A_D) - V_{SO} \frac{d}{dr} f(r, R_D, A_D) \vec{\ell} \cdot \vec{S} \quad (1.10)$$

Where U_c is the long-ranged (repulsive) Coulomb potential and f describes the shape of the short-ranged interaction potential. The optical potential normally includes derivative terms to account for interactions which take place at the surface of the nucleus, such as the spin orbit interaction between the incident and target nuclei. The short-ranged potential f is commonly described using a spherically symmetric Woods-Saxon shape [Sat83], which has the form

$$f(r, R, A) = \frac{1}{1 + \exp\left(\frac{r - R}{A}\right)} \quad (1.11)$$

where $A = Z + N$ is the mass number of the nucleus. This potential has the approximate shape of the nucleus. Figure 1.11a shows the shape of the Woods-Saxon potentials that are used in the optical model. The numerous V (W), R and A terms in equation 1.10 are known as the optical model parameters, which are determined phenomenologically. There are readily avail-

able global parameters such as those of Perey and Perey [PP76] which come from global fits to many data sets, however it is standard practice to use the global parameters as a starting point and optimize the potential further using experimental elastic scattering data. In this work, the latter experimental optimization procedure was used, which is discussed further in section 5.1.

In scattering theory, the transition matrix (or $\mathscr{T}$-matrix) describes the amplitude of a reaction. The cross-section for the reaction is therefore proportional to the square modulus of the $\mathscr{T}$-matrix element for $\alpha \to \beta$. A full derivation of the $\mathscr{T}$-matrix can be found in reference [Sat83], and so will not be given in this thesis. The $\mathscr{T}$-matrix element for $\alpha \to \beta$ in DWBA theory is

$$\mathscr{T}^{DWBA}_{\beta\alpha} = \left\langle \chi^{(-)}_{\beta} \Phi_{\beta} \middle| \mathcal{V} \middle| \Phi_{\alpha} \chi^{(+)}_{\alpha} \right\rangle \tag{1.12}$$

where $\chi^{(\pm)}$ are the incoming and outgoing asymptotic (Coulomb) distorted waves for $r \to \infty$ and $\Phi_{\alpha,\beta}$ are intrinsic wavefunctions which describe the bound state wavefunction of the neutron in the entrance channel α and the exit channel β, respectively.

The $\mathcal{V}$ term in equation 1.12 describes the total interaction potential and can be expressed in terms of the entrance channel α

$$\mathcal{V} = V_{\nu A} + V_{bA} - U_{\alpha} \tag{1.13}$$

or equivalently, in terms of the exit channel β

$$\mathcal{V} = V_{\nu b} + V_{bA} - U_{\beta} \tag{1.14}$$

where $V_{\nu A}$ and $V_{\nu b}$ are called the binding potentials for the composite systems B and a, respectively. The binding potentials are required to calculate the bound state wavefunction of the transferred neutron in the entrance and exit channels. The $U_{\alpha,\beta}$ correspond to the optical potentials that were defined in equation 1.10, which describe elastic scattering of the nuclei in the α and β channels, respectively. V_{bA} is called the core-core interaction potential, and represents the interaction between the cores b and A during the reaction. V_{bA} is usually described using an optical potential.

In summary, there are several inputs that are required to calculate the cross section for a reaction. It is necessary to define optical potentials for the entrance and exit channels, as these produce the distorted waves in equation 1.12. Ideally, these potentials are optimized by fitting to experimental elastic scattering data. Given that the reaction cross section is dominated by elastic scattering, a good description of the optical potentials is essential. As was previously mentioned, the core-core potential is also well-described by the optical model. For (d,p) reactions, the core-core potential is taken to be approximately the same as the the optical potential for the outgoing (exit) channel. This approximation is especially good for (d,p) reactions involving heavy nuclei, since the difference between the (N, Z) core and the $(N + 1, Z)$ composite is very small.

It is also necessary to describe the overlap wavefunction between the core and composite nucleus in both the entrance and exit channel. It is standard practice to obtain the overlap wavefunctions by solving the radial Schrödinger equation within a Woods-Saxon potential and matching the bound state wavefunction to the asymptotic distorted wave. The binding Woods-Saxon potential is usually assigned standard R and A values which approximate the size and shape of the nucleus, while the potential depth is adjusted manually to reproduce the experimental separation energy of the bound neutron [TN09]. With these physical inputs defined, the reaction calculations can be carried out using standard codes.

In this work, cross sections for ^{94,95}Sr(p,p), ^{94,95}Sr(d,d) and ^{94,95}Sr(d,p) were calculated using the DWBA code FRESCO [Tho88]. An example FRESCO input file is shown in appendix A.

The final state overlap wavefunctions were assumed to be pure single particle states, where the transferred neutron populates a single valence orbital. For example, the $\frac{1}{2}^+$ ground state wavefunction of ^{95}Sr is assumed to be made up of the $J^\pi = 0^+$ ground state wavefunction of ^{94}Sr coupled to a neutron in the $2s\frac{1}{2}$ ($\ell = 0$) orbital, which is written as

$$\left|^{95}\text{Sr}; \tfrac{1}{2}^+\right\rangle = \left|^{94}\text{Sr}; 0^+\text{g.s.}\right\rangle \otimes \left|\nu 2s\tfrac{1}{2}\right\rangle \tag{1.15}$$

This particular description of the reaction denotes an $\ell = 0$ transfer, and leads to a distinctive shape in the differential cross section (or equivalently angular distribution) curve as a function of the center-of-mass scattering angle. The DWBA angular distributions for ^{94}Sr(d,p) for different ℓ transfers can be seen in figure 1.11b. Other descriptions, such as $\ell = 4$ (which denotes the transfer of the neutron into the $0g\frac{7}{2}$ orbital), predict very different angular distributions and total reaction cross sections. It is these unique characteristics of the DWBA curves which allow the angular momentum transfer, ℓ, of the experimental states to be determined. The shape of the angular distribution and total cross section for a reaction is also dependent on the Q-value of the reaction, and so different excited states would have different calculated curves. More details on how the DWBA calculations were carried out can be found at the end of section 4.4.

(a) (b)
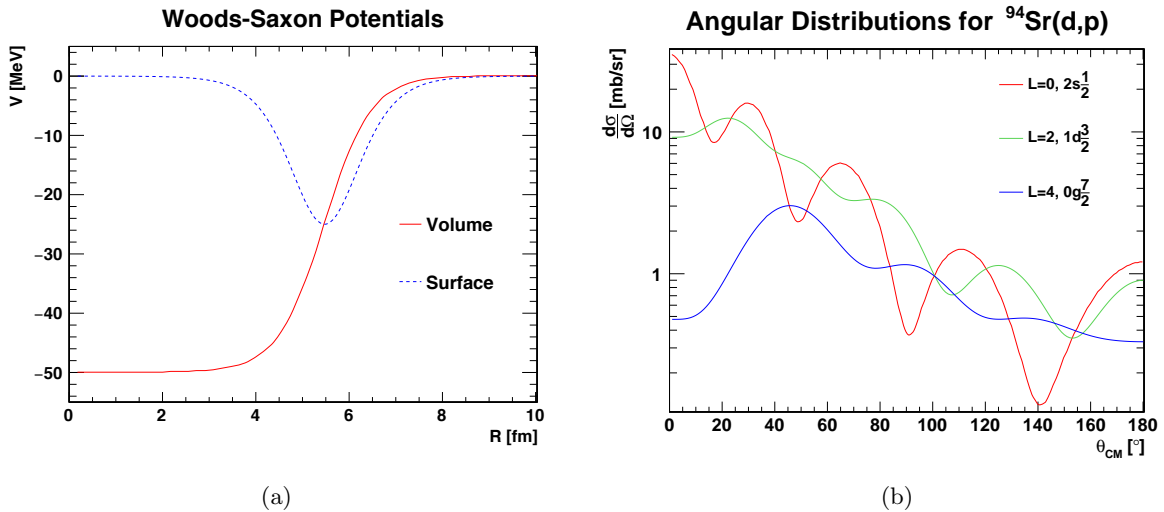
Figure 1.11: (a) Shape of a Woods-Saxon potential. The surface potential is defined mathematically as the derivative of the volume potential. (b) Example DWBA angular distribution calculations for different orbital angular momentum transfer.

As was discussed in section 1.4, the wavefunctions of the ^{94,95,96}Sr states are expected to consist of many different configurations. For this reason, the experimental cross sections will be less than those predicted by the pure single particle configurations that are assumed in the DWBA calculations. By comparing experimental cross sections to DWBA calculations it is therefore possible to obtain information about the purity of the single particle configuration in the real

wavefunction. In mathematical terms

$$\left[\frac{\delta\sigma}{\delta\Omega}(\theta)\right]_{exp} = \mathcal{SF}\left[\frac{\delta\sigma}{\delta\Omega}(\theta)\right]_{DWBA} \tag{1.16}$$

where $\mathcal{SF}$ is the experimental spectroscopic factor, which is defined as the overlap between the real wavefunction with the pure single particle wavefunction that is calculated [Sat83]. In other words, the spectroscopic factor gives the extent to which a populated state is described by the ground state of the core nucleus plus a neutron in a single particle orbital, as shown in equation 1.15. Clearly, states that are not populated, or that are populated very weakly, in a (d,p) reaction do not have a strong component of these single particle configurations in their wavefunctions.

An important consideration for this work is the population strength of the excited $0^+_{2,3}$ states in ^{96}Sr through ^{95}Sr(d,p). Both 0^+ states contain a mixture of spherical and deformed configurations, as is described by equations 1.5 and 1.6. Here we assume that the deformed configuration 0^+_{def} will not be directly populated through ^{95}Sr(d,p) as the reaction cannot be described as a single step process. The relative population strength of the $0^+_{2,3}$ states in ^{96}Sr through ^{95}Sr(d,p) will therefore measure the relative amounts of spherical configurations 0^+_{sph} in each of the states. This can be formulated as

$$\frac{\mathcal{SF}(0^+_3)}{\mathcal{SF}(0^+_2)} = \frac{1-a^2}{a^2} \tag{1.17}$$

1.5.2 Inverse Kinematics

For many years, (d,p) reactions have been successfully carried out using deuterium beams to study the single particle structure of stable and long-lived nuclei. In more recent times, the nuclei to be studied are short-lived and so cannot be fabricated into target materials. It is therefore necessary to carry out (d,p) reactions in *inverse kinematics* [Jon13], where the deuterium is the target nucleus and the exotic nucleus under study is produced as a radioactive beam. Inverse kinematics experiments are more challenging than normal kinematics experiments for a number of reasons that will briefly be discussed.

Inverse kinematics (d,p) experiments have much larger center-of-mass motion than normal kinematics experiments, which leads to less favourable angular coverages for detection of the ejected protons [Cat14]. Although there have been many significant advances in the production of radioactive ion beams, the beam intensities which are currently achievable are many orders of magnitude less than those which are possible for stable beams (such as deuterium). Consequently, much thicker targets must be used to produce comparable experimental yields. This presents a challenge, as the heavy ion beam loses a large amount of energy as it passes through the thick target and this leads to a substantial degradation of the energy resolution. When transfer reactions are carried out in inverse kinematics it is important to be able to separate the different populated states, and so γ-ray detectors are commonly used to identify the states.

1.6   Overview of Thesis

In summary, the aim of this experimental work is to measure the spins and parities, and to study the single particle structure of low-lying states in ^{95,96}Sr through ^{94,95}Sr(d,p). It is also a primary goal of this work to measure the relative population strengths of the excited 0^+ states in ^{96}Sr through ^{95}Sr(d,p) so that the mixing strength of the underlying configurations can be determined.

In the next chapter of this thesis, the ^{94,95}Sr(d,p) experiments are described in detail. Important results from simulations of the experiments are given in chapter 3. The analysis procedures that were carried out in this work are explained in chapter 4. The experimental results are presented in chapter 5, and these are compared to shell model calculations in chapter 6. A summary and overview is given in section 7.

Chapter 2

Experiment

2.1 Overview of Experiments

States in ^{95,96}Sr were investigated through the reactions ^{94,95}Sr(d,p)^{95,96}Sr in inverse kinematics using a 5.5 MeV/u beam impinged on a deuterated polyethylene (CD$_2$) target. A combination of position-sensitive particle detection (SHARC) and γ-ray detection (TIGRESS) systems made it possible to carry out proton angular distribution and cross section measurements and also to use γ-particle coincidences to extract information about the excited ^{95,96}Sr states which were populated. Figure 2.1 shows a schematic diagram of the experiment.

Both experiments were carried out at TRIUMF, Canada's national laboratory for particle and nuclear physics research. The ^{94}Sr(d,p) and ^{95}Sr(d,p) experiments were carried out in June 2013 and June 2014, respectively, and were the first high mass (A>30) experiments with a re-accelerated secondary beam to be performed at TRIUMF. Consequently, this campaign marks an important step forward for TRIUMF and serves as a demonstration of the enhanced capabilities of the laboratory to study heavier exotic nuclei through nuclear reactions involving accelerated exotic beams.

In this chapter, the general discussion of beam delivery and experimental setup will focus primarily on the ^{95}Sr(d,p) experiment, as both studies were carried out under very similar conditions. Some details of ^{94}Sr(d,p) experiment will also be presented throughout the subsequent chapters, so that significant differences and important experimental details can be highlighted.
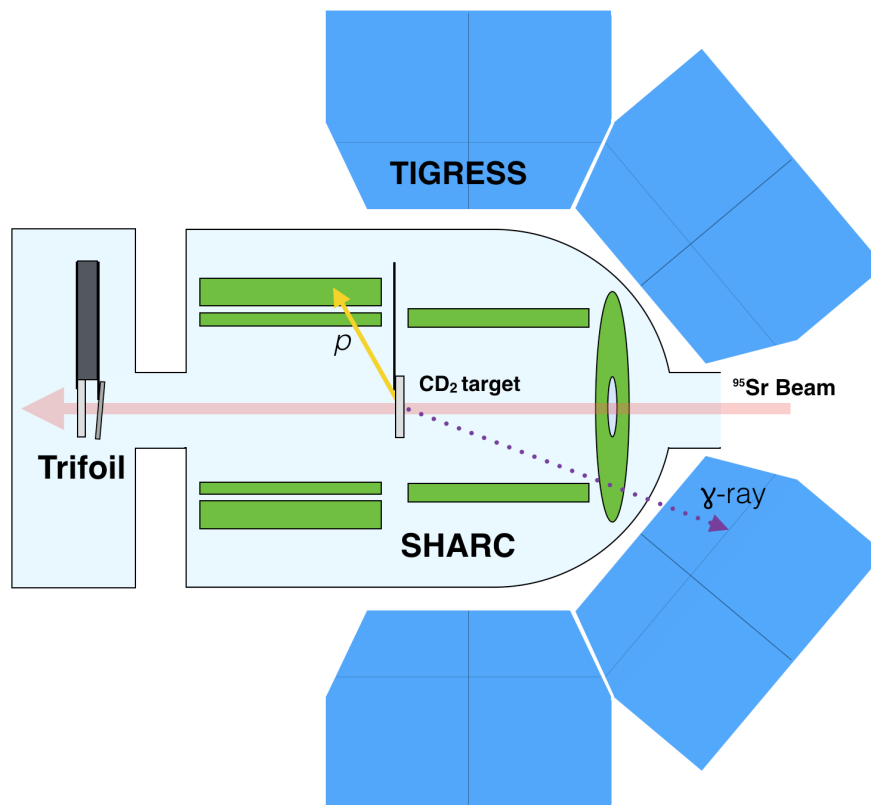
Figure 2.1: Schematic diagram of the experiment, showing the detector set-up.

2.2 RIB Production

There are two main techniques that are used to produce radioactive ion beams (RIBs); in-flight fragmentation and isotope separation online (ISOL). In-flight fragmentation facilities such as NSCL, GSI and RIKEN are driven by heavy ion beams which are impinged upon thin targets at high energies (> 50 MeV/u). The beam loses very little energy in the target but can undergo fragmentation as a result of its interaction with the target nuclei, resulting in a fast cocktail beam which requires mass separation online. This makes it possible to study nuclei with very short half-lives but production cross sections tend to be low and beam energy distributions can be broad. Contrastingly, the ISOL technique which is used at TRIUMF and ISOLDE makes use of a very thick target which is bombarded with a light primary beam such as protons or helium nuclei. The primary beam loses a large amount of its energy within the target, which maximizes the production yield but introduces an inherent challenge to promptly and efficiently extract the produced isotopes. The production target is operated at typical temperatures of

several thousand kelvins so that the produced radioisotopes diffuse to the surface to decrease the extraction time. It remains a limitation of the ISOL method that nuclides with very short half-lives ($\lesssim$10 ms) cannot be presently studied using this approach. For nuclear reaction studies it is also necessary to re-accelerate the RIB produced using the ISOL method. While re-acceleration of the RIB introduces additional inefficiencies which lower the secondary beam yield, it is possible to produce precise final beam energies using this technique.

2.2.1 Beam Delivery at TRIUMF

The TRIUMF 500 MeV proton cyclotron was used to produce a high intensity beam of protons with a beam current of up to 10 μA [DKM14]. The beam was then sent to the TRIUMF Isotope Separator and Acceleration (ISAC) facility where it impinged on a thick Uranium Carbide (UCx) target. Proton-induced uranium fission and spallation within the target produced a yield consisting of a wide range of nuclei. The isotopes were extracted from the UCx target and numerous stripping and filtering techniques were utilized in order to optimize the purity and rate of the ^{95}Sr beam.

Surface ions were ionized into a singly charged (1^+) state using the TRIUMF Resonant Ionization Laser Ion Source (TRILIS) [DKM14]. TRILIS uses multiple high-intensity laser beams to ionize atoms using multistep resonant photon absorption, which makes possible efficient and element selective ionization. TRILIS was used to enhance the extraction rate of ^{95}Sr compared to contaminants which are also produced within the production target. The cocktail beam was then sent through the ISAC mass separator, which has a resolution of $\frac{\Delta A}{A} \sim 10^{-4}$ [DKM14], to produce a beam with only $A = 95$ isotopes. The beam was then transported to the Charge State Booster (CSB) where the isotopes were charge-bred by an Electron Cyclotron Resonance (ECR) plasma source to a 16^+ charge state. This was necessary so that the beam could next be sent to the Radio-Frequency Quadrupole (RFQ), which accepts a maximum mass-to-charge ratio (A/q) of 30 [DKM14]. Inside the RFQ, time-dependent electric fields were tuned to accelerate the specific A/q of ^{95}Sr ions. Contaminant isotopes in the beam were mismatched with the acceleration phase of the RFQ and so did not undergo any acceleration. Following the RFQ, these contaminants were deflected out of the beam using the bending dipole magnets in the accelerator chain.

The highly charged ^{95}Sr beam was then transported to the ISAC-II facility where its kinetic energy was increased to 524 MeV (5.515 MeV/u) using the superconducting linear accelerator [DKM14] before finally being delivered to the TIGRESS experimental station in the ISAC-II experimental hall. An overview of the ISAC-I and ISAC-II facilities is shown in figure 2.2.
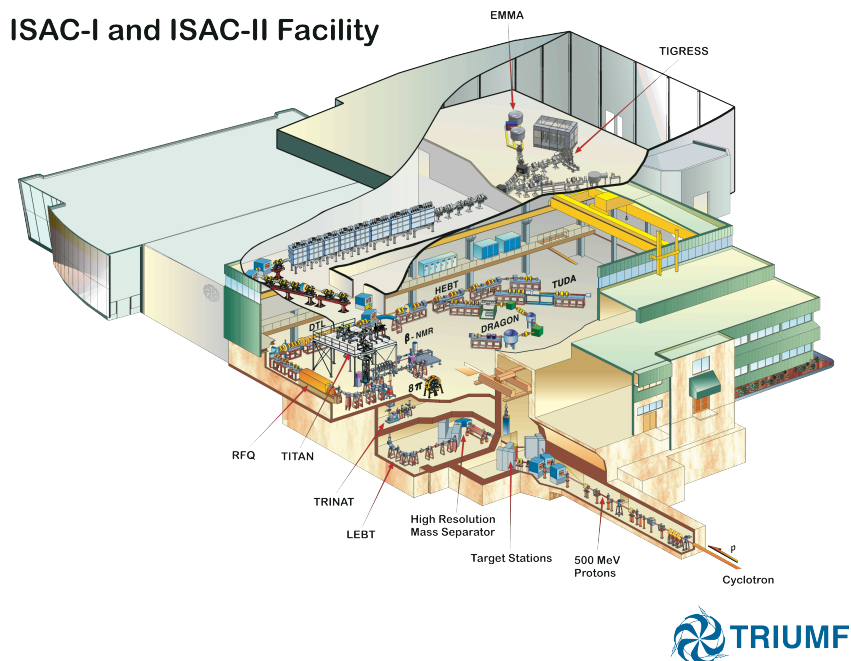
Figure 2.2: Diagram of TRIUMF-ISAC facility [BHK16]. The ^{95}Sr^{16+} beam was delivered to the TIGRESS experimental station in ISAC-II.

The beam composition at the experimental station was monitored using the TRIUMF Bragg (TBragg) detector [Nob13] and was found to be composed of ~98% ^{95}Sr, with some small contamination due to ^{95}Rb and ^{95}Mo. The TBragg detector is described in section 2.4.1. The mass 95 beam composition as measured by the TBragg detector is shown in figure 2.3.

The beam intensity was monitored periodically throughout the experiment using the ISAC-I FC4 Faraday cup, which was positioned upstream of the TIGRESS experimental station. The total running time of the ^{95}Sr experiment was approximately 2.5 days, with an average ^{95}Sr beam intensity of approximately 10^6 s^{-1}. This sustained high beam rate caused a hole to be
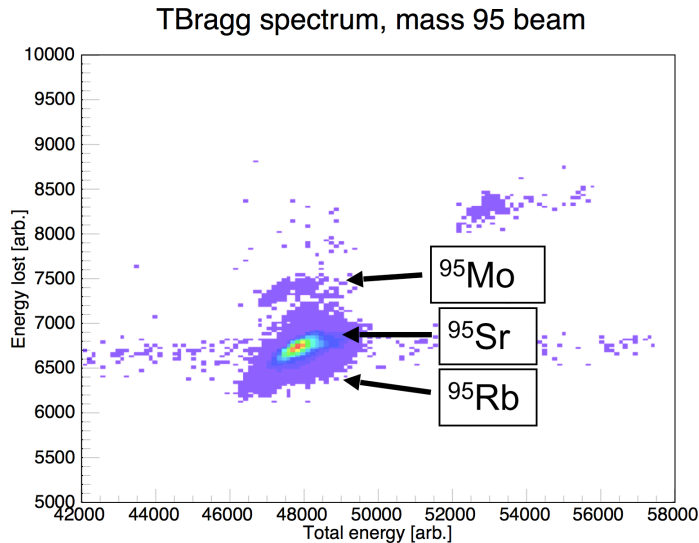
Figure 2.3: Beam identification plot of energy loss versus total energy as measured in the T-Bragg spectrometer. The beam was 98.5(5)% ^{95}Sr. See section 2.4.1 for more details.

burned through the CD_2 target, at which point the experiment was ended. The burned-out target can be seen in figure 2.7. In both experiments, there was substantial fluctuation of the beam intensity. In the 2013 ^{94}Sr experiment, there was also some fluctuation in the beam composition throughout the beam time, although the main constituent of the beam remained ^{94}Sr. The Table 2.1 gives a summary of the beam delivery for the ^{94,95}Sr experiments.

Beam	Average Rate [s^{-1}]	Total Duration [days]	Purity [%]
^{94}Sr	$\sim$3x10^4	3	$\sim$80
^{95}Sr	$\sim$1x10^6	2.5	$\sim$98

Table 2.1: Summary of ^{94,95}Sr beam delivery

2.3 Target Composition

The deuterated polyethylene (CD_2) target was manufactured with a specified nominal thickness of 5.0μm. This thickness was chosen as a satisfactory trade-off between total reaction cross section and energy broadening due to energy loss effects, both of which increase with the target thickness. The presence of elastic proton scattering in the data indicated that the target was

not fully deuterated, and so the ratio of hydrogen to deuterium in the target was determined using the (d,d) and (p,p) elastic scattering data. It was found that the target deuteration in the 2014 [95]Sr experiment was 92(1)%, which is discussed further in section 5.1.

It was possible to determine the thickness of the target, Δx, in a consistent way using the known deuteration factor by measuring the energy loss of α-particles using a simple experimental setup and comparing this to stopping power calculations that were carried out using TRIM [ZZB10] in order to find a corresponding thickness. A triple-α ([239]Pu [241]Am [244]Cm) calibration source was positioned behind the target in a zero-degree configuration. The energies and intensities of the α-particles emitted from the source are summarized in table 4.1.

(a)   (b)
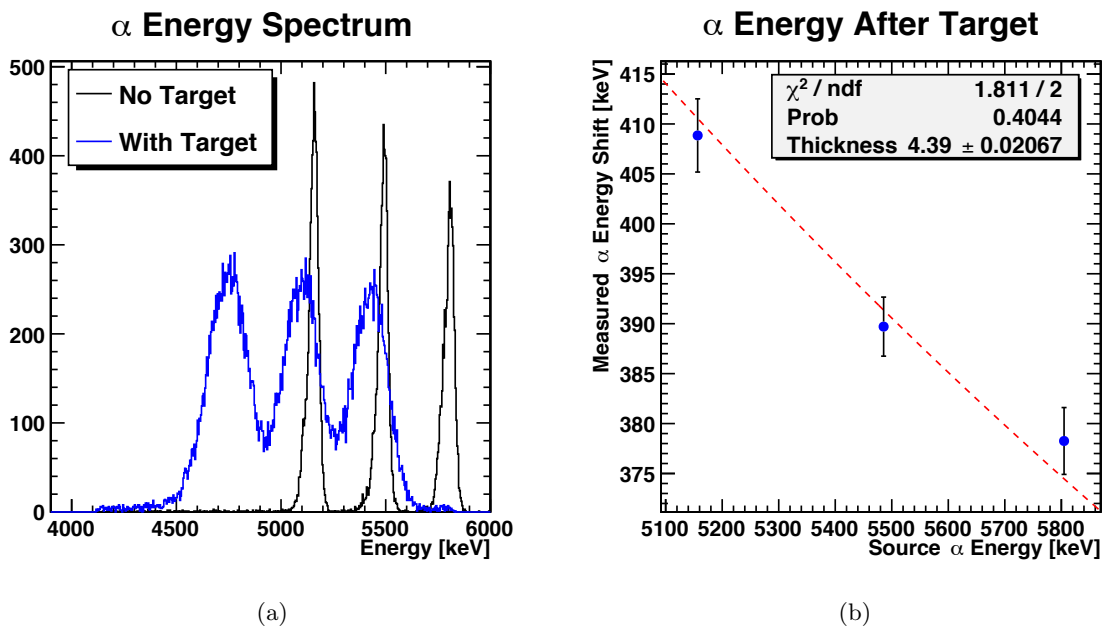
Figure 2.4: (a) Measured α-particle energy spectrum, with and without the target foil present. (b) Target thickness fit.

Figure 2.4a shows measured α-particle energies, both with and without the target foil. Figure 2.4b shows the fit of the energy loss measurements to TRIM data, including the measured ratio of ^{2}H to [1]H. The nominal thickness was used as the free parameter to be minimized in the fit. An additional estimated uncertainty of 10% was also added to account for theoretical uncer-

tainty of the ion stopping power. Best agreement between the measurements and theory was achieved for $\Delta x = 4.4(4)\mu$m. In the ^{94}Sr experiment, the target thickness was not measured after the experiment, and so was taken to be 5.0μm.

2.4 Detector Systems

The various detectors used for the experiments covered by this thesis are described in the following sections together with their basic operational principles.

2.4.1 TBragg

The energy loss of charged particles in matter is well described by the Bethe-Bloch formula, details of which can be found in [KAW77]. The features of the Bethe-Bloch formula which are relevant for this work are summarized in equation 2.1.

$$\frac{dE}{dx} \propto -\frac{mz^2}{E} \tag{2.1}$$

The energy loss of an ion in a given medium as a function of distance (or stopping power) depends on its kinetic energy E, mass m, and atomic number z.

The TBragg detector [Nob13] is a gas-filled ionization chamber used for identifying heavy ions which are present within the radioactive cocktail beam. As the beam ions enter the chamber they lose energy in the gas and produce many free electrons, which are then collected at an anode at the end of the chamber under the action of an applied longitudinal electric field. The gas pressure controls the penetration depth of the beam into the chamber, and must be chosen so that the beam is completely stopped within the chamber so a full energy measurement can be made. The strength of the electric field determines how quickly and efficiently the electrons can be collected. A pulse shape analysis of the electrical signal is used to extract information about the incident ion: the slope of the signal is related to the stopping power of the ion, $\frac{dE}{dx}$, and the total signal amplitude is proportional to the total ion energy, E.
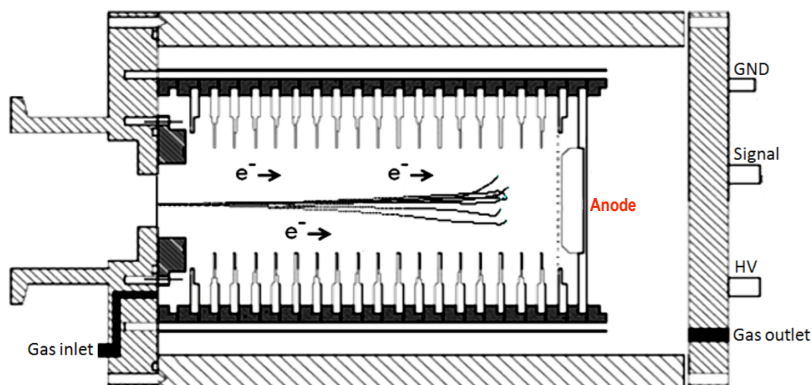
Figure 2.5: Schematic diagram of a Bragg ionization chamber, adapted from [Nob13]. Ions enter the chamber and lose energy (example ion paths are drawn), creating free electrons (also indicated). The electrons are then drifted to an anode using an applied electric field.

2.4.2 SHARC

The Silicon Highly-segmented Array for Reactions and Coulex (SHARC) is a multi-purpose compact array of double sided silicon detectors (DSSDs) which is designed to have almost 4π acceptance in its full instrumentation [DFS$^+$11]. It is optimized for angular distribution measurements due to its excellent angular resolution. Figure 2.6a shows a schematic diagram of SHARC as it was used in this experiment.

The array was designed and built by the University of York and the University of Surrey, and the silicon detectors are all manufactured by Micron. Each detector unit of the array is mounted on a separate PBC backing which is then attached to an aluminium frame. The modular design of SHARC makes it possible to configure different detector arrangements so that specific experimental needs can be satisfied.

There are several distinct detector types within the array; DSSD ΔE detectors, quadrant ΔE detectors and pad (E) detectors. The arrangement of these detectors within the array is shown schematically in figure 2.6a.

- The BB11 DSSDs (Double-Sided Strip Detectors) are rectangular detectors with dimensions of 72mm x 48mm. The front face is divided into 24 strips which run parallel to the longer dimension with 3mm pitch and the back face is divided into 48 strips which

run parallel to the shorter dimension with 1mm pitch. The DSSDs are configured so that the side with highest segmentation runs perpendicular to the beam axis, giving the best possible resolution in θ. The largest θ range subtended by any strip was for BS0, with $\Delta\theta_{BS0} \sim 1.3$ °. Four DSSDs are then combined into ϕ-like rings to form open-ended boxes, also known as barrel detectors. The compact arrangement of the DSSDs within barrel detectors is such that they are mounted approximately 42mm from the beam axis. The target is placed between two barrel detectors, which have a small separation at $90°$. In this work, the upstream and downstream DSSD barrel sections are referred to as UBOX and DBOX respectively.

- The QQQ2 quadrant detectors (or QQQ for short) are also double sided. The front face is divided into 16 annular strips which span from 9-41 mm and the back face is divided into 24 annular strips which span a ϕ angular range of $81.6°$. The largest θ range subtended by any strip was for FS15, where $\Delta\theta_{FS15} \sim 1.7$ °. The quadrant detectors are mounted in groups of four in SHARC to produce CD detectors which cover almost all ϕ angles and act as end-caps on both the upstream and downstream sections of SHARC. The naming conventions for the upstream and downstream end-caps are UQQQ and DQQQ respectively.

- The MSX-35 pad detectors are thick silicon detectors which are not segmented. They are mounted immediately behind the wafer DSSDs and so the position of the measured particles can be taken from the DSSDs. The pad detectors are designed to enable full particle energy measurements at forward angles where the kinetic energy is largest. The use of ΔE-E detector arrangements also allows for particle identification (PID).

The specifications of each SHARC detector are summarized in table 2.2 and the naming conventions that will be used in this thesis are also introduced.

This configuration was chosen to optimize sensitivity to small center-of-mass angles for (d,p) and maximize overall geometrical coverage, while minimizing the risk of damage to the detectors. The downstream QQQ detectors were not instrumented as this was at risk of hard radiation damage due to high energy carbon nuclei elastically scattering from the deuterated
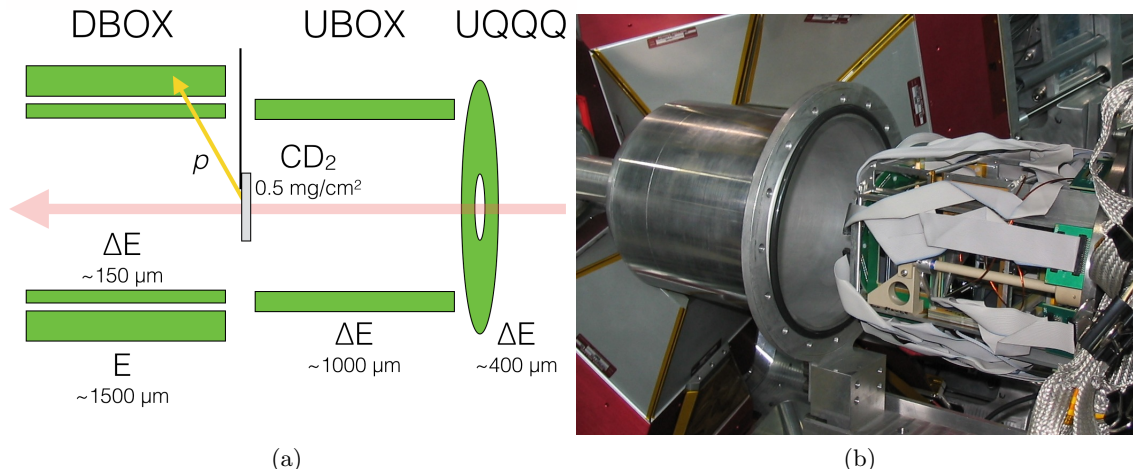
Figure 2.6: (a) Schematic diagram SHARC detector, indicating main sections and target position with respect to beam. (b) A photograph of SHARC detector being installed [DFS^{+}11]. The micro-pitch ribbon cables and PCB feedthroughs are also visible.

polyethylene target at small laboratory angles. A thick (~ 1 mm) aluminium foil was placed in front of the downstream CD section (DQQQ) to protect the detectors. It was later found during the analysis that a large amount of beam-like nuclei were implanted into the aluminium foil as a result of elastic scattering off carbon in the target, which led to a large amount of β-decay data also being taken during the experiment. This is discussed further in appendix D. There was approximately 90% ϕ coverage over the following theta ranges; 35°-80° in the downstream box (DBOX), 95°-142° in the upstream box (UBOX) and 148°-172° in the upstream CD (UQQQ) section.

The SHARC detector signals were read out with micro-pitch ribbon cables which are connected to PCB feedthroughs. These can be seen in figure 2.6b, which is a photograph taken during installation into the target chamber. Each channel was connected to fixed-gain pre-amplifier boards. The gain was set to limit the maximum energy to be 25 MeV. This is well above the kinematic energy of the transfer protons, although carbon elastic scattering would cause saturation.

A custom pre-amplifier rack was built for SHARC in this experiment which was hung from the overhead TIGRESS cable track. This can be seen in figure 2.9. It was built to allow the

Name	Type	Dimension [mm]	Segmentation	Thickness [μm]	Deadlayer [μm]
DBOX 5	BB11	72 x 48	24(J) x 48(O)	141	0.1
DBOX 6	BB11	72 x 48	24(J) x 48(O)	142	0.1
DBOX 7	BB11	72 x 48	24(J) x 48(O)	133	0.1
DBOX 8	BB11	72 x 48	24(J) x 48(O)	143	0.1
PAD 5	MSX-35	72 x 48	1(J) x 1(O)	1534	1.0
PAD 6	MSX-35	72 x 48	1(J) x 1(O)	1535	1.0
PAD 7	MSX-35	72 x 48	1(J) x 1(O)	1535	1.0
PAD 8	MSX-35	72 x 48	1(J) x 1(O)	1539	1.0
UBOX 9	BB11	72 x 48	24(J) x 48(O)	999	0.1
UBOX 10	BB11	72 x 48	24(J) x 48(O)	1001	0.1
UBOX 11	BB11	72 x 48	24(J) x 48(O)	1001	0.1
UBOX 12	BB11	72 x 48	24(J) x 48(O)	1002	0.1
UQQQ 13	QQQ2	9-41 x 81.6°	16(J) x 24(O)	390	0.7
UQQQ 14	QQQ2	9-41 x 81.6°	16(J) x 24(O)	390	0.7
UQQQ 15	QQQ2	9-41 x 81.6°	16(J) x 24(O)	383	0.7
UQQQ 16	QQQ2	9-41 x 81.6°	16(J) x 24(O)	385	0.7

Table 2.2: SHARC detector summary table. The array is arranged into several sections; DBOX+PAD, UBOX and UQQQ. D(U) prefixes in detector names refer to downstream(upstream) components.

pre-amplifiers be positioned as close as possible to SHARC, and to minimize the cable lengths. This is beneficial as longer cables have higher capacitance than short cables.

Several targets and a 2mm collimator were mounted on a target wheel to facilitate online beam alignment and target changing. Figure 2.7 shows the target holder in SHARC at the end of the 2014 ^{95}Sr experiment. Heavy damage is clearly visible on the 0.5 mg/cm^2 CD$_2$ primary target.

2.4.3   TIGRESS

The TRIUMF-ISAC Gamma-Ray Escape Suppressed Spectrometer (TIGRESS) is an array of Hyper-Pure Germanium (HPGe) clover detectors [SPH$^+$05]. When it is fully implemented there are 16 clover detectors in the array. However, when it used in conjunction with SHARC a maximum of 12 detectors can be used. This is due to space being taken up by the SHARC pre-amplifiers. TIGRESS is purpose-built for use in reaction studies where photons are emitted
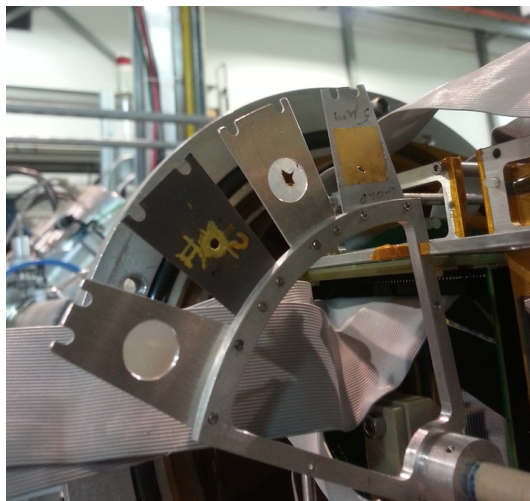
Figure 2.7: The target wheel photographed at the end of the experiment. From left to right: 5.0 mg/cm^2 CD$_2$, 2mm collimator, 0.5 mg/cm^2 CD$_2$ primary target. The primary target was burned through after approximately 2.5 days due to the high beam rate delivered.

from moving nuclei and so an important design feature of the array is good angular resolution.

Each TIGRESS clover detector is made up of four closed-ended n-type coaxial HPGe crystals. The individual crystals contain an electrical core contact and an eight-fold electrical segmentation; four quadrants and a lateral divide. This produces an overall 32-fold segmentation within each clover. This provides very good sensitivity to the emission angle of the γ-ray, which means that precise Doppler reconstruction is possible. The segmented design also makes it possible to improve the quality of the data taken in TIGRESS by using addback algorithms, as will be described in section 4.2.2. Figure 2.8b depicts the segmentation within a single clover detector.

The clover detectors are arranged into constant θ rings surrounding the target chamber, with their centres at 45°, 90° and 135°. There is close to full ϕ coverage within each ring. As was previously mentioned, TIGRESS was restricted to 12 of the 16 HPGe detectors, and so the 45° ring (with respect to the beam dump) was not implemented in this experiment. Each clover is surrounded by a set of four Bismuth Germanate (BGO) Compton suppressor shields, which can be used as a veto for γ-rays Compton scattering in the detector and escaping from the Ge crystal [SPH+05]. Figure 2.9 shows a photograph of the TIGRESS array as it was used in this
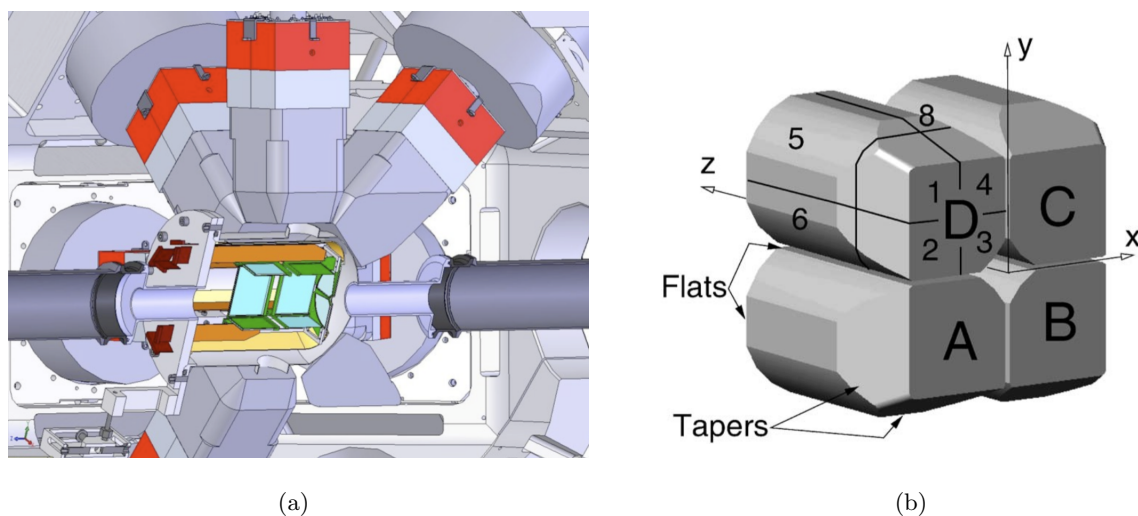
Figure 2.8: (a) CAD cutaway drawing of TIGRESS surrounding the SHARC detector. (b) TIGRESS clover detector with indication of crystal segmentation [SPH$^+$05].

work. The 90° ring of clovers can be seen alongside one of the four retracted BGO shields which accompanies each detector. The SHARC pre-amp rack is also visible, as is the beam line and target chamber.

There are two operational modes for the array; optimized peak-to-total and high-efficiency. In optimized peak-to-total mode, the clovers are pulled back and the BGO shields are brought forward so that they are flush with the front face of the clover detectors at a distance of 14cm from the reaction target. This increases the peak-to-total efficiency of the array as partial energy measurements are detected by the shields and can then be removed from the data.

In high-efficiency mode, all of the clover detectors are brought forward so that their front faces form a continuous detector surface (a rhombicuboctohedron) surrounding the target chamber at a distance of 11cm from the reaction target. The Compton suppressor shields must be withdrawn in high-efficiency mode, and so suppression cannot be fully implemented. The advantage of this operational mode is that it maximizes the geometrical efficiency of the array and therefore maximizes the total statistics. The 22.5° tapering at the front of each clover detector allows the front segments of adjacent clovers to pack together tightly. The clover design makes it possible to add together the energies of Compton scattered γ-rays between neighbouring crystals,

Figure 2.9: Detector arrangement used for this experiment. TIGRESS can be seen in high efficiency mode surrounding the target chamber, which contains SHARC. The mounted pre-amp rack and cabling setup, suspended above the beam line adjacent to TIGRESS, is also visible in this photograph.

which increases the photo-peak efficiency of the array. This will be described in more detail in section 4.2.2. Figure 2.8a shows a cut-away CAD drawing of TIGRESS set-up in high efficiency mode. The shields, which would be pulled back in this configuration, are not included in the diagram.

Each TIGRESS clover contains an in-built pre-amplifier and high voltage supply for every segment, and also one for the core contact. These are all connected to a shared cryostat which is maintained at 77K using a liquid nitrogen LN2 reservoir.

2.4.4 Trifoil

The trifoil scintillator is an auxiliary detector system which was operates as a zero-degree scintillator [W+12]. It is comprised of a 10 μm BC400 foil held within a plexiglass frame and connected to a set of three photomultipliers. The very fast scintillation light signals from the

BC400 foil allows for very high counting rates, enabling this detector to be used as a RIB beam counter. Figure 2.10a shows a schematic diagram of the trifoil as it was used in this experiment and figure 2.10b is a photograph of the trifoil detector before the experiment. This detector was set-up downstream of the target chamber, as can be seen in figure 2.1.

(a)   (b)
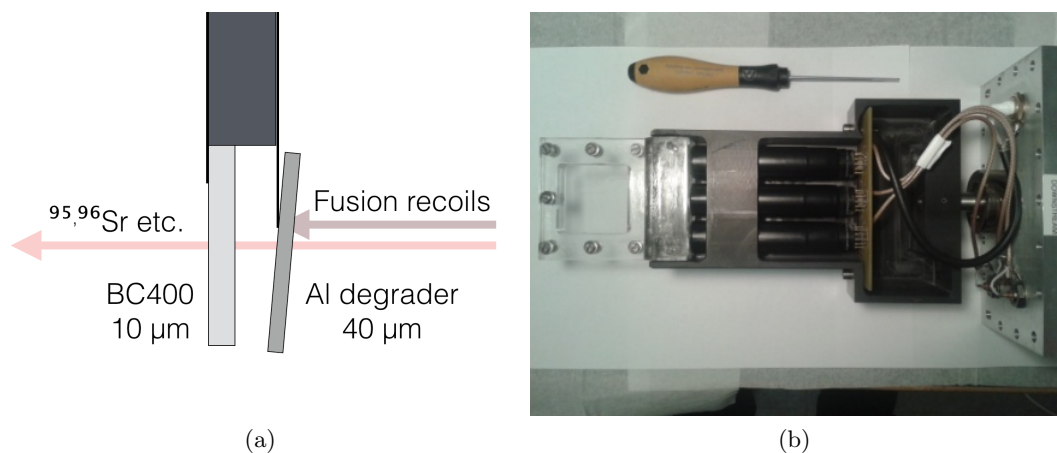
Figure 2.10: (a) Schematic diagram of trifoil degrader-scintillator arrangement. (b) Trifoil detector, photographed during setup.

The mass-95 radioactive beam can undergo fusion within the target and then quickly evaporate several light particles into SHARC. These particles can be indistinguishable from the transfer protons of interest and so this can make the analysis very difficult. It is possible to suppress these fusion reactions using the trifoil by mounting an aluminium degrader foil in front of the trifoil which stops the heavy fusion recoils but not the light ^{95}Sr and ^{96}Sr nuclei. The thickness of aluminium degrader foil was selected to be 40 μm, and this was mounted on a rotating flange so that the effective thickness could be adjusted to be up to 56.6 μm by adjusting the angle of the foil up to 45°.

The trifoil was installed approximately 30% into the beam time during both experiments. During the ^{95}Sr experiment, the BC400 foil sustained heavy radiation damage due to the intense beam, gradually lowering the light collection efficiency around the beam spot. This made it difficult to determine the efficiency of the trifoil, which is essential for a quantitative analysis.

For this reason the trifoil was used as a qualitative tool, primarily to check if γ-ray peaks were coincident with beam-like nuclei or fusion events. Figure 2.11a shows the heavily damaged trifoil caused by the 2014 RIB.
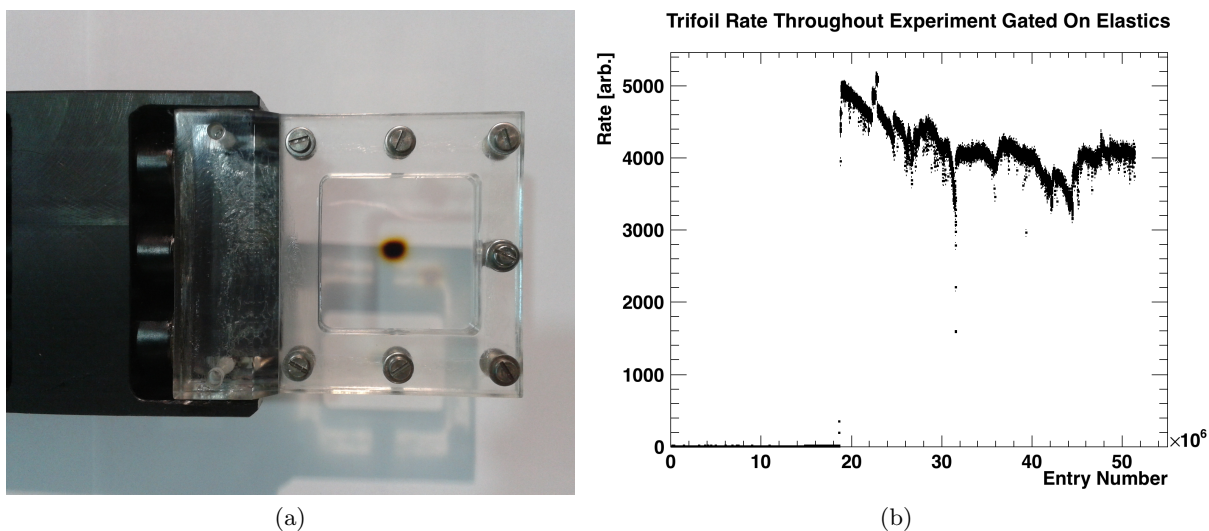
Figure 2.11: (a) Damage caused to the BC400 foil during the experiment by the high beam intensity made it difficult to use the trifoil in analyzing the data. (b) Count rate of the trifoil throughout the experiment.

The trifoil operates using a logical discriminator which requires two of the three photomultipliers to trigger in order for the signal to be read out. This was implemented using a NIM coincidence module, which had a 6.5 ns resolving time. The fast NIM output from the coincidence unit was sent directly to the TIG-10 input in the data acquisition system.

2.4.5 Data Acquisition System

The pre-amplified signals from SHARC, TIGRESS and the trifoil were processed in the data acquisition system (DAQ) before the data could be written to disk. TIGRESS and SHARC use a novel custom DAQ that was built in-house at TRIUMF to serve the specific requirements of the highly-segmented arrays. The advantage to using such a system is that every output signal from the detector only needs a single channel on a single module to create an energy, time and trigger logic. By comparison, older systems, where traditional NIM electronics are

used, require a number of modules to perform the same task. The custom digital DAQ allows for the thousands of TIGRESS and SHARC channels to be practically readout. Nevertheless, the simpler wiring diagram comes at the cost of the complexity of the firmware running on the individual digitizers and associated software on the DAQ computers needed to write the data to disk. Firmware problems during the setup of the 2014 ^{95}Sr experiment created issues with the SHARC triggering time signals, which prevented the use of SHARC timing gates in the analysis. Timing gates are a very powerful tool for discriminating between correlated and random events, and are especially useful for determining whether charged particles and γ-rays are emitted simultaneously from a source. It was possible, however, to use the RF phase to distinguish between subsequent beam bunches which was the basis of the DAQ triggering system.

Figure 2.12 shows a diagram of the DAQ system logic. The front-end (FE) of the TIGRESS and SHARC DAQ architecture was made up of TIG-10 (10-channel) and TIG-64 (64-channel) front end modules, respectively. The TIG-10 modules were used to digitize a sample of each
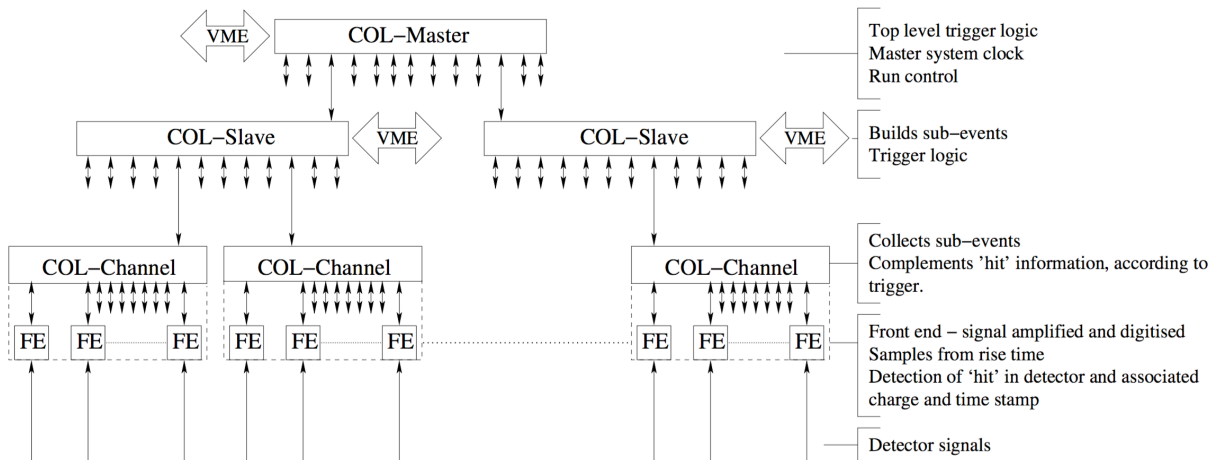
Figure 2.12: Diagram of DAQ logic. Detector signals were sent to the TIG-10 front-end (FE) modules before digitization, logical discrimination and event assembly.

pulse shape using a 10 ns timing window. The time stamp assigned to the measured pulses in the TIG-10 modules was determined using a constant-fraction discriminator (CFD) circuit. Each TIG-10 output data stream was then sent to a slave port in the TIG-C collector module,

which builds sub-events from the input streams. As was briefly mentioned earlier, it was not possible to determine the time stamp of the SHARC signals due to firmware issues. Instead, the SHARC time stamps were bootstrapped to the RF timing signals. In the collector module, a triggering condition was used which required that all SHARC events had a simultaneous DSSD front-back hit. Upon passing this condition, the good SHARC hit was read out and used as a master trigger for the DAQ. All TIGRESS and trifoil signals that were measured within 1 μs of the silicon trigger were then taken to be associated with the same event, and so were also written to disk.

Chapter 3

Simulations

Simulations are an essential part of many physics experiments, especially in nuclear and particle physics. They provide a valuable tool for understanding experimental data, devising new experiments and also designing detectors. For data analysis, simulations allow analysis techniques to be developed and tested using user-specified input data. Geant4 is a powerful simulation software package developed by CERN and others [Ago03] which allows users to build sophisticated models of detector systems and carry out monte-carlo simulations of experiments. Geant4 uses high-quality descriptions of physics processes such as the interactions of particles with matter to generate realistic data.

At the time of this work, a Geant4 implementation of the integrated SHARC and TIGRESS detector system was not available and so simulations including both particles and γ-ray were not possible. Instead, separate simulations were carried out for the detection of charged particles and γ-rays.

3.1 SHARC Simulations

Experiments using heavy ion beams in inverse kinematics are limited to rather poor energy resolution in the measured ejectile particles. The use of a thick target contributes to substantial energy broadening due to considerable beam energy loss within the target. A limiting factor in the analysis of this experiment was therefore the energy resolution of measured particles in SHARC, which was studied using NPTool.

NPTool, developed by Adrian Matta [Mat], is a Geant4-based framework for nuclear physics which contains a detailed implementation of SHARC. This can be seen in figures 3.1a and 3.1b. In NPTool, an experiment is modelled through two stages, simulation and analysis.

Firstly, a Geant4 simulation is carried out which models the various processes that take place in a reaction: Firstly, the beam loses energy in the target before a reaction takes place at some randomly selected point. An input angular distribution is used to define the center-of-mass angle of emission for the reaction products. The angular distribution is multiplied by $\sin\theta_{CM}$ and then normalized to produce a probability density function (PDF). The reaction products are boosted into the laboratory frame using Lorentz vectors and propagated until there is no remaining energy or the particles have reached the edge of the simulated volume. The latter situation arises if particles pass through the detector but are not stopped entirely, or if the particle misses the detector.

(a)   (b)
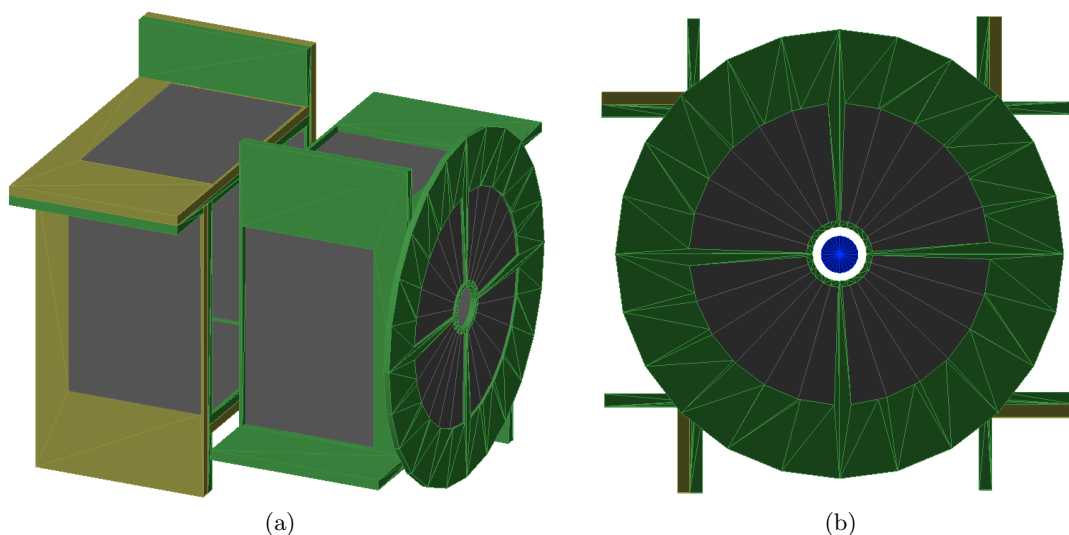
Figure 3.1: (a) NPTool implementation of SHARC including DBOX, UBOX and UQQQ sections. (b) Beam-line view, showing the CD_2 target.

The second stage of the modelling process is an analysis of the calculated detector hits so that the reaction can be studied in the same way as an experiment. In reality, the reactions take place approximately equally at all positions in the target (within the beam profile) although this position information cannot be determined experimentally. Instead, each measured particle in SHARC must be assumed to have been created in a reaction at the center of the target. The simulated data was also analyzed in this way and so all energy losses of the particle were added

back to reconstruct the total energy of the particle, assuming it propagated from the center of the target along the beam axis.

A series of reactions were simulated using a 4.5μm CD_2 target and a 5.515 MeV/u ^{95}Sr beam, which are summarized in table 3.1. A Gaussian function with $\sigma \sim 0.5$ mm was used to model the beam profile, which is a reasonable description of the beam profile delivered in this experiment. Simulations of the equivalent reactions involving a ^{94}Sr were also carried out and had very similar results, however for the sake of brevity only the ^{95}Sr results are presented.

Several reactions were studied using NPTool. Elastic scattering was simulated assuming pure Rutherford scattering angular distributions so that the energy losses and energy resolution could be investigated. Each of the elastic scattering reactions were simulated using 10^6 events. Realistic ^{95}Sr(d,p) simulations were also carried out for a series of different states in ^{96}Sr, where the excitation energy E_{exc} of these states is given in table 3.1. FRESCO [Tho88] was used to generate the DWBA angular distributions and the number of simulated reactions was chosen to reflect the relative total cross section for each reaction, assuming a spectroscopic factor of unity.

Reaction	E_{exc} [keV]	Angular Distribution	Number of Reactions
^{95}Sr(p,p)	0	Pure Rutherford	1 x 10^6
^{95}Sr(d,d)	0	Pure Rutherford	1 x 10^6
^{95}Sr(^{12}C,^{12}C)	0	Pure Rutherford	1 x 10^6
^{95}Sr(d,p)	0	Flat	1 x 10^6
	0	ℓ=0 DWBA	3.6 x 10^5
	815	ℓ=2 DWBA	1 x 10^6
^{95}Sr(d,p)	1229	ℓ=0 DWBA	4.9 x 10^5
	1465	ℓ=0 DWBA	5.1 x 10^5
	1792	ℓ=4 DWBA	3.4 x 10^5

Table 3.1: Summary of NPTool simulations carried out for ^{95}Sr reactions in SHARC.

Elastic Scattering Simulations

Each of the elastic scattering simulations listed in table 3.1 was carried out and analyzed separately which ensured that every particle and reaction was identified correctly. This is an ideal

case. Under real experiment conditions, different reaction products can be measured at the same position with the same energy energy which can lead to ambiguities in particle identification.

Figure 3.2a shows the reconstructed kinematic energy of the elastically scattered particles. The increasing number of counts as θ approaches $90°$ is characteristic of Rutherford scattering in inverse kinematics. It can be seen that the elastically scattered carbon has a much greater spread of energies than the protons and deuterons. This is because the energy lost by a carbon ion is much more than for a proton or deuteron, and so the approximation that every reaction occurred in the center of the target induces a much bigger error. The lower statistics of carbon data is also a result of the large stopping power. For angles close to $\theta_{LAB}=90°$, the differential cross section is maximum but the amount of target material that the ion travels through is also larger and so most of the carbon is stopped within the target.

(a)   (b)
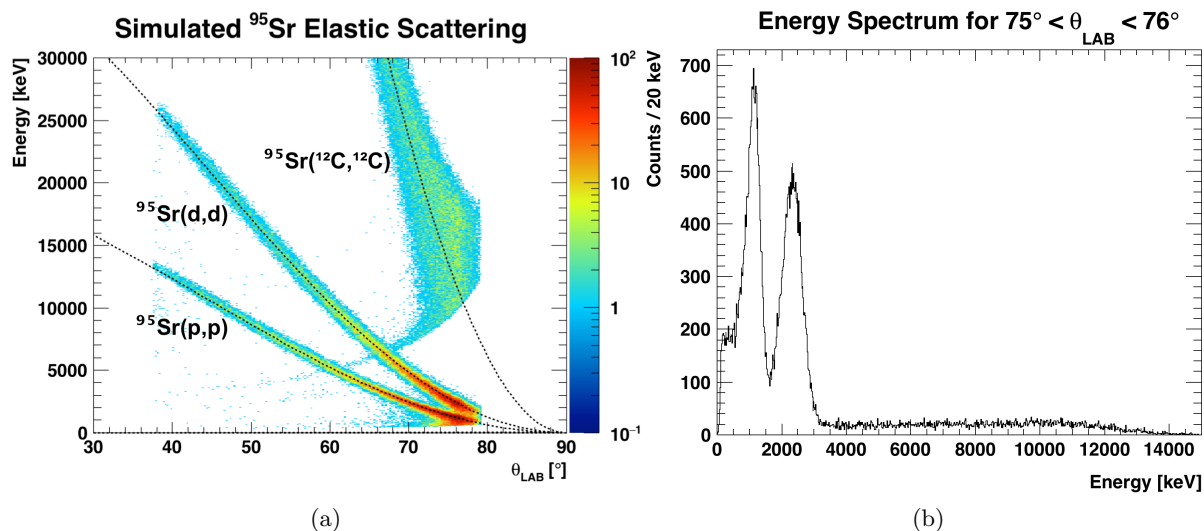
Figure 3.2: (a) Simulation results for ^{95}Sr(p,p), ^{95}Sr(d,d) and ^{95}Sr(^{12}C,^{12}C) kinematics. (b) Simulated energy spectrum for a small angular range in SHARC (more details in the text).

Figure 3.2b shows the raw energy spectrum gated on a small angular range. The elastically scattered protons and deuterons form well-defined peaks while the carbon data forms a very broad distribution which is very difficult to fit. For this reason, the carbon data will not be

analyzed in this thesis. It is also clear that the elastically scattered protons and deuterons have similar energies and so their peaks increasingly overlap as θ approaches 90°. In this angular region their low kinetic energy means that they do not punch through the ΔE detectors and so they cannot easily be separated. It is necessary to fit them together in this region so that the angular distribution can be extracted. Moreover, inelastic scattering of deuterons will not be resolvable from elastically scattered protons in this region.

Transfer Reaction Simulations

The expected energy resolution and angular coverage for ^{95}Sr(d,p) was investigated by simulating an $\ell = 0$ ground state transfer reaction. Figure 3.3a shows the reconstructed kinematic energy of the protons. The gap in the data at $80° < \theta_{LAB} < 100°$ in figure 3.3a is due to the spacing between the DBOX and UBOX sections in SHARC, which can be seen in figure 3.1a. At small laboratory angles, the protons punch through the pad detector and so do not deposit all of their energy, which can be seen through the departure of the data from the expected kinematic line at $\theta_{LAB} < 60°$. This reduces the effective angular coverage of SHARC, since a full energy measurement is required for a correct description of the reaction. Figure 3.3b shows the number of measured protons as a function of lab angle which have a complete energy measurement compared to those with incomplete energy measurements. The protons with incomplete energy measurement were selected using a graphical cut in figure 3.3a.

Figure 3.4a shows the reconstructed excitation energy of the simulated reactions as a function of center-of-mass angle. The gap in the data at $45° < \theta_{CM} < 65°$ in figure 3.4a is again due to the spacing between the DBOX and UBOX sections in SHARC. The intensity pattern is caused by the probability density function combined with the geometrical detector efficiency (including the previously mentioned pad punch-through). It can be seen that the distribution of excitation energies is centered close to the appropriate energy (0 keV) with a small negative offset, but has a significant width. This width is different for each section of SHARC, and increases with θ_{CM}.

Figure 3.4b shows a projection of the data for the individual sections of SHARC. The pro-
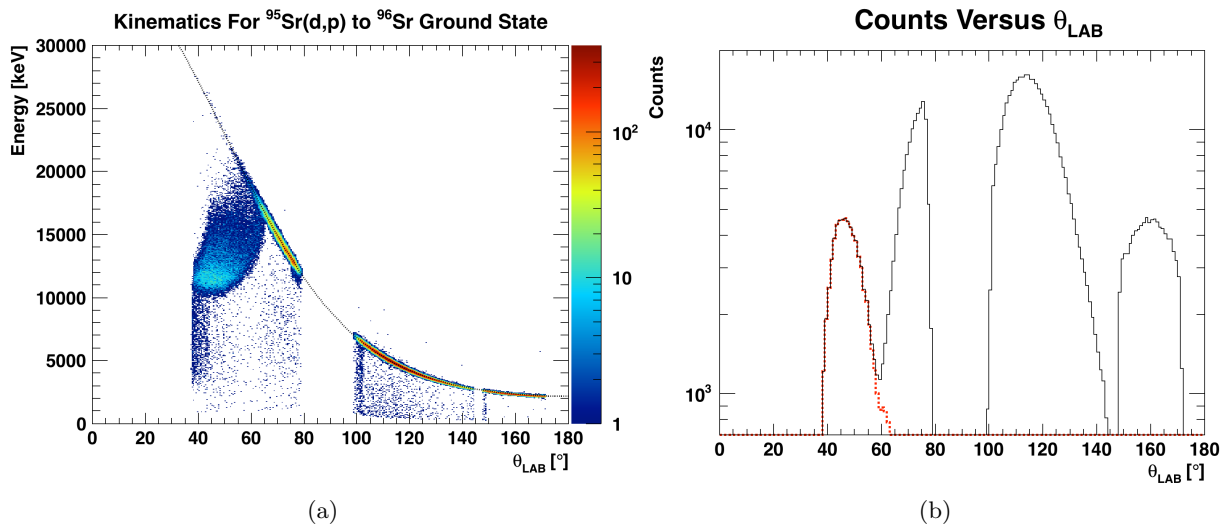
Figure 3.3: (a) Simulation results for $\ell = 0$ ^{95}Sr(d,p) kinematics. (b) Counts versus lab angle for all data (black) and for $|E_{\text{exc}}| > 500$ keV (red). The latter data corresponds to incomplete energy measurement.

jections were fitted using a Gaussian function so that the width of the distribution could be described quantitatively. The UQQQ section has the best energy resolution but the lowest total counts, even though the input angular distribution file has maximum cross section at θ_{CM}=0°. This is because angles close to 0° and 180° have a smaller weight in the probability density function due to the $\sin \theta_{CM}$ factor, as mentioned earlier in this section. The UBOX section has a slightly larger distribution width and contains most of the data, while the DBOX section has much worse energy resolution and a centroid offset. The combined energy resolution of each of the SHARC sections was found $\sigma \sim 140$ keV for an $\ell = 0$ angular distribution, however this value depends on the amount of data in each of the detector sections. If the input angular distribution instead has a maximum cross section at a large angle (or equivalently, describes a larger angular momentum transfer) there will be more weighting towards larger center-of-mass angles, and so the total resolution would reflect this.

The simulations were used to demonstrate that the angular momentum transfer and total cross section (or equivalently the spectroscopic factor) could be extracted from the SHARC measurements. The measured counts were plotted against center-of-mass angle for three states; 0 keV
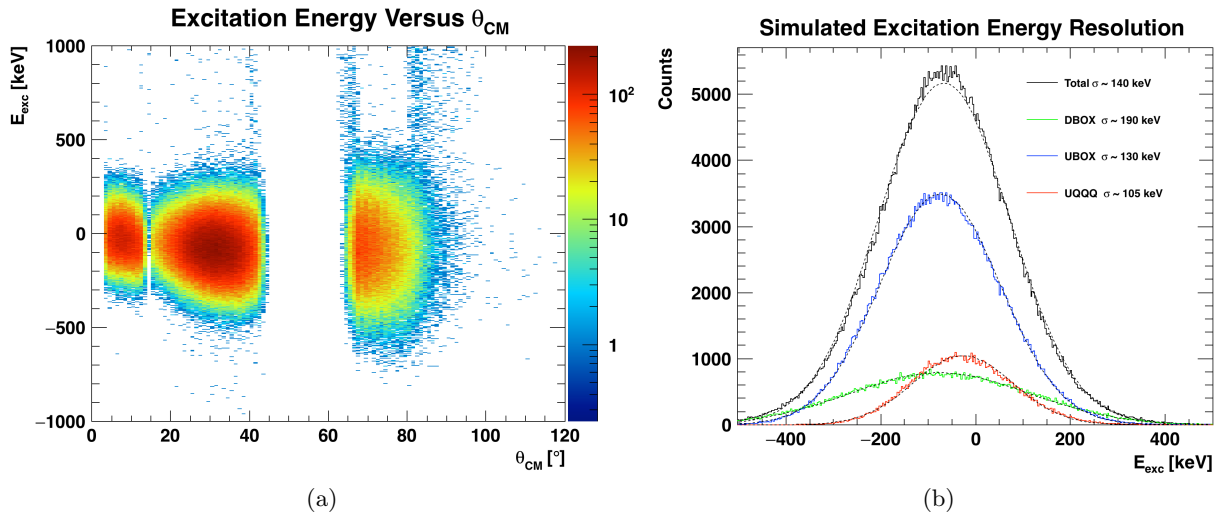
Figure 3.4: (a) Simulation results for (d,p) analysis. (b) Excitation energy resolution for SHARC.

$(\ell = 0)$, 815 keV $(\ell = 2)$, 1792 keV $(\ell = 4)$. An excitation energy window of 1000 keV was used to extract the counts from each state, which account for the energy resolution. The measured counts at each angular position is the scaled probability density function (PDF) multiplied by the efficiency of SHARC at that angle. The scaled PDF is the PDF multiplied by the total number of simulated reactions. The same SHARC efficiency curve was used in the simulations and the experimental analysis, which is described in section 4.1.3.

Figure 3.5a shows the angular distribution analysis, where the data points represent the measured counts and the error bands represent the expected distributions. Overall, the results were in good agreement with the expected measurements. Small deviations between the expected and measured counts were primarily due to a slight discrepancy in the description of the geometry and position of SHARC in the NPTool model versus the real detector. Protons punching through the DBOX pad detectors can be seen as the sudden drop in measured counts at large center-of-mass angles. Figure 3.5a represents a situation where the measured states can be identified and analyzed separately. This is possible to do using $p - \gamma$ coincidence measurements as long as the states can be identified using unique γ-ray transitions. It is also useful to consider situations where the states cannot be selected using γ-rays, such as when the statistics are very low or when states that are close in energy decay via the same γ-ray. The latter is true in the

case of the excited ^{96}Sr $0^+_{2,3}$ states, as both states are coincident with a 414 keV γ-ray.
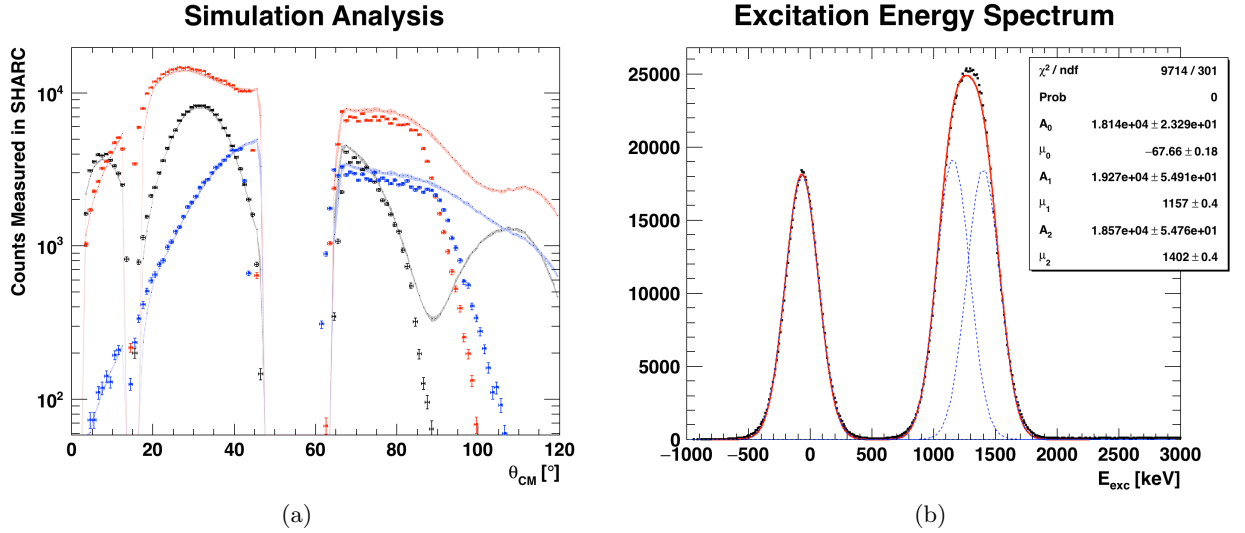
Figure 3.5: (a) Measured counts versus center-of-mass for the simulated 0 keV (black), 815 keV (red) and 1792 keV (blue) ^{96}Sr states, compared to efficiency-corrected input. (b) Excitation energy resolution of SHARC for ^{95}Sr(d,p) reactions in inverse kinematics.

Figure 3.5b shows the projected excitation energy spectrum for the $0^+_{1,2,3}$ states ^{96}Sr. It was found that the 1229 keV state and 1465 keV state could be fitted together in a reliable way only by constraining the width of the Gaussian functions to be $\sigma \sim$135 keV. The ground state is also featured in figure 3.5b to show that the choice of σ was appropriate to describe the individual peaks. Figure 3.5b shows that analyzing states which are less than approximately 250 keV apart in excitation energy (that cannot be separated using γ-rays) will be challenging, even with a large amount of statistics. This is because of the limiting resolution of SHARC in this experiment. A γ-ray analysis of the 650 keV $0^+_3 \rightarrow 2^+_1$ transition would therefore be very useful in identifying the 0^+_3 state.

3.2   TIGRESS Simulations

Simulations of γ-ray decays within TIGRESS were also carried out. In this way, the dependency of the Doppler correction and photo-peak resolution on the life-time of a given state could be studied. The Doppler reconstruction in both the simulation and experiment employed

the approximation that the nucleus decayed at the reaction point, which is discussed further in section 4.2.4. For isomers or states with long lifetimes, this approximation becomes invalid as the fast moving recoil nucleus may decay far from this point. The isomeric 0_3^+ state in ^{96}Sr has a half-life of 6.7(10) ns [Lab], and given the kinematics of the reaction it would travel approximately 20 cm in that time. Clearly, the Doppler reconstruction for this state would perform poorly. The 0_2^+ state in ^{96}Sr has a half-life of 115 ps, which would mostly decay within 1 cm. In addition, most of the isomer decays would happen outside of the TIGRESS array, causing the geometrical efficiency to be substantially smaller. By using a simulation it was possible to investigate these effects so that the sensitivity of TIGRESS to the γ-ray decay of the 1465 keV 0_3^+ state in ^{96}Sr could be better understood.

(a)   (b)
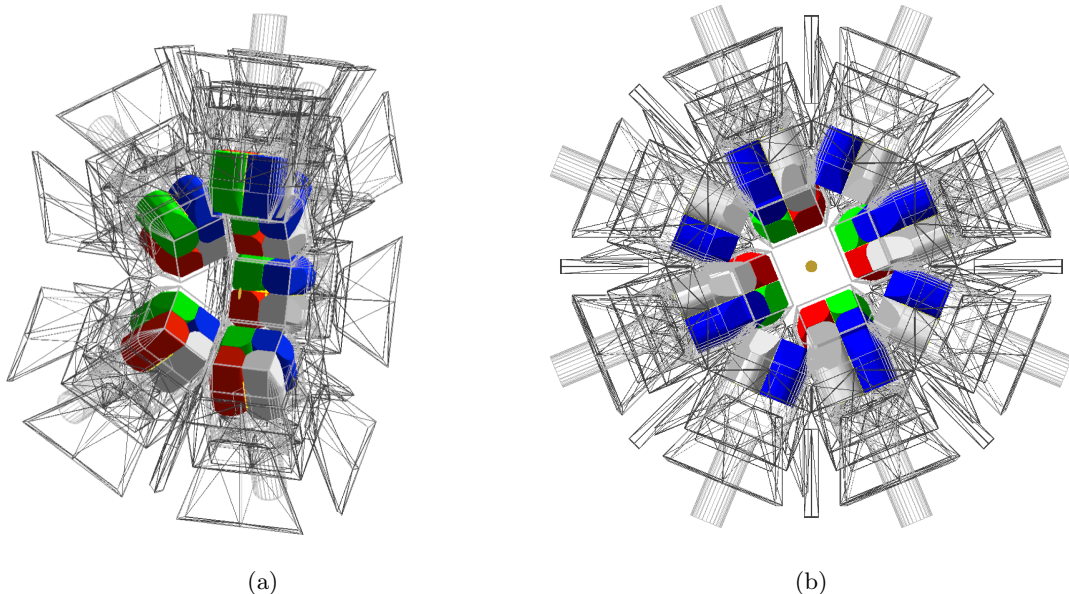
Figure 3.6: (a) Geant4 model that was used to study decays in TIGRESS. (b) Beam-line view, showing the CD$_2$ target.

A fully implemented model of TIGRESS was not available at the time of this work. Instead, simulations of γ-ray detection were carried out using a model of GRIFFIN, which is geometrically equivalent but does not have segmentation within the clover crystals [SG14]. For this reason, crystal positions were used in Doppler reconstruction of the simulated decays. This led

State Energy [keV]	γ-ray Energy [keV]	$t_{\frac{1}{2}}$ [ps]	Photo-peak Counts	Efficiency [%]
815	815	4.8	1.253×10^5	12.53
1229	414	$5^{\dagger}$	1.917×10^5	19.17
1465	650	$5^{\dagger}$	1.448×10^5	14.48
1506	692	6.2	1.372×10^5	13.72
1995	1180	$5^{\dagger}$	1.019×10^5	10.19

Table 3.2: Simulated states used for efficiency calibration. States marked with † were assigned 5 ps half-lives (more details in the text).

to a slight broadening of the simulated peaks compared to fully segmented crystals.

Five low energy ^{96}Sr state decays were simulated so that the photo-peak efficiency could be determined for the simulated array. Table 3.2 lists the γ-ray transitions that were used for the photo-peak efficiency calibration. 10^6 events were simulated for each decay. Each state was simulated using a short half-life so that all of the decays occurred within the target. The states marked with a † symbol were assigned artificially short half-lives so that the Doppler reconstruction would perform optimally and the detector acceptance was not reduced due to decays outside the array. In this way, the Doppler reconstruction and efficiency of the array for long-lived states could be benchmarked against the ideal case.

The γ-ray spectra for these states are shown in figure 3.7a. The absolute photo-peak efficiency of the array at each of the γ-ray energies are shown in the table, and the corresponding efficiency curve is shown figure 3.7b.

Simulating Long-Lived States

There are two decay scenarios that must be considered in order to measure the mixing strength between the excited 0^+ states in ^{96}Sr. Firstly, the 1229 keV 0_2^+ state in ^{96}Sr can be populated directly (with strength S_2) through ^{95}Sr(d,p), and then decay via the 815 keV 2_1^+ state to the ^{96}Sr ground state. Alternatively, the 1465 keV 0_3^+ state in ^{96}Sr can populated directly (with strength S_3) through ^{95}Sr(d,p), which would then go on to feed the 1229 keV state. Even though both scenarios have similar decay signatures, the latter case involves the decay of an isomeric state and so it would be measured with a different efficiency and photo-peak shape.
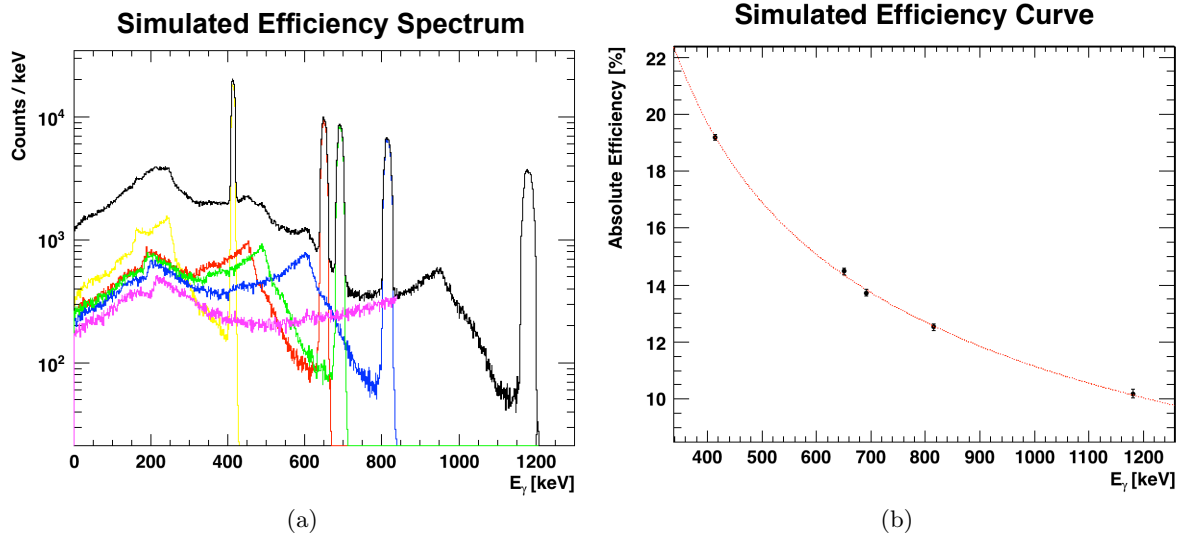
Figure 3.7: (a) Simulated γ-ray spectrum using the decays listed in table 3.2. The sum spectrum is drawn in black. (b) Absolute efficiency curve produced using the decays listed in table 3.2.

The 235 keV $0_3^+ \rightarrow 0_2^+$ electromagnetic transition is of pure monopole character, and so cannot take place through the emission of a γ-ray due to angular momentum selection rules (which are discussed in appendix E). The two decay scenarios can be seen in figure 3.8.

The expected number of $0_3^+ \rightarrow 2_1^+$ 650 keV γ-rays observed in TIGRESS, N_3^γ, can be written as

$$N_3^\gamma \quad = \quad \varepsilon_3 \varepsilon_g B_3 S_3 \tag{3.1}$$

where S_3 is the total direct population strength of the 1465 keV ^{96}Sr state, ε_3 is the efficiency of TIGRESS for a decay at the reaction point which emits a 650 keV γ-ray, B_3 is the branching ratio of the $0_3^+ \rightarrow 2_1^+$ transition and ε_g is the lowered acceptance of TIGRESS for an isomer which has a half-life of 6.7 ns and is travelling at $v = 0.1c$. ε_g can be determined by simulating an isomer decay and a prompt decay using a realistic model of the detector system and taking the ratio of the values. ε_g is independent of energy, and simply reflects the decreased geometrical efficiency of the array as the fast moving recoil decays along the z axis.

Similarly, the total number of $0_2^+ \rightarrow 2_1^+$ 414 keV γ-rays observed in TIGRESS, N_2^γ, can be
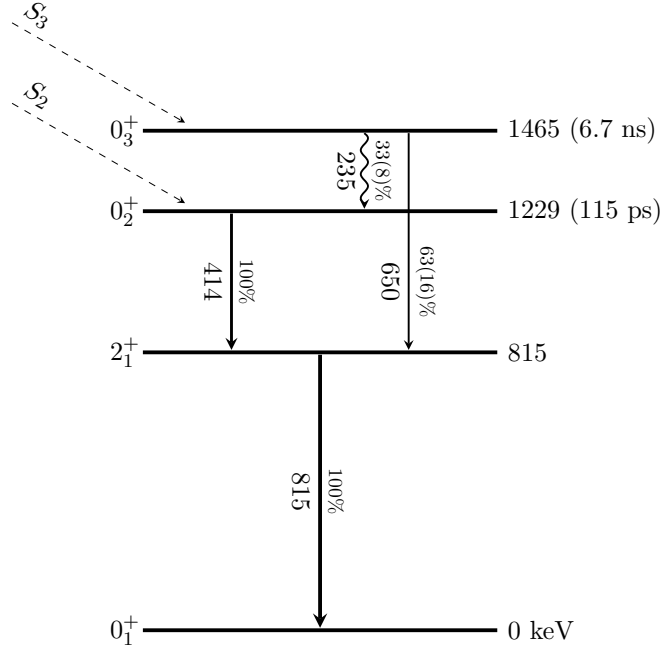
Figure 3.8: Decay scheme for $0_{2,3}^+$ ^{96}Sr states, indicating transition energies (given in units of keV) and branching ratios (given as a percentage). The $0_3^+ \rightarrow 0_2^+$ and $0_3^+ \rightarrow 2_1^+$ branching ratios were taken from [Jun80].

written as

$$N_2^\gamma = \varepsilon_3(S_2 + \varepsilon_g B_2 S_3) \tag{3.2}$$

where S_2 is the total direct population strength of the 1229 keV ^{96}Sr state and $B_2 = 1 - B_3$. The additional term in equation 3.2 explicitly includes feeding from the 0_3^+ state. Combining equations 3.2 and 3.1 provides an expression which relates the population strengths of the $0_{2,3}^+$ states to the observed counts, $N_{2,3}^\gamma$.

$$\frac{S_3}{S_2} = \frac{\mathcal{R}}{\varepsilon_g\big[B_3(1+\mathcal{R}) - \mathcal{R}\big]} \tag{3.3}$$

where $\mathcal{R} = \frac{\varepsilon_2 N_3^\gamma}{\varepsilon_3 N_2^\gamma}$.

The 0_2^+ state decay was simulated using its known half-life of 115 ps [Lab]. It was found that this lifetime caused a small shift in the photo-peak energy of approximately -1 keV due to

the Doppler reconstruction error. There was also a decrease in photo-peak counts by less than 1% compared to a decay that occurred within the target. The 0_2^+ state decays to the ground state through the 2_1^+ state, and so this increased lifetime also affected the 2_1^+ decay peak in the same way. These increased lifetime effects were considered to be negligibly small, and so the experimental γ-ray data associated with the direct population of the 0_2^+ state did not need to be analyzed differently to other short-live states.

The decay of the $0_{2,3}^+$ and 2_1^+ states were also simulated using a life-time of 6.7 ns. This represents the feeding of states from the long-lived 0_3^+ state. In actuality, there would be an increased lifetime for each of the lower states, but their lifetimes were very small compared to the 0_3^+ and so they were considered negligible. 10^6 decays were simulated for the $0_{2,3}^+$ and 2_1^+ states (which emit 414 keV, 650 keV and 815 keV γ-ray rays respectively). The simulated spectrum for a 650 keV $\rightarrow$ 414 keV $\rightarrow$ 815 keV γ-ray cascade with 6.7 ns half-life is shown in figure 3.9a. The simulated spectrum for a 414 keV $\rightarrow$ 815 keV γ-ray cascade with 115 ps half-life is also shown in 3.9a for comparison. It can be seen that the total number of measured γ-rays in TIGRESS drops as a result of the long lived isomer state. The total counts in the 414 keV, 650 keV and 815 keV γ-ray peaks were found to decrease by approximately 50% compared to table 3.2. This suggests that the total geometrical coverage for these long-lived states dropped by approximately 50%. The shape of the Doppler corrected γ-ray peak also becomes very skewed and is shifted to lower energy as a result of the poor Doppler correction.

The clover detectors in TIGRESS are arranged into rings of constant θ, called coronas. Furthermore, the crystals within each clover allow each corona ring to be divided into two sub-rings of constant θ, giving a total of four unique θ rings of TIGRESS crystals. The four rings are centered at approximately $\theta_{TIG} = 80°$, $100°$, $124°$ and $144°$. The performance of the Doppler correction was found to be very dependent on the position of the corona ring. This is shown in figure 3.9b, where the black line is the total peak and the coloured lined are the Doppler reconstructed peaks from individual θ_{TIG} rings. The $\theta_{TIG} \sim 80°$ ring, drawn in red, shows that the Doppler correction performed poorly at this position. This is because the error on the angle of γ-ray emission is very large, and as a result the estimated Doppler shift was not well known. In addition, γ-rays that were emitted outside the array could also be detected through
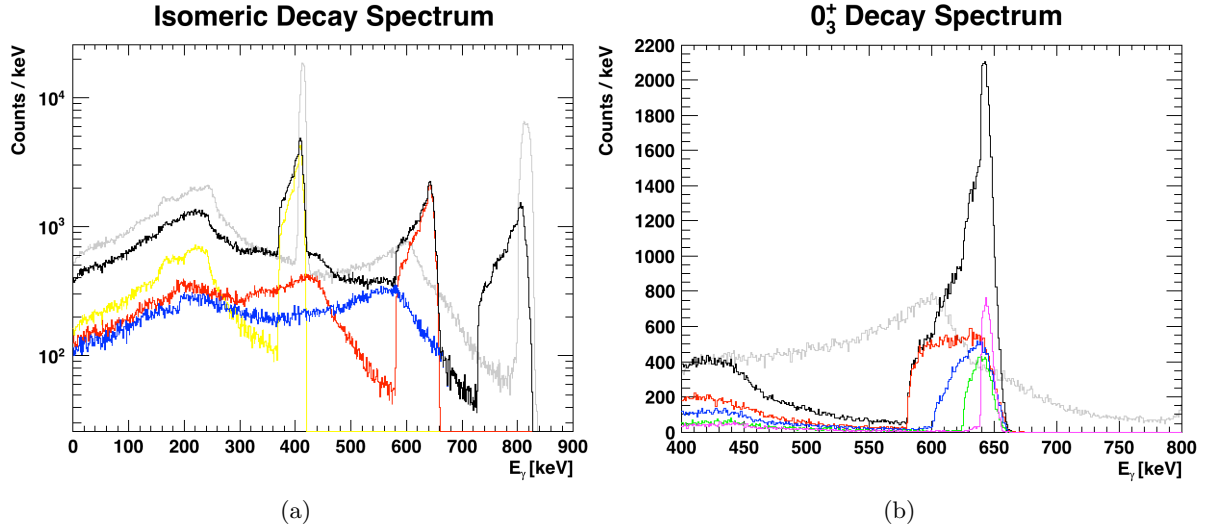
Figure 3.9: (a) Comparison of simulated spectra for states fed by isomeric 0_3^+ (black) to direct decay (grey). (b) Contributions to total photo-peak (black) from each ring of detectors (more details in the text).

the side of the crystal as this provides a large additional detector surface area. The $\theta_{TIG} \sim 100°$ ring, drawn in blue, shows a slight improvement in resolution. This is mostly because γ-rays could not enter the side of the crystals since this was obstructed by the $\theta_{TIG} \sim 80°$ ring. The $\theta_{TIG} \sim 124°$ ring, drawn in green, shows further improvement in resolution and less asymmetry in the peak. The $\theta_{TIG} \sim 144°$ ring, drawn in pink, shows that the Doppler reconstruction worked reasonably well for large TIGRESS angles. This is because the error in the angle of γ-ray emission is smallest in this region.

A matter of practical concern for the measurement of the 650 keV γ-rays is the position of the 815 keV γ-ray Compton edge, which is drawn in grey in 3.9b. Since the 2_1^+ state is a strong collecting state for the excited ^{96}Sr nucleus, it is to be expected that the 815 keV peak will have more statistics than the 650 keV peak from the 0_3^+ state. It would therefore be very difficult to extract the counts in the 650 keV peak for TIGRESS detectors close to 90° as this would overlap with the Compton edge of the 815 keV peak. The simulation shows that the 650 keV γ-ray from the 0_3^+ state would be most separated from the 815 keV γ-ray Compton edge at $\theta_{TIG} \sim 144°$.

Figure 3.10a shows the simulated γ-ray spectrum for the $\theta_{TIG} \sim 144°$ ring, using equal direct population strengths $S_2 = S_3 = 10^6$. Feeding effects are also included. A 62.5% branching ratio and a 37.5% branching ratio were used for the $0_3^+ \rightarrow 2_1^+$ and $0_3^+ \rightarrow 0_2^+$ transitions respectively, as given in figure 3.8. The blue spectrum in figure 3.10a corresponds to the decay of the 0_2^+ state, and so both an 414 keV and an 815 keV γ-ray are emitted. The red spectrum in figure 3.10a correspond to the decay of the 0_3^+ state, which emits a 650 keV γ-ray in addition to the 0_2^+ decay transitions. The black spectrum is the total, and so is what we would observe in the experiment.
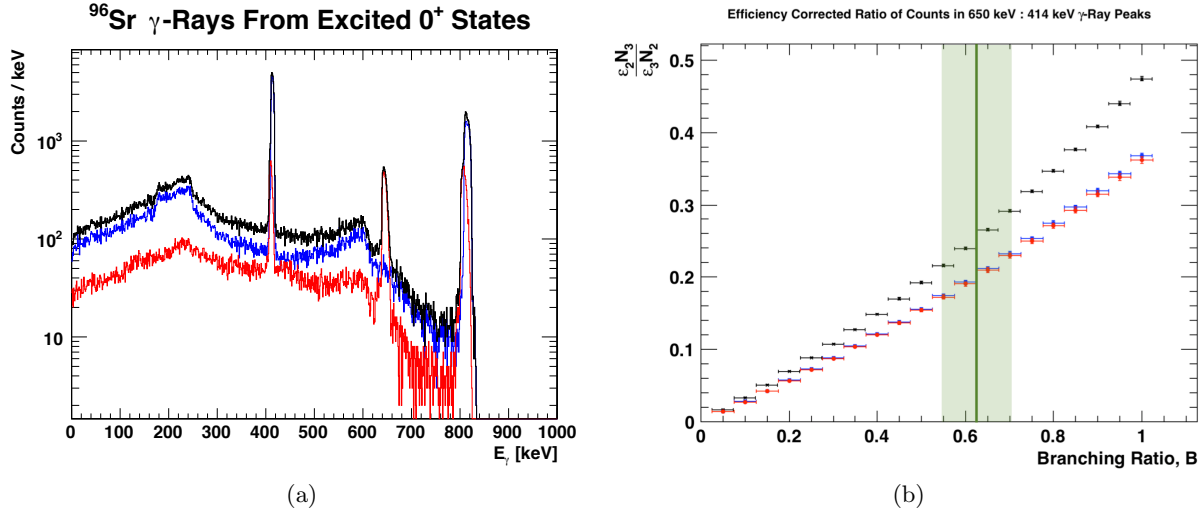
Figure 3.10: (a) Simulated γ-ray spectrum for the decay of the ^{96}Sr 0_2^+ state (blue) and 0_3^+ state (red) for $S_2 = S_3 = 10^6$, using only TIGRESS crystals positioned at $\theta > 135°$. Total spectrum is drawn in black. (b) Simulated results for the ratio of counts in the 650 keV γ-ray peak to the 414 keV peak, plotted as a function of the $0_3^+ \rightarrow 2_1^+$ branching ratio for all TIGRESS angles (black), $\theta_{TIG} > 120°$ (blue) and $\theta_{TIG} > 135°$ (red). The green band indicates the experimental branching ratio from [Lab] with its uncertainty.

The ratio of counts in the 650 keV γ-ray peak compared to the 414 keV γ-ray peak is plotted as a function of the $0_3^+ \rightarrow 2_1^+$ branching ratio in figure 3.10b. The simulation results presented in figure 3.10b include an efficiency correction to account for the lower efficiency of TIGRESS at 650 keV compared to 414 keV. The black data points in figure 3.10b represent the efficiency-corrected counts ratio for all of TIGRESS, and the blue and red data points represent the

same ratio using TIGRESS detectors positioned at $\theta_{TIG} \geq 124°$ and $\theta_{TIG} \geq 144°$, respectively. Given the measured branching ratio of 62.5±15.6% from [Jun80], the expected ratio of counts is 0.20(6) for $\theta_{TIG} \geq 124°$ and 0.19(6) for $\theta_{TIG} \geq 144°$. This means that an experimentally observed ratio of counts in the 650 keV γ-ray peak compared to the 414 keV γ-ray peak of 0.19-0.20, after efficiency correction, would be consistent with equal direct population of the excited $0^+_{2,3}$ states.

Chapter 4

Analysis Methods

In this chapter, the analysis procedure will be outlined. Both data sets were analyzed within the same framework, and so the 2014 ^{95}Sr(d,p) analysis will be the primary focus. Important differences between this and the ^{94}Sr(d,p) analysis will be highlighted.

The software package GRSISort [BBD$^+$], developed by Peter Bender and others, was used as the basis for this analysis. Details of the specific programs that were developed for this work can be found in appendix C.

4.1 SHARC Calibrations

Before each of the experiments, calibration data was taken using a triple-α source.

It was found that during the 2014 ^{95}Sr(d,p) experiment, the pre-amplifier gain values changed abruptly in the time between α-source calibrations and beam delivery. After this gain shift each of the detector channels within the SHARC units (DBOX, UBOX and UQQQ) were still well gain-matched but no longer had the correct energy scaling. The underlying cause was determined to be a floating common ground for the pre-amplifier rack. Because of this issue, the full energy calibration was carried out using the ^{95}Sr elastic scattering data. The (d,d) and (p,p) elastic channel kinematic lines were used to fully calibrate all DBOX detectors, including the pads. These kinematic lines were also used to determine the nominal target position within the array, which was fixed to a rotating mount. At angles greater than $90°$ there was no available elastic scattering data, so the ground state of ^{95}Sr(d,p)^{96}Sr was used for calibration.

For the 2013 ^{94}Sr experiment, the α-source data was sufficient to fully calibrate the ΔE detectors in each section of SHARC. The pad detectors were calibrated using in-beam data, in the

same way as was done for the 2014 pad calibrations.

Each step in the energy calibrations of SHARC is described in the following sections, which focuses on the 2014 data set.

4.1.1 α Source Gain-Matching

Each SHARC detector (with the exception of the pads) was gain matched using a double-sided ^{239}Pu ^{241}Am ^{244}Cm α-source placed in the target position. The energies and intensities of α-particles from the α-source are shown in table 4.1. The strongest α-decay branch for each isotope was used (which are highlighted in bold) and a 3-point calibration was carried out on each front strip in SHARC.

The observed α-particle energy (E_{meas}) in SHARC is the source energy (E_0) minus energy deposited in insensitive regions (δE_i) such as the target and detector deadlayers. A general description of this is given in equation 4.1, although this simplifies considerably for a calibration source.

$$E_{meas}(\theta, \phi) = E_0(\theta, \phi) - \sum^{i} \delta E_i(\theta, \phi) \tag{4.1}$$

Where the angle-dependence of the energy loss terms δE_i is a result of the changing effective thickness of the detectors and their deadlayers with angle. For a BOX detector the effective thickness $d(\theta, \phi)$ is

$$d(\theta, \phi) = \frac{d_0}{\sin\theta \cos\phi'} \tag{4.2}$$

where d_0 is the perpendicular thickness (the values quotes in table 2.2) and ϕ' is limited to the range $\frac{-\pi}{4} < \phi' < \frac{\pi}{4}$. Note that any detector can be rotated to express ϕ in this range without loss of generality.

For a QQQ detector this is simplified to

$$d(\theta, \phi) = \frac{d_0}{\cos\theta} \tag{4.3}$$

as there is no ϕ dependence for a cylindrically-symmetric geometry.

Isotope	α-particle energy [keV]	Intensity [%]
^{239}Pu	5105	11.5
	5143	15.1
	5155	**73.4**
^{241}Am	5388	1.4
	5442	12.8
	5486	**85.2**
^{244}Cm	5763	23.3
	5805	**76.7**

Table 4.1: Energies and intensities of ^{239}Pu ^{241}Am ^{244}Cm α-source, taken from [Lab]. Strong α-branches are highlighted in bold text.

In the case of the α-calibration source, E_0 is independent of angle and the only unseen energy loss is due to the deadlayer of the ΔE detector. The energy lost due to SHARC deadlayers was determined using table 2.2 and TRIM stopping power tables [ZZB10] to predict the energy lost in the nominal deadlayer thicknesses. For α-particles with approximately 5 MeV of energy propagating through silicon, $\delta E \sim 150$ keV per 0.1μm. As the energy variation within a front strip due to the effective deadlayer thickness was very small, the calibration was done on a front strip basis instead of for each individual pixel. An effective deadlayer was calculated for every front strip, reflecting the deadlayer thickness in the centre of each strip.

The calibrated channels can be seen in figure 4.1a. The energy axis represents the measured energy, including deadlayer energy loss. The discontinuity of energies at approximately channel 310 is due to a different nominal deadlayer in the UQQQ compared to the BOX detectors. Some missing channels can also be seen, as can some bad channels. These were removed in the full analysis, as will be discussed later in this chapter. Each charge spectrum was fitted with two gaussian curves for each isotope listed in table 4.1. Figure 4.1b shows a typical spectrum fit, indicating the extracted peaks for the strong α branches.

It was found that the calibration coefficients from the α-source did not reproduce expected kinematic energies in the ^{95}Sr beam data. The pre-amplifier settings had shifted after the α-source was taken out. The reason for this was determined to be a floating common ground shared by the pre-amplifiers.
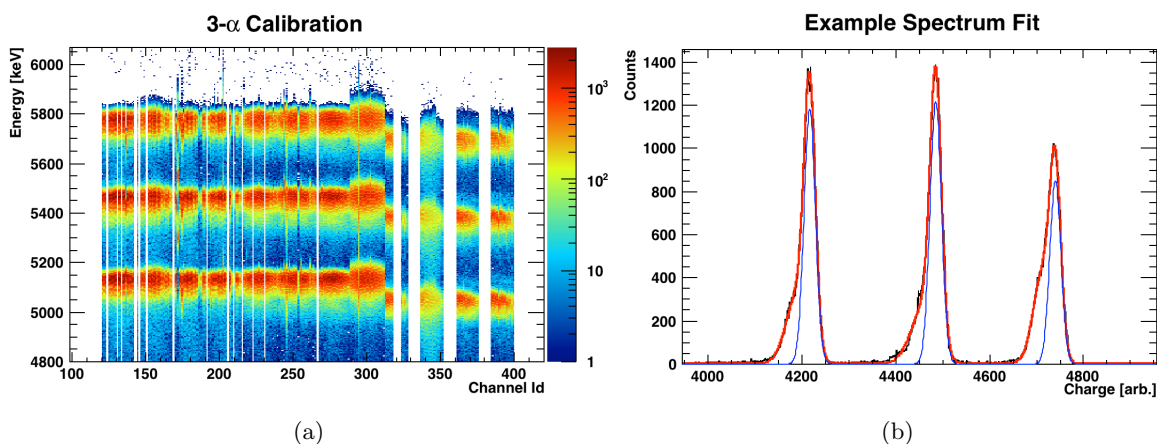
Figure 4.1: (a) Calibrated α-source energy vs. channel matrix. (b) Example α-source spectrum with total fit (red) and extracted calibration peaks (blue).

It was possible, however, to use the α-coefficients to gain match all of the front strips within the DBOX, UBOX and UQQQ detectors. The channels within each unit retained a good relative calibration, which was investigated by plotting the energy spectrum of a single channel and comparing this to the sum energy spectrum of each channel within that unit. The energy resolution was the same in the case of many overlaid spectra, which indicated a good relative calibration. It was therefore necessary to carry out further energy calibrations on each of the SHARC units.

4.1.2 Full Energy Calibrations

DBOX Calibrations

After the α-source calibration coefficients were applied, the downstream box (DBOX) unit was analyzed as a single channel. It was then necessary to fully calibrate the DBOX ΔE detectors using ^{95}Sr(p,p) and ^{95}Sr(d,d) elastic channel kinematics data. ^{95}Sr(^{12}C,^{12}C) data was also taken, but this was not analyzed because the energy resolution was very poor due to significant energy losses. The ^{95}Sr(^{12}C,^{12}C) data will be discussed further in section 4.3.

Calibrations using reaction data are more challenging than calibrations using mono-energetic sources as there is a strong angular dependence of the ion energy with θ and ϕ and worse energy resolution due to the inverse kinematics of the reaction and the target thickness. The segmen-

tation and compact geometry of SHARC made it possible to produce calibration spectra using very small θ and ϕ opening angles so that the kinematic energy broadening could be mitigated.

In order to calibrate the DBOX ΔE detectors it was necessary to have a full energy measurement of the elastically scattered particles. It was observed that the protons and deuterons punched through the DBOX ΔE detectors at $\theta \sim 62°$ and $\theta \sim 67°$ respectively, and so data beyond these cut-offs was not used. Additionally, the calibrations were carried out using only the central front strips 11 and 12. This was done in order to restrict the opening angle of the calibration region which improved the resolution of the spectra. A gain-matched charge spectrum was produced for each back strip up to the point where the particles began punching through the ΔE detectors. The approximate angular range covered by each back strip was $\theta \sim 1.3°$. The spectra were fitted using two Landau functions convoluted with a Gaussian kernel. The Landau functions describe the characteristic distribution of ion energies due to energy loss effects and the convoluted Gaussian simulates the detector response. An example spectrum fit is shown in figure 4.2b. The low energy background was caused by β-decay and also evaporated light particles from fusion events. This background was fitted using a linear function, which was a good approximation over this energy range. For the smallest back strips, the kinematic lines of the (p,p) and (d,d) and (^{12}C,^{12}C) reactions were closest together and so the peaks overlapped significantly. The carbon elastic scattering data was fitted as a background in these regions. The two peaks correspond to protons and deuterons, with deuterons having a broader energy distribution and higher peak energy. The centroids from the fitted proton and deuteron Landau distributions were extracted. The energy of the elastic peaks ΔE was calculated using equation 4.4

$$\Delta E(\theta, \phi) = E_0(\theta) - \delta E_{target}(\theta) - \delta E_{\Delta}(\theta, \phi) \tag{4.4}$$

where the kinematic energy is $E_0(\theta)$ and the energy lost in the target and deadlayer of the ΔE detector are $\delta E_{target}(\theta, \phi)$ and $\delta E_{\Delta}(\theta, \phi)$ respectively. The energy losses were calculated using TRIM stopping power tables.

The position of the reaction point within SHARC was also examined by comparing the number of counts in each of the DBOX detectors, and it was found to be well-centered within the array.
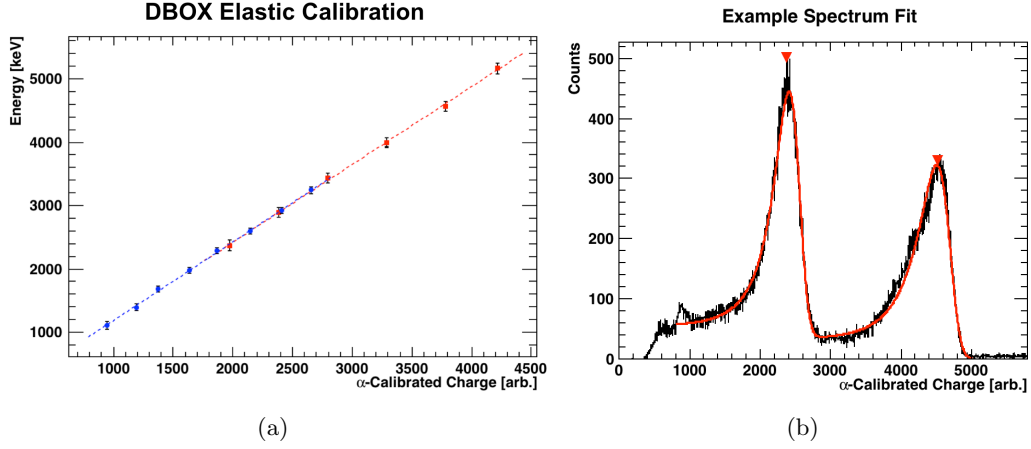
Figure 4.2: (a) Full energy calibration of DBOX ΔE detectors using ^{95}Sr(p,p) (blue) and ^{95}Sr(d,d) (red) data. (b) An example gain-matched charge spectrum showing ^{95}Sr(p,p) and ^{95}Sr(d,d).

Pad Calibrations

The DBOX pad detectors were also calibrated using ^{95}Sr(p,p) and ^{95}Sr(d,d) data. This was done in a very similar way to the DSSD ΔE detectors.

As the charged particles must pass through the target, the ΔE detector (including deadlayer) and pad detector deadlayer before they are measured in the pad detector, the explicit calibration energy is given as equation 4.5

$$E_{pad}(\theta, \phi) = E_0(\theta) - \delta E_{target}(\theta) - \delta E_{\Delta}(\theta, \phi) - \Delta E(\theta, \phi) - \delta E_{pad}(\theta, \phi) \tag{4.5}$$

where the kinematic energy is $E_0(\theta)$, the energy lost in the target and deadlayer of the ΔE detector are $\delta E_{target}(\theta, \phi)$ and $\delta E_{\Delta}(\theta, \phi)$ respectively, $\Delta E(\theta, \phi)$ is the energy deposited in the ΔE detector and $\delta E_{pad}(\theta, \phi)$ is the energy lost in the pad detector deadlayer. The energy losses were calculated using TRIM stopping power tables.

The calibration was carried out using two separate approaches. In one approach, $\Delta E(\theta, \phi)$ was calculated using the tabulated detector thicknesses in table 2.2. In the other approach, the

calibrated ΔE detectors were used to provide an experimentally measured value. Aside from uncertainties due to TRIM, the two methods were expected to produce very similar results. A discrepancy, especially one which varied across the four pad detectors would indicate that the detector thicknesses or deadlayers were not consistent with the quoted values in table 2.2. Figure 4.3a shows the calibration result for PAD 7 using both approaches. The fully calculated approach, drawn using broken lines and open symbols, shows a slight discontinuity between the (p,p) data and (d,d) data. This signifies that the exact thicknesses of the DSSDs are not well known. Instead, the experimental value of the ΔE was used in the calibration, which is drawn using solid lines and solid symbols. The quality of the pad calibration was very good using this approach.

The installation of the trifoil scintillator resulted in a sudden unexpected shift of pre-amplifier settings for pad 5, and so a piecewise calibration was also required so that this data was not lost. This shift is believed to be caused by the same floating ground issue as was noted between the α-source calibration and ^{95}Sr beam time. The piecewise calibration was carried out by following the aforementioned calibration procedure twice; once using only data before the sudden shift and then a second time using only data after the shift.

The measured energy $E_{meas}(\theta, \phi)$ can be used to determine the kinematic energy $E_0(\theta)$ by adding each $\delta E(\theta, \phi)$ energy loss back in the appropriate way. Figure 4.3b shows the fully reconstructed kinematic energy $E_0(\theta)$ of the SHARC DBOX after all energy calibrations.

UBOX and UQQQ Calibrations

At backwards lab angles ($\theta > 90°$) it was not possible to calibrate SHARC using ^{95}Sr(p,p) and ^{95}Sr(d,d) data. Instead, the clearly visible ground state kinematic line of ^{95}Sr(d,p) was used.

With the known target position offset of (0,0,0) mm, it was possible to produce a kinematic line using the α-calibrated charge. A series of α-calibrated charge spectra were produced by projecting θ-slices. The well-defined ground state peak was fitted using a Gaussian function. Equation 4.4 was used to calculate the measured energy of the transfer protons.
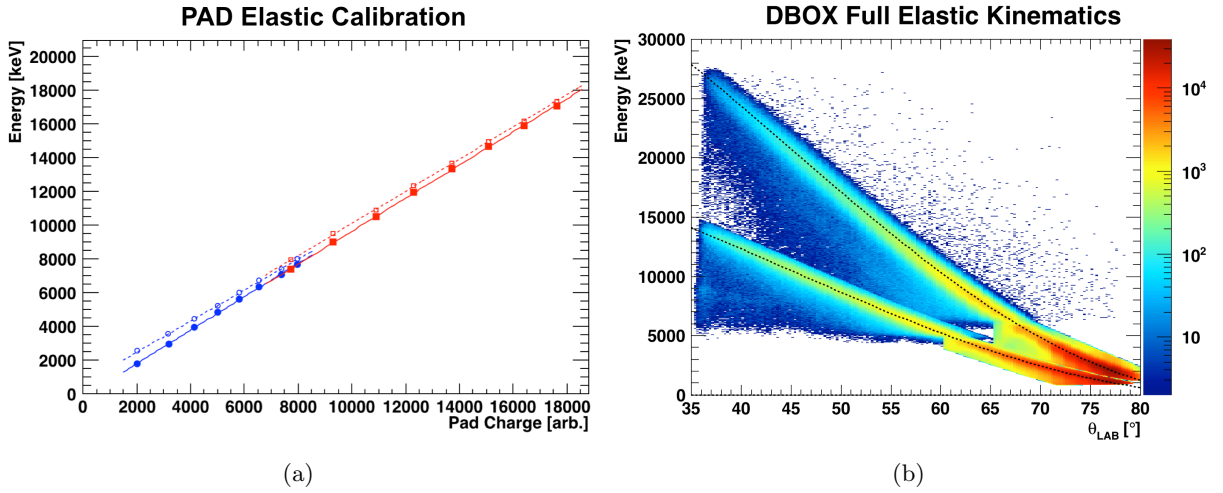
Figure 4.3: (a) Energy calibration of a pad detector using ^{95}Sr(p,p) (blue) and ^{95}Sr(d,d) (red) data. Solid lines and closed symbols indicate a calibration performed using experimental ΔE values, while broken lines and open symbols show the calibration result using only calculated ΔE values (see text for more details). (b) Calibrated DBOX showing kinematics curves for ^{95}Sr(p,p) and ^{95}Sr(d,d) compared to theory curves. Details of the cuts used are given in section 4.3.

The calibration fit for the UBOX detectors is shown in figure 4.4a and the calibrated data is shown compared to the ground state kinematic line of ^{95}Sr(d,p) in figure 4.4b.
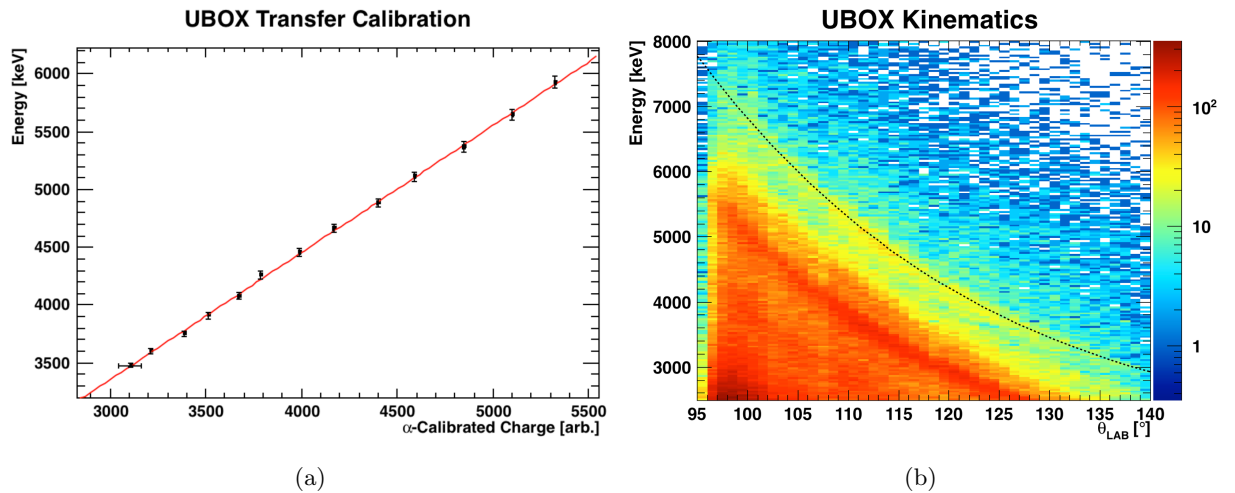
Figure 4.4: (a) Calibration fit for UBOX detector using ^{95}Sr(d,p) data. (b) Calibrated UBOX showing kinematics curve of ^{95}Sr(d,p) ground state transfer compared to theory curve.

The calibration fit for the UQQ detectors is shown in figure 4.5a and the calibrated data is shown compared to the ground state kinematic line of ^{95}Sr(d,p) in figure 4.5b.

(a)   (b)
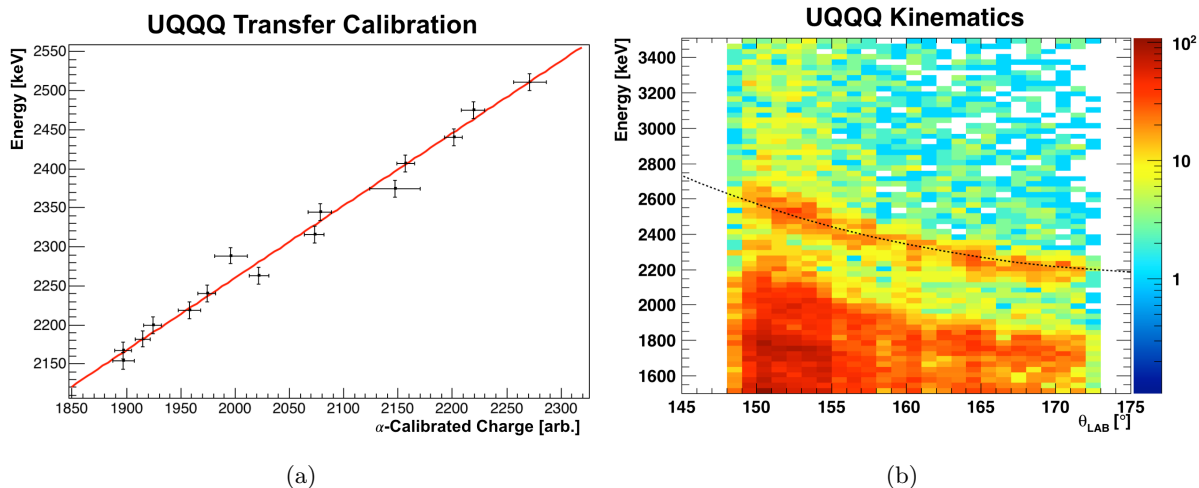
Figure 4.5: (a) Calibration fit for UQQQ detector using ^{95}Sr(d,p) data. (b) Calibrated UQQQ showing kinematics curve of ^{95}Sr(d,p) ground state transfer compared to theory curve.

4.1.3 SHARC Efficiency

The geometrical efficiency of SHARC was determined using a Monte-Carlo simulation. A large number of detector hits were simulated using a uniform distribution across every pixel in SHARC, and the solid angle of the pixels were used as weight factors. The randomized positions and pixel solid angles were combined into a weighted histogram. The weighted histogram was then divided by the number of particles simulated within each pixel in order to produce the efficiency curve, which is shown in figure 4.6a. Details on how the solid angle of each pixel was calculated is given in appendix B.

The geometrical coverage and efficiency of SHARC are shown in figures 4.6a and 4.6b respectively. The total geometrical efficiency of SHARC is calculated to be approximately 90% within the DBOX, UBOX and UQQQ sections. There is a slightly larger geometrical efficiency in the DBOX section because the DSSDs must be mounted closer to the beam-line so that the pad detector can also be instrumented.

107 of the 736 instrumented pre-amplifier channels (14.5%) were excluded from the 2014 ^{95}Sr analysis, either because they were absent or because they were performing inconsistently with other channels. These strips are listed in table B.2. The geometrical efficiency of SHARC with these strips removed is also shown in figure 4.6a. Similarly, 204 channels (27.7%) were excluded from the 2013 ^{94}Sr analysis, and these strips are listed in table B.1.
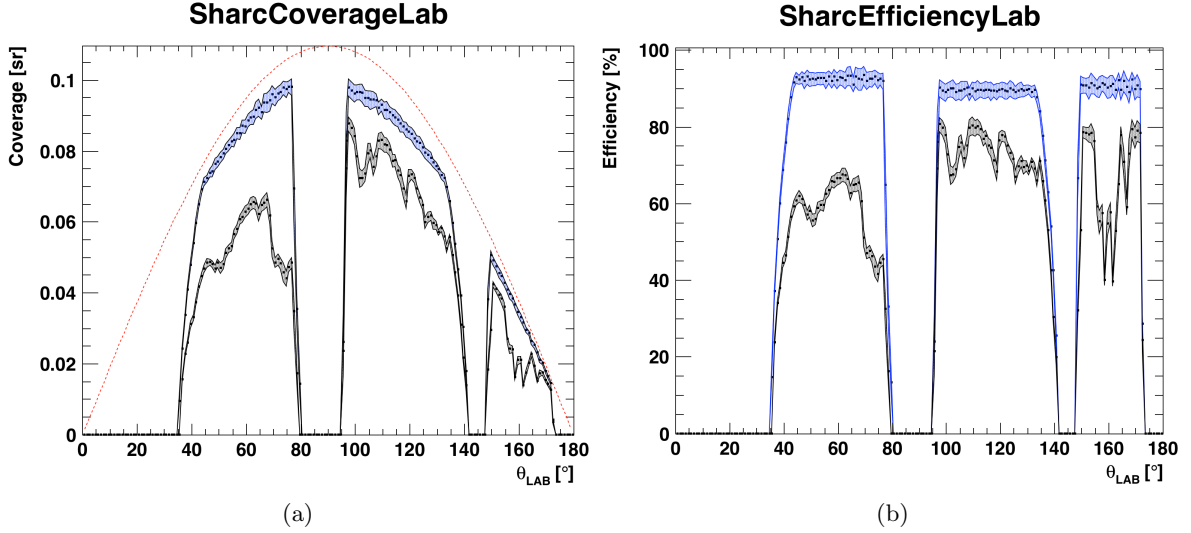
Figure 4.6: (a) SHARC solid angle coverage in lab frame with all strips included (blue), strips from table B.2 removed (black) and maximum coverage $2\pi \sin\theta d\theta$ (red), (b) SHARC geometrical efficiency in lab frame, with colours indicating the same as before.

For a reaction such as ^{95}Sr(d,p) the intensity distribution becomes more complicated. Even if the protons are emitted isotropically in the center-of-mass (CM) frame there is an additional kinematic boost which skews the intensity distribution in the lab frame, as was seen in the NPTool simulation results in chapter 3.1. There is also a non-linear conversion between CM frame angles and lab frame angles which also creates a non-uniform intensity distribution. The CM frame geometrical coverage was calculated by converting the lab frame geometrical coverage simulation pixel by pixel. The resulting geometrical coverage and efficiency curves for ^{95}Sr(d,p) are shown in figures 4.7a and 4.7b respectively.
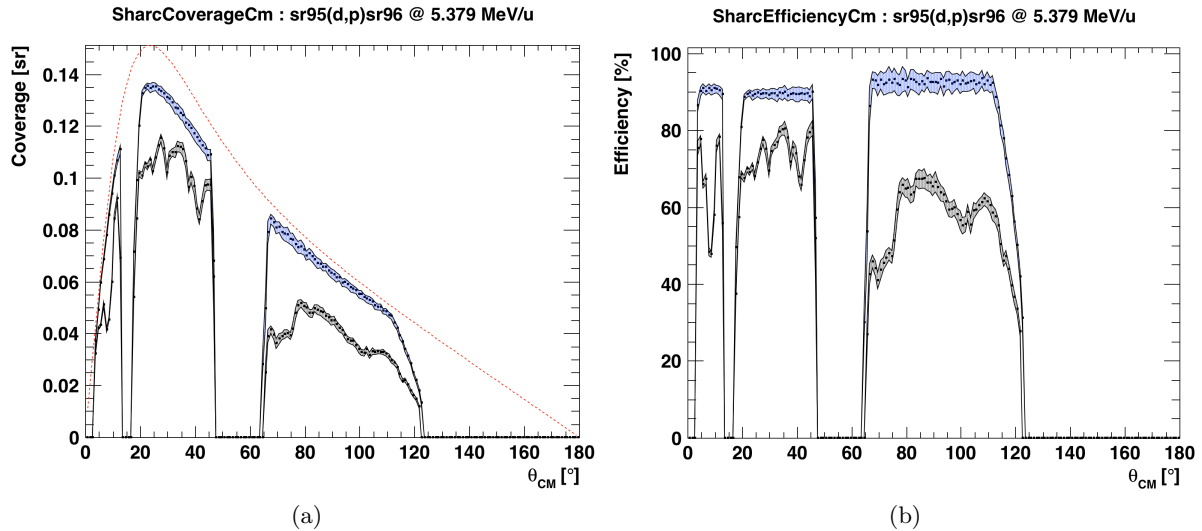
Figure 4.7: (a) SHARC solid angle coverage in centre-of-mass frame with all strips included (blue), strips from table B.2 removed (black) and maximum coverage (red), (b) SHARC geometrical efficiency in centre-of-mass frame, with colours indicating the same as before.

4.2 TIGRESS Calibrations

4.2.1 ^{152}Eu Calibration

A ^{152}Eu γ-ray source was used to calibrate energies and efficiencies of the TIGRESS array. The energies and intensities of the strongest transitions are given in table 4.2, and the peaks used in this calibration are highlighted in boldface.

A charge spectrum was produced for each clover crystal in TIGRESS and the γ-ray peaks were fitted. The centroid of each peak was extracted and a linear calibration fit was carried out. Figure 4.8a shows the calibrated energy for each crystal in TIGRESS and figure 4.8b shows the sum spectrum of all the crystals in TIGRESS. The continuous horizontal lines in the energy matrix indicate that each channel was well calibrated. This was further tested by comparing the resolution of the sum spectrum to that of an individual crystal. It was found that the sum spectrum peaks had the same width as those in a single spectrum, further confirming the good calibration quality.

γ-ray energy [keV]	Relative Intensity [%]
121.8	**141 (4)**
244.7	**36.6 (11)**
344.3	**127.2 (13)**
367.8	**4.19 (4)**
411.1	**10.71 (11)**
444.0	**15.00 (15)**
488.7	**1.984 (23)**
586.3	**2.24 (5)**
678.6	2.296 (28)
688.7	4.12 (4)
778.9	**62.6 (6)**
867.4	**20.54 (21)**
964.0	**70.4 (7)**
1005.1	**3.57 (7)**
1085.8	48.7 (5)
1089.7	8.26 (9)
1112.1	**65.0 (7)**
1212.9	**6.67 (7)**
1299.1	**7.76 (8)**
1408.0	**100.0 (1)**

Table 4.2: Energies and intensities of ^{152}Eu γ-ray calibration source [Lab]. Intensities are given relative to the 1408 keV γ-ray transition. The γ-rays highlighted in bold were used for calibrations.

The ^{152}Eu data was also used to determine the relative photo-peak efficiency of TIGRESS. The sum spectrum from figure 4.8b was used to produce a relative efficiency curve by dividing the counts within each fitted peak by the respective intensity listed in table 4.2. The efficiency data was fitted using a standard formula [Rad] which is given in equation 4.6.

$$\log_{10}(\varepsilon(E_\gamma)) = A + B\log_{10}(E_\gamma) + C\log_{10}(E_\gamma)^2 + \frac{D}{E^2} \qquad (4.6)$$

where the free parameters A, B, C and D are fitted to the data. The fit is shown as the red curve in figure 4.9a. The slope of the curve contains an important physics result: the decreasing photo-peak efficiency with energy is due to the decreasing cross section of γ-rays depositing all of their energy in a single interaction (photo-electric effect).
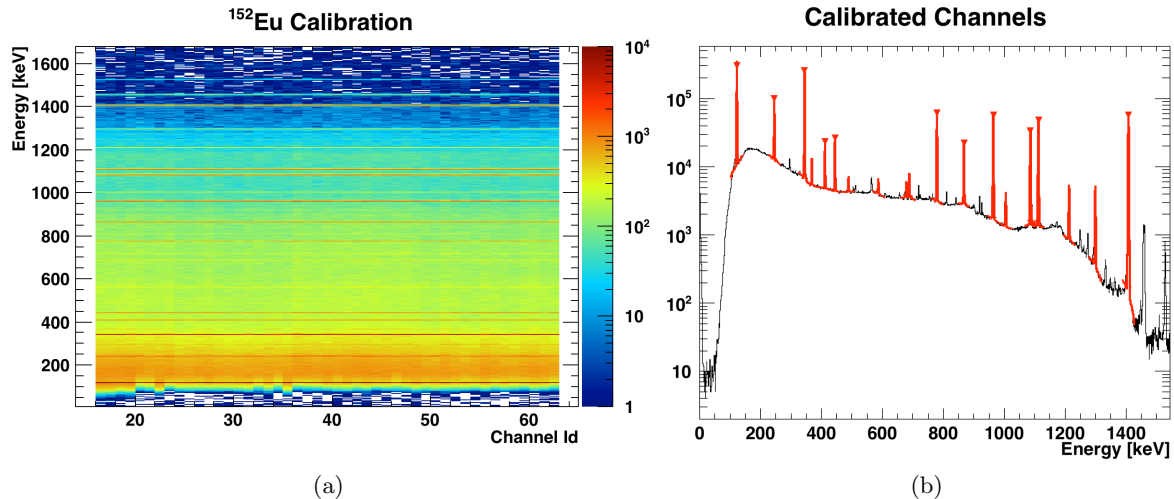
Figure 4.8: (a) Plot showing the calibrated channels of TIGRESS using a ^{152}Eu source. (b) Calibrated sum spectrum of all crystals using a ^{152}Eu source.

4.2.2 Add-Back

A γ-ray will often scatter multiple times before being completely absorbed. This is measured as a series of simultaneous energy signals distributed across different detector channels. The interactions are usually localized within a single crystal or clover detector, however adjacent clovers can also share full energy measurements. The photo-peak efficiency of TIGRESS can therefore be improved by adding together the energies of these separate signals to reconstruct a single event which contains the total energy. This technique is called add-back. The expected number of interactions increases with γ-ray energy, and so the improvement offered by add-back also depends on the total γ-ray energy. Low energy photo-peaks at ~ 500 keV or less will be largely unaffected as the dominant interaction process in this energy regime is the photo-electric effect, which results in a single interaction. At higher energies the efficiency improvement available through the use of add-back depends on the specific details of the algorithm used, and is ultimately limited by the segmentation and the geometry of the detector system.

The add-back algorithm that was used in this experiment used the following conditions to determine whether to add together different hits: In cases where multiple segments detected a signal within a single clover crystal, the total energy of the hit was taken from the core contact.

The segment hits were then ordered from largest to smallest energy deposited and this was assumed to be the order of interactions effectively describing the γ-ray track. In this approach, the angle of incidence of the γ-ray was determined using the position of the first (largest energy) hit and the final position was taken from the last (lowest energy) hit. A single add-back hit was thus created with the total core energy and an initial and final position.

If two or more crystals fired, the hits were ordered from largest to smallest core energy and the first hit in this sorted list was taken as the first add-back hit. The final interaction point in the first add-back hit was compared to the first interaction point of the other hits. If the interaction points were both in front or back segments, their separation was required to be less than 54 mm. If the interaction points were in some front to back segment combination, their separation was required to be less than 105 mm. This effectively forbids a γ-ray to travel across an active volume of germanium without scattering. It was also required that the absolute time difference between the first add-back hit and any other hit was less than 200 ns. Upon satisfying all of these conditions, the two hits were combined into a single add-back hit. The two core contact energies were summed and the timestamp of the hit was set to be that of the highest energy hit. The list of sorted segment hits were concatenated to give a new final γ-ray position. Hits that did not match the add-back criteria were left as individual hits.

The add-back algorithm was benchmarked by producing a calibrated ^{152}Eu sum spectrum and extracting a relative efficiency curve, as described in the previous section. The ratio of efficiencies between the add-back curve and the no-add-back curve was used to determine the improvement in photo-peak efficiency (also known as the add-back factor). It was found that the photo-peak efficiency of TIGRESS could be increased by over 40% by adding together hits with the following conditions;

The corresponding add-back curve is compared to the no-add-back efficiency curve in figure 4.9a. The ratio of these curves is shown in figure 4.9b.

4.2.3   Absolute Efficiency Calibration

A low activity ^{60}Co source was placed in the TIGRESS array after the experiment for absolute efficiency calibrations. ^{60}Co β^- decays into ^{60}Ni with a half-life of 5.2 years and produces a very
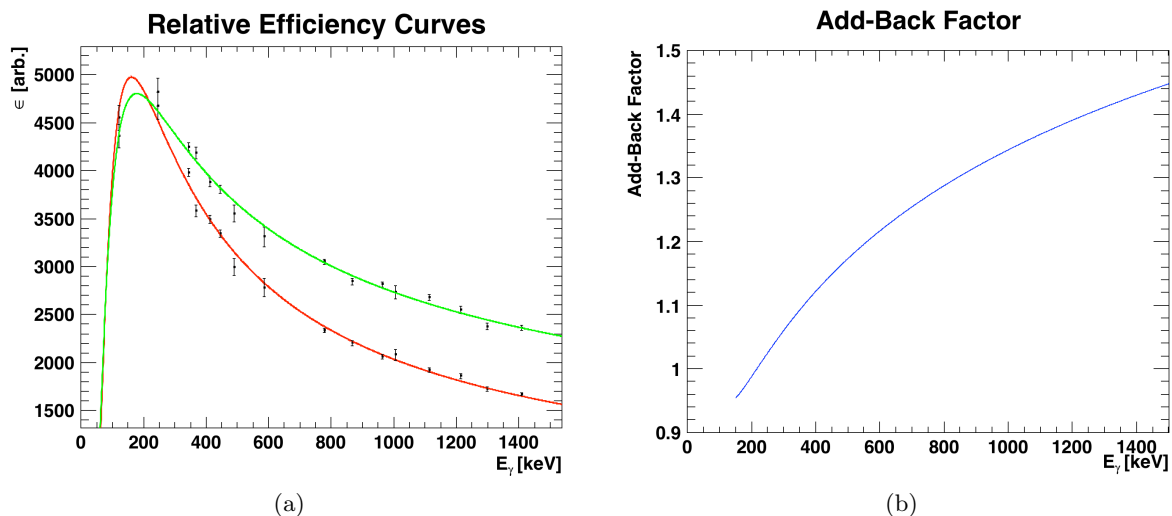
Figure 4.9: (a) Relative ^{152}Eu efficiency curves made with and without add-back. (b) Ratio of efficiency curves, giving the add-back factor.

γ-ray energy [keV]	Intensity [%]	$N(\gamma_i)$	$N(\gamma_i|\gamma_j)$
346.93 (7)	0.0076(5)		
826.28 (7)	0.0076(8)		
1173.237 (4)	**99.9736 (7)**	$4.592(7) \times 10^5$	$2.31(2) \times 10^4$
1332.501 (5)	**99.9856 (4)**	$4.267(7) \times 10^5$	$2.32(2) \times 10^4$
2158.77 (9)	0.0011 (2)		

Table 4.3: Energies and intensities of ^{60}Co γ-ray calibration source [Lab].

simple γ-ray spectrum with two coincident γ-rays of similar energy. These coincident γ-rays can be used to extract the absolute efficiency of TIGRESS. Details of the ^{60}Co decay scheme are given in figure 4.3.

γ-ray coincidences are an effective way of determining the absolute efficiency. This is because they are independent of detector dead time and source activity.

Consider a situation where two γ-rays, γ_1 and γ_2, with energies E_1 and E_2 are emitted in quick succession from a source. One can extract the absolute efficiency at energy E_2 by comparing the number of γ-rays in the coincidence spectrum photo-peak to the number of γ-rays in the

singles spectrum photo-peak, as is described by equation 4.7.

$$\varepsilon(E_2) = \frac{N(\gamma_2|\gamma_1)}{N(\gamma_1) \times BR} \tag{4.7}$$

Where $N(\gamma_2|\gamma_1)$ is the total number of γ-rays at energy E_2 given that a γ-ray was measured with energy E_1, $N(\gamma_1)$ is the number of γ-rays with with energy E_1 in the singles spectrum and BR is the branching ratio (which is effectively 100% for ^{60}Co).

When a γ-ray is measured in TIGRESS, the associated detector becomes briefly inactive while the signal is read out. This is called dead time. γ-rays in a cascade are generally emitted within picoseconds (discounting isomeric state decays) and so one of the TIGRESS detectors would be inactive as the second γ-ray is detected. This reduces the effective number of detectors in the array by one, as the two γ-rays must interact with different detectors or no coincidence event will be measured. The absolute efficiency ε_{abs} of TIGRESS is therefore the apparent efficiency (that which is observed) multiplied by a factor which accounts for the reduced number of detectors.

$$\varepsilon_{abs} = \varepsilon_{app}\frac{\eta}{\eta - 1} \tag{4.8}$$

Where η is the total number of detectors (12) and ε_{app} is the efficiency that was determined using equation 4.7. The absolute efficiency that was extracted using the ^{60}Co data was used to scale the ^{152}Eu relative efficiency curve, producing an absolute efficiency curve. This absolute efficiency curve is shown in figure 4.10.

4.2.4 Doppler Correction

γ-rays emitted from the ^{96}Sr recoil nuclei will be Doppler shifted due to the motion of their source. This effect depends on the angle of emission of the γ-ray with respect to the recoil, and also the angle of the recoil with respect to TIGRESS. The measured energy E' is related to the energy of emission in the ^{96}Sr rest frame, E, by equation 4.9.

$$E = E'\gamma(1 - \beta\cos\theta) \tag{4.9}$$
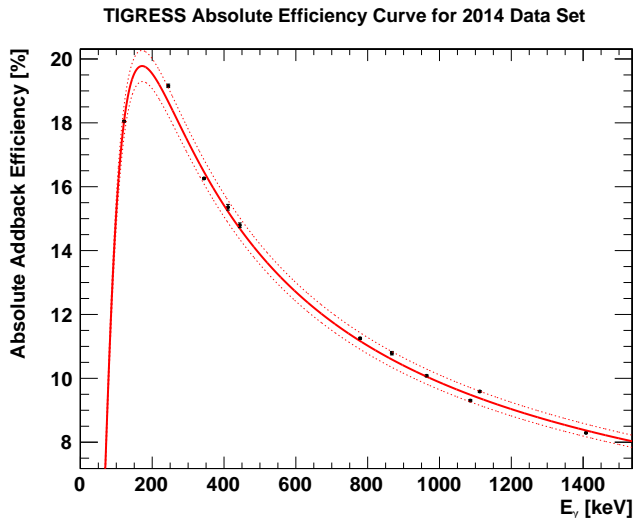
Figure 4.10: Absolute efficiency curve of TIGRESS (solid red line) with $\pm 1\sigma$ uncertainty bands (broken red lines).

Where $\beta = \frac{v}{c}$ is the speed of recoil nucleus as a fraction of the speed of light and $\gamma = \frac{1}{\sqrt{1-\beta^2}}$, both of which are known from the reaction kinematics. θ is defined as the angle between the motion of the recoil nucleus and the position of measurement in TIGRESS.

In this experiment, the maximum angle of the ^{96}Sr recoil nucleus with respect to the beam axis was $\theta_{max} \sim 1°$. This means that, to a good approximation, the recoil nucleus can be described as travelling parallel to the beam (along the z axis) after the reaction. In this case, θ is simply the angle of the detector, θ_{TIG}. This angle of incidence was determined using the segment position of the largest γ-ray interaction in TIGRESS. It should be noted that the angle of emission of the ^{96}Sr recoil nucleus affects the kinematic energy and the β value.

Using an approximate value of $\sim 0.1c$ for the recoil velocity, the distance travelled per picosecond is 30 μm. Since excited nuclear states have typical lifetimes in excess of a picosecond it is reasonable to assume that the ^{96}Sr recoil nuclei would travel through the remaining target material before subsequently emitting a γ-ray. The speed of the recoil nucleus as it leaves the target is affected by the position in the target where the reaction happens. This is because the beam loses energy in the target before the reaction and the recoil loses energy in the target after the reaction. The range of possible recoil speeds due to different reaction positions was

calculated to be less than 0.5% and so this effect was considered negligible. All reactions were assumed to take place in the center of the target.

In this work, the Doppler correction was carried out on an event-by-event basis. The measured proton ejectile angle and energy were used to reconstruct the momentum vector of the heavy recoil. The recoil energy lost in the target was calculated, giving a final β value which was then used to Doppler correct the γ-ray energy.

Figure 4.11a shows the effect of the Doppler correction on the data. Without a Doppler correction the separate TIGRESS detector positions measure different energies from the ^{96}Sr γ-ray decays. The result is a smeared-out spectrum without clearly defined peaks. The broad raw energy peaks which surround the corrected 815 keV peak are from the ring of clover detectors centered at $\theta = 90°$. The separate feature at roughly 90% of the peak energy is due to the $\theta = 135°$ clover ring. Each detector in TIGRESS has an angle dependent energy correction applied which makes all of the separate spectra consistent. The separate peaks from each detector can be seen to merge into a single peak under the action of the Doppler correction.

(a)   (b)
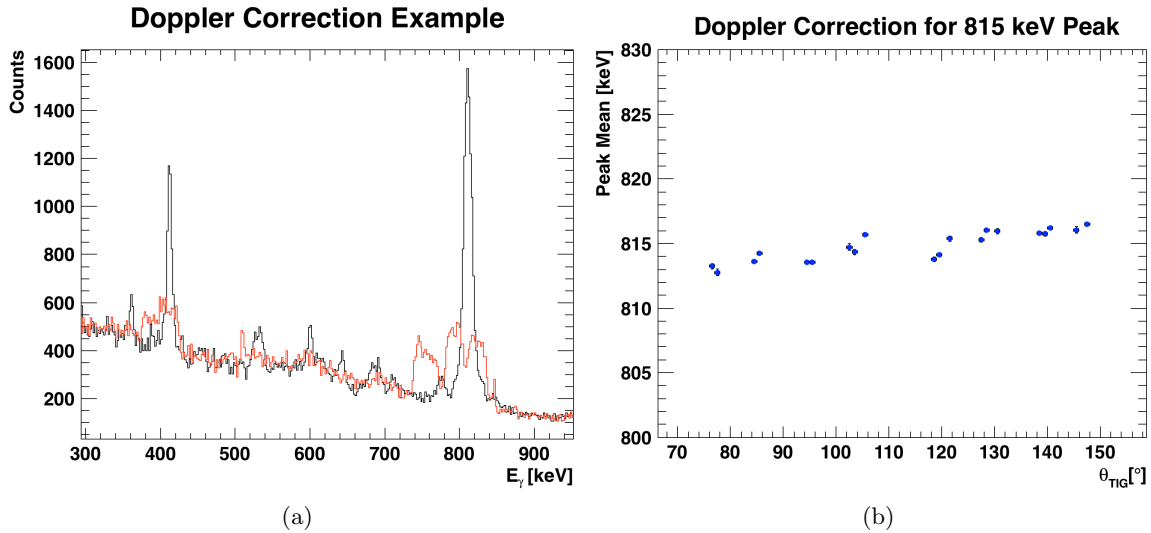
Figure 4.11: (a) Comparison of raw experimental γ-ray spectrum (red) to Doppler corrected spectrum (black). (b) Doppler correction of fitted 815 keV γ-ray peak centroid as a function of θ_{TIG}.

The Doppler correction can be examined in more detail by plotting the γ-ray energies versus TIGRESS angle. This was done by fitting a specific photo-peak in each angular slice and plotting the fitted peak centroid as a function of $\cos\theta_{TIG}$. The quality of the Doppler correction used in this analysis is demonstrated in figure 4.11b, which shows that the fitted centroid of the prominent 815 keV ^{96}Sr γ-ray is flat versus angle to within 0.5%. The approximate width of the 815 keV peak in each of the underlying angular slices was $\sigma \sim 6$ keV, and so the total increase in resolution due to the small Doppler correction error was on the order of 1σ across the entire θ_{TIG} range. This was found to give satisfactory overall γ-ray energy resolution.

4.2.5   TIGRESS Energy Resolution

The intrinsic energy resolution of the TIGRESS HPGe detectors is very good, with typical FWHM ~ 3 keV. In this experiment, the width of the γ-ray photo-peaks in TIGRESS was limited by the Doppler correction.

The energy resolution curve of TIGRESS was determined by examining a series of prominent peaks in the γ-ray singles spectrum across a large energy range. A Gaussian function with a linear background fit was found to be adequate for estimating the peak width, σ. The peak width was then plotted as a function of photo-peak energy. Figure 4.12 shows the energy resolution of TIGRESS.
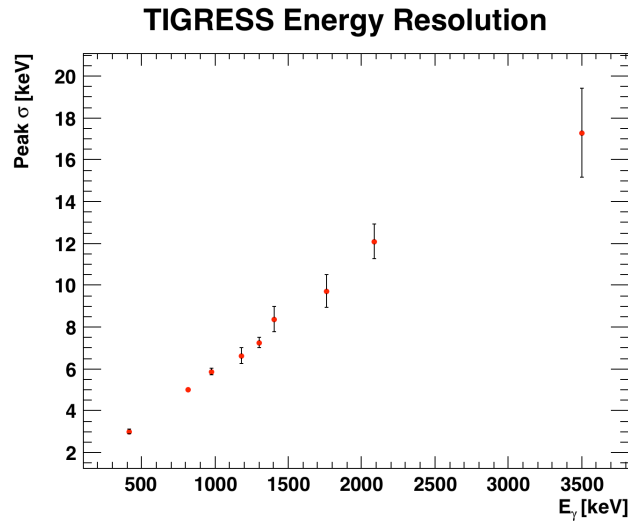
Figure 4.12: Empirically determined photo-peak width as a function of photo-peak energy.

The resolution curve is a useful tool for differentiating between real γ-ray peaks and false peaks. Examples of false peaks are γ-ray decays from reactions such as fusion evaporation, decays from nuclei at rest (such as e^+e^- annihilation γ-rays) and also statistical fluctuations. The effect of the Doppler correction on the different peaks versus θ_{TIG} is also useful for identifying false peaks.

It should also be noted that this curve assumes that each γ-ray was emitted by a state that is not isomeric. States with long half-lives will have larger photo-peak widths.

4.3   Particle Identification

Figures 4.13a and 4.13b show the measured ΔE and pad energy of particles in SHARC versus θ_{LAB} respectively. There are different reactions that can be seen, such as ^{95}Sr elastic scattering and ^{95}Sr(d,p). It can also be seen that the different reaction channels cannot be separated without the simultaneous measurement of both the ΔE and pad energy, as multiple reactions overlap in figures 4.13a and 4.13b. Several kinematic lines are drawn in figure 4.13a as a visual aid. The data is systematically lower in energy than these lines because of energy losses in the target and dead-layers. Punch-through can also be seen in the (p,p) and (d,d) data, beyond which point the ΔE energy decreases in figure 4.13a and the pad energy increases in figure 4.13b.

Figure 4.13a also shows that there is considerable low energy background which is mostly from β-decay of the radioactive beam constituents. This is discussed in more detail in appendix D. Fusion evaporation products also contribute to the background. The ^{95}Sr(^{12}C,^{12}C) data can be seen to have much worse energy resolution than the (p,p) and (d,d) data, which was previously discussed in section 3.1. The very high energy of the scattered carbon also caused the pre-amplifiers to saturate which is shown as the intense line at ΔE$\sim$18000 keV with constant energy. The carbon data was not analyzed for these reasons.

Figure 4.14 shows the kinetic energy of various particles measured in SHARC as a function of the lab angle θ_{LAB}. This plot was made by reconstructing the full kinematic energy of the
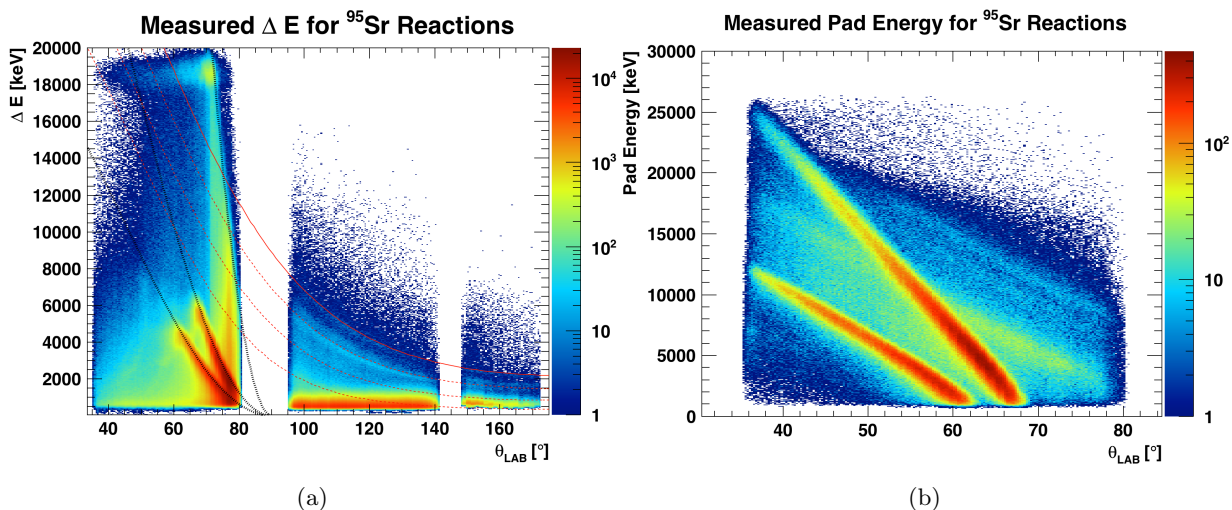
Figure 4.13: (a) Measured ΔE kinematics drawn with kinematic lines corresponding to various ^{95}Sr reactions. Black curves show elastic scattering channels (p,p), (d,d) and (^{12}C,^{12}C), while red curves show (d,p) kinematics for 0 (solid), 2, 4 and 6 MeV (dashed) excitation energy. (b) Measured pad energy kinematics. More details are given in the text.

particles by adding the measured energy to the unmeasured energy lost, as is described in equation 4.1. This procedure is the same as the calibration procedure. In order to appropriately reconstruct the full kinematic energy of each measured particle, the associated nuclear reaction must be identified.

For backward lab angles ($\theta_{LAB} > 90°$), all data was taken to be (d,p) data. Some fusion evaporation products would also be measured in this angular range, although these particles form a smooth continuum instead of sharp individual peaks and can therefore be treated as a background. The only cut that was used at backward angles was a low energy threshold $\Delta E > 1$ MeV.

At forward lab angles ($\theta_{LAB} < 90°$) it can be seen that there is elastic scattering data in addition to the (d,p) data, which necessitates some form of particle identification. Moreover, the (d,d) data has the same total energy as the (d,p) data as indicated by the overlapping curves in figure 4.14. One important difference between these reaction channels is that the (d,p) protons, owing to their large energy, punch through the ΔE detector and deposit energy in the pad

Kinematics For ^{95}Sr
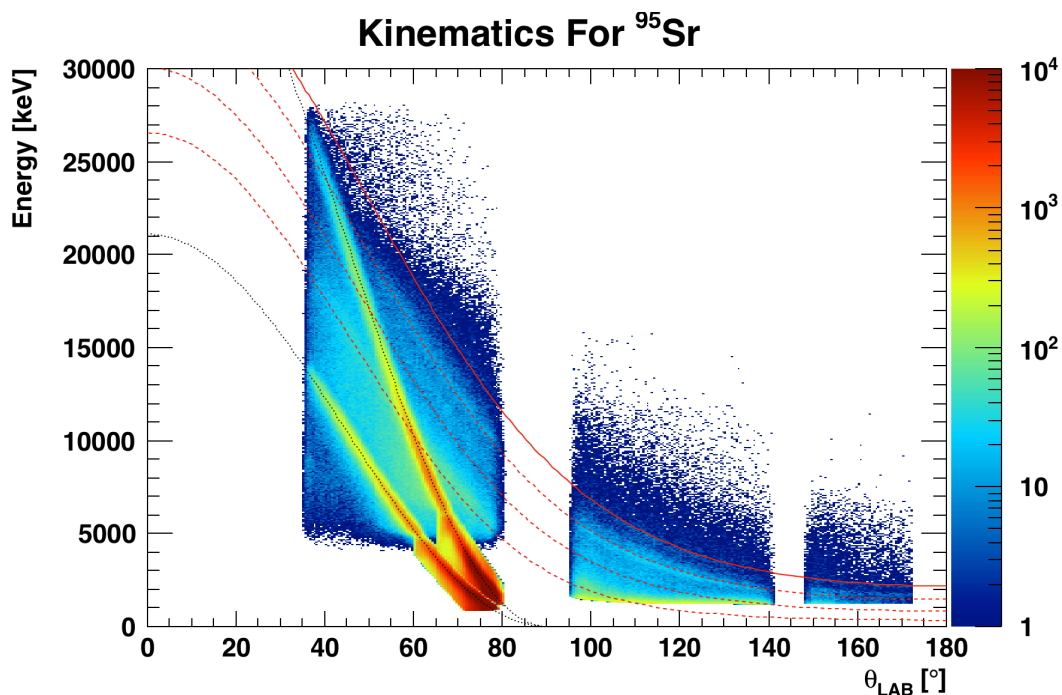
Figure 4.14: Kinematics of various ^{95}Sr reactions. Black curves show elastic scattering channels, (p,p) and (d,d) and red curves show (d,p) kinematics for 0 (solid), 2, 4 and 6 MeV (dashed) excitation energy.

detector across the entire DBOX section. Contrastingly, for angles closest to $\theta_{LAB} = 90°$ the kinematic energy of the elastically scattered particles is much lower and so they are completely stopped within the ΔE detectors. In this region, a kinematic (ΔE versus θ_{LAB}) cut was used to select only the elastically scattered protons and deuterons. Figure 4.14 shows that the only DBOX data which was used with total energy less than ~5 MeV is from (p,p) and (d,d) events, and the sharp cut-off around these data indicate the cut shapes. The carbon data and large low energy background was removed through the use of these cuts.

Beyond this point, they punch through the ΔE detectors and deposit energy in the pad (E) detectors. The transition from ΔE-only data to ΔE plus E data can be identified through the sudden change in width of the (p,p) and (d,d) kinematic line in figure 4.14.

From this point it was possible to identify the protons and deuterons using the ΔE-E detector arrangement and so particle identification (PID) plots were made for this purpose. The geometry of the DBOX detectors causes uneven energy loss across the ΔE detector due

to angular dependence of the effective thickness, which is formulated in equation 4.2. This is true for both mono-energetic sources and reaction products. The measured ΔE, divided by the effective thickness angular terms removed the angular spread of energies across the DBOX detectors. This allowed for a much cleaner PID plot that could then be used to distinguish between the different particles. Figure 4.15a shows the PID plot produced using only the ΔE and pad energies, while figure 4.15b shows the improvement caused by the effective thickness correction.
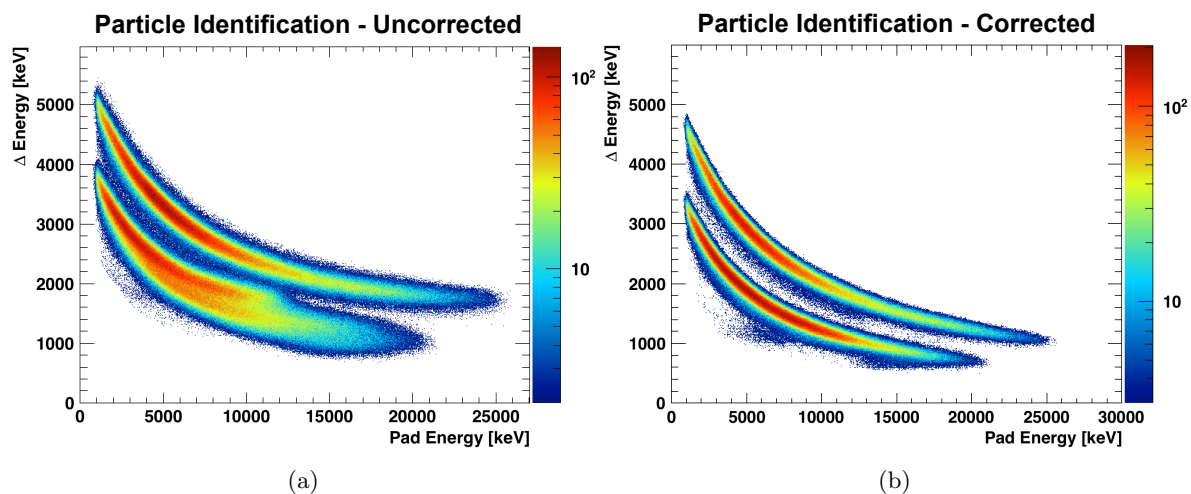
Figure 4.15: (a) Particle identification (PID) plot for all pads in DBOX section. Protons have lower Δ energy for a given pad energy than deuterons, forming two separate loci. (b) Same as before, but with an effective thickness correction (see text for details).

Without the effective thickness correction, the protons from (p,p) and (d,p) lie on separate PID curves due to their distinct kinematics. Figure 4.15a shows that this effect is visible in the PID spectrum. The large distribution of proton energies caused proton identification curve to overlap with the deuteron identification curve, which makes particle identification ambiguous in some cases. The PID spectrum shown in figure 4.15b was used to make graphical cuts which unambiguously identified the particles as protons or deuterons.

4.3.1 Angular Ranges and Excitation Energy Ranges

In addition to the geometrical efficiency of SHARC that was described in section 4.1.3, the particle cuts that were used introduced further limitations to the effective detector coverage. The angular and excitation energy sensitivity for each reaction was shaped by the energy thresholds of SHARC, the kinematic cuts and also the PID cuts that were used. These cuts were optimized to maximize the sensitivity of SHARC to (d,p) data, while preserving important information about the elastic scattering data.

Once the measured particles were identified, the excitation energy of the states which were populated was reconstructed. This was done by converting the measured lab frame kinetic energy of these particles into the centre-of-mass frame. In this frame, the kinetic energy of the final state particles is directly related to the reaction Q value, or equivalently, the excited state which was populated in the reaction.

Figures 4.16a and 4.16b show reconstructed excitation energy versus centre-of-mass angle of the identified (p,p) and (d,d) elastic scattering data respectively.

Care was taken to include as much (p,p) and (d,d) data close to the target (small centre-of-mass angles) as possible. In the centre-of-mass frame, small angles are dominated by pure Rutherford scattering. This region is important for cross section studies as it is less sensitive to the optical model used in the DWBA fit (described in section 1.5), which helps to reduce uncertainty in the absolute normalization. Ensuring a large excitation energy range for the (p,p) and (d,d) inelastic scattering data was not considered to be important for this analysis. Only the ground state (elastic) angular distribution for this data was required for normalization and to optimize the DWBA optical model. Note that the discontinuity in counts versus centre-of-mass angle which is present in each of the two figures corresponds to particles punching through the ΔE detector and depositing energy in the pad detectors. The pad detector energy thresholds result in a region where protons have punched through the ΔE but no pad signal is measured, which can be seen as a sharp, short rise in excitation energy followed by a decrease in counts.

Figure 4.17 shows reconstructed excitation energy versus centre-of-mass angle of the identified
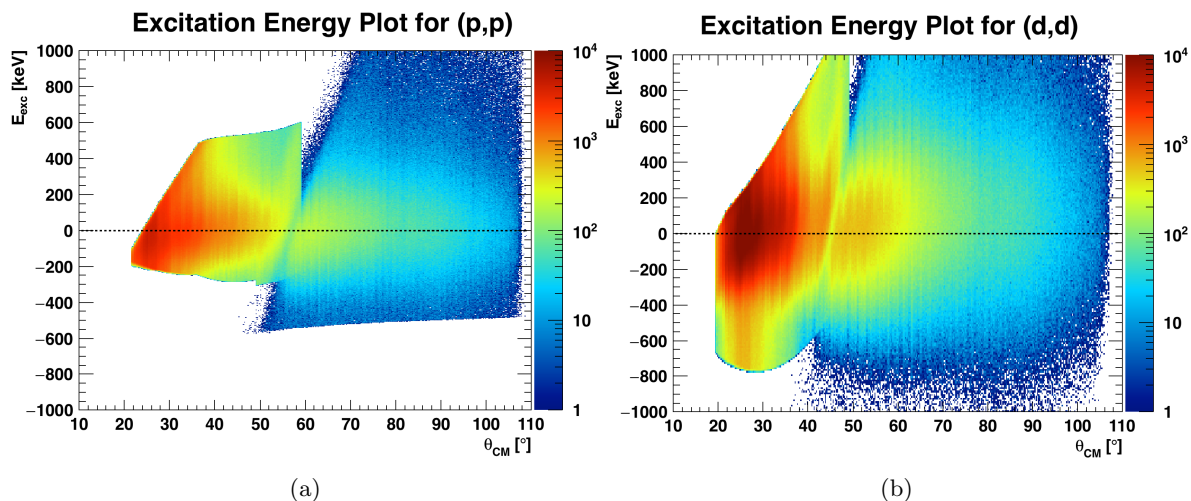
Figure 4.16: (a) Excitation energy versus centre-of-mass angle for (p,p), showing angular and energy ranges of the PID cuts. The black line indicates 0 keV excitation energy. (b) Same as (a), but for (d,d).

(d,p) protons.

For the (d,p) data, an effort was made to include all available excitation energy and angles wherever possible. At large backward lab angles ($\theta_{LAB} > 140°$) the kinematic energy of (d,p) protons was close to the detector threshold and so reactions which populated highly excited states could not be studied in this angular range. At small forward angles ($\theta_{LAB} < 60°$) the protons punched through the pad detectors (as was seen in the NPTool simulation results discussed in section 3.1) and so this data was also irretrievable. This introduced an upper angular limit for studying reactions which populated low-lying ^{96}Sr states. The conversion between laboratory frame and canter-of-mass frame angles is dependent on excitation energy, which can also be seen in figure 4.17.

Protons associated with highly excited ^{96}Sr states (above ~8 MeV) could not be distinguished from (p,p) protons as can be seen in figure 4.14. It was also not possible to cleanly distinguish between these reactions using PID cuts. This was not an issue because the upper excitation energy limit was beyond the one neutron separation energy ($S_n =$5.879 MeV), and states above this energy decay by neutron emission and only partially via γ-ray emission. The excited ^{96}Sr states in this region are currently under analysis by the Lawrence Livermore group as part of

Excitation Energy Plot for (d,p)
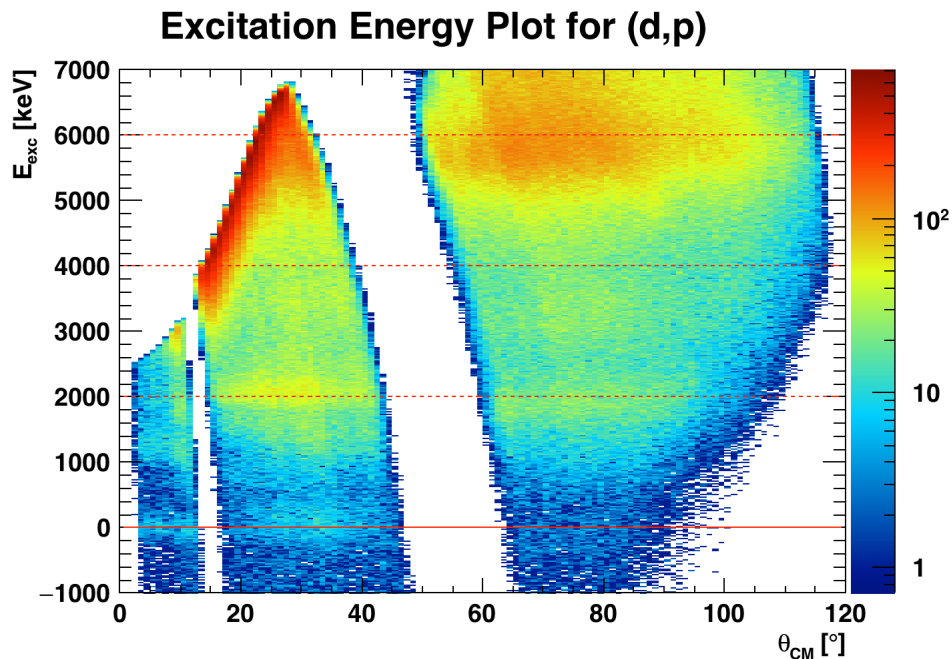
Figure 4.17: Excitation energy versus centre-of-mass angle for (d,p), showing angular and energy ranges of the PID cuts. The solid red line indicates 0 MeV excitation energy and the broken red lines indicate 2, 4 and 6 MeV.

a study of (n,γ) surrogate reactions.

4.4 Method of Extracting Angular Distributions

In this experiment a number of angular distribution measurements were made.

The large quantity of low energy β decay background that was measured in the UBOX and UQQQ sections of SHARC during both experiments restricted the angular distribution analysis for laboratory angles greater than 90°. In the ^{94}Sr(d,p) experiment, ^{95}Sr states above 1 MeV could not be analyzed at center-of-mass angles less than approximately 60°. In the ^{95}Sr(d,p) experiment, ^{96}Sr states above 2.7 MeV could not be analyzed at center-of-mass angles less than approximately 15°. The larger excitation energy range that could be analyzed in the ^{95}Sr(d,p) experiment is primarily a result of the larger Q-value for the reaction.

Each angular distribution was produced using the same procedure, including the elastic scattering data. An excitation energy versus center-of-mass angle matrix was made and then divided

into angular bins of equal size, producing an excitation energy spectrum for each angular bin. The counts associated with the state under analysis were extracted from each excitation energy spectrum. A number of different methods were used to extract the counts from the excitation energy spectra. The chosen of method extraction depended on the character of the background and whether the spectra contained unresolved peaks. Figures 4.16a and 4.16b show the excitation energy versus center-of-mass angle matrices for the ^{95}Sr elastic scattering data and figure 4.17 shows the excitation energy versus center-of-mass angle matrix for measured protons from ^{95}Sr(d,p).

For excited states, detected γ-rays in TIGRESS were used in conjunction with the particle energies and positions measured in SHARC. The populated excited states were first identified using a matrix of excitation energy versus γ-ray energy. The matrix was projected to produce a γ-ray spectrum gated on a narrow excitation energy window. The size of excitation energy window was chosen to be 800 keV as this was large enough to collect all particles associated with a given state in the UQQQ and UBOX sections of SHARC. The window did not generally collect all contributions from the DBOX section due to the slight energy offset in this region, however most of the measured γ-rays were in coincidence with protons measured in the UBOX section and so this was not a problem for simply identifying states. The energy window was shifted and each γ-ray peak that was observed was compared to known transitions so that a level scheme could be made. A γ-gated γ-ray spectrum for protons within the excitation energy window was also produced to help elucidate feeding.

The angular distributions for excited states were extracted using γ-gated excitation energy versus center-of-mass angle matrices. Three matrices were made for each γ-gate. A matrix which contained the particles in coincidence with the γ-ray peak was made. Two background matrices were also made which sampled the γ-ray background immediately above and below the peak. The background matrices were added together and weighted to account for any differences in statistics due to window size. The background matrices were both subtracted from the peak matrix, which effectively removed the background under the γ-ray peak. This γ-gated excitation energy versus center-of-mass angle matrix was then analyzed in the same way as the

particle-only matrices; by producing a set of excitation energy spectra corresponding to equal-sized angular bins. The counts were taken from the γ-gated excitation spectra by integrating the total counts under the peak. Figure 4.18 gives an example of how the 1995 keV ^{96}Sr state was analyzed.
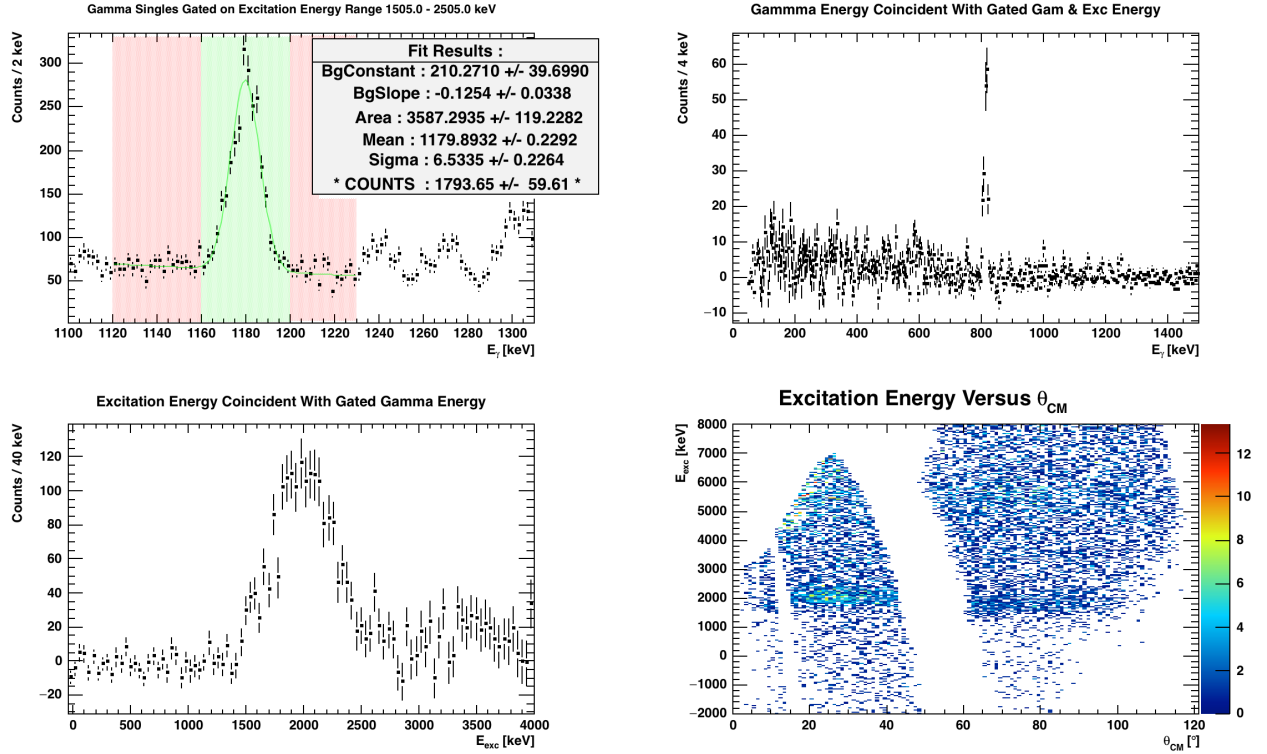
Figure 4.18: Example analysis for 1995 keV ^{96}Sr state (top to bottom, left to right). (a) γ-ray singles spectrum gated on the excitation energy range 1500-2500 keV, with estimated peak counts. (b) Coincident γ-rays with the 1180 keV transition in the same excitation energy range. (c) Excitation energy spectrum coincident with 1180 keV γ-ray rays projected over all center-of-mass angles. (d) Excitation energy versus center-of-mass angle coincident with 1180 keV γ-ray rays.

Each angular distribution was obtained using equation 4.10

$$\frac{d\sigma}{d\Omega}(\theta) = \mathcal{N}\frac{N(\theta)}{\varepsilon_{\mathrm{P}}\Delta\theta\sin\theta}\frac{1}{B\varepsilon_\gamma} \tag{4.10}$$

where $\mathcal{N}$ is the normalization constant, ε_{P} is the particle detection and identification efficiency, $N(\theta)$ is the total number of counts measured at angle θ and $\Delta\theta$ is the size of the angular bins.

The $\sin\theta$ factor arises from the definition of the solid angle element in equation B.1 in appendix B. For γ-ray gated angular distributions, the absolute efficiency of TIGRESS and the branching ratio of the gated transition were also corrected for, and are given by the additional factors ε_γ and B respectively.

The angular bin size was chosen to be as small as possible given the available statistics of the specific reaction. Small angular bins of $\Delta\theta = 1°$ were used for the elastic scattering as there was a lot of statistics and so that the oscillatory features of the differential cross section could be clearly seen in the data. Most of the (d,p) states were analyzed using $\Delta\theta = 5°$ angular bins as this made it possible to extract several points from within the UQQQ and UBOX sections of SHARC. This made it possible to compare the shape of the angular distribution to DWBA calculations more precisely. Smaller angular bin sizes $\Delta\theta = 3°$ or $4°$ were used for states that were strongly populated in the ^{95}Sr(d,p) experiment. Figure 4.19 shows the angular distribution that was extracted for ^{95}Sr(d,p) to the 1995 keV ^{96}Sr state.
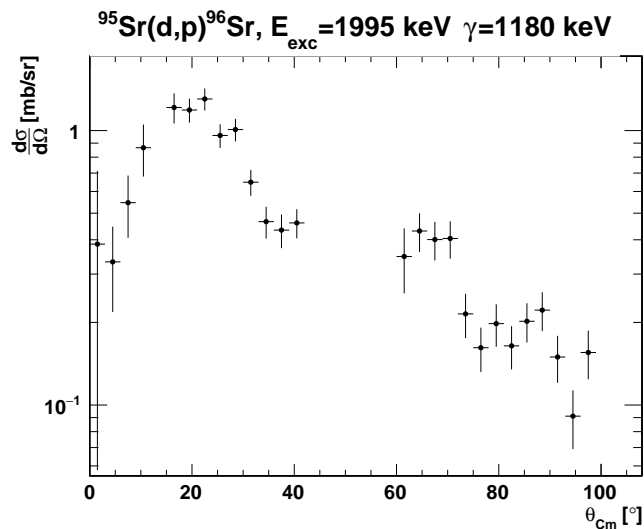
Figure 4.19: Experimental angular distribution for ^{95}Sr(d,p) to the 1995 keV ^{96}Sr state.

A number DWBA calculations were carried out using the coupled-channels reaction code FRESCO [Tho88] and these were compared to the extracted angular distributions. The elastic scattering data in each data set was used to optimize the optical model potentials and deter-

mine the normalization constant $\mathcal{N}$. This is discussed in section 5.1.

For the (d,p) reactions, a single-step DWBA calculation was carried out for each neutron configuration, using the excitation energy of the state to determine the Q-value and neutron separation energy.

This single step description of ^{94}Sr(d,p) allows ^{95}Sr to be populated adding a single neutron into one of four different single particle orbitals. The one neutron configurations corresponding to adding a neutron to these orbitals are; $[3s\frac{1}{2}]$ through $\ell = 0$, $[2d\frac{3}{2}]$ and $[2d\frac{5}{2}]$ through $\ell = 2$ and $[1g\frac{7}{2}]$ through $\ell = 4$. These configurations correspond to final state J^{π} values of $\frac{1}{2}^{+}$, $\frac{3}{2}^{+}$, $\frac{5}{2}^{+}$ and $\frac{7}{2}^{+}$ respectively. The $1h\frac{11}{2}$ orbital was omitted from the DWBA calculations as transfer reaction cross sections strongly favour low orbital angular momentum transfer. Because of this, the population of high spin states would not be significant in this data.

The theoretical treatment of ^{95}Sr(d,p) as a single step process is slightly more complicated than in the ^{94}Sr(d,p) process, owing to the unpaired valence neutron in ^{95}Sr. This valence neutron can couple to the transferred neutron to give two possible spins for each orbital populated in the reaction. If we assume a spherical seniority 1 description of the ^{95}Sr $\frac{1}{2}^{+}$ ground state, the unpaired neutron is in the $3s\frac{1}{2}$ orbital as this is the only possible way to create the required spin and parity. As was described for ^{94}Sr(d,p), the added neutron populates one of four different single particle orbitals. The two neutron configurations corresponding to adding a neutron to these orbitals are; $[3s\frac{1}{2}]^{2}$ through $\ell = 0$, $[3s\frac{1}{2}2d\frac{3}{2}]$ and $[3s\frac{1}{2}2d\frac{5}{2}]$ through $\ell = 2$ and $[3s\frac{1}{2}1g\frac{7}{2}]$ through $\ell = 4$. Each of these configurations except for $[3s\frac{1}{2}]^{2}$ can result in two distinct spins corresponding to the two neutrons aligning or anti-aligning their intrinsic spins. Adding the transferred neutron to the $2d\frac{3}{2}$ orbital would populate 1^{+} and 2^{+} states while adding the transferred neutron to the $2d\frac{5}{2}$ orbital would populate 2^{+} and 3^{+} states. Similarly, 3^{+} and 4^{+} states can be populated by adding a neutron into the $1g\frac{7}{2}$ and coupling it to the ^{95}Sr ground state. In the case of an $[3s\frac{1}{2}]^{2}$ configuration, only 0^{+} states can be populated.

Each of the calculated angular distributions were fitted to the experimental data using χ^{2} minimization, and these results were used to judge the configuration which is most consistent with the data. It must be noted, however, that the DWBA model is a simple description of

the reaction and while the shape of the DWBA curve should approximate the experimental angular distribution, the quantitative agreement is unlikely to be perfect. Instead, the χ^2 values obtained from fitting the data to the different calculated configurations were used to judge the most likely ℓ transfer and to determine the spectroscopic factor of the populated states. The DWBA calculation which best fit the data is drawn as a solid line in the angular distribution plots, although it can be seen that there were frequently multiple configurations which produced almost identical χ^2 values. The MINUIT [Jam] minimizer was used to perform single parameter χ^2 minimization fits of the spectroscopic amplitudes ($\mathcal{SA}$) to the data, which are defined as the square root of the spectroscopic factors. The uncertainty of the spectroscopic amplitude was determined by using $\chi^2 + 1$ confidence intervals. The minimized values were therefore squared to produce the extracted spectroscopic factors that are presented in table 5.4. The uncertainties of the spectroscopic factors were determined by combining the relative uncertainties of all absolute scale factors that were applied to the experimental data with the relative uncertainty of the spectroscopic factor, as is shown in equation 4.11. The errors of these absolute scaling factors were added in quadrature.

$$\frac{\delta \mathcal{SF}}{\mathcal{SF}} = \sqrt{\left(\frac{\delta \mathcal{N}}{\mathcal{N}}\right)^2 + 4\left(\frac{\delta \mathcal{SA}}{\mathcal{SA}}\right)^2 + \left(\frac{\delta \varepsilon_\gamma}{\varepsilon_\gamma}\right)^2 + \left(\frac{\delta B}{B}\right)^2} \tag{4.11}$$

where $\mathcal{N}$ is the normalization constant, $\mathcal{SA}$ is the spectroscopic amplitude (note the additional factor of four), ε_γ is the absolute efficiency of TIGRESS at the γ-ray gated energy and B is the branching ratio for the corresponding γ-ray transition. For states that were analyzed without γ-ray gating, the last two terms in equation 4.11 did not apply.

Chapter 5

Results

5.1 Elastic Scattering Data

The normalization constant $\mathcal{N}$ in equation 4.10 was determined by fitting the elastic scattering data to DWBA calculations. This data was also used to optimize the optical potentials that were introduced in section 1.5.1 for the (d,p) calculations.

Equation 5.1 relates the measured angular distribution of elastically scattered particles to the DWBA calculation.

$$\left[\frac{\delta\sigma}{\delta\Omega}(\theta)\right]_{DWBA} = \frac{1}{\mathcal{L}n_t\Delta x}\left[\frac{\delta N(\theta)}{\delta\Omega}(\theta)\right]_{exp} \tag{5.1}$$

where the constants $\mathcal{L}$, n_t and Δx are the integrated beam current, the number density of target nuclei and the target thickness respectively. The normalization constant $\mathcal{N}$ is defined as

$$\mathcal{N} = \frac{1}{\mathcal{L}n_t\Delta x} \tag{5.2}$$

and is determined by scaling the experimental angular distribution to the DWBA calculation.

When two electrically charged point-like objects undergo elastic scattering, the resulting angular distribution is described by the Rutherford scattering formula which varies as $\sin^{-4}\frac{\theta}{2}$. When one or both of the scattered objects has an extended size, a diffraction pattern is produced. This is true even if the distance of closest approach is larger than the combined radii of the objects. If viewed in normal kinematics, the incident kinetic energy of the elastically scattered protons would be ~5.4 MeV in both experiments. At this energy, the distance of closest approach between the beam and target nuclei is greater than their combined radii and so the angular distribution would be dominated by pure Coulomb scattering. The kinetic en-

ergy of the elastically scattered deuterons was ∼10.8 MeV in both experiments, when viewed in normal kinematics. In this case, the distance of closest approach between the beam and target nuclei is less than their combined radii and so the nucleus size plays a significant role in the scattering process. Other nuclear reactions can also occur when the nuclei are at close range, and this causes a decrease in cross section in the elastic channel. The elastic scattering of two nuclei can be described as the scattering of distorted waves off a potential which has a real and an imaginary component. This is called the optical model. It is standard practice to modify the parameters of the optical potential so that the calculated angular distribution is in good agreement with data. In this way the optimized potential provides a good description of the physics underlying the scattering process, including inelastic effects that remove flux. The deuteron elastic scattering data was used to optimize the optical model (OM) parameters used in the calculated (d,p) reactions.

At small center-of-mass angles, the proton and deuteron kinematic lines were close in energy and so the counts were extracted by fitting both peaks together using Gaussian functions plus a background fit. Fits in this angular range were carried out using a linear background model and an exponential background model, as are shown in figures 5.1a and 5.1b respectively. The counts and uncertainties were taken to be the average and difference of these models respectively. At larger center-of-mass angles the particles could be identified using the pad detector and so the counts were extracted by subtracting a fitted background from the total counts. The background was estimated by excluding the peak region and fitting the remaining data using a polynomial model. An example of this is is shown for (d,d) data and (p,p) data in figures 5.2a and 5.2b respectively, where the deuteron data used a linear model and the proton data used a quadratic model.

Figures 5.3a and 5.3b show the experimental proton elastic scattering angular distributions compared to various optical models, which are described in table 5.1. The global optical model parameters V_0 and W_D given in table 5.1 have a weak dependence on the neutron number N and the mass number A of the strontium nucleus. The difference in these values for the ^{94}Sr(p,p) and ^{95}Sr(p,p) was very small, and so the same potential was used in each case. All of

$\theta_{CM} = 30°$: Exponential Fit

Delta Energy [keV]

(a)

$\theta_{CM} = 30°$: Linear Fit

Delta Energy [keV]

(b)
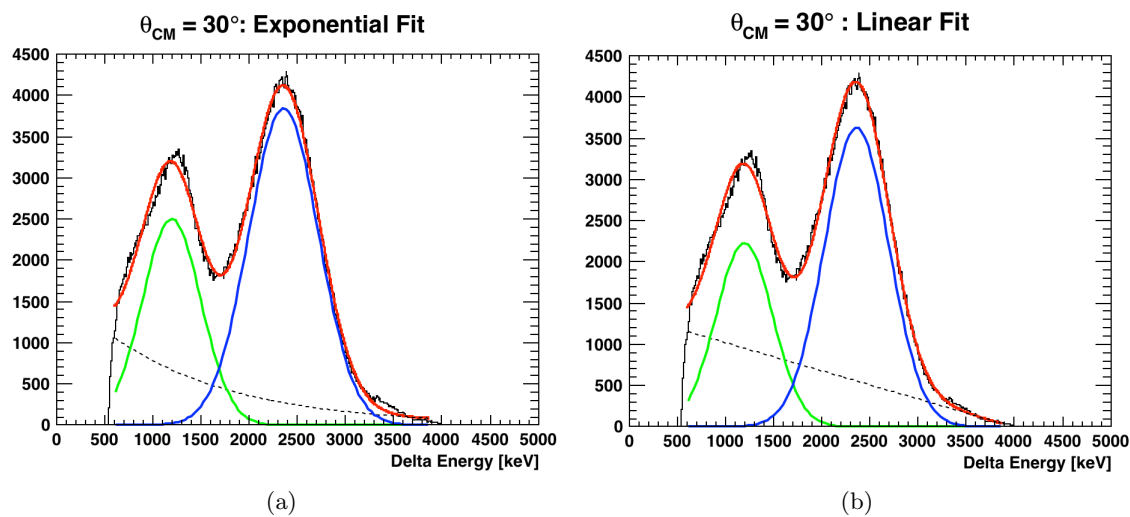
Figure 5.1: Example fit of small center-of-mass angle (p,p) and (d,d) data using (a) exponential background model (b) linear background model.

$\theta_{CM} = 66°$: (d,d) Background Subtraction

E_{exc} [keV]

(a)

$\theta_{CM} = 66°$: (p,p) Background Subtraction

E_{exc} [keV]

(b)
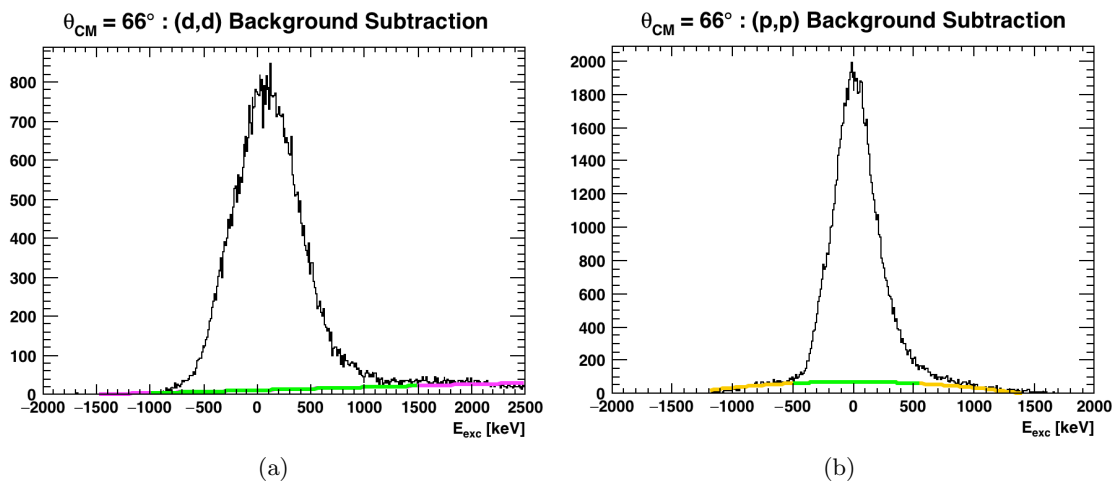
Figure 5.2: Example of large center-of-mass angle background subtraction for ^{95}Sr (a) (d,d) data and (b) (p,p) data. The green region was taken to be the peak region and so the counts were extracted by subtracting the background curve from the total counts in that range.

the optical models predict almost pure Rutherford scattering, and are in generally reasonable agreement with the data. Given that the data does not offer sensitivity to discriminate between the different parameter sets, the Perey and Perey [PP76] optical model potential was chosen to describe this reaction channel for the (d,p) calculations.

Parameter	BG [BG69]	CH [V+91]	PP [PP76]
R_c	1.25	1.266	1.25
V_0	60.41	57.314	58.725
R_0	1.17	1.201	1.25
A_0	0.75	0.69	0.65
W_0	0.00	0.558	0.00
W_D	12.856	10.292	13.5
R_D	1.32	1.238	1.25
A_D	0.65	0.69	0.47
V_{so}	6.2	5.9	7.5
R_{so}	1.01	1.077	1.25
A_{so}	0.75	0.63	0.47

Table 5.1: Global optical model parameters that were used to fit ^{94,95}Sr proton elastic scattering angular distributions; Becchetti and Greenlees (BG), Chapel Hill (CH) and Perey and Perey (PP).
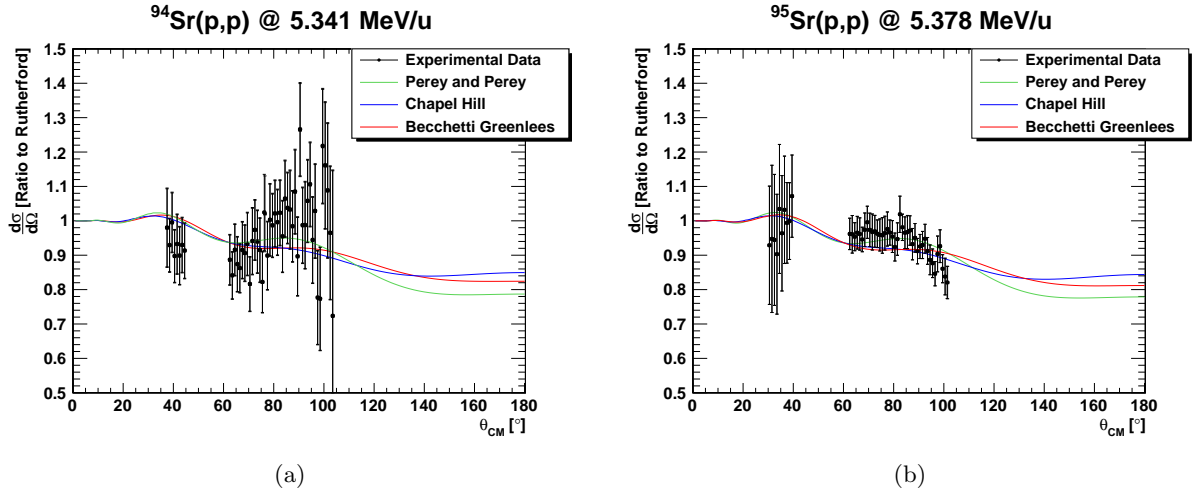
Figure 5.3: Comparison of various optical model potentials to experimental angular distributions for (a) ^{94}Sr(p,p) elastic scattering (b) ^{95}Sr(p,p) elastic scattering.

Figures 5.4a and 5.4b show the experimental deuteron elastic scattering angular distributions

compared to various optical models, which are described in table 5.2. As was discussed earlier, the very small difference in V_0 and W_D between ^{94}Sr(d,d) and ^{95}Sr(d,d) due to the different neutron number and mass number was considered negligible. All of the optical models predict similar angular distributions, however none of them reproduced the data to a high quality. The calculated curves predict a cross section maximum at approximately 95°, however both data sets showed that this maximum is below 90°. For the ^{95}Sr(d,d) data, the gradient in the angular range 53-58° was also not well reproduced. The small angle ^{94}Sr(d,d) data was also underestimated by the curves. Several optical model parameters were adjusted to improve the fit to the ^{94}Sr(d,d) and ^{95}Sr(d,d) data.
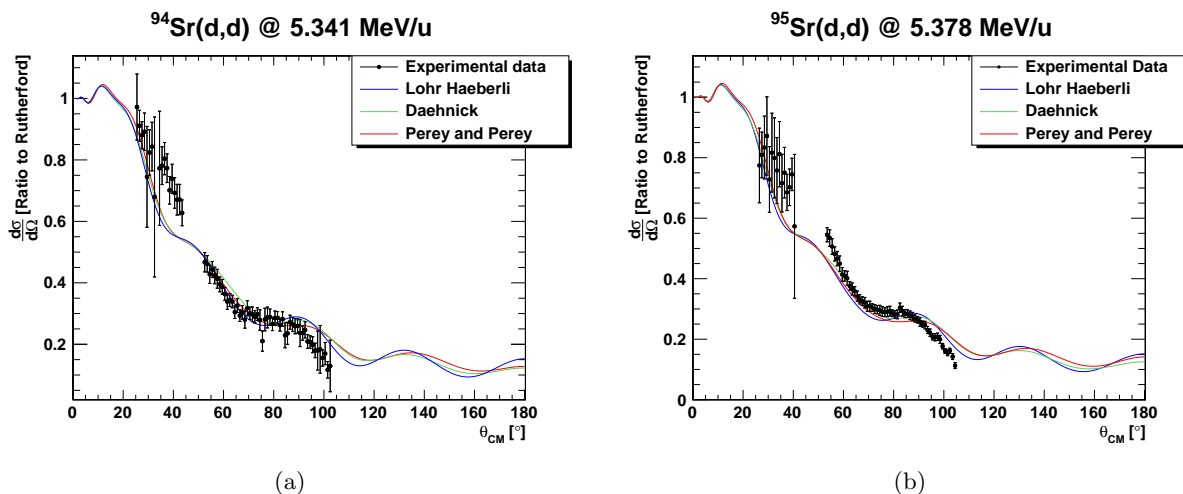
Figure 5.4: Comparison of various optical model potentials to experimental angular distributions for (a) ^{94}Sr(d,d) elastic scattering (b) ^{95}Sr(d,d) elastic scattering.

The Lohr and Haeberli [PP76] global optical model potential was used as a starting point for the modified optical model as it was fitted exclusively to data in the energy range 8-13 MeV which is best suited to this work. The inconsistency between calculated curves and the data at large angles signifies that the radius of the potential was too large, and so in both data sets the parameters R_0 and R_D were adjusted.

In the case of the ^{94}Sr(d,d) data, decreasing the radius of the optical potential was the only modification necessary in order to get excellent agreement. The set of optimized radii was

obtained by performing a two parameter minimization fit using R_0 and R_D as free parameters. SFRESCO [Tho88], which uses the MINUIT [Jam] minimization package, was used to carry out a χ^2 minimization fit. SFRESCO is part of the FRESCO software package that is designed to fit the DWBA calculation to experimental data. This is achieved by adjusting the fit parameters and updating the DWBA calculation until χ^2 minimization is achieved between the calculated curve and experimental data.

In order to achieve good agreement with the ^{95}Sr(d,d) data, the potential depth parameters V_0 and W_D were adjusted in addition to the potential radius parameters R_0 and R_D. The optimized R_0 and R_D values from the ^{94}Sr(d,d) data were used as a starting point for the fit, however it was found that the four parameter minimization was not reliable using SFRESCO, even with reasonable parameter starting points and constrained upper and lower bounds. Instead, each parameter was varied in turn by hand until satisfactory agreement between theory and experiment was obtained. Using this approach, the hand-fitted optical model required only a small adjustment from the Lohr and Haeberli parameter set, in a way that was also consistent with the ^{94}Sr(d,d) optical model fit. Figures 5.5a and 5.5b show the resulting fit of the modified optical model potentials to both data sets.

(a) (b)
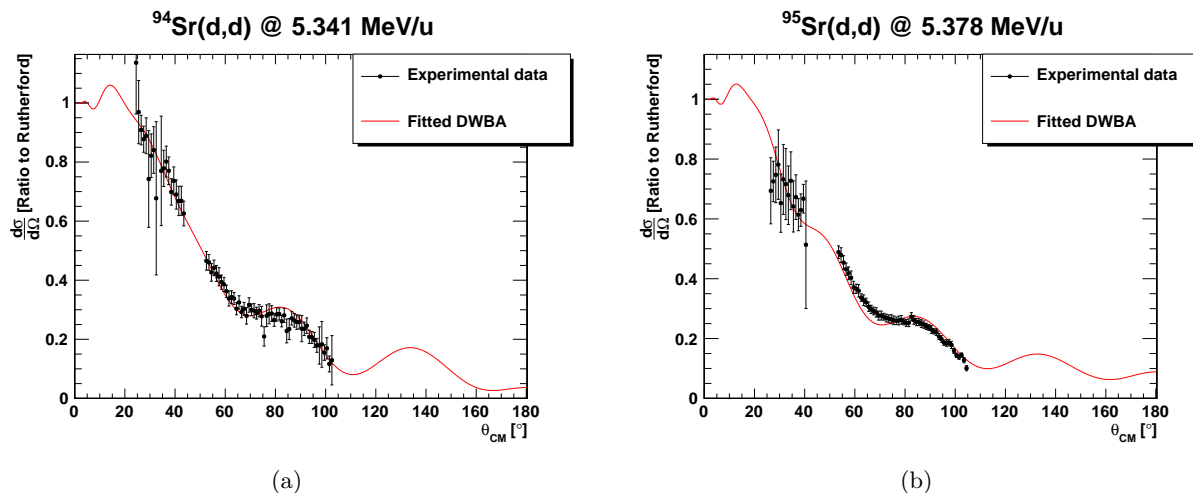
Figure 5.5: (a) Measured angular distribution for ^{94}Sr(d,d) elastic scattering. (b) Measured angular distribution for ^{95}Sr(p,p) elastic scattering.

Parameter	^{94}Sr	^{95}Sr	LH [PP76]	D [DCV80]	PP [PP76]
R_c	1.3	1.3	1.3	1.3	1.3
V_0	109.45	130.0	109.45	93.032	95.28
R_0	0.903	0.97	1.05	1.17	1.15
A_0	0.86	0.86	0.86	0.727	0.81
W_D	10.417	12.0	10.417	12.336	16.99
R_D	1.11	1.25	1.43	1.3 25	1.34
A_D	0.771	0.771	0.771	0.849	0.68
V_{so}	7.0	7.0	7.0	7.0	0
R_{so}	0.75	0.75	0.75	1.07	0
A_{so}	0.5	0.5	0.5	0.66	0

Table 5.2: Optical model parameters used to fit ^{94,95}Sr deuteron elastic scattering angular distributions compared to global parameter fits; Lohr and Haeberli (LH), Daehnick (D) and Perey and Perey (PP)

It was found that the optimized optical potentials led to a significant change in calculated differential cross section compared to the global parameters. This can be seen in figures 5.6a and 5.6b as the large difference between the global optical model calculations and the fitted optical model calculations. The resulting (d,p) spectroscopic factors were therefore strongly dependent on the choice of optical model parameters. For this reason the spectroscopic factors presented in the following sections can be compared within a given model (relative) but the absolute value is not well known. It is important to note that the modified optical potentials did not introduce ambiguity in the (d,p) calculations between different orbital angular momentum transfers. The position of the differential cross section maxima and minima for different ℓ transfers were all shifted in unison, so that it remained possible to distinguish between them. It was important to ensure that this was true, otherwise the spins of the populated states could not be assigned using these DWBA calculations.

The normalization constants for ^{94,95}Sr(p,p) and ^{94,95}Sr(d,d) are given in table 5.3. The normalization constants for (p,p) and (d,d), $\mathcal{N}_{p,d}$, were combined using equation 5.2 to estimate the ratio of protons to deuterons in the target, as is shown in equation 5.3.

$$\frac{\mathcal{N}_d}{\mathcal{N}_p} = \frac{n_p}{n_d} \tag{5.3}$$

(a)

(b)
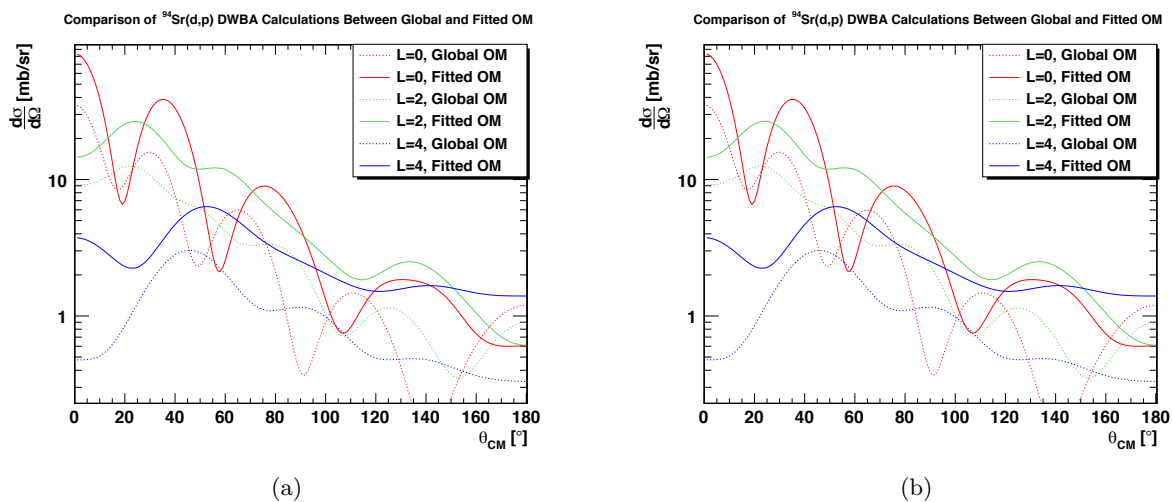
Figure 5.6: Comparison of global and fitted DWBA differential cross sections for (a) ^{94}Sr(d,p) and (b) ^{95}Sr(d,p). The large difference in calculated angular distributions between the optical model parameter sets for a given reaction indicates that there is a very large uncertainty on the overall cross sections for the reactions, which means that the absolute value of the resulting spectroscopic factors is not well-known.

This number of proton and deuterons in the target is expressed in table 5.3 as the target composition fraction.

Reaction	Normalization [mb]	Target Composition [%]
^{94}Sr(p,p)	4.5(1) x 10^{-1}	3.8(1)
^{94}Sr(d,d)	1.79(2) x 10^{-2}	96(2)
^{95}Sr(p,p)	5.87(6) x 10^{-3}	8.2(1)
^{95}Sr(d,d)	5.25(4) x 10^{-4}	92(1)

Table 5.3: Normalization constants extracted from $\frac{d\sigma}{d\Omega}$ fits of (p,p) and (d,d) data to DWBA calculations.

$\left(\frac{11}{2}^{+}\right)$ — 1666

427   1109

$\left(\frac{9}{2}^{+}\right)$ — 1238

683   887

$\left(\frac{3}{2}^{+}, \frac{5}{2}^{+}\right)$ — 681

125

$\left(\frac{7}{2}^{+}\right)$ — 556, $t_{\frac{1}{2}} = 21.9(5)$ ns

329   204

$\left(\frac{3}{2}^{+}\right)$ — 352

352   681

$\frac{1}{2}^{+}$ — 0 keV, $t_{\frac{1}{2}} = 23.90(14)$ s
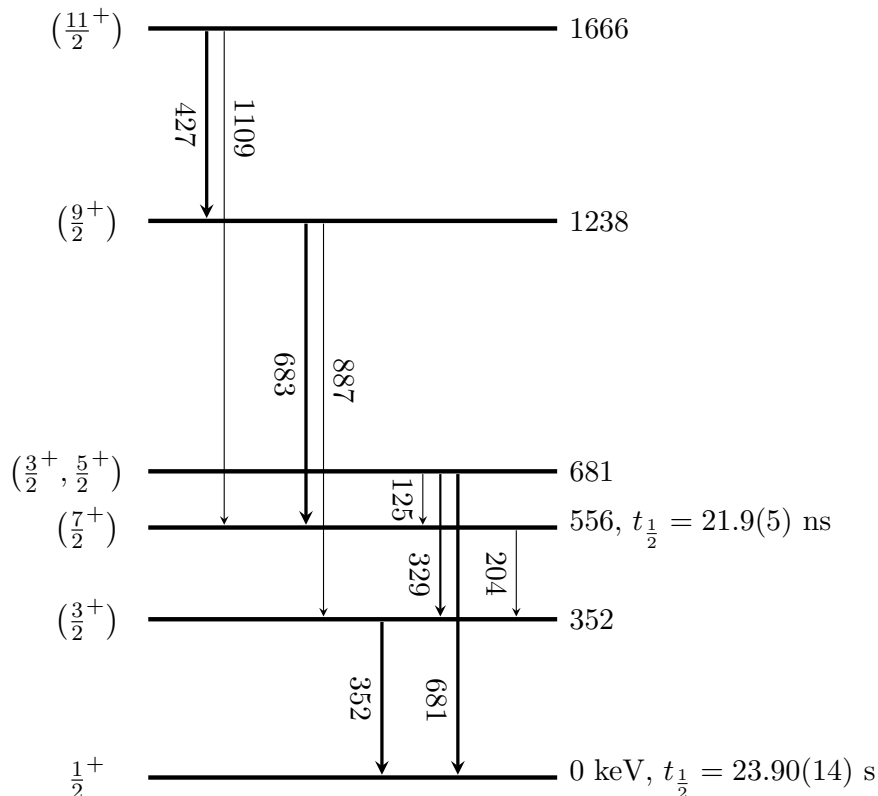
Figure 5.7: Level scheme for ^{95}Sr states populated through ^{94}Sr(d,p). Level energies, lifetimes and spin assignments are taken from [Lab].

5.2 ^{94}Sr(d,p) Results

Figure 5.7 shows the level scheme that was built from this experiment. Spins and parities that are given in figure 5.7 are from previous work. Those given in parentheses are tentative assignments. The γ-rays that were measured in this experiment are consistent with available literature for ^{95}Sr [Lab]. Figure 5.8a shows the measured ^{95}Sr γ-rays coincident with ^{94}Sr(d,p) protons. The labelled peaks indicate known transitions in ^{95}Sr. Figure 5.8b shows the γ-ray energy plotted against ^{95}Sr excitation energy. It can be seen through the constant strength of the 329 keV, 352 keV and 681 keV γ-ray energies as a function of excitation energy that the 352 keV and 681 keV are strong collecting states from higher lying levels. This means that many of the excited states cascade through these states. A $\gamma - \gamma$ coincidence was not possible for any of the states in this experiment due to low statistics.

It was found that the 352 keV and 681 keV ^{95}Sr excited states were populated directly with
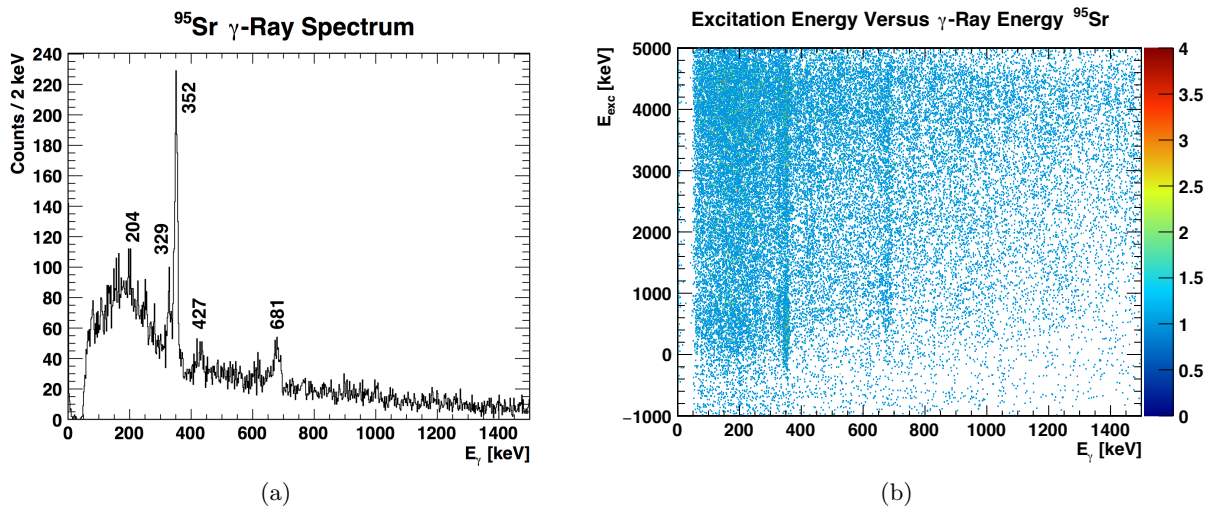
Figure 5.8: (a) γ-ray spectrum for ^{95}Sr. (b) Excitation energy versus γ-ray matrix for ^{94}Sr.

enough strength to extract angular distributions. The 1666 keV ^{95}Sr state was also identified through the 427 keV γ-ray line, although the limited angular range of SHARC at that excitation energy meant an angular distribution measurement was not possible. Significant ^{95}Sr ground state population was also observed. Results for of these states will be discussed in the subsequent sections.

Angular distributions were simultaneously extracted for the ground state, 352 keV and 681 keV states using a constrained three (Gaussian) peak plus exponential background fit. The separation between the peaks was fixed to preserve the energy spacing 0-352-681 keV. Additionally, the peaks were required to have the same width and the centroid positions could be adjusted in unison by up to 50 keV to allow the fit to reproduce the data well. The background was also constrained to be the same shape within each of the sections of SHARC to model the observed background distribution. Example fits for two different center-of-mass angles are shown in figures 5.9a and 5.9b. Spectroscopic factors for the 352 keV and 681 keV states were also extracted using γ-ray gates.

The 21.9 ns half-life of the isomeric 556 keV state [Lab] substantially lowered the γ-ray detection efficiency for the 204 keV transition (see figure 5.7), and so it was difficult to estimate the direct population strength of this states. As can be seen in figure 5.8a, there was a small excess

of counts at 204 keV in the TIGRESS γ-ray spectrum which have been labelled. However, it was difficult to determine whether this was in fact due to the direct population and subsequent decay of the 556 keV state or whether it is a statistical fluctuation, or some combination of both. Given the low statistics, it was not possible to rule out the signal as a statistical fluctuation based on the width of the distribution at 204 keV. It was found that there was good quantitative agreement between spectroscopic factors obtained using a particle analysis and particle-γ analysis for the 352 keV and 681 keV states, which suggests that the direct population of the 556 keV state was negligible. A strongly deformed configuration of this state has been proposed [HRH$^+$04], which would predict weak single particle character and thus weak population cross section through (d,p). This interpretation is supported by our measurements. Nevertheless, it was possible to assign a spin of $\frac{7}{2}^+$ to this state based on results of this experiment, as is presented in table 5.4. Further discussion of this state can be found later in this chapter.

The angular distribution analysis results for $^{94}Sr(d,p)$ are summarized in table 5.4. The table shows multiple results for the 681 keV ^{95}Sr state as the angular distribution analysis produced two possible spin values for the state. The J^π for each state is given, and those drawn in bold typeface indicate new spin assignments. The previous limits on the spins and parities for each state are outlined in the following sections, and new constraints from this work are also discussed. The γ-ray gate that was used, if any, is given in the table. The DWBA spectroscopic factor that was found to best reproduce the experimental data is also presented. The final column gives the total cross section for each state, which is the integral of the differential cross section over all θ values. The total cross sections were also calculated using FRESCO.

^{95}Sr State [keV]	J^π	ℓ	γ-ray gate [keV]	Spectroscopic Factor	σ_{tot} [mb]
0	$\frac{1}{2}^+$	0	fit	0.087(15)	8.0(14)
352	$\mathbf{\frac{3}{2}^+}$	2	352	0.122(13)	11.5(12)
556	$\mathbf{\frac{7}{2}^+}$	-	-	-	-
681	$\frac{3}{2}^+, \frac{5}{2}^+$	2	fit, 329, 681	0.072(15), 0.045(9)	7.0(14), 6.6(15)

Table 5.4: Table of spectroscopic factors for directly populated ^{95}Sr states.
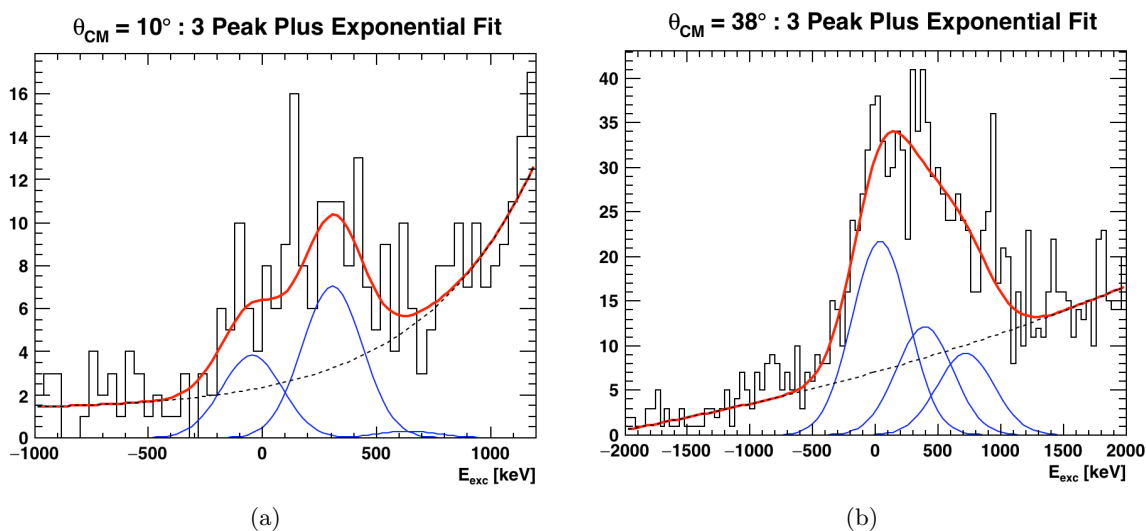
Figure 5.9: Example 3 peak fits for (a) $\theta_{CM} = 10°$ (b) $\theta_{CM} = 38°$.

^{95}Sr Ground State

The angular distributions shown in 5.10a and 5.10b were produced by using a constrained three (Gaussian) peak plus exponential background fit, as was previously described. Figures 5.10a and 5.10b compare the data to DWBA calculations produced using the fitted deuteron optical potential and an unmodified optical potential, respectively. The agreement with the data is significantly improved using the modified optical potential. The shape of the ground state angular distribution in figure 5.10a is in excellent agreement with the $\ell = 0$ DWBA calculation, which is consistent with the known spin of $\frac{1}{2}^+$.

^{95}Sr 352 keV State

Figure 5.11a was produced using the same three peak fit, as was previously described. A 352 keV γ-ray gated angular distribution, corrected for the γ-ray ray efficiency, was also produced and is shown in figure 5.11b. The spectroscopic factors that were extracted using each of these methods are 0.119(24) and 0.128(29) respectively, which are consistent within errors. This indicates that there was not significant feeding from the higher lying 681 keV ^{95}Sr state. The weighted average of the two spectroscopic factors is given in table 5.4.
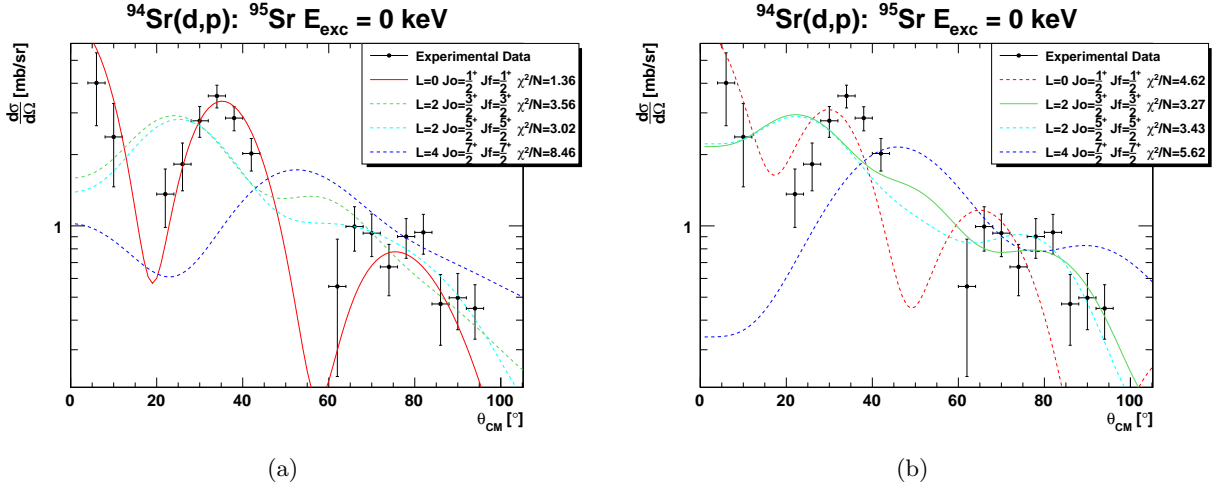
Figure 5.10: Angular distribution for $^{94}Sr(d,p)$ to the ^{95}Sr ground state compared to DWBA calculations using (a) fitted optical potential (b) unmodified optical potential.

The shape of the extracted angular distributions in figures 5.11a and 5.11b are both in good agreement with the $\ell = 2$ DWBA calculation, constraining the spin and parity of this state to be $J^\pi = \frac{3}{2}^+$ or $\frac{5}{2}^+$. The transferred angular momentum, together with the established M1 character of the 352 keV γ-ray transition to the ^{95}Sr ground state allows a firm spin and parity assignment of $\frac{3}{2}^+$ for this state.
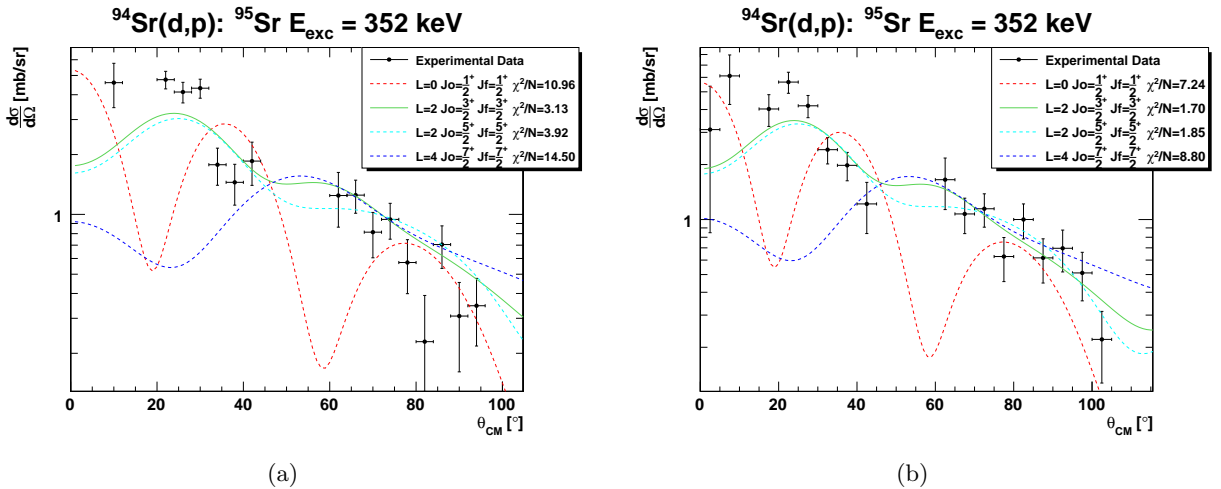
Figure 5.11: Angular distribution for $^{94}Sr(d,p)$ to the ^{95}Sr 352 keV state extracted using a (a) three peak fit, (b) 352 keV γ-ray gate.

^{95}Sr 556 keV State

Although direct population of the long-lived ^{95}Sr 556 keV state in this experiment could not be confirmed due to the low γ-ray detection efficiency for the 204 keV transition, its spin and parity can be constrained by combining the assigned spin and parity of the 352 keV state in this work with previous measurements.

The 204 keV γ-ray transition from the 556 keV to 352 keV state was previously measured to have E2 character using conversion electron spectroscopy [Lab]. The firmly assigned $\frac{3}{2}^+$ spin and parity of the 352 keV combined with the multipolarity of the 204 keV γ-ray constrains the spin and parity of the 556 keV ^{95}Sr state to be $\frac{5}{2}^+$ or $\frac{7}{2}^+$. For a spin and parity of $\frac{5}{2}^+$, the 204 keV γ-ray would contain a mixture of M1 and E2 multipolarities. One can estimate the transition rate using the so-called Weisskopf approximation, which is discussed in appendix E. A Weisskopf estimate for the M1 transition strength predicts that it would be large enough to have been observed in other studies. As no M1 component of the transition has been reported, the 556 keV state spin and parity is assigned to be $\frac{7}{2}^+$.

Moreover, the absence of any observed 556 keV γ-rays in previous studies indicates that the transition rate for a direct decay to the ^{95}Sr ground state is very low. The $\frac{7}{2}^+$ assignment of the 556 keV state would make the 556 keV γ-ray an M3 transition, which is consistent with its non-observation.

^{95}Sr 681 keV State

Figure 5.12 was produced using the same three peak fit as for the ground state and 352 keV state. Spectroscopic factors were also determined for this state using 329 keV and 681 γ-ray gates. The γ-ray gated angular distributions are shown in figures 5.13a and5.13b. All three analyses give consistent spectroscopic factors and favour $\ell = 2$ transfer, which constrains the spin and parity of this state to be $\frac{3}{2}^+$ or $\frac{5}{2}^+$. The spectroscopic factors for a spin and parity of $\frac{3}{2}^+$ were found to be 0.080(21), 0.074(29) and 0.060(26) using the three peak fit, 329 keV γ-ray and 681 keV γ-ray respectively. Similarly, the spectroscopic factors for a spin and parity of $\frac{5}{2}^+$ were 0.050(13), 0.046(18) and 0.037(15) using the three methods of extraction. The weighted average of these values for both $\frac{3}{2}^+$ and $\frac{5}{2}^+$ are given in table 5.4.

Information about the multipolarities of transitions from the 681 keV ^{95}Sr state to lower-lying states can also be used to constrain the spin and parity assignment of this state. A possible M1 component in the 681 keV γ-ray transition to the ^{95}Sr ground state would rule out a spin and parity of $\frac{5}{2}^+$, however the existence of the M1 component has not been confirmed [Lab]. Another result from ^{95}Rb β decay was a measurement of the $\log ft$ value for the decay of the of ^{95}Rb $\frac{5}{2}^-$ ground state to this state. A $\log ft$ value is essentially a measurement of transition strength and can be used to constrain the change in spin and parity between the parent and daughter nuclear states. The measured $\log ft$ value of 6.0 is most consistent with a first forbidden transition. A first forbidden transition causes a parity change (in this case - to +) and also a spin change of $\Delta I = 0, 1, 2$ units of angular momentum, which would require the spin and parity of the 681 keV ^{95}Sr state to be $\frac{1}{2}^+$ to $\frac{7}{2}^+$.

All of these measurements taken together constrain the spin and parity to be $\frac{3}{2}^+$ or $\frac{5}{2}^+$.
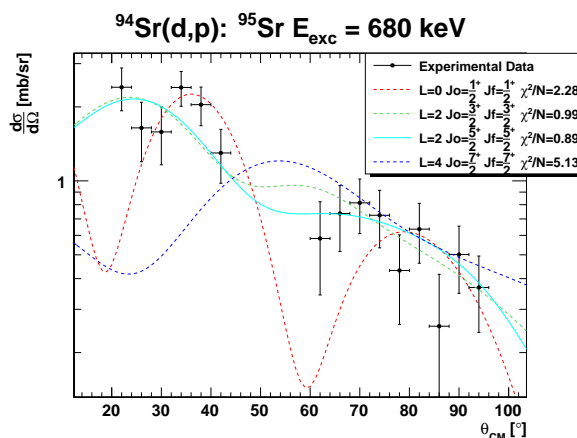
Figure 5.12: Angular distribution for ^{94}Sr(d,p) to ^{95}Sr the ^{95}Sr 681 keV state extracted using a three peak fit.

Higher Lying ^{95}Sr States

The γ-ray spectrum shown in figure 5.14a was produced by gating on the excitation energy range 1-2 MeV, using only the particles measured in the DBOX section of SHARC. The strong 427 keV peak indicates that the 1666 keV ^{95}Sr state was populated in this reaction. It was not
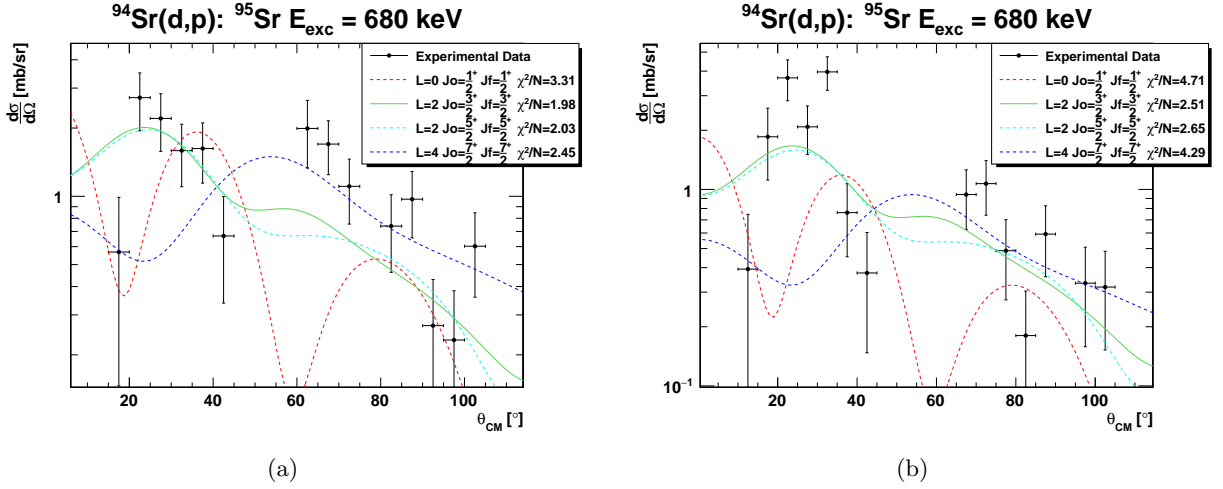
Figure 5.13: Angular distribution for ^{94}Sr(d,p) to ^{95}Sr 681 keV state extracted using a (a) 329 keV γ-ray gate, (b) 681 keV γ-ray gate.

possible to determine the extent of direct population to the 1238 keV ^{95}Sr state in this work as the strongest transition from this state produces a 682 keV γ-ray which could not be distinguished from the 681 keV γ-ray line given the γ-ray spectrum energy resolution and available statistics. The observed 329 keV γ-ray in this excitation energy range suggests that there is feeding of the 681 keV ^{95}Sr state from directly populated states in the excitation energy range 1-2 MeV. The intensity of the observed 329 keV γ-ray is not consistent with the suggested branching ratios.

The 1238 keV ^{95}Sr state was observed in ^{95}Rb β decay and ^{96}Rb β-n decay. The measured $\log ft \geq 7.6$ from the decay of the ^{95}Rb $\frac{5}{2}^-$ ground state to the 1238 keV state is consistent with a first forbidden decay which changes the total angular momentum by $\Delta I = 0, 1, 2$ and changes the parity of the daughter state. This constrains the 1238 keV spin and parity to be $\frac{1}{2}^+$ to $\frac{9}{2}^+$. The measured multipolarity of the γ-ray transition from the 1238 keV state to the $\frac{7}{2}^+$ 556 keV isomer is M1+E2, which leads to a tentative spin assignment of $\frac{9}{2}^+$ for this state. The 1666 keV ^{95}Sr state was not reported in either of the decay studies.

Both the 1238 keV and 1666 keV ^{95}Sr states were observed in ^{252}Cf spontaneous fission (SF) decay [HRH$^+$04], a reaction which preferentially populates high spin states. The proposed level scheme from the ^{252}Cf SF work is shown in figure 5.14b. The 1666 keV state was assigned a

tentative spin and parity of $\frac{11}{2}^+$ based on the strong branching ratio to the 1238 keV state, however the substantial population strength of the 1666 keV state in this experiment makes the assignment unlikely. The addition of a single neutron to the ^{94}Sr ground state can directly populate ^{95}Sr states with spins and parities of $\frac{1}{2}^+, \frac{3}{2}^+, \frac{5}{2}^+, \frac{7}{2}^+$ and $\frac{11}{2}^-$, although the cross section for $\ell = 5$ transfer would be very low, and so it would be less favourable.

(a)   (b)
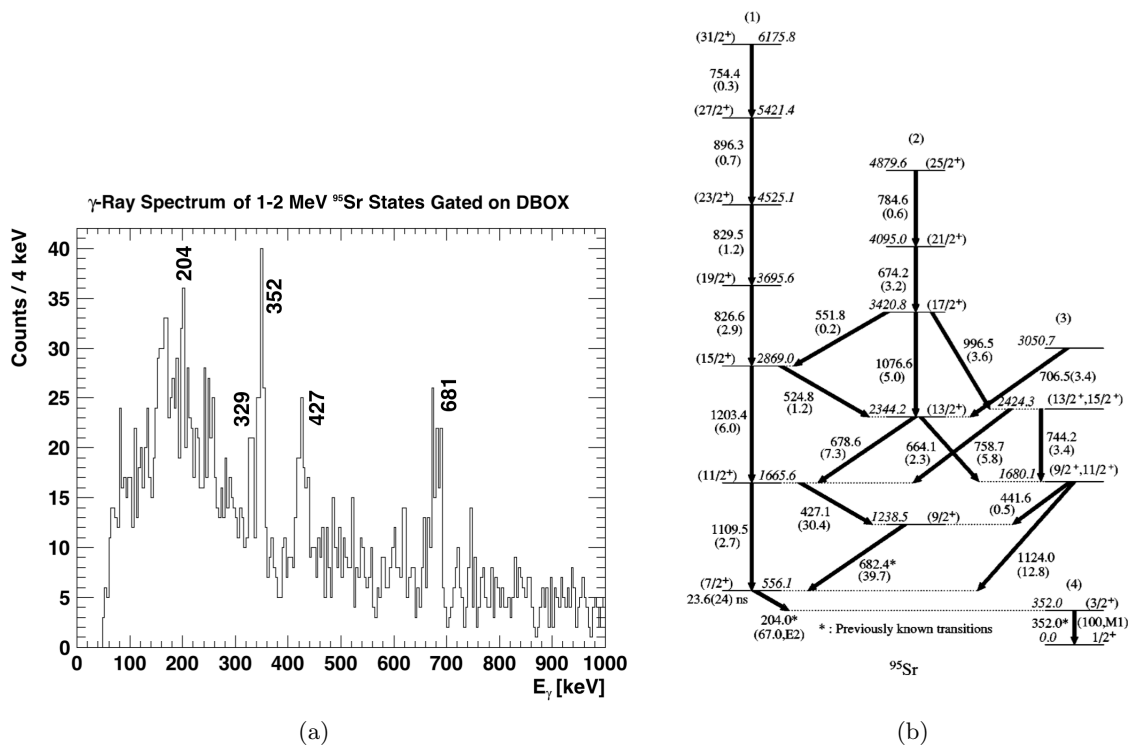
Figure 5.14: (a) Measured γ-rays coincident with ^{95}Sr excitation energies of 1-2 MeV using transfer protons in the DBOX section of SHARC only. The 427 keV γ-ray indicates direct population of the 1666 keV state. (b) Level scheme taken from ^{252}Cf SF [HRH$^+$04], indicating three possible band structures in ^{95}Sr.
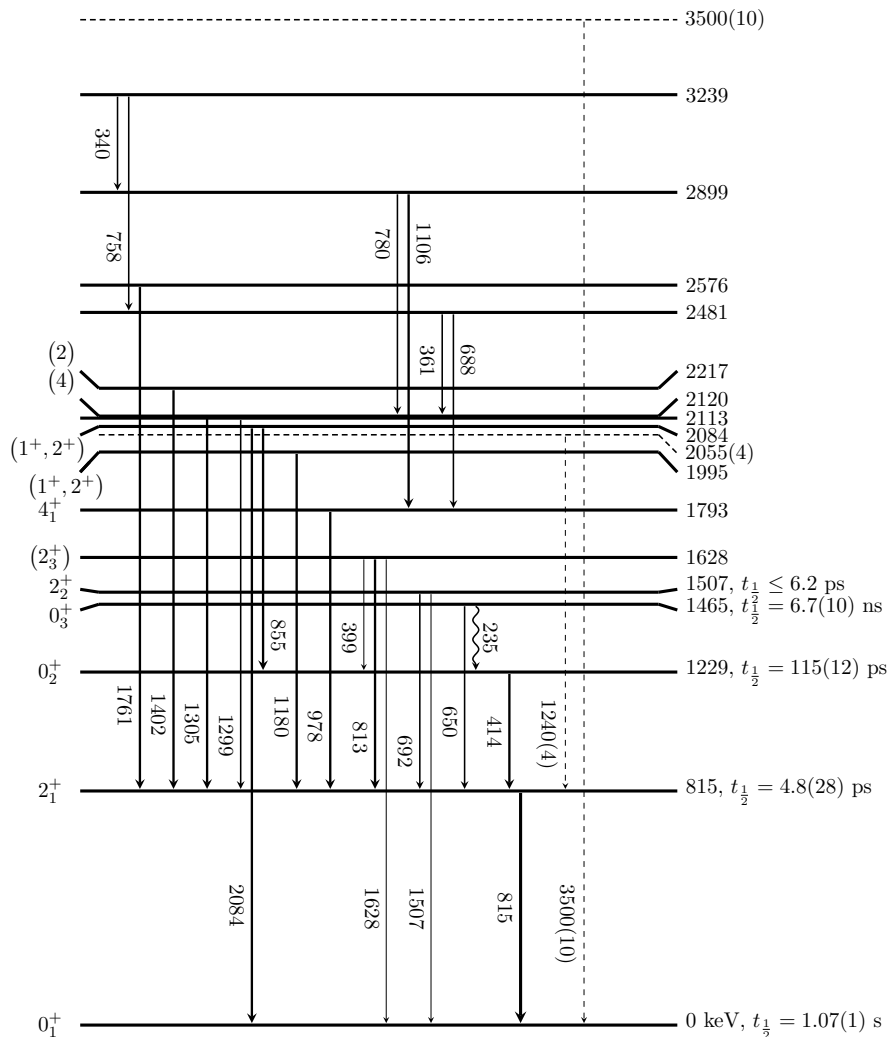
Figure 5.15: Level scheme for ^{96}Sr states populated through $^{95}Sr(d,p)$. Level energies, lifetimes and spin assignments are taken from [Lab]. Dashed lines represent proposed new states and transitions. The 235 keV E0 transition was not seen in this work.

5.3 ^{95}Sr(d,p) Results

Figure 5.16 shows a spectrum of the measured ^{96}Sr γ-rays coincident with $^{95}Sr(d,p)$ protons. The labelled peaks indicate known transitions in ^{96}Sr, with the exception of the 538 keV peak which is not known, and could not be placed in the level scheme. Figure 5.15 shows the level scheme that was built from this experiment. Spins and parities that are given in figure 5.15 are from previous work. Two new candidate states were observed in this experiment, with energies 2055(4) keV and 3500(10) keV. These are discussed later in this chapter.

Figure 5.17b shows the γ-ray energy plotted against ^{96}Sr excitation energy. As was also seen in ^{95}Sr, the 815 keV first excited state in ^{96}Sr is a strong collecting state from higher levels. This can be seen by the very strong γ-ray line coincident with ^{96}Sr states all the way up to the neutron separation energy at 5.88 MeV. Some direct transitions from excited states to the ground state were observed, although most of the states which were analyzed used γ-ray gates on strong transitions to the 2_1^+ state. It was found that many of the weaker observed γ-ray transitions in figure 5.16 were produced by cascades from higher excited states rather than direct population. For this reason, it was not possible to extract angular distributions for each of the populated states by γ-ray gating on the associated transition. As can be seen in figure 5.17b, ^{95}Sr(d,p) directly populated ^{96}Sr states up to the neutron separation energy. However, it was not possible to identify individual states above 3.5 MeV as unique γ-ray transitions could not be found. Figure 5.17a shows the $\gamma - \gamma$ coincidence matrix, where the strongest coincidence is for 813 keV and 815 keV γ-rays which are from the 1628 keV ^{96}Sr state.
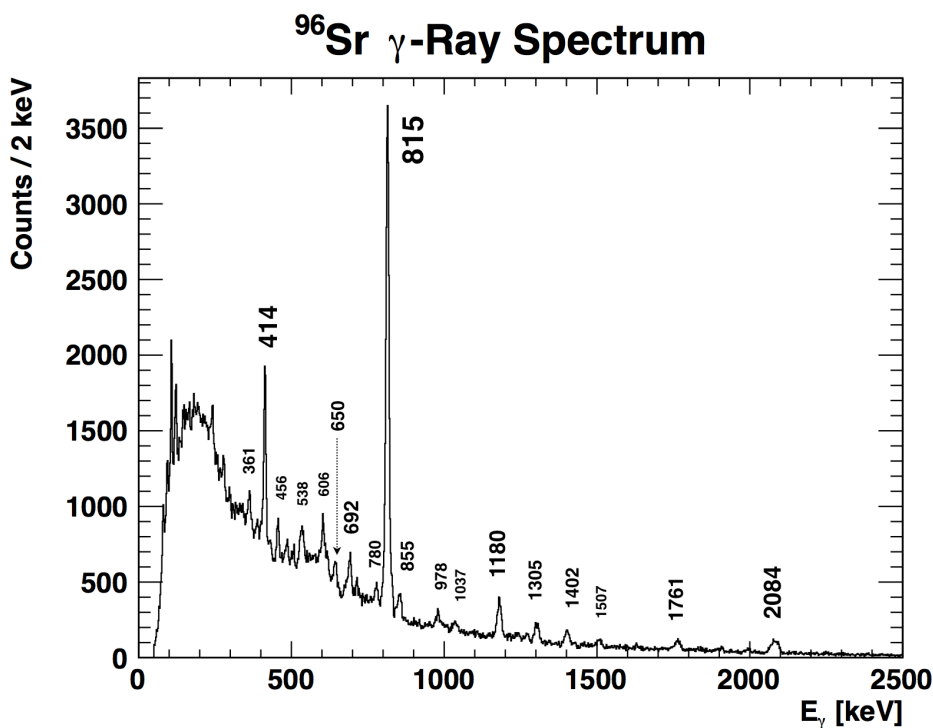
Figure 5.16: γ-ray spectrum for ^{96}Sr.
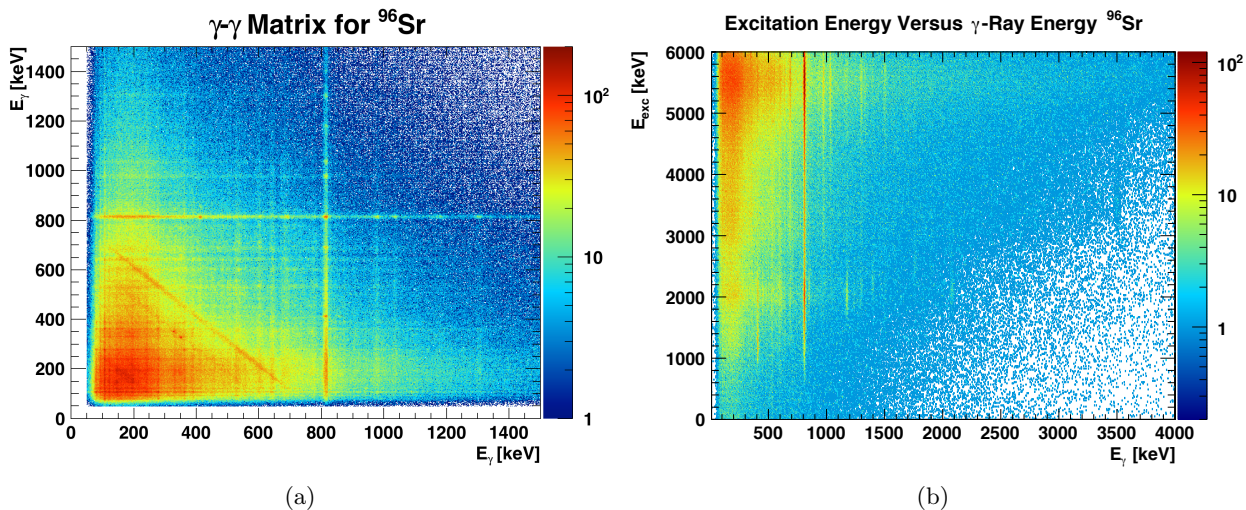
Figure 5.17: (a) $\gamma - \gamma$ matrix for ^{96}Sr. (b) Excitation energy versus γ-ray matrix for ^{96}Sr.

The unpaired valence neutron in ^{95}Sr can couple to the transferred neutron to produce two different possible spins. For this reason, it is not possible to firmly assign the spin of states in ^{96}Sr by measuring only the angular momentum (ℓ) transfer. Results from this work are combined with those from previous measurements wherever possible, to further constrain the spins and parities of the ^{96}Sr states. The DWBA calculations predict very similar shapes for the different spin couplings (such as $\ell = 2, j = 1^+$ and $\ell = 2, j = 2^+$). Spin values which correspond to aligned neutron spin vectors were calculated to have higher cross sections than those with anti-aligned spins due to the presence of a spin-spin interaction in the calculations, and so significantly different spectroscopic factors were obtained using the two couplings. All possible spins and parities that are consistent with the DWBA fits in this work and with previous constraints are given in results table 5.5. For states with more than one possible spin and parity, spectroscopic factors are given for each J^π so that each possible interpretation could be compared to shell model calculations in chapter 6. For cases when the spin was already firmly established, a single spin coupling for each ℓ value is compared to the data to contrast their shapes.

Table 5.5 gives the spectroscopic factors and constraints on the spin and parity of states that were analyzed. Each individual state is discussed in the subsequent sections.

^{96}Sr State [keV]	J^π	l	γ-ray gate [keV]	Spectroscopic Factor	σ_{tot} [mb]
0	0^+	0	fit	0.114(16)	1.17(16)
815	2^+	-	815	$0.014(5)^\dagger$	$0.6(2)^\dagger$
1229	0^+	0	414	$0.19(2), 0.16(3)^\dagger$	$2.0(2), 1.7(3)^\dagger$
1465	0^+	-	650	$0.18(7)^\dagger$	$1.9(7)^\dagger$
1507	2^+	2	792	0.025(8)	0.7(2)
1628	2^+	2	813 & 815	0.050(18)	1.4(5)
1793	4^+	4	978	0.049(11)	0.52(12)
1995	$1^+, 2^+$	2	1180	0.178(30), 0.100(17)	3.1(5), 2.9(4)
2084	$1^+, 2^+$	2	2084	0.214(47), 0.121(27)	3.7(8), 3.5(8)
2120	$\mathbf{4^+}$	4	1305	0.136(29)	1.5(3)
2217	$\mathbf{2^+}$	2	1402	0.034(7)	1.0(2)
2576	$1^+, 2^+$	2	1761	0.062(12), 0.036(7)	1.0(2), 0.97(19)
3239	$3^+, 4^+$	4	978	0.72(18), 0.54(14)	6.0(15), 5.8(15)
3500(10)	$1^+, 2^+$	2	3500	0.075(20), 0.042(12)	0.76(20), 0.74(20)

Table 5.5: Table of spectroscopic factors for directly populated ^{96}Sr states. †Spectroscopic factors and cross sections determined using a relative γ-ray analysis.

^{96}Sr 0^+ States

Figure 5.18a was produced by projecting $\Delta\theta = 2°$ slices and using an exponential function to fit the background shape over a large energy range with an exclusion window around the well-defined ground state peak. The background function was constrained to have the same slope within each of the SHARC sections. Figure 5.18b shows an example fit for this state. The counts were taken to be the excess above fitted background within the excitation energy window, as indicated in green in figure 5.18b. The angular distribution is in very good agreement with the calculated $\ell = 0$ DWBA curve.

Figure 5.19a was produced by gating on the $0_2^+ \rightarrow 2_1^+$ 414 keV γ-ray. Significant feeding from the 2084 keV to the 1229 keV state was observed. This was identified through the strongly coincident 414 keV and 854 keV γ-rays. The excitation energy spectrum coincident with 414
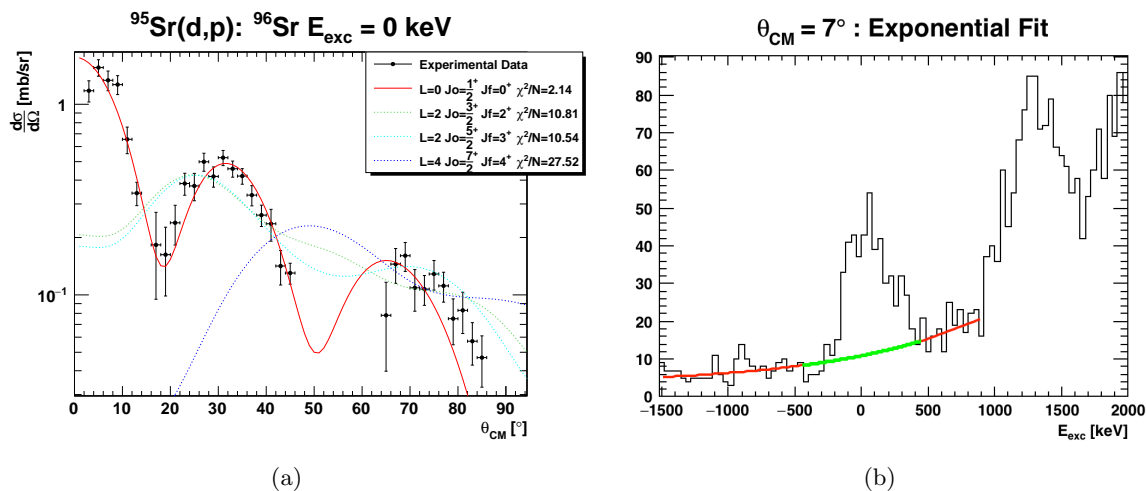
Figure 5.18: (a) Angular distribution for $^{95}Sr(d,p)$ to the ^{96}Sr 0_1^+ ground state. (b) An example exponential background fit, indicating the peak region (green) where the counts above the background were assigned to the 0_1^+ state.

keV γ-rays in the UQQQ and UBOX sections of SHARC ($\theta_{CM} < 50°$) is shown in figure 5.19b, which clearly indicates the direct population of the 1229 keV and 2084 keV states. The DBOX section of SHARC was excluded in figure 5.19b as the energy resolution of the projected excitation energy spectrum is depreciated significantly by adding the DBOX section. The 1229 keV state and the 2084 keV state can clearly be distinguished in the projection when only the UQQQ and UBOX sections of SHARC are used.

A fixed excitation energy window of 800-1650 keV was used for the angular range corresponding to the UBOX and UQQQ detectors to remove any feeding from the 2084 keV state. Significant direct population of the 1628 keV ^{96}Sr state was also observed through coincident 815 keV and 813 keV γ-rays, which has a 4.5(3)% branching ratio to the 1229 keV state. The excitation energy window that was used would include approximately 50% of the protons associated with the direct population of the 1628 keV state, effectively lowering the total efficiency for detecting the 1628 keV state to 2.3(2)%. The spin and parity of the 1628 keV state is established to be 2^+ and so the angular distribution of the background arising from feeding from the 1628 keV state would be predominantly of $\ell = 2$ character. The very good agreement of the 1229 keV experimental angular distribution with the $\ell = 2$ DWBA calculation confirms that the amount of 1628 keV feeding is negligibly small.
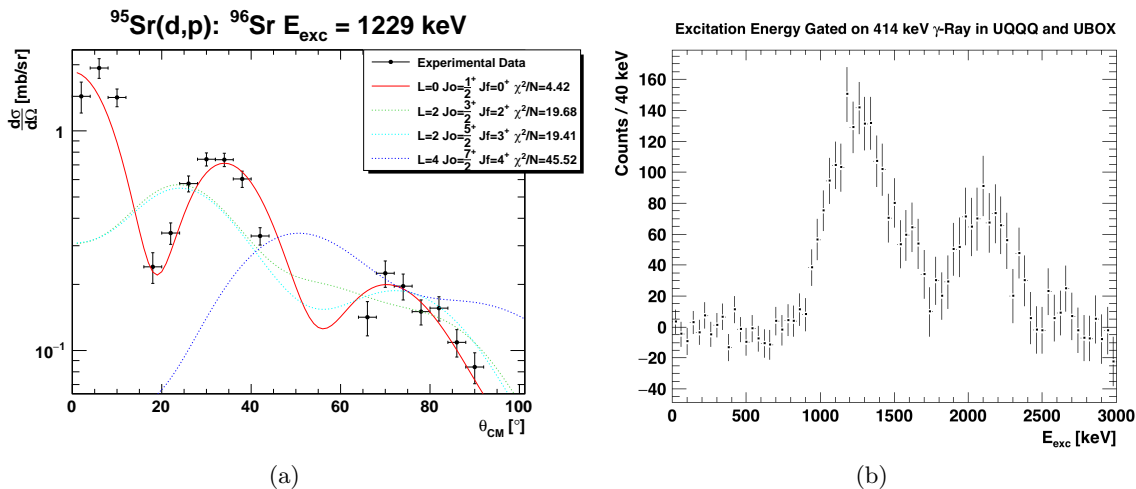
Figure 5.19: (a) Angular distribution for ^{95}Sr(d,p) to the ^{96}Sr 1229 keV 0_2^+ state. (b) Excitation energy spectrum gated on the UQQQ and UBOX SHARC sections, coincident with 414 keV γ-rays.

Figure 5.20a was produced by gating on the $0_3^+ \rightarrow 2_1^+$ 650 keV γ-ray. As was discussed in section 3.2, the long lifetime of this state resulted in a lower γ-ray detection efficiency. It was not possible to produce an angular distribution for this state using only TIGRESS detectors positioned at $\theta_{TIG} > 120°$ because the statistics were too low. The poor Doppler reconstruction of long-lived states also increased the photo-peak width and caused a large amount of skewness in the photo-peak of γ-rays emitted from the long-lived isomer, which made it difficult to distinguish between the $0_3^+ \rightarrow 2_1^+$ 650 keV γ-ray and the Compton edge of the strong 815 keV $2_1^+ \rightarrow 0_1^+$ γ-ray.

The 1465 keV state angular distribution shown in figure 5.20a has a large amount of scatter, particularly for small center-of-mass angles where the particle statistics were lowest in SHARC. The characteristic maximum at $\theta_{CM} \sim 30°$ is in quite good agreement with an $\ell = 0$ transfer reaction, however this could also be caused by unwanted gating on the large 815 keV γ-ray Compton edge which would include protons associated with $\ell = 0$ transfer to the 1229 keV state. Equal amounts of γ-ray background were subtracted from above and below the 650 keV γ-ray peak so that the contributions form the 815 keV γ-ray Compton edge would be mini-
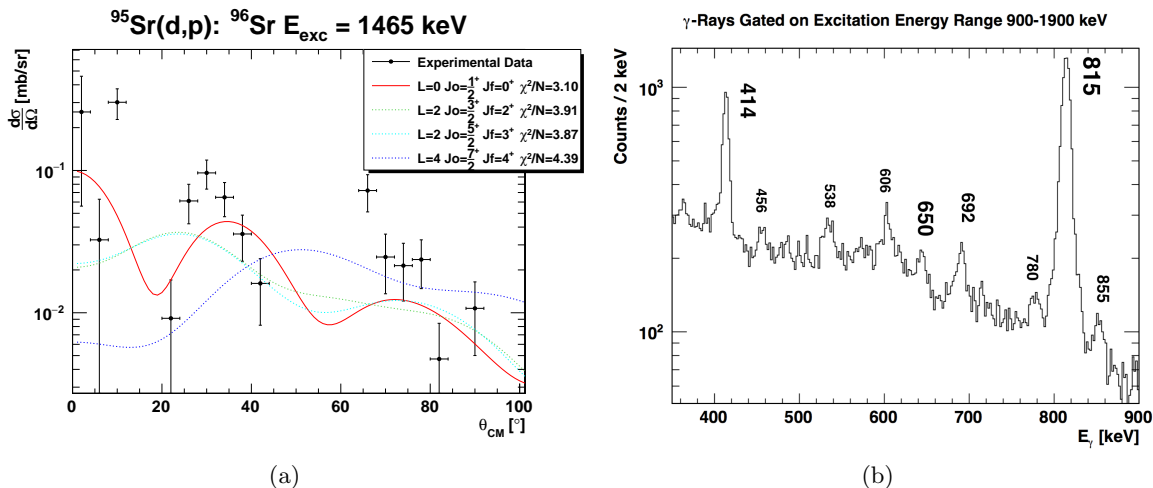
Figure 5.20: (a) Angular distribution for $^{95}Sr(d,p)$ to the ^{96}Sr 0_2^+ 1465 keV state. (b) ^{96}Sr γ-ray spectrum gated on the excitation energy range 900-1900 keV.

mized. Moreover, the γ-ray efficiency correction that was applied to the angular distribution in figure 5.20a did not include the lowered efficiency of detecting long lived states as this is not well known, and so the spectroscopic factor that was obtained from the fit was not meaningful. Figure 5.20b shows the γ-ray spectrum gated on excitation energies of 900-1900 keV, using TIGRESS detectors at all angles. The labelled 650 keV peak can be seen in the spectrum.

A γ-ray analysis was used to determine the relative population strengths of the two excited 0^+ states in ^{96}Sr. The 414 keV $0_2^+ \rightarrow 2_1^+$ transition and the 650 keV $0_3^+ \rightarrow 2_1^+$ transition are both pure E2, and so the ratio of the number of γ-rays emitted from these states is expected to form isotropic γ-ray angular distribution.

A series of excitation energy-gated γ-ray spectra were made using only the 135° TIGRESS corona ring and the UBOX and UQQQ SHARC sections in order to improve the energy resolution of both TIGRESS and SHARC. A 1 MeV excitation energy window was used so that both the 1229 keV and 1465 keV ^{96}Sr states could be fully included within the energy window, given the resolution of SHARC. The center of the energy window was increased from 500 keV to 2300 keV in steps of 100 keV and a γ-ray spectrum was made for each excitation energy range. Using this approach, it was possible to plot the counts in the 414 keV and 650 keV γ-ray peaks as a function of excitation energy, and compare them. The shape of the resulting

θ_{TIG}	$\mathcal{R}_{exp}$	$\mathcal{R}_{sim}$	$\frac{S_3}{S_2}$	$\mathcal{SF}(0_3^+)$ [x10^{-2}]
>120°	0.22(4)	0.20(6)	1.1(4)	18(7)
>135°	0.27(7)	0.19(6)	1.4(6)	23(11)

Table 5.6: Comparison of experimental and simulated counts ratio for 414 keV and 650 keV γ-rays gated on different angular ranges in TIGRESS. The simulated ratio is discussed in section 3.2.

curve for a given peak is expected to increase with excitation energy, as the overlap between the energy window and the excitation energy peak becomes larger, and then saturate when the peak is fully inside the window.

Figure 5.21a shows the counts in the 414 keV and 650 keV γ-ray peaks as a function of the center of excitation energy window. The counts in both peaks can be found to increase as a function of energy and then saturate at around 1300 keV, which corresponds to the energy where all of the direct population of the two states is included in the excitation energy window. The feeding of the 1229 keV state from higher lying ^{96}Sr states, as shown in figure 5.19b, caused a further increase in counts in the 414 keV γ-ray peak with energy. Similarly, the constant number of counts in the 650 keV γ-ray from the saturation energy up to beyond 2000 keV indicates that this state is also fed from higher lying ^{96}Sr states. The ratio of counts in the 650 keV peak to the 414 keV peak is given as a function of energy in figure 5.21b. The ratio of counts in the 650 keV peak to the 414 keV peak was obtained by averaging the ratio at 1300 keV and 1400 keV, which corresponds to the energy at which the excitation energy window is centered between 1229 keV and 1465 keV. This value was determined to be 0.22(6). This analysis was repeated using TIGRESS detectors positioned at $\theta_{TIG} > 120°$, and the ratio was measured to be 0.18(3). These results, adjusted to account for the different photo-peak efficiency of TIGRESS at 414 keV versus 650 keV, are compared to the simulation results from section 3.2 in table 5.6. The experimental results for each TIGRESS angular range indicate that the measured 414 keV and 650 keV γ-ray rays are consistent with equal population of both excited 0^+ states.

Given these relative population strengths, the feeding of the 1229 keV 0_2^+ state from the 1465 keV 0_3^+ state in the 1229 keV angular distribution can also be estimated. Using a population
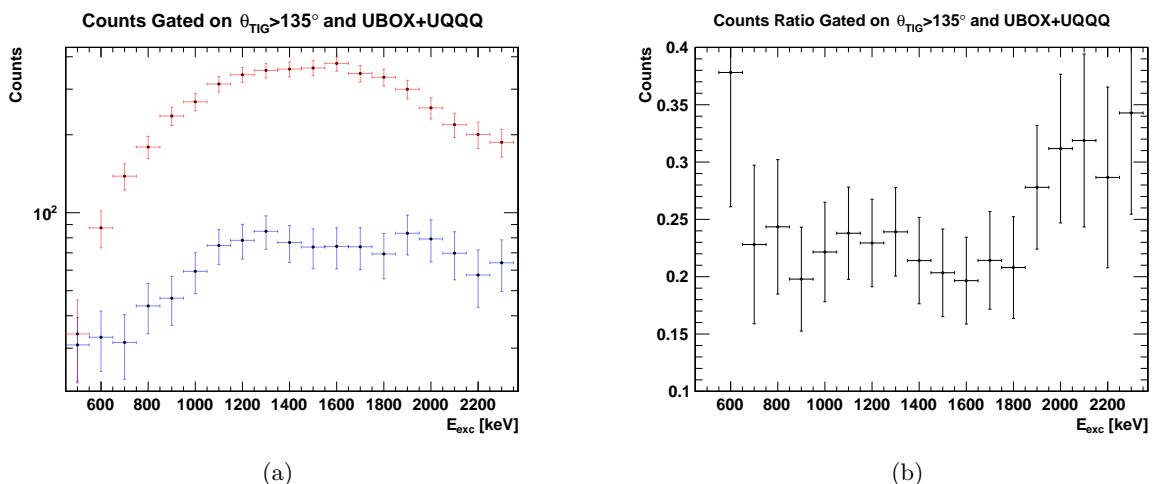
Figure 5.21: (a) Counts in 414 keV (red) and 650 keV (blue) γ-ray peaks as a function of excitation energy. (b) Ratio of counts in 650 keV γ-ray peak to 414 keV γ-ray peak as a function of excitation energy (more details in the text).

strength ratio of $\frac{S_3}{S_2} = 1.1$, approximately 15% of the total number of 414 keV γ-rays in the excitation energy range that was used for the 1229 keV ^{96}Sr state angular distribution would be expected to be fed from the 1465 keV state. In other words, the $\ell = 0$ spectroscopic factor that was extracted for the 1229 keV ^{96}Sr state must be reduced by 15% in order to remove feeding effects from the 1465 keV ^{96}Sr state. The reduced spectroscopic factor for the 1229 keV state is given in table 5.5. The spectroscopic factor that is given for the 1465 keV state in table 5.5 is taken from the $\theta_{TIG} > 120°$ measurement as this contained the most statistics.

^{96}Sr 815 keV State

It was not possible to produce an angular distribution for this state due to the strong feeding from the 1229 keV state and the resolution of SHARC. This feeding was removed using a γ-ray analysis instead. An excitation energy range of 400-1200 keV, gated on the UBOX and UQQQ sections of SHARC, was used so that all contributions from the 815 keV ^{96}Sr state were included. The counts in the 414 keV γ-ray peak were corrected for the efficiency of TIGRESS and subtracted from the efficiency-corrected counts in the 815 keV peak, giving the estimated number of particles associated with the direct population of the 815 keV ^{96}Sr state. This value was compared to the number of counts in the same angular range associated with

direct population of the 1628 keV 2^+ state, and the ratio was found to be 0.34(6). The same analysis was carried out in the DBOX section of SHARC and the ratio was found to be 0.5(1). The spectroscopic factor for the direct population of the 815 keV ^{96}Sr state in table 5.5 is the weighted average of the counts ratios multiplied by the spectroscopic factor of the 1628 keV ^{96}Sr state.

^{96}Sr 1507 keV State

Figure 5.22a was produced by gating on the $2_2^+ \rightarrow 0_1^+$ 1507 keV γ-ray. It was found that this state was weakly populated through ^{95}Sr(d,p). The measured angular distribution is consistent with the established spin of 2^+ [JPA+80].
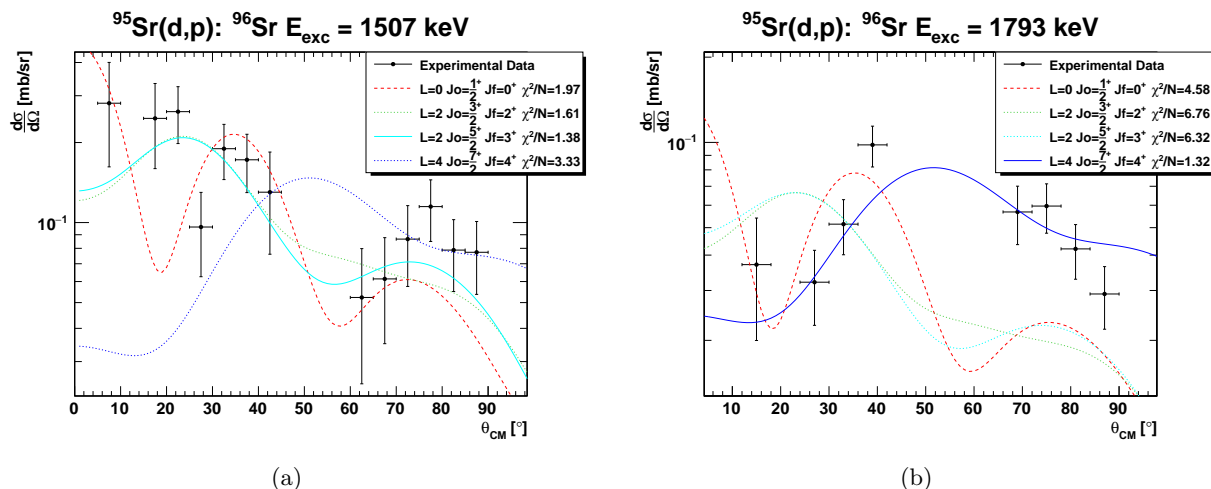
Figure 5.22: Angular distribution for ^{95}Sr(d,p) to (a) ^{96}Sr 1507 keV state and (b) ^{96}Sr 1793 keV state.

^{96}Sr 1628 keV State

Figure 5.23a was produced by $\gamma - \gamma$-gating on the strongly coincident 813 keV and 815 keV γ-rays. The almost identical γ-ray energies allowed the same γ-gate to be used for both transitions, which effectively doubled the sensitivity of TIGRESS to this state. Figure 5.23b shows the excitation energy spectrum for all sections of SHARC that was measured in coincident with both 813 keV and 815 keV γ-rays, clearly indicating that the 1628 keV was populated directly in ^{95}Sr(d,p). This state is fed by states above $\sim$2 MeV, however it was possible to remove most

of the feeding data by using a narrow excitation energy window in each of the SHARC sections. It is estimated that less than 5% of the data in the angular distribution is from other states, and so the spectroscopic factor in table 5.5 is an upper bound.

The measured angular distribution is in very good agreement with the $\ell = 2$ DWBA calculation, which constrains the spin and parity to be 1^+, 2^+ or 3^+. A suggested spin and parity of 2^+ was assigned to this state though β decay studies of ^{96}Rb [JPA$^+$80] using γ-γ angular correlation between the 813 keV and 815 keV γ-rays, although 1^+ could not be firmly ruled out given the available statistics. The observed branching ratios of this state to the $0^+_{1,2}$ states make it is highly unlikely that this state has spin and parity 3^+. If this state was 1^+, the decay to the $0^+_{1,2}$ states would be purely M1 transitions. The Weisskopf estimates for the strength of these M1 transitions indicate that they would be similar in strength to the 813 keV M1+E2 γ-ray, which is not observed as they are both an order of magnitude less intense. These observations favour a spin and parity assignment of 2^+ for the 1628 keV ^{96}Sr state.
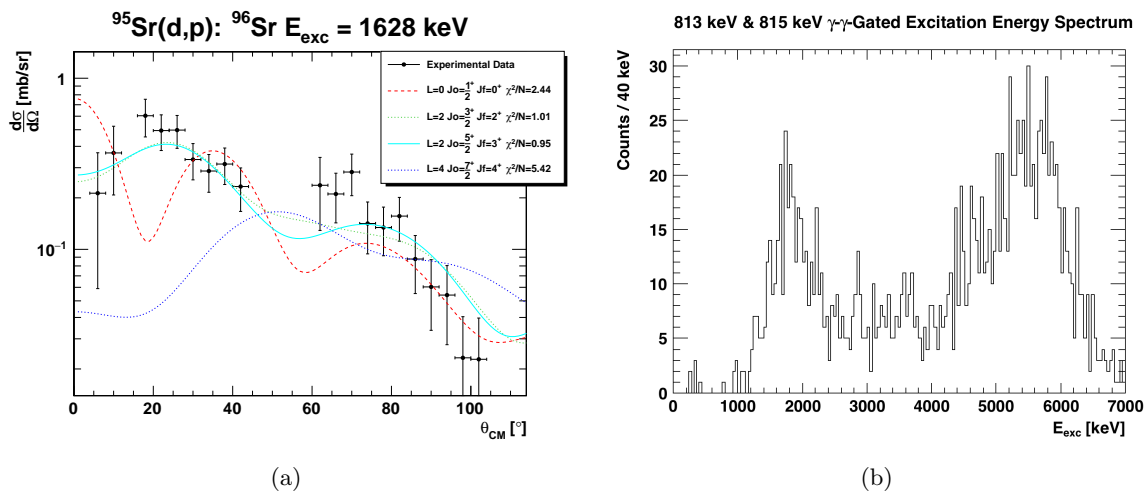
Figure 5.23: (a) Angular distribution for ^{95}Sr(d,p) to the ^{96}Sr 1628 keV state. (b) Excitation energy $\gamma - \gamma$-gated on the 813 keV and 815 keV γ-rays.

^{96}Sr 1793 keV State

Figure 5.22b was produced by gating on the $4^+_1 \rightarrow 2^+_1$ 978 keV γ-ray. It was found that this state was weakly populated, with most of the strength coming from feeding from higher levels.

The measured angular distribution is consistent with the established spin of 4^+ [JPA$^+$80].

^{96}Sr 1995 keV State

Figure 5.25a was produced by gating on the 1180 keV γ-ray. This state was strongly populated directly through the transfer reaction, and feeding from higher states was negligible. This state can be clearly seen in figure 5.17b as the strong 1180 keV γ-ray in coincidence with the excitation energy range 1600-2400 keV.

The measured angular distribution shows strong $\ell = 2$ character which constrains the spin and parity to be 1^+, 2^+ or 3^+. A spin and parity of 3^+ is a very unlikely assignment based on the observed decay branches to the $0^+_{1,2}$ ^{96}Sr states as these would correspond to M3 transitions which, when calculated using standard matrix elements, are predicted to be extremely weak transitions. A suggested spin and parity of 1^+ was assigned to this state though β decay studies of ^{96}Rb [JPA$^+$80] using γ-γ angular correlation between the 1180 keV and 815 keV γ-rays, although 2^+ could not be firmly ruled out given the available statistics. It was argued in reference [JPA$^+$80] that $J^\pi = 2^+$ is unlikely since the 1180 keV transition would connect 2^+ states with a low E2 admixture which has been observed infrequently, and so $J^\pi = 1^+$ is a favourable spin assignment.

^{96}Sr 2055 keV State

A candidate 1240(3) keV γ-ray was observed in the γ-ray singles spectrum gated on excitation energies 1600-2600 keV spectrum, which is shown in figure 5.26b. Figures 5.24a and 5.24b show the excitation energies and γ-ray rays which were measured in coincidence with the 1240(3) keV γ-ray respectively. The 1240(3) keV γ-ray was found to be in strong coincidence with the 815 keV γ-ray, and also possibly with an unknown 830 keV γ-ray. Given the known resolution of TIGRESS at 815 keV, it is more likely that the 830 keV peak is a fluctuation associated with the 815 keV state. The width of the peak at 1270 keV is not consistent with the known detector resolution at that energy, and so is likely a statistical fluctuation.

These observations support a proposed ^{96}Sr state at 2055(3) keV. No angular distribution analysis was possible for this state due to low statistics.
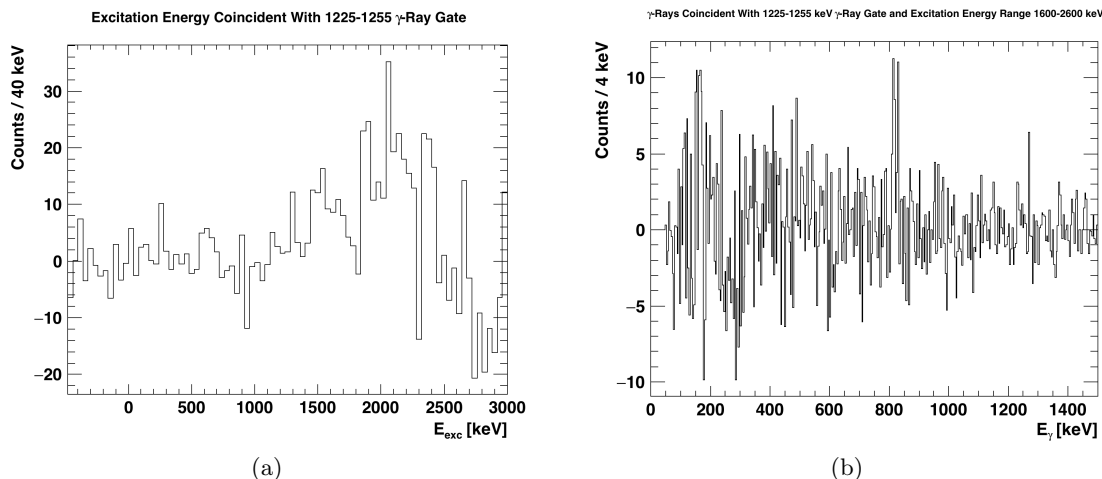
Figure 5.24: (a) ^{96}Sr excitation energies in coincidence with a 1240 keV γ-ray. (b) γ-rays in coincidence with a 1240 keV γ-ray.

^{96}Sr 2084 keV State

Figure 5.25b was produced by gating on the 2084 keV direct γ-ray decay to the ground state. This state was strongly populated directly through the transfer reaction, and feeding from higher states was negligible. The direct ground state decay of the 2084 keV state can be clearly seen in figure 5.17b as the strong 2084 keV γ-ray in coincidence with the excitation energy range 1600-2400 keV. The measured angular distribution shows clear $\ell = 2$ character, and the strong population of this state confirms that it has positive parity. The spin and parity is constrained to be $1^+, 2^+$ or 3^+. Using similar arguments as for the 1995 keV ^{96}Sr state, the strong decay branch to the $0^+_{1,2}$ ^{96}Sr states effectively rules out 3^+.

The $\log ft$ value of the β decay of the ^{96}Rb $2^{(-)}$ ground state to the 2084 keV ^{96}Sr state was measured to be 6.3 [JPA$^+$80]. Given the change in parity and taking the parity of the ^{96}Rb ground state to be negative, the decay is most likely first forbidden which gives $\Delta I = 0, 1, 2$. Combining the angular distribution measurements with the $\log ft$ value constrains the 2084 keV ^{96}Sr state to have spin and parity 1^+ or 2^+.
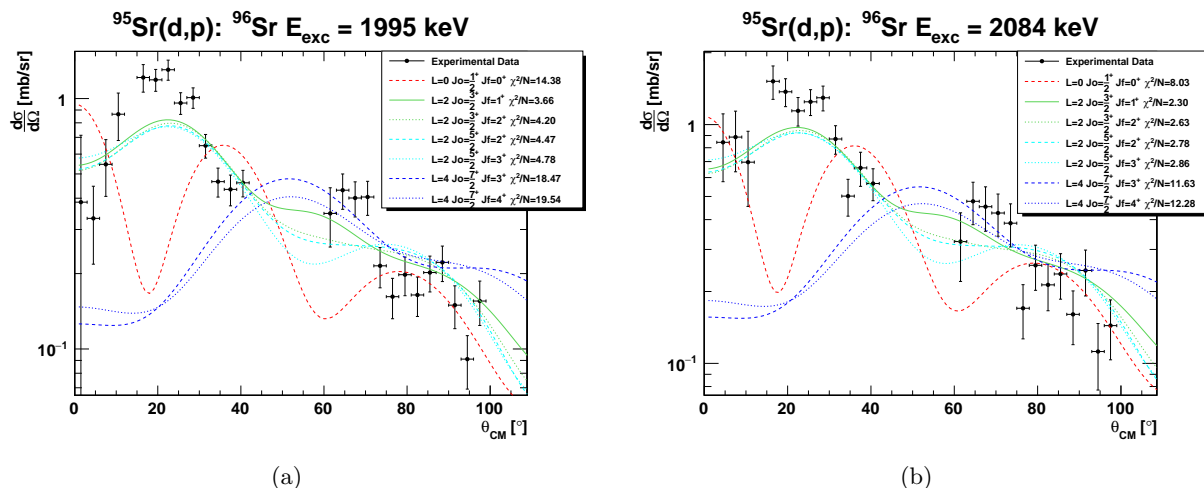
Figure 5.25: Angular distribution for $^{95}Sr(d,p)$ to (a) ^{96}Sr 1995 keV state and (b) ^{96}Sr 2084 keV state.

^{96}Sr 2120 keV State

Figure 5.26a was produced by gating on the $\sim$1300 keV γ-ray transition to the 815 keV 2_1^+ state. The 2113 and 2120 keV ^{96}Sr states decay most strongly via a (39%) 1299 keV and a (91%)1305 keV γ-ray respectively. This difference in γ-ray energies could not be resolved. The centroid of the fitted γ-ray peak at $\sim$1300 keV was determined to be 1302.7(5) keV. Figure 5.26b shows the γ-rays in coincidence with the excitation energy range 1600-2600 keV. A $\gamma - \gamma$ analysis of the different 2113 keV state decay branches was was not possible due to the available statistics. The weak 328 keV (10%) γ-ray associated with the 2120 keV and the weak 321 keV (6%) γ-ray associated with the 2120 keV state were not observed. The (21%) 485 keV and (35%) 607 keV γ-rays associated with the 2113 keV state were observed, however it was not possible to extract angular distributions using these γ-ray gates based on the statistics. The counts in the 485 keV and 607 keV γ-ray peaks were approximately consistent with the tabulated intensities and indicate that the population strength of the two states are 25(20)% 2113 keV and 75(20)% 2120 keV.

The angular distribution shown in figure 5.26a has strong $\ell = 4$ character, although it could also contain a mixture of $\ell = 2$ and $\ell = 4$. Spontaneous fission decay studies of ^{248}Cm have established the spin of the 2120 keV ^{96}Sr state to be $J = 4$ [WHC$^+$04]. This is in agreement

with the observed angular distribution, which would support a 4^+ spin and parity assignment for the 2120 keV ^{96}Sr state. The 2113 keV was populated weakly in ^{96}Rb β and β-n decay and has not been assigned a spin or parity, however a 0^+ assignment is very unlikely due to the observed decay to the 1793 4_1^+ state. The angular distribution for the 2113 keV state is therefore constrained to have $\ell = 2$ or $\ell = 4$ character, or a mixture of both.

The angular distribution shown in figure 5.26a is assumed to be mostly in association with the 2120 keV state. The spectroscopic factor given in table 5.5 assumes 100% 2120 keV and 0% 2113 keV, and so it is an upper limit. A nominal uncertainty of 10% was also assigned to the branching ratio of this state.

(a)   (b)
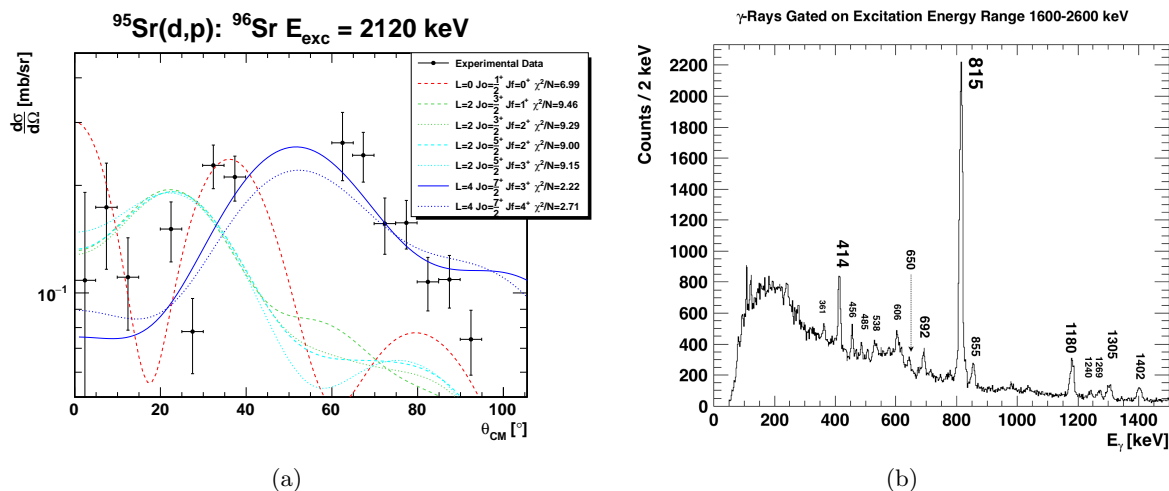
Figure 5.26: (a) Angular distribution for ^{95}Sr(d,p) to the ^{96}Sr 2217 keV state. (b) ^{96}Sr γ-rays gated on excitation energy range 1600 keV to 2600 keV.

^{96}Sr 2217 keV State

Figure 5.27a was produced by gating on the 1402 keV γ-ray transition to the 815 keV 2_1^+ state. A suggested spin of 2 was assigned to this state though β decay studies of ^{96}Rb [JPA$^+$80] using γ-γ angular correlation between the 1402 keV and 815 keV γ-rays. The state was not seen in other ^{96}Sr measurements. The measured angular distribution in this work shows clear $\ell = 2$ character, and so it is expected that this state has $J^\pi = 2^+$.

^{96}Sr 2576 keV State

Figure 5.27b was produced by gating on the 1761 keV γ-ray transition to the 815 keV 2_1^+ state. This state has been observed only though β decay studies of ^{96}Rb [JPA$^+$80] and no suggested spin was given. The angular distribution measurement in this work has strong $\ell = 2$ character, constraining the spin and parity to be 1^+, 2^+ or 3^+.
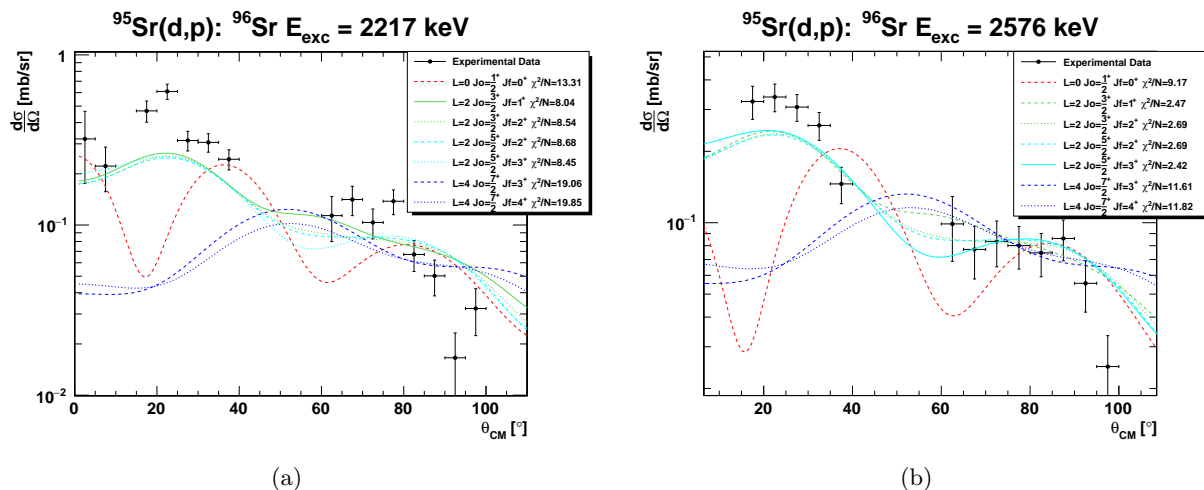
Figure 5.27: Angular distribution for ^{95}Sr(d,p) to (a) ^{96}Sr 2217 keV state and (b) ^{96}Sr 2576 keV state.

^{96}Sr 3239 keV State

A very strong 978 keV $4_1^+ \rightarrow 2_1^+$ γ-ray peak was observed for excitation energies in the range 2800-3600 keV, however it was not possible to confidently identify the state which was populated in this range. A small number of 688 keV and 1107 keV γ-rays were observed in coincidence with the 978 keV γ-ray, indicating that the 2481 keV and 2899 keV ^{96}Sr states were both fed from this state (or collection of states). A $\sim$1300 keV γ-ray peak was also seen in the γ-ray singles spectrum, which is consistent with the known feeding of the 2120 keV state from the 2481 keV and 2899 keV ^{96}Sr states. Evidence was also found for the feeding of the 2113 keV state from the 2481 keV and 2899 keV states, based on a weak 321 keV γ-ray in coincidence with the 978 keV γ-ray.

The 3239 keV ^{96}Sr state was seen in ^{248}Cm studies and is currently the only known state which

decays to both the 2481 keV and 2899 keV states, through 758 keV and 340 keV γ-rays respectively. The maximum of the 978 keV γ-gated excitation energy distribution was found to be at approximately 3200 keV which is consistent with this state. A small number of 340 keV and 758 keV γ-rays were observed in the γ-ray singles spectrum gated on excitation energies of 2800-3600 keV, which correspond to the decay of the 3239 keV state to the 2481 keV and 2899 keV states respectively. These transitions were not seen in coincidence with the 978 keV γ-ray, as is shown in figure 5.28b. A 538(3) keV γ-ray was also seen in coincidence with the 978 keV although this could not be placed in the level scheme.

The angular distribution for this state (or collection of states) shows $\ell = 4$ character, constraining the spin to be 3^+ or 4^+.

(a)   (b)
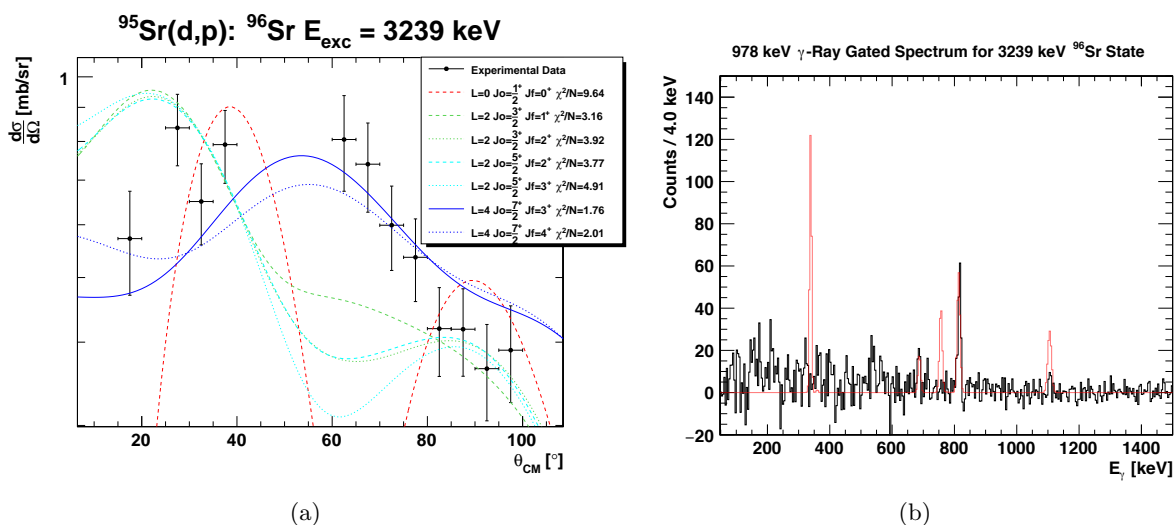
Figure 5.28: (a) Angular distribution for $^{95}Sr(d,p)$ to ^{96}Sr 3239 keV state. (b) Comparison of measured coincidence 978 keV spectrum (black) with simulated coincidence spectrum (red) using known decays and intensities. The simulated spectrum includes appropriate efficiency scaling and energy resolution to generate a realistic photo-peak spectrum.

^{96}Sr 3500 keV State

Figure 5.29 was produced by gating on the direct transition to the ground state of ^{96}Sr. This transition can be seen in figure 5.17b. The measured angular distribution is consistent with $\ell = 2$ transfer.

This state is not consistent with any previously measured ^{96}Sr state and so we propose a newly identified excited state in ^{96}Sr at 3500(10) keV, where the error indicated the uncertainty on the measured γ-ray. No other new transitions were observed in this energy range, indicating that the branching ratio for the 3500 keV γ-ray is 100%. An uncertainty of 10% was assumed for the branching ratio from this state to account for the limited sensitivity and statistics available in this experiment. Due to the observed direct transition to the ground state, it is highly unlikely that this transition is of higher multipole order than 2. This constrains the spin and parity to be 1^+, 2^+.
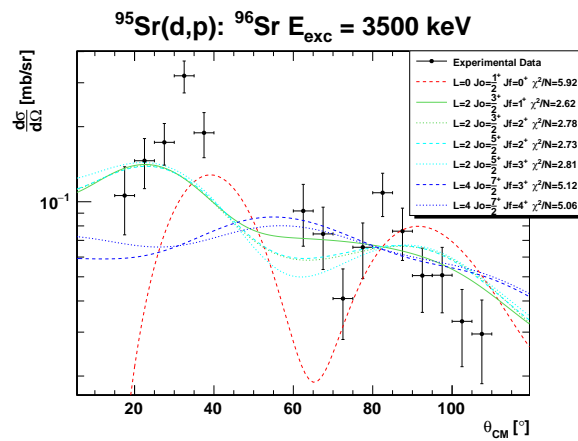
Figure 5.29: Angular distribution for ^{95}Sr(d,p) to ^{96}Sr 3500 keV state.

Chapter 6

Interpretation

In this chapter, the experimental results for ^{94}Sr(d,p) and ^{95}Sr(d,p) are discussed. Both data sets are compared to energy levels and spectroscopic factors that were calculated using the shell model. The results are also compared to other experiments and calculations, where available.

As was discussed in section 5.1, the absolute experimental spectroscopic factors were found to be strongly dependent on the optical potential that was used in the DWBA calculations. The shell model calculations predict significantly larger spectroscopic factors than were measured in both data sets, which also indicates that the absolute scaling of the experimental values is not well known. However, since the ratio of spectroscopic factors within a given data set are independent of the unknown absolute scaling factor, the relative spectroscopic strengths within each data set are still meaningful.

For this reason, the experimental spectroscopic factors are discussed relative to the ground state spectroscopic factor when they are compared to the shell model calculations.

6.1   Discussion of ^{94}Sr(d,p) results

6.1.1   Comparison to ^{94}Sr(d,p) Shell Model Calculations

The shell model code NushellX [BR14] was used to calculate the energy levels and wavefunctions of ^{94,95,96}Sr using two model spaces and interactions; jj45 [EHJH$^+$93] and glek [MWG$^+$90]. As was discussed in section 1.4, the glek interaction and model space was found to be more suitable for describing the energy levels in Sr isotopes than the jj45 interaction. For this reason, only the glek calculation results are compared to the results from this experimental work.

Spectroscopic factors for ^{94}Sr(d,p) were calculated in the shell model so that the experimental

results could be compared to shell model configurations. This is carried out by calculating the wavefunction overlap between the ^{94}Sr ground state plus a neutron in a single valence orbital with numerous states in ^{95}Sr. In this section, the experimental spectroscopic factors are compared to shell model results for each of the model spaces that were discussed in section 1.4, also allowing for the investigation of the effect of the proton degrees of freedom on the spectroscopic factors.

Table 6.1 compares the ^{94}Sr(d,p) experimental spectroscopic factors to the shell model results.

E [keV]	J^π	$\mathcal{SF}$ [This Work]	$\mathcal{SF}$ [glek] : ⓐ	$\mathcal{SF}$ [glek] : ⓑ	$\mathcal{SF}$ [glek] : ⓒ
0	$\frac{1}{2}^+$	1.00 (0.087)	1.00 (0.553)	1.00 (0.453)	1.00 (0.413)
352	$\frac{3}{2}^+$	1.40±0.24 (0.122)	1.56 (0.865)	1.69 (0.767)	1.80 (0.744)
681	$\frac{5}{2}^+$	0.52±0.14 (0.045)	0.26 (0.146)	0.39 (0.177)	0.49 (0.202)

Table 6.1: Comparison of experimental to calculated spectroscopic factors for ^{94}Sr(d,p), relative to the $\frac{1}{2}^+$ state spectroscopic factor. Values in parentheses are absolute spectroscopic factors. ⓐ, ⓑ and ⓒ denote the different model spaces that were calculated with the glek interaction, as discussed in section 1.4.

The model spaces ⓐ, ⓑ and ⓒ have the same meaning as in section 1.4 and so they correspond to a closed proton $1p\frac{3}{2}$ core, an intermediate $1p\frac{3}{2} + 1p\frac{1}{2}$ proton valence space and a larger $1p\frac{3}{2} + 1p\frac{1}{2} + 0g\frac{9}{2}$ valence space, respectively. Once again, a maximum of two protons were permitted to occupy the $0g\frac{9}{2}$ orbital in model space ⓒ. Each of the three models predicted similar spectroscopic factors of the excited ^{95}Sr states relative to the $\frac{1}{2}^+$ ground state spectroscopic factor, as can be seen in table 6.1. It can be seen in table 6.1 that calculated ground state spectroscopic factor decreases from 0.553 in model space ⓐ to 0.453 in model space ⓑ to 0.413 in model space ⓒ. This indicates that the added proton degrees of freedom cause further fragmentation of the wavefunctions which reduces the spectroscopic factors. In a full model space calculation it is expected that the calculated spectroscopic factors would be even smaller. Once again, while the absolute values of the experimental spectroscopic factors are

considerably lower than the shell model calculations it may be that this is due to uncertainty in the absolute scaling factor and the truncated space of the calculations.

The calculated spectroscopic factor of the first excited $\frac{3}{2}^+$ ^{95}Sr state relative to the calculated $\frac{1}{2}^+$ ground state calculated spectroscopic factor is consistent with the experimental value of 1.40(24) for all of the model spaces. The larger spectroscopic factor for the $\frac{3}{2}^+$ excited state compared to the $\frac{1}{2}^+$ ground state that can be seen in table 6.1 simply reflects that there are more available substates within the $1d\frac{3}{2}$ orbital than in the $2s\frac{1}{2}$ orbital that can be populated by the transferred neutron. In other words, the total spectroscopic strength for an empty valence orbital is equal to $2j+1$, which is called the transfer reaction sum rule. In reality, the mixed wavefunction of the ^{94}Sr ground state contains nonzero occupations of valence orbitals which are above the Fermi energy and so the total spectroscopic strength for each of the orbitals is $2j+1-\langle\hat{n}\rangle$. Similarly, the mixed wavefunction contains partially unfilled orbitals below the Fermi energy such as the $1d\frac{5}{2}$, and so there is also some spectroscopic strength which is available for this orbital.

The calculations predict a low-lying $\frac{5}{2}^+$ state with substantial spectroscopic strength. The spectroscopic strength of this state relative to the ground state steadily increases as more proton orbitals are included in the model space, which is a result of the wavefunctions further fragmenting within the larger model spaces. The calculations predict a spectroscopic factor for the low-lying $\frac{5}{2}^+$ state to be 0.39 and 0.49 of the ground state strength in model spaces ⓑ and ⓐ, respectively. These values are in good agreement with the experimental spectroscopic factor of the 681 keV ^{95}Sr state, which was found to be 0.52(14) of the ground state for $\ell = 2$, $j = \frac{5}{2}^+$. The shell model calculations did not predict significant spectroscopic strength for higher lying $\frac{3}{2}^+$ states in any of the model spaces. The combined spectroscopic strength of all of the higher lying $\frac{3}{2}^+$ states up to 2 MeV was found to be on the order of 20% of the ground state spectroscopic factor, which indicates that these states would not be observed in this experiment. In addition, large scale shell model calculations that have been carried out for ^{97}Zr (N=57) also predict a low-lying $\frac{5}{2}^+$ state and a second $\frac{3}{2}^+$ state at a much higher energy [HEHJ+00] [SNL+09]. Taken together, it is therefore very likely that the 681 keV ^{95}Sr state,
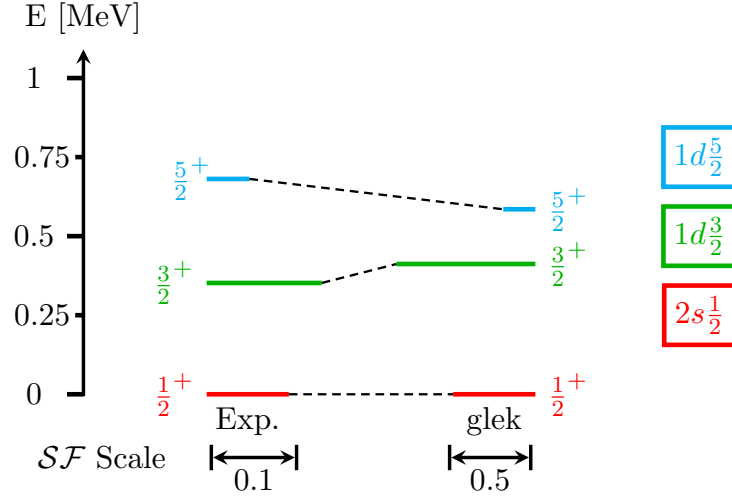
Figure 6.1: Selected low-lying ^{95}Sr states compared to shell model calculations, where the length of each line represents the spectroscopic factor. The ground state spectroscopic factors are normalized to one, and all excited state spectroscopic factors are drawn relative to the ground state.

which has a previous assignment of $(\frac{3}{2}^+, \frac{5}{2}^+)$ has spin and parity of $\frac{5}{2}^+$.

The spectroscopic factors and level energies that were calculated using model space ⓑ give the best overall agreement with ^{94}Sr(d,p) experimental data. Figure 6.1 compares the ^{94}Sr(d,p) experimental spectroscopic factors to the shell model results using model space ⓑ.

The substantial spectroscopic strength of a low energy $\frac{5}{2}^+$ in ^{95}Sr is an interesting experimental result. A simplistic, independent particle model description of the ground state of ^{94}Sr would predict that the neutron $1d\frac{5}{2}$ orbital is fully occupied. In this case, a neutron could not be added to the already full $1d\frac{5}{2}$ orbital and so the spectroscopic factor for a $\frac{5}{2}^+$ state in ^{95}Sr would be zero. The significant spectroscopic strength of the 681 keV $\frac{5}{2}^+$ state in ^{95}Sr suggests that the ground state wavefunction of ^{94}Sr does not consist of a fully occupied $1d\frac{5}{2}$ orbital, and so contains a substantial component of $[2s\frac{1}{2}]^2$, $[1d\frac{3}{2}]^2$ and possibly $[0g\frac{7}{2}]^2$ configurations. Substantial occupation of the neutron $2s\frac{1}{2}$ orbital in the ground state wavefunction of ^{94}Sr would also inhibit the spectroscopic strength of $\ell = 0$ transfer, which would lower the absolute spectroscopic factor for the $\frac{1}{2}^+$ ^{95}Sr ground state. This is consistent with the experimental findings.

In conclusion, it can be seen in table 6.1 that adding proton degrees of freedom in the valence space of the calculation leads to more fragmented wavefunctions, which reduces the pure single particle character and spectroscopic factors of the states. Further fragmentation of the shell model wavefunctions is expected to occur as the valence space (and hence the number of possible configurations) of both protons and neutrons increases in the calculations. The dependence of the calculated spectroscopic factors on proton degrees of freedom indicates that proton excitations cannot be neglected when describing the low energy states in ^{95}Sr. Such fragmentation of the wavefunctions may also explain the small absolute spectroscopic factors that were extracted in this experiment.

Large scale shell model calculations which include fully optimized SPEs and more proton and neutron degrees of freedom, such as the full proton $0g\frac{9}{2}$ orbital, would be an important next step towards an improved description of ^{95}Sr, however such calculations are beyond the scope of this thesis.

Comparison to Other Experiments

We can also compare the relative ^{94}Sr(d,p) spectroscopic factors from this work to other (d,p) experiments which populated states in N=57 nuclei close to A=100. At this time, the only neutron transfer studies that have been performed in this mass region are ^{96}Zr(d,p)^{97}Zr (Z=40) [BF73] and ^{98}Mo(d,p)^{99}Mo (Z=42) [MM69], and so the results of this work are compared to these experiments in this section.

As ^{95}Sr, ^{97}Zr and ^{99}Mo are all N=57 nuclei, their neutron configurations can be compared by using the spectroscopic factors of the first few states. Differences that arise between the spectroscopic factors of these experiments can be used to discuss the changing effective single particle energies and proton degrees of freedom in the low-lying states.

In ^{97}Zr (Z=40), the relative energy spacing and branching ratios of the $\frac{3}{2}^+$, $\frac{7}{2}^+$ and $(\frac{3}{2}^+,\frac{5}{2}^+)$ low-lying excited states are very similar to the low-lying states states in ^{95}Sr [Lab]. However,

the energy of the first excited $(\frac{3}{2}^+)$ state is at 1103 keV which is quite large for an even-odd nucleus. This can be explained by a Z=40 proton sub-shell closure, due to a significant energy gap between the full $1p\frac{1}{2}$ proton orbital and the empty $0g\frac{9}{2}$ proton orbital. The residual interaction between nucleons provides additional correlation energy by mixing different configurations. A large energy gap between the $1p\frac{1}{2}$ and $0g\frac{9}{2}$ orbitals would suppress the scattering of protons from the $1p\frac{1}{2}$ orbital into the $0g\frac{9}{2}$ and correlation energy associated with these mixed configurations would not be available. This would therefore increase the energy of the low-lying ^{97}Zr states compared to those in ^{95}Sr.

Contrastingly, in ^{99}Mo (Z=42) there are 18 excited states in ^{99}Mo below 1 MeV [Lab]. Two valence protons occupy the $0g\frac{9}{2}$ orbital above the full $1p\frac{1}{2}$ (Z=40) sub shell, which allows strong configuration mixing to take place between valence neutrons and protons. The interactions between the valence nucleons provides a large amount of correlation energy and results in a high density of low energy states. This is further supported by the very low-lying $\frac{11}{2}^-$ state in ^{99}Mo at 684 keV, which is above 2 MeV in excitation energy in ^{95}Sr and ^{97}Zr. Table 6.2 compares the relative spectroscopic factors from this work to results for $^{96}Zr(d,p)$ and $^{98}Mo(d,p)$.

J^π	$\mathcal{SF}$ [this work]	$\mathcal{SF}$, $^{96}Zr(d,p)$ [BF73]	$\mathcal{SF}$, $^{98}Mo(d,p)$ [MM69]
$\frac{1}{2}^+$	1.00 (0.087)	1.00 (1.02)	1.00 (0.67)
$\frac{3}{2}^+$	1.40±0.24 (0.122)	0.67 (0.68)	0.64 (0.43)
$\frac{5}{2}^+$	0.52±0.14 (0.045)	†	0.31 (0.21)

Table 6.2: Experimental spectroscopic factors for N=57 nuclei relative to the ground state spectroscopic factor. Values in parentheses are absolute spectroscopic factors. † no $1d\frac{5}{2}$ analysis was carried out for the $^{96}Zr(d,p)$ experiment, and so all $\ell = 2$ transfer states were assumed to be $\frac{3}{2}^+$.

The relative spectroscopic factors of the excited $\frac{3}{2}^+$ states compared to the ground state in $^{96}Zr(d,p)$ and $^{98}Mo(d,p)$ are significantly different to $^{94}Sr(d,p)$. In this work, the spectroscopic factor of the 352 keV $\frac{3}{2}^+$ ^{95}Sr state was found to be 1.40(24) relative to the ground state. Contrastingly, the spectroscopic strength of the first excited $\frac{3}{2}^+$ state in ^{97}Zr and ^{99}Mo was found to be less than that of the ground state. In the $^{96}Zr(d,p)$ experiment, it was assumed that the

$d\frac{5}{2}$ orbital was fully occupied and so every $\ell = 2$ orbital angular momentum transfer that was measured was assumed to be from population of the $d\frac{3}{2}$ orbital.

Most of the spectroscopic strength for the valence neutron orbitals was found to reside in the first state of each spin and parity in ^{97}Zr. This suggests that these low energy states are well described by pure single particle excitations. In ^{99}Mo, the spectroscopic strength was found to be more fragmented across several states, again indicating that the configurations were more mixed.

The significant discrepancies between the measured spectroscopic factors in ^{94}Sr(d,p), ^{96}Zr(d,p) and ^{98}Mo(d,p) further supports the conclusion that proton degrees of freedom play an important role even at low energies.

6.2   Discussion of ^{95}Sr(d,p) results

6.2.1   Comparison to ^{95}Sr(d,p) Shell Model Calculations

Spectroscopic factor calculations were carried out for ^{95}Sr(d,p) in NushellX using the same interaction and valence space as the ^{94}Sr(d,p) calculations. In this section, model spaces ⓑ and ⓒ are compared to the ^{95}Sr(d,p) experimental results.

Figure 6.2 compares the experimental spectroscopic factors to the calculation results using both model spaces. Only calculated spectroscopic factors greater than 0.03 (approximately 5% of the ground state strength) are shown in figure 6.2. There are many more calculated states with smaller (1-5%) spectroscopic factors. The calculations did not predict any significant spectroscopic strength for the $1d\frac{5}{2}$ orbital, which is in contrast to the calculation results for ^{94}Sr(d,p). This can be interpreted as a mostly full $1d\frac{5}{2}$ orbital in the ground state of ^{95}Sr, as can be seen in table 6.4. This is because the $\frac{1}{2}^{+}$ ground state of ^{95}Sr contains an unpaired neutron in the $2s\frac{1}{2}$ orbital, which prevents neutron pairs from being scattered into the $2s\frac{1}{2}$ orbital from the lower lying $1d\frac{5}{2}$ orbital. Instead, they must scatter into the higher-lying $1d\frac{3}{2}$ orbital to vacate the $1d\frac{5}{2}$ which is a less energetically favourable configuration.

There are substantial differences between the calculated states and the known low-lying ^{96}Sr states and so it is difficult to quantitatively compare the experimental results to the calculations. Additionally, many of the excited ^{96}Sr states do not have firm spin and parity assignments and so choosing which experimental state corresponds to each calculated state can be ambiguous. For this reason, figure 6.2 presents the calculated levels which have substantial spectroscopic factors alongside the experimental data so that qualitative similarities can be seen. The calculations correctly predict that there is substantial spectroscopic strength for the $1d\frac{3}{2}$ and $0g\frac{7}{2}$ orbitals at approximately 2 MeV, which is distributed across several states. Both of the models predict a strongly populated $\ell = 2, J^\pi = 1^+$ state at $\sim$2 MeV which is in agreement with the experimental result for the $(1^+, 2^+)$ 1995 keV ^{96}Sr state. There is, however, no prediction for any strongly populated $\ell = 2$ or $\ell = 4$ states above 3 MeV in either calculation which is in disagreement with the experimental results. At higher excitation energies, the truncated model spaces will have an increasingly important effect on the calculated states. This is because configurations that are explicitly excluded, such as proton excitations from the $0f\frac{5}{2}$ orbital [TTO$^+$16] and neutron excitations into the $0h\frac{11}{2}$ orbital, will become increasingly important [RUSU$^+$09]. Furthermore, the limited occupation of two protons in the $0g\frac{9}{2}$ orbital will also increase the systematic error in the calculated wavefunctions as the excitation energy increases. The substantial differences between experiment and theory indicate that more comprehensive large scale shell models are required for this nucleus.

The spectroscopic factors of the 1229 and 1465 keV 0^+ states are combined into a single spectroscopic factor in figure 6.2, which is drawn at an excitation energy of 1347 keV. This represents the total $2s\frac{1}{2}$ strength in the excited 0^+ states which is associated with a spherical configuration. As was discussed in section 1.3, the excited 0^+ states would be closer together in energy in the absence of mixing between the spherical and deformed 0^+ configurations. Given that the excited 0^+ states have been found to contain about equal mixtures of spherical and deformed configurations, the unperturbed energies of both configurations would be nearly degenerate and halfway between the experimental energies (which is 1347 keV). The deformed configuration in the excited 0^+ states would not be predicted in the shell model, and so this is
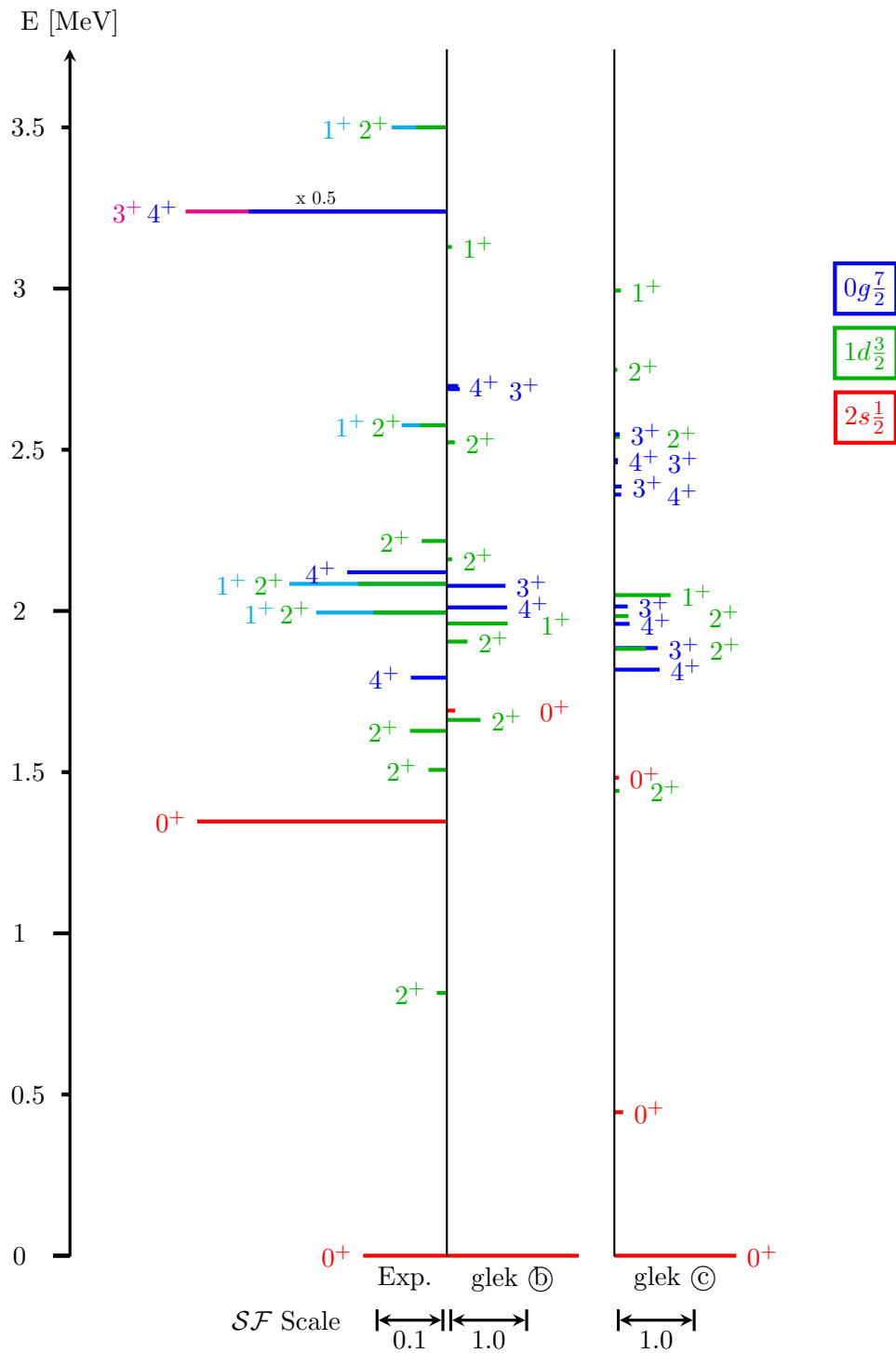
Figure 6.2: Selected low-lying ^{96}Sr states compared to shell model calculations, where the length of each line represents the spectroscopic factor. The experimental ground state spectroscopic factor is normalized to one, and all experimental excited state spectroscopic factors are drawn relative to the ground state. The calculated spectroscopic factors are drawn to scale (more details in the text).

not included in figure 6.2.

The spectroscopic factors for the 0^+ states are significantly different to the experimental results. The addition of the proton $0g\frac{9}{2}$ orbital in model space ⓒ lowered the energy of the first excited 0^+ state to well below the experimental value, which may indicate that the SPE of the $0g\frac{9}{2}$ is too low. Table 6.3 compares the spectroscopic factors for the ^{96}Sr 0^+ states to the shell model calculations.

J^π	$\mathcal{SF}$ [This Work]	$\mathcal{SF}$ [glek] : ⓑ	$\mathcal{SF}$ [glek] : ⓒ
0_1^+	1.00 (0.114)	1.00 (1.575)	1.00 (1.455)
0_2^+	2.98±0.79 (0.34)	0.06 (0.098)	0.07 (0.105)

Table 6.3: Comparison of experimental to calculated spectroscopic factors for 0^+ states in ^{96}Sr, relative to the ground state spectroscopic factor. Values in parentheses are absolute spectroscopic factors. ⓑ and ⓒ denote the different model spaces that were calculated with the glek interaction, as discussed in section 1.4.

The ground state of ^{96}Sr was calculated to contain approximately 90% of the $2s\frac{1}{2}$ spectroscopic strength. This is not in agreement with the experimental result, which indicates that the ground state contains at most ∼25% of the $2s\frac{1}{2}$ spectroscopic strength. This large discrepancy can be addressed further by comparing the underlying orbital occupancies for each of the 0^+ states in ^{96}Sr to the ^{95}Sr ground state. These occupation numbers are given in table 6.4, where orbital can contain a maximum of $2j + 1$ nucleons. It can be seen that the calculated occupation numbers for the ground state of ^{95}Sr are very similar to the ground state of ^{96}Sr for both of the models. Additionally, both wavefunctions are calculated to contain almost pure seniority (ν) zero configurations, where all nucleon pairs are coupled to $J = 0$. This makes a single step transfer between the two states possible, as there is minimal re-coupling required to transition between the states.

On the other hand, there is a significant difference between the calculated occupation numbers for the ground state of ^{95}Sr and the excited 0^+ states in ^{96}Sr. The underlying single particle configurations for these states are therefore less similar to those in the ^{95}Sr ground state. Both

J^π	$\pi 1p\frac{3}{2}$	$\pi 1p\frac{1}{2}$	$\pi 0g\frac{9}{2}$	$\nu 1d\frac{5}{2}$	$\nu 2s\frac{1}{2}$	$\nu 1d\frac{3}{2}$	$\nu 0g\frac{7}{2}$	Seniority, $\nu = 0$ [%]
ⓑ ^{95}Sr $\frac{1}{2}^+$	3.90	0.10	0.00	5.54	1.03	0.37	0.05	94.5
ⓑ ^{96}Sr 0_1^+	3.92	0.08	0.00	5.47	1.87	0.55	0.10	95.7
ⓑ ^{96}Sr 0_2^+	3.76	0.24	0.00	4.48	1.48	1.38	0.67	83.4
ⓑ ^{96}Sr 0_3^+	3.64	0.36	0.00	4.11	1.28	1.14	1.48	73.4
ⓒ ^{95}Sr $\frac{1}{2}^+$	3.43	0.10	0.47	5.48	1.03	0.38	0.11	94.1
ⓒ ^{96}Sr 0_1^+	3.36	0.09	0.56	5.19	1.82	0.62	0.37	90.6
ⓒ ^{96}Sr 0_2^+	2.21	0.09	1.70	3.55	1.57	0.99	1.89	42.0
ⓒ ^{96}Sr 0_3^+	2.38	0.17	1.45	3.46	1.28	1.23	2.02	49.7

Table 6.4: Occupation numbers for the calculated ground state of ^{95}Sr and the 0^+ states in ^{96}Sr.

models predict that the excited 0^+ states contain a substantial component of $1d\frac{5}{2}$ two-particle two-hole $(2p-2h)$ excitations into the $1d\frac{3}{2}$ and $0g\frac{7}{2}$ orbitals. Model space ⓒ also predicts that the $[0g\frac{7}{2}]^2$ configurations are accompanied by proton $[0g\frac{9}{2}]^2$ configurations, which indicates that there is substantial correlation energy associated with these orbitals. This is consistent with the deformation-driving mechanism in this mass region that was put forward by Federman and Pitel [FP79], where the strong proton-neutron residual interaction between spin-orbital partner orbitals lowers the energy of deformed configurations. The occupation of the proton $0g\frac{9}{2}$ and neutron $0g\frac{7}{2}$ spin-orbit partner orbitals indicate that this indeed is a low energy configuration.

The excited 0^+ states in ^{96}Sr are also calculated to have significant $\nu \neq 0$ components in their wavefunctions. As a result of this, the ground state of ^{95}Sr would require additional nucleon pairs to be broken in order to populate the excited 0^+ states in ^{96}Sr through the transfer of a neutron, and so this process cannot be described as a simple single step process. The dissimilar configurations between the calculated ^{95}Sr ground state and excited 0^+ states in ^{96}Sr greatly reduce the spectroscopic factor, as can be seen in figure 6.2.

Comparison to Other Shell Model Work

The occupation numbers from this work can also be compared to shell model calculations for ^{97,98}Zr from [SNL+09] and [HEHJ+00], as is shown in table 6.5. It is expected that the neutron configurations for Sr and Zr will be similar. The occupation numbers for the ground state of ^{97}Zr are presented alongside the 0^+ states in ^{98}Zr so that their similarities can be discussed qualitatively.

J^π	$\pi 0f\frac{5}{2}$	$\pi 1p\frac{3}{2}$	$\pi 1p\frac{1}{2}$	$\pi 0g\frac{9}{2}$	$\nu 1d\frac{5}{2}$	$\nu 2s\frac{1}{2}$	$\nu 1d\frac{3}{2}$	$\nu 0g\frac{7}{2}$	$\nu 0h\frac{11}{2}$
[SNL+09] ^{97}Zr $\frac{1}{2}^+$	5.66	3.78	1.84	0.71	5.54	0.96	0.17	0.15	0.16
^{98}Zr 0_1^+	5.52	3.76	1.77	0.93	5.37	1.57	0.33	0.40	0.32
^{98}Zr 0_2^+	5.41	3.60	1.53	1.44	5.07	0.71	0.54	1.26	0.40
[HEHJ+00] ^{97}Zr $\frac{1}{2}^+$	6.00	4.00	1.91	0.09	5.73	0.99	0.15	0.03	0.11
^{98}Zr 0_1^+	6.00	4.00	1.91	0.09	5.76	1.87	0.17	0.06	0.15
^{98}Zr 0_2^+	6.00	4.00	1.56	0.44	5.50	0.26	1.26	0.72	0.27
^{98}Zr 0_3^+	6.00	4.00	0.59	1.41	5.49	0.58	0.98	1.46	0.19

Table 6.5: Occupation numbers for the calculated ground state of ^{97}Zr and the 0^+ states in ^{98}Zr from references [SNL+09] and [HEHJ+00].

The results in table 6.5 are in qualitative agreement with the neutron occupation numbers presented in table 6.4. The ground states of ^{97,98}Zr are predicted to have very similar occupation numbers to each other, which was also found in table 6.4. Additionally, the excited ^{98}Zr 0^+ states contain $1d\frac{5}{2}$ $2p - 2h$ excitations into the $1d\frac{3}{2}$ and $0g\frac{7}{2}$ orbitals, which would result in much smaller spectroscopic factors compared to ground state transfer.

To summarize, the present experimental findings for ^{95}Sr(d,p) show that there is approximately three times more spectroscopic strength for populating the excited 0^+ state in ^{96}Sr than the 0^+ ground state. This indicates that there is a larger overlap between the wavefunctions of the ground state of ^{95}Sr and the excited 0^+ ^{96}Sr configuration than the ^{96}Sr ground state. This inversion of spectroscopic strength was not correctly predicted by shell model calculations that were carried out using several different, although limited, model spaces. Large scale shell

model calculations with optimized SPEs and TBMEs in addition to a less restricted model space would therefore be an important next step to investigating this result further, although these calculations are beyond the scope of this thesis.

6.3 Mixing Between the Excited 0^+ States in ^{96}Sr

As was discussed in section 1.3, the very large $\rho^2(E0)$ value between the excited 0^+ states in ^{96}Sr is an indicator of shape coexistence. This means that there are two 0^+ configurations at effectively the same energy which have different shapes and significant mixing.

It is expected that one of the unmixed states is a strongly deformed configuration that would not be populated directly through the ^{95}Sr(d,p) reaction, while the other unmixed state is a nearly spherical configuration which would be populated through ^{95}Sr(d,p). A consequence of the mixing between the excited 0^+ states is that they will both contain some component of the spherical configuration, and so both can be populated through direct one-nucleon transfer. The γ-ray analysis of the 1465 keV ^{96}Sr state in section 5.3 indicates that the two excited 0^+ states were populated with approximately equal strengths through ^{95}Sr(d,p).

The measured relative population strength $\frac{S_3}{S_2} = 1.1(4)$ that was given in table 5.6 is consistent with a mixing strength of $b^2 = 1 - a^2 = 0.52(19)$ or $a^2 = 0.48(17)$. From this result the degree of quadrupole deformation, β, can be determined by rearranging equation 1.3

$$\beta = \sqrt[4]{\frac{16\pi^2}{9Z^2} \frac{\rho^2(E0)}{a^2(1-a^2)}} \tag{6.1}$$

and using the previously measured monopole strength $\rho^2(E0) = 0.185(50)$ from [Jun80] with the experimental value of $a^2 = 0.48(17)$ from this work. The uncertainty of the β value is calculated using the standard error propagation formula

$$\delta\beta = \sqrt{\left(\frac{\partial\beta}{\partial x}\right)^2 x^2 + \left(\frac{\partial\beta}{\partial y}\right)^2 \delta y^2} \tag{6.2}$$

139

where $x = \rho^2(E0)$ and $y = a^2$.

This gives a quadrupole deformation of $\beta = 0.31^{+0.03}_{-0.02}$. The small relative error in the calculated deformation arises because the partial derivative $\frac{\partial \beta}{\partial y}$ is effectively zero for $y = a^2 \sim 0.5$. Figure 6.3 shows a plot of equation 6.1, illustrating the uncertainties of a^2, $\rho^2(E0)$ and β.
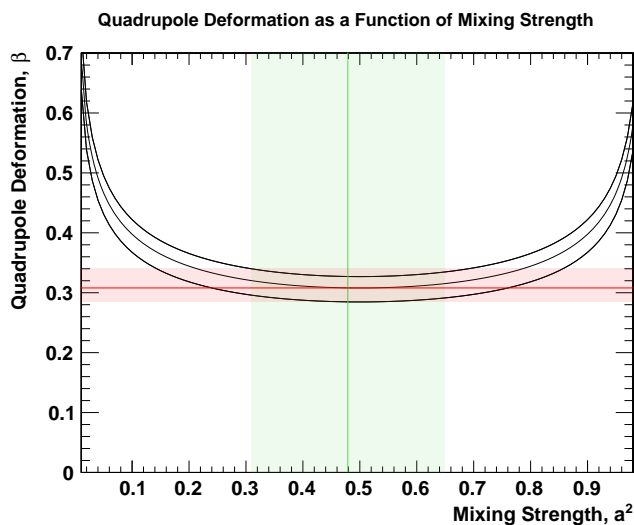
Figure 6.3: Quadrupole deformation as a function of mixing strength for a monopole transition strength $\rho^2(E0) = 0.185(50)$. The drawn bands represent 68% confidence intervals.

The mixing strength that was determined in this work can also be discussed in a broader context. Taking the two excited 0^+ states in ^{96}Sr as having equal components of spherical and deformed configurations, one would expect approximately equal populations of these states through other reactions and also through decays from higher-lying states. There are four higher-lying states which are known to feed the 1229 keV state. These states, with their branching ratios, are summarized in table 6.6.

Given a mixing ratio of $a^2 \sim 0.5$, the matrix element for the γ-ray transition between a higher-lying state and each of the excited 0^+ states would be the same. For this reason, the relative branching ratios for decay to the 1229 keV state and the 1465 keV state would be related by the energy dependence of the transition, which follows $E^{2\ell+1}$ for a transition with multipolarity ℓ. At this time, none of the decay branches to the 1465 keV state have been measured.

State Energy [keV]	$\mathcal{B}_{exp}^{1229}$	$\mathcal{B}_{calc.}^{1465}$ [M1]	$\mathcal{B}_{calc.}^{1465}$ [E2]
1628	5.3(4)	0.36(3)	0.06(1)
1995	5.0(4)	1.66(1)	0.79(6)
2084	51(4)	19.4(15)	10.1(8)
2217	8.3(11)	3.66(5)	2.12(3)

Table 6.6: Branching ratios for states which are known to feed the 1229 keV ^{96}Sr state, expressed relative to the strongest decay branch. Estimated branching ratios to the 1465 keV state are also given, assuming a mixing strength of $a^2 = 0.5$, for a pure M1 and a pure E2 transition (as labelled).

Nevertheless, for many of the states in table 6.6 the calculated branching ratios can be seen to be very small and so may be beyond sensitivities of previous experiments. The exception to this is the rather strong 2084 keV→1229 keV transition, which would have been measured in the work of Jung [Jun80]. Given that the spin of the 2084 keV state is not firmly established, both M1 and E2 multipolarities could contribute to the transition to the 1465 keV state, which would predict a branching ratio of at least 20% of the 2084 keV→1229 keV strength. If we instead assume a mixing strength of $1 - a^2 = 0.3$, which is the lower limit from this work, the ratio of matrix elements between the 1465 keV state and 1229 keV would drop to 0.43 and so the calculated branching ratio to the 1465 keV state would drop by more than a factor of two.

In the recent work of Clément et al. [CZP$^+$16b], a measurement was made of the shape of the 1229 keV excited 0$^+$ state, while there was no observation of the 1465 keV state. It is not known at this time whether the experiment had sufficient sensitivity to measure both states, or whether the long lifetime of the 1465 keV state prevented a γ-ray analysis from being carried out.

Taken together, these experimental results favour a smaller mixing strength, where the 1229 keV state contains more of the spherical configuration and the 1465 keV state is dominated by the deformed configuration.

One can also use the measured mixing ratio to estimate the interaction strength, V, between

the 0^+ configurations. In section 1.3, the coexisting 0^+ configurations were described using a two-level mixing model. The experimental result of effectively 50:50 mixing between the configurations simplifies this discussion considerably as it indicates that the unmixed states were degenerate in energy. As a result, the energy spacing between the 1229 keV state and the 1465 keV state is entirely due to the interaction between them, or $\Delta E_p = 2V$. This gives an interaction strength of approximately 118 keV.

We can now use this result to discuss the observed transition from a spherical to a deformed ground state at $N = 60$ in the Sr isotopic chain. The deformed 0^+ configuration in ^{96}Sr is less strongly deformed than the ground state of ^{98}Sr, which has $\beta = 0.43$ [Par12]. The difference in deformation between these structures in ^{96}Sr and ^{98}Sr can be explained in terms of the two additional neutrons in ^{98}Sr. It is expected that the additional neutrons in ^{98}Sr will increase the occupancy of the neutron $0g\frac{7}{2}$ orbital, which in turn causes increases the occupancy of the proton $0g\frac{9}{2}$ spin-orbit partner orbital through the strong isoscalar residual $p - n$ interaction. It has been argued by Federman and Pittel [FP79] that this residual interaction is the driving mechanism behind the emergence of low energy deformed structures in these nuclei, and so the added neutrons will lower the energy of the deformed configuration further. Indeed, in ^{98}Sr the deformed structure becomes the lowest energy configuration available and so it is the ground state.

However, the mixing coefficient $b^2 = 1 - a^2$ for the coexisting 0^+ states in ^{98}Sr was measured to be $b^2 = 0.0146$ [Par12], which is much lower than has been observed in ^{96}Sr. The mixing coefficient is defined as

$$b = \frac{1}{\sqrt{1 + \left[\frac{R}{2} + \sqrt{1 + \frac{R^2}{4}}\right]^2}} \tag{6.3}$$

where $R = \frac{\Delta E_u}{V}$, V is the interaction strength between the unmixed configurations and ΔE_u is the energy spacing between the unmixed states, as before. In the weak mixing limit $(R \gg 1)$, the energy shift due to the mixing interaction V is very small, and so the perturbed energies

are approximately the same as the unperturbed energies ($\Delta E_p \sim \Delta E_u$) which gives

$$b \sim \frac{V}{\Delta E_u} \sim \frac{V}{\Delta E_p} \tag{6.4}$$

From this, the interaction strength can be determined using the experimental energy spacing between the coexisting 0^+ states in ^{98}Sr. Given that the excited 0^+ state is at 215 keV, the interaction strength $V \sim 26$ keV. Such an interaction strength predicts that the difference in the energies of the unmixed configurations is $\Delta E_u \sim 209$ keV.

From this analysis, the strong $\rho^2(E0)$ values between the low-lying 0^+ states in ^{96}Sr and ^{98}Sr appear to originate from different scenarios. In the case of ^{96}Sr, the unmixed configurations have a substantial deformation difference of $\beta \sim 0.31$ and are degenerate in energy. There is a strong interaction between the configurations ($V \sim 118$ keV) which causes an energy splitting of 235 keV and maximally mixed wavefunctions. Contrastingly, there is weak mixing in ^{98}Sr between 0^+ configurations that have a very large deformation difference of $\beta \sim 0.43$. The weak mixing is caused by an unperturbed energy difference of $\Delta E_u \sim 209$ keV and a weak interaction strength ($V \sim 26$ keV) between the coexisting 0^+ states.

From this, a picture of competing structures in the Z$\sim$40, N$\sim$60 region begins to emerge. There are both deformed and spherical structures which are available to the nucleus at low energy cost, which are a result of the rearrangement of a few nucleons across important valence orbitals (namely the $\pi 0g\frac{9}{2}$ and $\nu 0g\frac{7}{2}$ orbitals). There is a delicate interplay between the attractive pairing interaction which couples like nucleons to $J = 0$ and favours sphericity, and the attractive residual $p - n$ interaction which has a tendency to produce non-spherical shapes. As the number of neutrons increases in this mass region, the energy of the deformed structure is gradually lowered and the degree of deformation increases. At $N = 58$, it becomes degenerate in energy with low-lying excited spherical 0^+ configurations which causes very large mixing and correspondingly large $E0$ transition rates. At $N = 60$, a critical point is reached where the deformed structure becomes the lowest energy configuration available, and this new binding energy minimum stabilizes until the neutron drip line.

Chapter 7

Summary and Outlook

In this work, successful measurements were made of the spins, parities and single particle character of states in ^{95}Sr and ^{96}Sr through ^{94}Sr(d,p) and ^{95}Sr(d,p) in inverse kinematics, respectively. For the first time, a direct measurement has been made of the $[2s\frac{1}{2}]^2$ component of low-lying 0^+ states in ^{96}Sr through ^{95}Sr(d,p), which indicates that there is substantially more spectroscopic strength in the excited 0^+ state configuration than in the ground state. Based on a γ-ray intensity analysis, it was found that the 1229 keV and 1465 keV excited 0^+ states were populated with approximately equal intensity, and this measurement allows an experimental constraint to be placed upon the mixing strength between the underlying spherical and deformed configurations of $a^2 = 0.48(17)$.

Firm spin assignments have been made for the first time and spectroscopic factors have been extracted for the low-lying 352 keV, 556 keV and 681 keV excited states in ^{95}Sr, and a constraint has been made on the spin of the higher-lying 1666 keV excited state in ^{95}Sr. These results have been compared to shell model calculations, and the agreement between calculated and experimentally determined spectroscopic factors for ^{95}Sr was found to be satisfactory. Similarly, spectroscopic factors have been extracted for 14 states in ^{96}Sr from ^{95}Sr(d,p), and new experimental constraints have been assigned to the spins and parities of 8 states in ^{96}Sr. Additionally, two new states have been added to the ^{96}Sr level scheme as of this work. While a detailed comparison of the experimental and theoretical ^{96}Sr spectroscopic factors was not possible at this time, it is my hope that large scale shell model calculations will be carried out so that the experimental results from this work can be further interpreted within the shell model. In particular, it remains a challenge to reproduce the experimentally observed $[2s\frac{1}{2}]^2$ component of low-lying 0^+ states in ^{96}Sr within the shell model.

During the 2013 and 2014 experiments, a substantial amount of ^{94,95}Sr(d,t) data was also taken, which is currently under analysis by one of the spokespeople for this experiment. In ^{94,95}Sr(d,t) reactions, a neutron is stripped from the Sr nuclei and so these reactions probe the overlap of the ^{94,95}Sr ground state wave function plus one neutron hole configurations with states in ^{93,94}Sr. These reactions are an excellent tool to study single particle structure and are very similar to (d,p) reactions, however they are suited to the study of occupied valence orbitals as opposed to empty orbitals in (d,p). Taken together, (d,p) and (d,t) experiments provide complimentary measurements of the configurations of valence neutrons across the valence orbitals. An analysis of the ^{94,95}Sr(d,t) data will also provide constraints on the spins and parities of states in ^{93,94}Sr, which are mostly unknown.

In addition, a ^{94}Sr(t,p) experiment has been approved at TRIUMF and will be undertaken some time in 2017. In ^{94}Sr(t,p), two neutrons are added to ^{94}Sr to populate states in ^{96}Sr. The cross section for this reaction favours the population of 0^+ states with configurations such as $[1d\frac{5}{2}]^2$, $[2s\frac{1}{2}]^2$, $[1d\frac{3}{2}]^2$ and $[0g\frac{7}{2}]^2$ where the two neutrons are added as an $S = 0$ pair in a single step. For this reason the ^{94}Sr(t,p) experiment will provide a very useful probe of the 0^+ states in ^{96}Sr. Furthermore, it is expected that this data will allow the experimental constraint of the mixing strength between the excited 0^+ states in ^{96}Sr to be further refined.

In conclusion, there are many exciting prospects for furthering our understanding of this region. The results from this thesis and combined with the (d,t) and (t,p) studies will constrain the spins and parities and elucidate the single particle configurations underlying states in ^{93,94,95,96}Sr. A systematic analysis of the underlying configurations of states across these nuclei will also offer a broad perspective of the role of evolving single particle structure in this transitional region. In turn, these experimental data will provide a benchmark for theoretical models which aim to describe shape coexistence in the N∼60, Z∼40 region, and we hope that this will further encourage the vibrant discussion that is taking place.

Bibliography

[Ago03] S. Agostinelli. GEANT4 - A Simulation Toolkit. *Nuclear Instruments and Methods in Physics Research Section A*, 506(3):250–303, 2003.

[BBD$^+$] P. C. Bender, V. Bildstein, R. Dunlop, et al. GRSISort - A Lean, Mean Sorting Machine (https://github.com/GRIFFINCollaboration/GRSISort) June 2017.

[BF73] C. R. Bingham and G. T. Fabian. Neutron Shell Structure in ^{93}Zr, ^{95}Zr, and ^{97}Zr by (d, p) and (n, He) Reactions. *Physical Review C*, 7(4), 1973.

[BG69] F. D. Becchetti and G. W. Greenlees. Nucleon-Nucleus Optical-Model Parameters, A>40, E<50 MeV. *Physical Review*, 182(1190), 1969.

[BHK16] G. C. Ball, G. Hackman, and R. Krücken. The TRIUMF-ISAC facility: Two Decades of Discovery with Rare Isotope Beams. *Physica Scripta*, 91(9), 2016.

[BR97] R. Brun and F. Rademakers. ROOT - An Object Oriented Data Analysis Framework. *Nuclear Instruments and Methods in Physics Research Section A*, 387, 1997.

[BR14] B. A. Brown and W. D. M. Rae. The Shell-Model Code NuShellX@MSU. *Nuclear Data Sheets*, 120, 2014.

[Cas00] R. F. Casten. *Nuclear Structure from a Simple Perspective*. Oxford Science Publications, 2 edition, 2000.

[Cat14] Wilton N. Catford. *The Euroschool on Exotic Beams, Vol. IV*, volume 879 of *Lecture Notes in Physics*. Springer Berlin Heidelberg, 2014.

[CZP$^+$16a] E. Clément, M. Zielińska, S. Péru, et al. Low-Energy Coulomb Excitation of ^{96,98}Sr Beams. *Physical Review C*, 94(5), 2016.

[CZP⁺16b] E. Clément, M. Zielińska, S. Péru, et al. Spectroscopic Quadrupole Moments in ⁹⁶,⁹⁸Sr : Evidence for Shape Coexistence in Neutron-Rich Strontium Isotopes at N=60. *Physical Review Letters*, 116(2):1–6, 2016.

[DCV80] W. W. Daehnick, J. D. Childs, and Z. Vrcelj. Global Optical Model Potential for Elastic Deuteron Scattering from 12 to 90 MeV. *Physical Review C*, 21, 1980.

[DFS⁺11] C. Aa. Diget, S. P. Fox, A. Smith, et al. SHARC: Silicon Highly-segmented Array for Reactions and Coulex used in Conjunction with the TIGRESS γ-ray Spectrometer. *Journal of Instrumentation*, 6(02):P02005–P02005, 2011.

[DKM14] J. Dilling, R. Krücken, and L. Merminga, editors. *ISAC and ARIEL: The TRIUMF Radioactive Beam Facilities and the Scientific Program.* Springer Netherlands, 1 edition, 2014.

[EHJH⁺93] T. Engeland, M. Hjorth-Jensen, A. Holt, et al. Structure of Neutron Deficient Sn Isotopes. *Physical Review C*, 48(2), 1993.

[EMS88] J. Eberth, R. A. Meyer, and K. Sistemich. *Nuclear Structure of the Zirconium Region*, volume 1. Springer-Verlag, 1988.

[Fes92] H. Feshbach. *Theoretical Nuclear Physics: Nuclear Reactions*, volume 2. John Wiley and Sons, 1992.

[FP79] P. Federman and S. Pittel. Unified Shell-Model Description of Nuclear Deformation. *Physical Review C*, 20(2), 1979.

[FPE84] P. Federman, S. Pittel, and A. Etchegoyen. Quenching of the $2p\frac{1}{2} - 2p\frac{3}{2}$ Proton Spin-Orbit Splitting in the Sr-Zr Region. *Physics Letters*, 140B, 1984.

[HEHJ⁺00] A. Holt, T. Engeland, M. Hjorth-Jensen, et al. Application of Realistic Effective Interactions to the Structure of the Zr Isotopes. *Physical Review C*, 61(August 1999):1–11, 2000.

[Hey90] K. Heyde. *The Nuclear Shell Model.* Springer-Verlag, 1 edition, 1990.

[HJS49] O. Haxel, J. H. D. Jensen, and H. E. Suess. On the "Magic Numbers" in Nuclear Structure. *Physical Review*, 75, 1949.

[Hod71] P. E. Hodgson. *Nuclear Reactions and Nuclear Structure*, volume 1. Clarenden Press, Oxford, 1971.

[HRH+04] J. K. Hwang, A. V. Ramayya, J. H. Hamilton, et al. High spin states in ^{95}Sr. *Physical Review C*, 69(067302), 2004.

[HW11] K. Heyde and J. Wood. Shape Coexistence in Atomic Nuclei. *Reviews of Modern Physics*, 83(December), 2011.

[Jam] F. James. MINUIT Function Minimization and Error Analysis (https://inspirehep.net/record/1258343?ln=en) June 2017.

[Jon13] K. L. Jones. Transfer Reaction Experiments with Radioactive Beams: From Halos to the R-Process. *Physica Scripta*, T152:014020, 2013.

[JPA+80] G. Jung, B. Pfeiffer, L. J. Alquist, et al. Gamma-Gamma Angular Correlations of Transitions in ^{94}Sr and ^{96}Sr. *Physical Review C*, 22(1), 1980.

[Jun80] G. Jung. *Nuclear Spectroscopy on Neutron Rich Rubidium With Even Mass Numbers.* PhD thesis, Justus Liebig-Universitat, Giessen, 1980.

[KAW77] G. E. Knoll, A. Arbor, and M. J. Wiley. *Radiation Detection and Measurement.* Wiley, 4th edition, 1977.

[Kra88] K. S. Krane. *Introductory Nuclear Physics.* John Wiley and Sons, 2 edition, 1988.

[Lab] Brookhaven National Laboratory. Evaluated Nuclear Structure Data File (http://www.nndc.bnl.gov/ensdf/) June 2017.

[LPK+94] G. Lhersonneau, B. Pfeiffer, K. L. Kratz, et al. Evolution of Deformation in the Neutron-Rich Zr Region from Excited Intruder State to the Ground State. *Physical Review C*, 49(3), 1994.

[Mat] A. Matta. NPTool, A ROOT/Geant4 Based Framework for Nuclear Physics (http://nptool.org/) June 2017.

[May49] M. G. Mayer. On Closed Shells in Nuclei. II. *Physical Review*, 75, 1949.

[MM69] J. B. Moorhead and R. A. Moyer. Nuclear-Structure Studies in Mo and Nb Isotopes via Stripping Reactions at 12 MeV. *Physical Review*, 184(4), 1969.

[MSI⁺16] P. Möller, A. J. Sierk, T. Ichikawa, et al. Nuclear Ground-State Masses and Deformations : FRDM (2012). *Atomic Data and Nuclear Data Tables*, 109-110:1–204, 2016.

[MWG⁺90] H. Mach, E. K. Warburton, R. L. Gill, et al. Meson-Exchange Enhancement of the First-Forbidden ^{96}Y(0^-) to ^{96}Zr(0^+) Beta Transition: Beta Decay of the Low-Spin Isomer of ^{96}Y. *Physical Review C*, 41(1), 1990.

[MXY⁺12] H. Mei, J. Xiang, J. M. Yao, et al. Rapid Structural Change in Low-Lying States of Neutron-Rich Sr and Zr Isotopes. *Physical Review C*, 85(3):1–10, 2012.

[Nob13] C. Nobs. Simulating and Testing the TRIUMF Bragg Ionisation Chamber. Master's thesis, University of Surrey, England, 2013.

[Par12] J. Park. Study of Shape Coexistence in ^{98}Sr, 2012.

[PP76] C. M. Perey and F. G. Perey. Compilation of Optical Model Parameters. *Atomic Data and Nuclear Data Tables*, 17(1-101), 1976.

[Rad] D. Radford. RadWare Software Package (http://radware.phy.ornl.gov/) June 2017.

[RGSR⁺10] R. Rodrguez-Guzman, P. Sarriguren, L. M. Robledo, et al. Charge Radii and Structural Evolution in Sr, Zr, and Mo Isotopes. *Physics Letters, Section B*, 691(4):202–207, 2010.

[RUSU⁺09] T. Rzạca-Urban, K. Sieja, W. Urban, et al. $(h\frac{11}{2},g\frac{7}{2})_{9^-}$ Neutron excitation in ^{92,94,96}Sr. *Physical Review C*, 79(2):2–11, 2009.

[Sat83] G. R. Satchler. *Direct Nuclear Reactions*. Oxford University Press, Oxford, 1983.

[SG14] C. E. Svensson and A. B. Garnsworthy. The GRIFFIN spectrometer. *Hyperfine Interactions*, 225(127-132), 2014.

[SNL+09] K. Sieja, F. Nowacki, K. Langanke, et al. Shell Model Description of Zirconium Isotopes. *Physical Review C*, 79(6):1–9, 2009.

[SPH+05] H. C. Scraggs, C. J. Pearson, G. Hackman, et al. TIGRESS Highly-Segmented High-Purity Germanium Clover Detector. *Nuclear Instruments and Methods in Physics Research Section A*, 543(2-3):431–440, 2005.

[Tho88] I. Thompson. Coupled Reaction Channels Calculations in Nuclear Physics. *Computer Physics Reports*, 7(167-212), 1988.

[TN09] I. Thompson and F. M. Nunes. *Nuclear Reactions for Astrophysics*. Cambridge University Press, 2009.

[TTO+16] T. Togashi, Y. Tsunoda, T. Otsuka, et al. Quantum Phase Transition in the Shape of Zr isotopes. *Physical Review Letters*, pages 1–5, 2016.

[V+91] R. L. Varner et al. A Global Nucleon Optical Model Potential. *Physics Reports*, 201(57), 1991.

[W+12] G. L. Wilson et al. Towards ^{26}Na via (d,p) with SHARC and TIGRESS and a Novel Zero-Degree Detector. *Journal of Physics: Conference Series*, 381(1), 2012.

[WHC+04] C. Y. Wu, H. Hua, D. Cline, et al. Multifaceted Yrast Structure and the Onset of Deformation in ^{96,97}Sr and ^{98,99}Zr. *Physical Review C*, 70(6):1–9, 2004.

[WZD+99] J. L. Wood, E. F. Zganjar, C. De Coster, et al. Electric Monopole Transitions from Low Energy Excitations in Nuclei. *Nuclear Physics A*, 651(4):323–368, 1999.

[ZZB10] J. F. Ziegler, M. D. Ziegler, and J. P. Biersack. SRIM - The Stopping Power and Range of Ions in Matter. *Nuclear Instruments and Methods in Physics Research Section B*, 268(1818-1823), 2010.

Appendix A

FRESCO

Figure A.1 gives an example FRESCO input file, which was used to calculate the DWBA cross section for ^{95}Sr(d,p) to the ^{96}Sr ground state assuming a pure $\left|^{95}\text{Sr}; \frac{1}{2}^{+}\text{g.s.}\right\rangle \otimes \left|\nu 2s\frac{1}{2}\right\rangle$ configuration.

```
95Sr(d,p)96Sr 0.000 MeV state l=0 total spin j=0 @ E = 5.378 MeV/u
NAMELIST
 &FRESCO
           hcm=0.1 rmatch=30.0 hnl=0.1 rnl=3.2 centre=-0.1 nnu=36 jtmax=30
           thmin=1.00 thmax=180.00 iter=1 chans=1 xstabl=1 elab=510.9 /

 &PARTITION
           namep='95Sr' massp=94.9194 zp=38 namet='d'    masst=2.0141   zt=1
           qval=0.000 pwf=F nex=1
           /
 &STATES
           jp=0.5 bandp=1            jt=1.0 bandt=1            cpot = 1 fexch=F /

 &PARTITION
           namep='96Sr' massp=95.9217 zp=38 namet='p'    masst=1.008   zt=1
           qval=3.654 pwf=F nex=1
           /
 &STATES
           jp=0.0 bandp=1 ep=0.000 jt=0.5 bandt=1 cpot=2 fexch=F/
 &partition /

 &POT      kp=1 ap=95 rc=1.300  / INCOMING CHANNEL: DETUERON + 95SR..
 &POT      kp=1 type=1 shape=0 p1=130.000 p2=0.970 p3=0.860 p4=0.000 p5=0.000 p5=0.000   / REAL VOLUME [WS]
 &POT      kp=1 type=2 shape=0 p1=0.000 p2=0.000 p3=0.000 p4=12.000 p5=1.250 p6=0.771   / IMAG SURFACE [WS]
 &POT      kp=1 type=3 shape=0 p1=7.000 p2=0.750 p3=0.500 p4=0.000 p5=0.000 p6=0.000   / SPIN ORBIT [WS]

 &POT      kp=2 ap=96 rc=1.250  / OUTGOING CHANNEL: PROTON + 96SR..
 &POT      kp=2 type=1 shape=0 p1=58.725 p2=1.250 p3=0.650 p4=0.000 p5=0.000 p5=0.000  / REAL VOLUME [WS]
 &POT      kp=2 type=2 shape=0 p4=0.000 p5=0.000 p6=0.000 p4=13.500 p5=1.250 p6=0.470  / IMAG SURFACE [WS]
 &POT      kp=2 type=3 shape=0 p1=7.500 p2=1.250 p3=0.470 p4=0.000 p5=0.000 p6=0.000  / SPIN ORBIT [WS]

 &POT      kp=3 ap=95 rc=1.3  / BINDING OF NEUTRON TO 95SR
 &POT      kp=3 type=1 shape=0 p1=50  p2=1.3  p3=0.66 / REAL VOLUME [WS]

 &POT      kp=4 at=1 rc=1.0  / BINDING OF NEUTRON TO PROTON
 &POT      kp=4 type=1 shape=2 p1=72.15  p3=1.538  p7=1.0 / REAL VOLUME [GAUS]

 &POT      kp=5 ap=96 rc=1.250  / INTERACTION BETWEEN CORES: PROTON TO 95SR [WS]
 &POT      kp=5 type=1 shape=0 p1=58.725 p2=1.250 p3=0.650 p4=0.000 p5=0.000 p5=0.000  / REAL VOLUME [WS]
 &POT      kp=5 type=2 shape=0 p4=0.000 p5=0.000 p6=0.000 p4=13.500 p5=1.250 p6=0.470  / IMAG SURFACE [WS]
 &POT      kp=5 type=3 shape=0 p1=7.500 p2=1.250 p3=0.470 p4=0.000 p5=0.000 p6=0.000  / SPIN ORBIT [WS]
 &pot /

 &OVERLAP
           kn1=1 ic1=1 ic2=2 in=2 kbpot=4 isc=1 nn=1 l=0 sn=0.5 j=0.5 be=2.225
           / N + P
 &OVERLAP
           kn1=11 ic1=2 ic2=1 in=1 kbpot=3 isc=1 nn=3 l=0 sn=0.5 j=0.5 be=5.879
           / N + 95Sr binding in 95Sr 0.000 MeV STATE
 &overlap
 / DESCRIBES THE BOUND STATE OF THE TRANSFERRED PARTICLE IN BOTH THE INITIAL AND FINAL STATE

 &COUPLING icto=2 icfrom=1 kind=7 ip1=0 ip2=-1 ip3=5 /
 &cfp      in=2 ib=1 ia=1 kn=1 a=1.0   / [DEUTERON]
 &cfp      in=1 ib=1 ia=1 kn=11 a=1.0  / [96Sr 0.000 MeV STATE]
 &cfp /
 &coupling /
```

Figure A.1: Example FRESCO input file for ^{95}Sr(d,p) to the ^{96}Sr ground state.

Appendix B

SHARC Solid Angles

A solid angle describes the two-dimensional angular coverage of an object in space, and is measured in steradians (sr). This is effectively an angular area. In spherical co-ordinates an infinitesimal solid angle $d\Omega$ is simply defined as

$$d\Omega = \sin\theta d\theta d\phi \tag{B.1}$$

and the total solid angle Ω is the closed surface integral over the angular range of the object

$$\Omega = \oint \sin\theta d\theta d\phi \tag{B.2}$$

which has a total integral over all possible angles of 4π. This is the maximum possible solid angle and physically reflects an object which is completely enclosed. For a non-spherical geometry, the general co-ordinate system-independent expression for the solid angle is defined as

$$\Omega = \oint \frac{\hat{\mathbf{r}} \cdot d\mathbf{A}}{r^2} \tag{B.3}$$

where $\hat{\mathbf{r}}$ is the unit vector from the origin and $d\mathbf{A}$ is an inifitesimal normal vector of the surface. The dot product $\hat{\mathbf{r}} \cdot d\mathbf{A}$ effectively maps this arbitrarily oriented surface element onto the unit sphere. The solid angle subtended by an object of fixed size decreases with its distance from the origin, which is accounted for by the $\frac{1}{r^2}$ term. This integral, computed over the entire surface $\mathbf{A}$, gives the total solid angle of any object from a given point in space. This expression can be used to calculate the total solid angle coverage of an array of separate objects, such as elements of a detector array.

The total acceptance of SHARC is the solid angle sum over all active detector regions. The most useful way to evaluate this sum is to divide the detector into a large set of small pixels and add up the solid angle of each of these. That way, individual strips can be easily excluded from the calculation if they are removed from the analysis.

SHARC has two principal sections, each with a symmetry which can be used to simplify the solid angle calculation. The QQQ detectors have cylindrical symmetry with respect to the beam axis and so the solid angle of each pixel in a QQQ can easily be calculated by simply using the θ and ϕ range subtended by the pixel as limits in equation B.2. The solid angle of pixels within the planar DSSD detectors are most readily calculated by converting to cartesian co-ordinates. For a surface in the x-z plane, equation B.3 simplifies to

$$\Omega = \int_{x_1}^{x_2} \int_{z_1}^{z_2} \frac{y}{(\sqrt{x^2 + y^2 + z^2})^3} dx dz = \left[\left[\arctan\left(\frac{xz}{y\sqrt{x^2+y^2+z^2}} \right) \right]_{x_1}^{x_2} \right]_{z_1}^{z_2} \tag{B.4}$$

where the integral limits can be chosen to calculate either an individual pixel or an entire strip. The calculated solid angle for all pixels of a DSSD detector and a QQQ detector are shown in figures B.1a and B.1b. The solid angles (in milli-steradian) are plotted as a function of strip
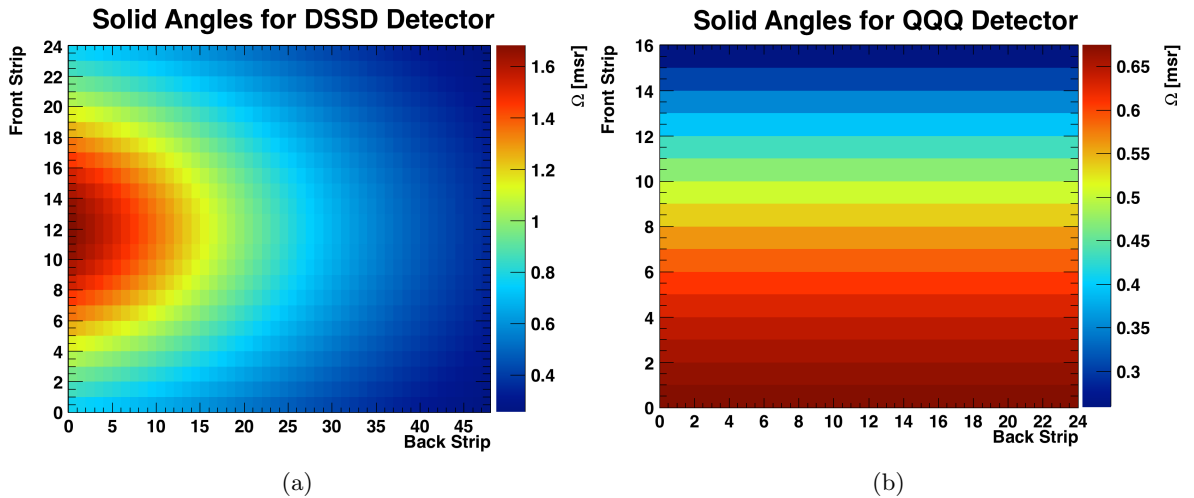
Figure B.1: Solid angle of each individual pixel in (a) a DSSD detector and (b) a QQQ detector.

number and not geometrical position, which is why the quadrant cylindrical geometry of a QQQ

detector is not shown in B.1b. As the number of counts in a given detector region is dependent on the solid angle of that detector element, these plots also describe the intensity pattern of a calibration source placed at the center of the array. The strips that were excluded from the analysis of the 2013 ^{94}Sr data set and the 2014 ^{95}Sr data set are listed in tables B.1 and B.1, respectively.

Detector	Front Strips Excluded	Back Strips Excluded
5	0, 23	47
6	0-23	0-47
7	0, 23	23, 39, 47
8	0, 23	41, 44, 47
9	1	2, 3, 21, 36, 46, 47
10	4, 12 ,19	21, 33, 35, 37
11	0, 1, 12, 16	11, 37
12	1, 2, 12	18, 28, 29, 32, 36
13	0-15	0-23
14	0-15	0-23
15	12	0, 5, 10, 11
16	6, 8	1, 16, 23

Table B.1: Summary table of SHARC the 204 strips that were excluded from the 2013 ^{94}Sr analysis.

Detector	Front Strips Excluded	Back Strips Excluded
5	0, 2, 3, 10, 13, 22, 23	24, 26 47
6	0, 1, 2, 3, 6, 23	0, 1, 2, 3, 3, 5, 37, 47
7	0, 2, 3, 5, 6, 7, 11	5, 6, 26, 41
8	0, 4, 6, 10, 13, 14, 17, 23	2, 10, 20, 24, 28, 29, 35, 38, 39, 40, 42, 44, 46
9	2, 6, 14	18, 36, 45
10	3, 7, 15	4, 5, 35, 47
11	2, 10	18, 25, 26, 29, 31, 33
12	2, 6	8, 35, 45
13	6, 7, 8, 9, 10	4, 16, 18, 19, 23
14	0	0, 23
15	0	1, 20, 23
16	5, 7, 9, 12	8, 16, 23

Table B.2: Summary table of SHARC the 107 strips that were excluded from the 2013 ^{95}Sr analysis.

Appendix C

Analysis Codes

The analysis for this project was carried out using the ROOT framework [BR97], which was adapted to suit the specific needs of this experiment. The data was stored as ROOT trees, and was sorted using the GRSISort package [BBD$^+$].

GRSISort

GRSISort [BBD$^+$] was founded and developed by P. C. Bender circa 2013, with ongoing development by the GRIFFIN collaboration. GRSISort is based on the ROOT framework, and provides additional detector classes which are designed to efficiently store the tree data and to describe in detail the geometry of detector systems such as SHARC and TIGRESS. The primary functionality of GRSISort is to produce lean trees which contain essential event information such as measured charges, calibrated energies, timestamps and addresses of detector elements.

A number of analysis tools have also been developed for GRSISort, several of which were my contributions. These are summarized as follows;

- TReaction - A relativistic two-body reaction kinematics class. The main feature of this tool is to calculate the kinematics of a general two-body reaction by using Lorentz transformations to boost between the laboratory (lab) frame and center-of-mass (CM) frame. This class was used to convert from measured lab frame kinetic energy to CM excitation energy, and to convert between lab and CM angles. Both of these functionalities were essential to the angular distribution analysis presented in this thesis. It was also used to determine the velocity of the recoil nucleus which was vital for the Doppler reconstruction of γ-rays. TReaction is also a useful tool for plotting kinematics curves, and was used to predict the angular coverage of SHARC for each of the reaction products.

- TNucleus - A nuclear data storage structure. TNucleus parses a mass file from [Lab] to look up the mass, Z and N of a given nucleus. By creating multiple instances of TNucleus, TReaction is able to determine the Q-value of reactions.

- TSRIM - An energy loss calculation tool. TSRIM parses the stopping power tables which are produced by the software package TRIM [ZZB10] to calculate the energy lost by ions in the target and in SHARC as a function of distance and energy. TSRIM was used extensively throughout this analysis to determine the reconstructed energy, as defined in equation 4.4.

A number of additional tools were also developed in order to make the analysis flexible and robust and to facilitate extensive consistency checks. The following short sections describe the main programs that were developed by myself for this thesis work.

TSharcAnalysis

TSharcAnalysis is a suite of functions that is designed to facilitate calibrations and analysis of SHARC experiments. The main functionalities are summarized as follows;

- Calculates the effective target and detector thicknesses as a function of angle (using formulae such as equations 4.2 and 4.3).

- Calculates the energy deposited by reaction products in SHARC by calculating energy losses in the target, detector dead layers and sensitive detector material (using TSRIM and TReaction). This functionality also works in reverse, and so can calculate the kinematic energy of the reaction products based on measured energies.

- Calculates the solid angle of each element within SHARC and uses this information to produce an acceptance curve (in both the lab frame and CM frame).

- Parses an optional bad strips file, which removes selected strips from the acceptance curve.

- Allows a position offset to be applied to the target within SHARC. An uncertainty can also be assigned to the target position, which is then included in the acceptance curve.

- Carries out simulated angular distribution measurements and particle spectra using DWBA curve outputs from FRESCO.

This code is freely available and can be found at `https://github.com/steffencruz/SharcAnalysis`.

TTigressAnalysis

TTigressAnalysis is a suite of functions for analysis of TIGRESS (plus SHARC) experiments. The primary analysis functionalities are summarized as follows;

- A separate program, MakeEasyMats, loops over the data trees to produce numerous 1D, 2D and 3D analysis histograms of excitation energy, γ-ray energy, and center-of-mass angle. These histograms are used as an input to TTigressAnalysis.

- TTigressAnalysis carries out projections on the 2D and 3D histograms from MakeEasy-Mats to create γ-gated and particle energy/angle gated histograms for analysis (such as those in figure 4.18).

- Calculates the TIGRESS absolute efficiency curve from raw data files and calculates the efficiency at any energy up to 4 MeV.

- Fits 1D γ-ray spectra to carry out background subtraction and to extract photo peak counts.

- Fits 2D γ-ray versus TIGRESS angle matrix as a series of 1D γ-ray energy spectra and fitting a user-specified photo-peak. In this way, the Doppler correction was examined by producing plots such as figure 4.11b. Angular correlations can also be calculated in a similar way.

In addition to these data analysis tools, a γ-ray simulation suite is also included in TTigress-Analysis. The main functions of this suite are summarized as follows;

- A text file containing the excitation energies, transition energies and transition intensities between states in a nucleus is parsed and us used to determine the photo-peak energies and areas of a theoretical γ-ray spectrum. Compton scattering effects are not included.

- The experimental efficiency and resolution of TIGRESS can be applied to the theoretical γ-ray spectrum to make realistic photo-peak spectra, which can also be gated on an excitation energy range.

- By adjusting the population strength of different states, a realistic γ-ray spectrum can be produced which reproduces the observed experimental γ-ray spectrum. These state strengths can also be saved and read for use across multiple sessions.

- Theoretical γ-gated γ-ray spectra and $γ - γ$ matrices can also be produced, and compared to data.

This code is freely available and can be found at `https://github.com/steffencruz/TigressAnalysis`.

TFrescoAnalysis

TFrescoAnalysis is a program that was developed to carry out DWBA analyses on the experimental angular distributions. The main functionalities are summarized as follows;

- Automatically constructs FRESCO files from various templates using a simple interactive user interface (within the GRSISort environment).

- Carries out DWBA calculations by running FRESCO in session with the generated input files.

- Fits data to calculated DWBA cross sections to extract normalization constant and spectroscopic factors.

- Enables multiple optical model parameters to be fitted in-session and parameter sets to be saved and read for use across multiple sessions.

- Performs $χ^2 + 1$ searches to give good estimations of parameter uncertainties

This code is freely available and can be found at `https://github.com/steffencruz/FrescoAnalysis`.

Appendix D

Low Energy Background in SHARC

A large quantity of β-decay was measured in the UBOX and UQQQ sections of SHARC. This was caused by the decay of radioactive beam-like nuclei in the downstream beam dump. Figure D.1a shows the overlaid ΔE energy spectrum for the UBOX and UQQQ sections in the 2014 ^{95}Sr experiment. It can be seen that the quantity of background data was substantially larger than the transfer data, with up to 100 times more statistics at very low energies.

Figure D.1b shows the γ-ray spectrum gated on all particles measured in the UBOX and UQQQ sections of SHARC for a series of different energy thresholds. For very low thresholds such as 400 keV and 600 keV, the γ-ray spectrum is dominated by the Doppler corrected β-decay transition lines. The Compton continuum created by these background γ-rays made it difficult to identify transitions from the nucleus of interest. An energy threshold of 1 MeV was therefore used in SHARC so that the γ-ray transitions of interest (those between states in ^{96}Sr in this example) were much larger in size than those from the β-decay background.
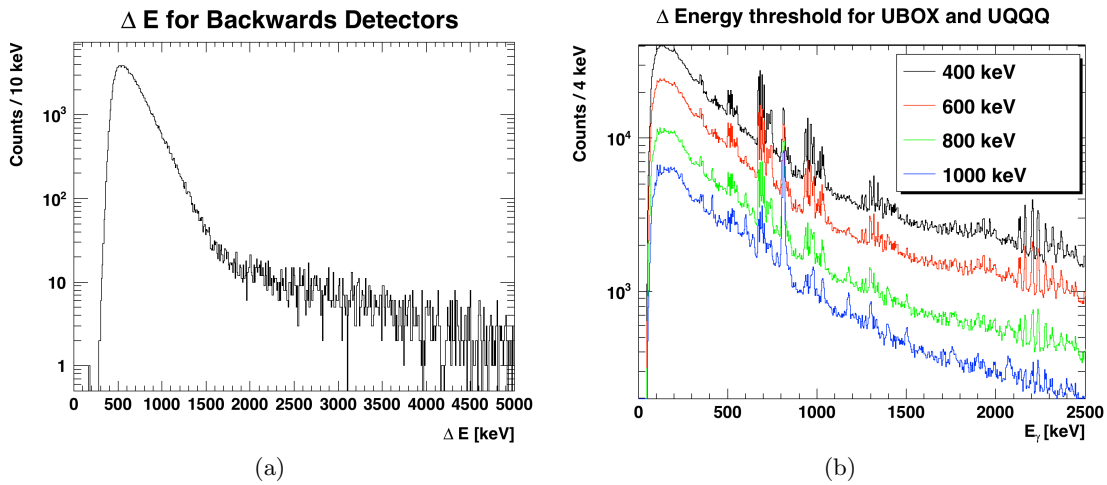
Figure D.1: (a) ΔE energy spectrum for upstream detectors. (b) γ-ray spectrum gated on particles with different threshold ΔE energy in upstream detectors.

Appendix E

Calculation of Electromagnetic Transition Rates

Electromagnetic transition rates can be calculated using the so-called Weisskopf approximation, which is a commonly used for order-of-magnitude estimates. This model assumes that the radiation is produced by the transition of a single nucleon within a nucleus of mass A from an initial state with energy E_i and spin I_i to a final state with E_f and I_f. The model assumes that there is maximal overlap between the initial and final wavefunction so that the matrix element for the transition is unity. In this way, the multipolarity and energy dependence of electromagnetic transitions can be studied [Cas00]. The emitted photon can carry angular momentum L which is restricted by the electromagnetic selection rules

$$|I_f - I_i| < L < I_f + I_i \tag{E.1}$$

Where L=0 is not allowed, since a photon has an intrinsic spin of $s = 1\hbar$. At a given multipole order, electric and magnetic transitions induce opposite parity changes.

$$\textbf{Electric:} \quad \Delta\pi \ = (-1)^L \tag{E.2}$$

$$\textbf{Magnetic:} \quad \Delta\pi \ = (-1)^{L+1} \tag{E.3}$$

All transitions that do not violate the selection rules will in principle occur, however contributions from higher multipole orders quickly become extremely small. In this way, only the first few multipole orders need to be considered when estimating electromagnetic transition rates. The total transition rate between two states is the sum of all possible multipole transitions. The transition rates for the first few multipole orders, $\lambda(\sigma L)$, are given in table E.1.

Multipole Order, L	$\lambda(EL)$	$\lambda(ML)$
1	$1.0 \times 10^{14} A^{\frac{2}{3}} E^3$	$5.6 \times 10^{13} E^3$
2	$7.3 \times 10^7 A^{\frac{4}{3}} E^5$	$3.5 \times 10^7 A^{\frac{2}{3}} E^5$
3	$34\ A^2 E^7$	$16\ A^{\frac{4}{3}} E^7$
4	$1.1 \times 10^{-5} A^{\frac{8}{3}} E^9$	$4.5 \times 10^{-6} A^2 E^9$

Table E.1: Weisskopf estimates for first few electromagnetic rates. Energy is in units of MeV.

In this work, positive parity to positive parity sates were studied, and so only M1, E2, M3 and E4 transitions need to be considered, which have relative strengths $1 : 1.4 \times 10^{-3} : 2.1 \times 10^{-10} : 1.3 \times 10^{-13}$. It is well known that E2 transition rates are frequently at least an order of magnitude larger than the Weisskopf estimates, suggesting that many nucleons participate in the transition. This is strong evidence for collectivity in nuclei. For this reason E2 transition rates can be comparable in magnitude to M1 rates. For an initial state that can decay to more than one final state, the transition rate is the sum of each individual (or partial) transition rates. The branching ratio for a given transition, B_i, is the ratio of the partial decay rate to the total decay rate.

$$B_i = \frac{\lambda_i}{\Sigma_k \lambda_k} \tag{E.4}$$

The branching ratios are usually expressed as a relative quantity so that the strongest transition is normalized to 100% strength. Table E.2 shows an example of calculated transition rates for the 2084 keV ^{96}Sr state using Weisskopf estimates. Each possible spin and parity assignment for the 2084 keV state leads to different prediction for the branching ratios to lower lying states.

Table E.3 compares these values to the measured branching ratios. All branching ratios in table E.3 are given relative to the strongest transition. The calculated Weisskopf estimates for the branching ratios were compared to experimental values using a χ^2 analysis.

$$\chi^2 = \sum \frac{(B_{\text{exp}} - B_W)^2}{\delta B_{\text{exp}}} \tag{E.5}$$

The branching ratios for $J^\pi = 1^+$ were in better agreement with the data than $J^\pi = 2^+$ and $J^\pi = 3^+$, indicating that this spin and parity assignment is the most likely. The significant

$J^{\pi}_{initial}$	E_{final} [MeV]	E_{γ} [MeV]	J^{π}_{final}	$\lambda(M1)$ [s^{-1}]	$\lambda(E2)$ [s^{-1}]	$\lambda(M3)$ [s^{-1}]	λ_{total} [s^{-1}]
$1^+, 2^+, 3^+$	1.507	0.577	2	$1.1\text{x}10^{13}$	$2.1\text{x}10^{9}$	$1.5\text{x}10^{2}$	$1.1\text{x}10^{13}$
1^+	1.229	0.855	0	$3.5\text{x}10^{13}$	$1.5\text{x}10^{10}$	$2.4\text{x}10^{3}$	$3.5\text{x}10^{13}$
2^+	1.229	0.855	0	-	$1.5\text{x}10^{10}$	$2.4\text{x}10^{3}$	$1.4\text{x}10^{10}$
3^+	1.229	0.855	0	-	-	$2.4\text{x}10^{3}$	$2.4\text{x}10^{3}$
$1^+, 2^+, 3^+$	0.815	1.269	2	$1.1\text{x}10^{14}$	$1.1\text{x}10^{11}$	$3.7\text{x}10^{4}$	$1.2\text{x}10^{14}$
1^+	0	2.084	0	$5.1\text{x}10^{14}$	$1.3\text{x}10^{12}$	$1.2\text{x}10^{6}$	$5.1\text{x}10^{14}$
2^+	0	2.084	0	-	$1.3\text{x}10^{12}$	$1.2\text{x}10^{6}$	$1.3\text{x}10^{12}$
3^+	0	2.084	0	-	-	$1.2\text{x}10^{6}$	$1.2\text{x}10^{6}$

Table E.2: Weisskopf estimates for the decay of the 2084 keV ^{96}Sr state to states with established spin and parity, using measured branching ratios from [Lab].

difference in calculated branching ratios between the 2084 keV to 1229 keV transition and 2084 keV to ground state transition is purely a result of the energy dependence of the Weisskopf formula. The experimentally measured values of 51% and 100% for these transitions indicates that the matrix elements could be significantly different, and that there may be enhanced E2 strengths due to collectivity in these transitions.

E_{final} [MeV]	E_{γ} [MeV]	$B_{\exp}$ [%]	B_W for $J^{\pi} = 1^+$ [%]	B_W, 2^+ [%]	B_W, 3^+ [%]
1.507	0.577	15.6(21)	2.1	9.4	9.4
1.229	0.855	51(4)	6.9	0.0	0.0
0.815	1.269	27(3)	22.5	100.0	100.0
0	2.084	100(11)	100	1.1	0.0
		χ^2/N	3.21	7.26	7.27

Table E.3: Weisskopf estimates for the decay of the 2084 keV ^{96}Sr state to states with established spin and parity, using known branching ratios.